



Universitat Autònoma de Barcelona

**ADVERTIMENT.** L'accés als continguts d'aquesta tesi queda condicionat a l'acceptació de les condicions d'ús establertes per la següent llicència Creative Commons:  [http://cat.creativecommons.org/?page\\_id=184](http://cat.creativecommons.org/?page_id=184)

**ADVERTENCIA.** El acceso a los contenidos de esta tesis queda condicionado a la aceptación de las condiciones de uso establecidas por la siguiente licencia Creative Commons:  <http://es.creativecommons.org/blog/licencias/>

**WARNING.** The access to the contents of this doctoral thesis it is limited to the acceptance of the use conditions set by the following Creative Commons license:  <https://creativecommons.org/licenses/?lang=en>

# **Liquid-gated transistors for biosensing applications**

***Simona Ricci***

Doctoral Thesis

PhD programme in Materials Science

**Director: Dr. Marta Mas Torrent**

**Tutor: Prof. Jordi Hernando Campos**

Institut de Ciència de Materials de Barcelona (ICMAB-CSIC)  
Chemistry Department, Science Faculty, Universitat Autònoma de  
Barcelona (UAB)

**2020**



Memòria presentada per aspirar al Grau de Doctor per:

Simona Ricci

Vist i plau:

Dra. Marta Mas Torrent

Prof. Jordi Hernando Campos

Bellaterra, 26 de Junio 2020



**MARTA MAS TORRENT**, Research Scientist of the Spanish Council of Research (CSIC) at the Materials Science Institute of Barcelona (ICMAB-CSIC) and **JORDI HERNANDO CAMPOS**, Professor at the Autonomous University of Barcelona (UAB)

CERTIFY:

That **Simona Ricci** has performed, under their supervision, the research work entitled “**Liquid-gated transistors for biosensing applications**”. This work has been carried out in the framework of the Materials Science PhD programme of the Chemistry Department of the Autonomous University of Barcelona.

And in witness whereof this is signed by

Director:

Dr. Marta Mas Torrent

Tutor:

Prof. Jordi Hernando Campos

June 2020



*“La vera saggezza sta in colui che sa di non sapere.”*

Socrate

*A mia madre*





## *Acknowledgments (Ringraziamenti)*

---

Time has come to acknowledge everyone who, somehow, have contributed to the fulfilment of this work. A special acknowledgement to Prof. Jaume Veciana and Prof. Concepció Rovira for letting me join the Nanomol Group.

First of all, I want to acknowledge my supervisor, Dr. Marta Mas Torrent, for allowing me to work in such a great and international research group. Thanks for trusting me in carrying out this challenging project, we can say that, finally, we made it. I know that I am not the easiest student in the world, always a bit pessimistic, but you encouraged me and supported in keeping on and not giving up. I look backwards, at the beginning of the PhD, and I know that I am a more self-confident, independent person and that I have a load of new knowledge and experiences that I will bring with me for a long time, so again, thank you.

Second, I have to acknowledge the person that introduced myself in the world of the bioelectronics, Dr. Stefano Casalini. You have been a tutor for me, but I prefer to say a mentor. Thank you for all your patience with me (sometimes I am a bit slow!), for forming me and for giving me all the tools to continue working by myself. But also thank you for keeping follow my path even when your stay at the ICMAB ended, always finding a moment in your busy agenda to discuss my results, to find an explanation and a way out. Every talk with you has always been enlightening. I couldn't have been luckier, so thank you!

And here I want to acknowledge the entire OFET team, and I really don't know where to start, so maybe I will start with the "seniors". A special thanks to Dr. Raphael Pfattner, for all your suggestions, useful discussions and your "physical" point of view on my experiments, but also for your availability to solve any practical issues in the labs. Thanks to Dr. Tommaso Salzillo, for always cheering me up and the entire lab mood, even in stressful situations. Thank you for your great collaboration, I will always remember the magic "bending apparatus" and the cycling lessons at the SAF. Thanks

to Dr. Francesca Leonardi and Dr. José Muñoz for all your tips, your support, and the shared moments in the lab. And now I want to acknowledge my lab/office friends who were already at the ICMAB when I started my PhD, Dr. Inés, Dr. Toni, Dr. Qiaoming and Adrián. Thank you for welcoming me in the group, for your precious help in the lab, for teaching me the basic of OFETs, from measuring them to treat data. And also thank you for making the lab atmosphere enjoyable and for sharing unforgettable moments also outside the lab. Last but not least, thanks also to the new OFET team members, Sara, Junghai and Lamiaa, thanks for the laughs during my (stressed) last months!

I want to mention my collaborators in Sweden, where I spent an unusual but memorable summer last year. In particular Dr. Simone Fabiano for giving me the opportunity to work in a really international and huge group, giving me free access to all the laboratory facilities and equipment. Thank you also for your kindness, for explaining to me a lot of (OECTs)-related issues, for showing me your point of view and for inducing me think critically. Dr. Valerio Beni for your precious suggestions about electrochemistry, for the discussions of the experimental results and your company in the office. Sincere thanks to Chiara. We spent a lot of time in the cleanroom (try&learn), you explained me everything with extreme clarity in a short period! Thank you also for introducing me to the group (I do not forget that you forced me to “do” a front flip!). I want to acknowledge also all the people I have shared some time with, Sergi, Xeno, Miriam, Nadia, Daniel, Maria, Tobias, Yannis, Vasilis, Gwen, Jee.

Finally, in these three years, in the Nanomol group, I met a lot of nice people and new friends, inside and outside the laboratory. I want to acknowledge them because they made the bad days in the lab less bad and the good days great! First of all, the *Unicorn team*, you have been my little Spanish family, and I write down here our promise to make a journey per year so that now our deal is official (to more pijamas parties)! A special thanks to Francesc, for listening to my worries for hours, for our dinners to *Chumi*, for being my official Spanish translator and for sharing a lot of moments! I want to mention all the people in the big office (big for the people, not the dimension!): Paula, Inés, Guillem, Nathalie (por nuestras noches latinas!), Toni, Qiaoming, Adrián, Edu, Dolores, Ramon, Jinghai, Lidia, Marc, Sara, Lamiaa, Lijia

and Tommaso. And finally, a heartfelt thank you to all (and I highlight **all!**) the *nanoniños!*

Un grazie a tutte le persone che, anche a distanza, mi hanno spronata, hanno creduto e tifato per me. Un abbraccio di cuore.

Un grazie ai miei genitori, per avermi appoggiata in ogni mia scelta ed avermi seguita in ogni direzione. A voi il grazie più importante.



In this thesis, we have studied different aspects related to liquid-gated organic transistors, in particular electrolyte-gated organic field-effect transistors (EGOFETs) and organic electrochemical transistors (OECTs). EGOFET devices were fabricated by depositing from solution small molecules organic semiconductors (OSC) blended with insulating polymers, through the bar-assisted meniscus-shearing technique (BAMS). BAMS is a rapid, low-cost and scalable technique that allows the formation of crystalline and uniform thin films. The EGOFETs were studied for the development of a biosensor for the detection of a biomarker for neurodegenerative diseases, including Parkinson's diseases, namely  $\alpha$ -synuclein. Further, OECT devices were employed for the biosensing of  $\alpha$ -synuclein, to give an insight into the possible use of these devices as immunosensors, field which is still less explored in literature. Finally, an all-flexible EGOFET based on a small molecule OSC blended with an insulating polymer thin film, was fabricated and its electrical response under bending strain was evaluated, for the first time, as far as we know, for liquid-gated OFETs.



## *List of abbreviations and symbols*

---

### **Abbreviations**

<b>μCP</b>	Microcontact printing
<b>Ab</b>	Antibody
<b>Ag</b>	Antigen
<b>BGBC</b>	Bottom-gate bottom-contact
<b>C<sub>8</sub>O-BTBT-OC<sub>8</sub></b>	2,7 - dioctyloxy[1]benzothieno[3,2,b]benzothiophene
<b>CP</b>	Conducting polymer
<b>CPD</b>	Contact potential difference
<b>CSF</b>	Cerebrospinal fluid
<b>CV</b>	Cyclic voltammetry
<b>D</b>	Drain electrode
<b>diF-TES-ADT</b>	2,8-difluoro-5,11-bis(triethylsilylethynyl)anthradithiophene
<b>DPV</b>	Differential pulse voltammetry
<b>EDL</b>	Electrical double-layer
<b>EG</b>	Ethylene glycol
<b>EGOFET</b>	Electrolyte-gated organic field-effect transistor
<b>EIS</b>	Electrochemical impedance spectroscopy
<b>F<sub>ab</sub></b>	Fragment antigen-binding
<b>F<sub>c</sub></b>	Crystallizable fragment
<b>G</b>	Gate electrode
<b>GI</b>	Glutaraldehyde
<b>GOPS</b>	3-glycidyoxypropyl
<b>HOMO</b>	Highest occupied molecular orbital
<b>IDE</b>	Interdigitated electrode
<b>Ig</b>	Immunoglobulin
<b>KPFM</b>	Kelvin probe force microscopy
<b>LOD</b>	Limit of detection
<b>LUMO</b>	Lowest unoccupied molecular orbital
<b>OECT</b>	Organic electrochemical transistor
<b>OFET</b>	Organic field-effect transistor
<b>OSC</b>	Organic semiconductor
<b>PBS</b>	Phosphate buffer saline
<b>PDMS</b>	Poly(dimethylsiloxane)
<b>PEDOT</b>	Poly(3,4-ethylenedioxythiophene)
<b>PEN</b>	Polyethylene naphthalate
<b>PFBT</b>	2,3,4,5,6-pentafluorothiophenol



<b>PG</b>	Recombinant histidine-tagged protein G
<b>PM-IRRAS</b>	Polarization modulation-Infrared reflection-absorption spectroscopy
<b>PMMA</b>	Poly(methyl methacrylate)
<b>POC</b>	Point-of-care
<b>PS</b>	Polystyrene
<b>PSS</b>	Polystyrene sulfonate
<b>PVD</b>	Physical vapour deposition
<b>RG</b>	Reference gate
<b>S</b>	Source electrode
<b>SAM</b>	Self-assembled monolayer
<b>SG</b>	Sensing gate
<b>SiO<sub>2</sub></b>	Silicon oxide
<b>SIP</b>	Surface-induced phase
<b>SPR</b>	Surface plasmon resonance
<b>TGBC</b>	Top-gate bottom-contact
<b>XPS</b>	X-ray photoelectron spectroscopy
<b>XRD</b>	X-ray diffraction

## Symbols

$E_F$	Fermi energy
$\mu_{FE}$	Field-effect mobility
$C$	Gate capacitance
$C_{dl}$	Double-layer capacitance
$C_{eff}$	Effective capacitance
$g_m$	Transconductance
$I_{DS}$	Source-drain current
$I_{GS}$	Source-gate current
$I_{on/off}$	On/off current ratio
$k$	Gauge factor
$L$	Channel length
$MW$	Molecular weight
$pI$	Isoelectric point
$R_{ct}$	Charge transfer resistance
$SS$	Subthreshold swing
$V_{DS}$	Source-drain voltage
$V_{GS}$	Source-gate voltage
$V_{th}$	Threshold voltage
$W$	Channel width
$\Delta R$	Reflectivity variation
$\varepsilon$	Strain

<b>CHAPTER 1: Introduction and objectives</b>	<b>1</b>
1.1. Organic electronics .....	1
1.2. Organic transistors: characteristics and operating principles .....	10
1.3. Biosensors .....	26
1.4. General objectives.....	36
<i>Bibliography</i> .....	37
<b>CHAPTER 2: Label-free immunosensing of <math>\alpha</math>-synuclein</b>	<b>49</b>
2.1. Introduction .....	49
2.2. Objectives.....	54
2.3. Design and preparation of engineered Ab functionalised Au surfaces .....	55
2.4. Characterization of the bio-engineered Au surfaces.....	58
2.5. Immunosensing with top-gated EGOFETs .....	72
2.6. Towards a self-standing chip .....	84
2.7. Summary.....	95
<i>Bibliography</i> .....	96
<b>CHAPTER 3: Organic Electrochemical Transistors: <math>\alpha</math>-synuclein immunosensing</b>	<b>103</b>
3.1. Introduction .....	103
3.2. Objectives.....	107
3.3. OECTs microfabrication and characterization .....	108
3.4. Sensing platform design and electrochemical characterization.....	112
3.5. $\alpha$ -synuclein detection: OECTs approach.....	115

3.6. Summary .....	125
<i>Bibliography</i> .....	126
<b>CHAPTER 4: Flexible (C<sub>8</sub>O-BTBT-OC<sub>8</sub>)-based EGOFET: stability and properties under mechanical stress</b>	<b>133</b>
4.1. Introduction .....	133
4.2. Objectives.....	138
4.3. Fabrication and characterization of C <sub>8</sub> O-BTBT-OC <sub>8</sub> -based EGOFETs....	139
4.4. Electrical properties under mechanical stress .....	158
4.5. Summary .....	165
<i>Bibliography</i> .....	166
<b>CHAPTER 5: General conclusions</b>	<b>175</b>
<b>CHAPTER 6: Experimental methodologies</b>	<b>179</b>
6.1. Materials .....	179
6.2. Au surface biofunctionalization.....	181
6.3. Morphological and Structural Thin films and SAMs Characterization.....	185
6.4. Devices fabrication and characterization .....	186
6.5. Electrochemistry.....	192
6.6. Surface Plasmon Resonance.....	195
6.7. Microfluidics fabrication .....	196
6.8. Bending measurement setup.....	198
<i>Bibliography</i> .....	201

# CHAPTER 1

## *Introduction and objectives*

---

### **1.1. Organic electronics**

The current state of the modern electronics is monopolized by inorganic materials, and among semiconductors, Silicon is the most widely used, because of its natural availability, good electrical properties and established fabrication processes. However, the discovery of the first organic metal<sup>1</sup> and the first organic conducting polymer<sup>2</sup> in the 1970s spread dramatically the research towards organic counterparts, giving birth to the so-called **organic electronics**. Using organic semiconductors have some advantages and some drawbacks with respect to inorganic semiconductors. Among the advantages the most relevant are i) lower cost of fabrication due to the possibility of solution-processing methods, opposite to the high-temperature processing conditions of Silicon, which raises the total cost of production, ii) lower power consumption, iii) lighter weight, iv) compatibility with flexible substrates and v) the possibility to tailor their molecular structure. The main drawbacks are i) lower stability under ambient conditions and ii) lower electrical performances, even if some organic semiconductors have reached mobility values on the order of that of amorphous Silicon.<sup>3</sup> Organic materials which display semiconducting properties are highly  $\pi$ -conjugated systems, as will be discussed later. The most explored applications of organic semiconductors, are organic light-emitting diodes (OLEDs), organic photovoltaic devices (OPVs) and organic field-effect transistors (OFETs).

In the next paragraphs, a brief introduction to the characteristics of organic semiconductors, along with their processability and a short description of the charge transport mechanisms are presented.

- **Organic semiconductors**

Organic semiconductors can be divided into two main categories: i) organic polymers and ii) small molecules. In turn, they can be classified depending on the type of mobile charge carriers. Indeed, if the majority of carriers are electrons, it is said that the organic semiconductor manifests an *n*-type behaviour, on the contrary, if the majority of carriers are holes, the conduction is referred to as *p*-type. A *p*-type molecule disposes of a high energy highest occupied molecular orbital (HOMO) level and electron-donating properties, whereas an *n*-type one has a low energy lowest unoccupied molecular orbital (LUMO) level and is electron-acceptor. Finally, organic semiconductors are ambipolar when both electrons and holes can transport current according to the applied electric field. Up to now, *p*-type materials have been more extensively investigated giving higher performance thanks to their enhanced stability in ambient conditions.

**Organic polymers** which show semiconducting properties are  $\pi$ -conjugated polymers presenting the band diagram illustrated in **Figure 1.1**. The  $\sigma$  bonding and  $\sigma^*$  antibonding levels originate from the linear combination of  $2sp^2$  hybrid carbon orbitals, whereas the  $\pi$ -band originates from the linear combination of the orthogonal  $2p_z$  carbon orbitals.

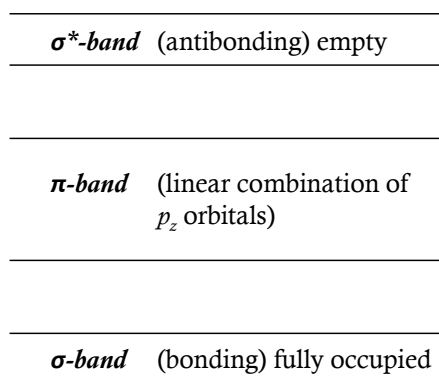


**Figure 1.1.** Schematic band diagram for  $\pi$ -conjugated polymers. Extracted from ref.4.

Despite their poor thin film crystallinity due to high molecular disorder, which lowers their charge carrier mobility, semiconducting polymers have the advantage to be compatible with solution-processing techniques, because of their typical solubility in organic solvents, increasing the interest for these materials. Poly(3-hexylthiophene) (**Figure 1.2,a**), P3HT, is likely the most exploited semiconductor polymer, exhibiting a mobility of around  $0.1 \text{ cm}^2/\text{V}\cdot\text{s}$ .<sup>5</sup> This mobility is achieved through the formation of a semicrystalline lamellar microstructures induced by the head-to-tail coupling of the hexyl side chains.<sup>5</sup> However, P3HT displays a low oxidation potential, which decreases its environmental stability. Another polymer in which a highly semicrystalline structure is formed, reaching a high mobility of  $1 \text{ cm}^2/\text{V}\cdot\text{s}$ , is poly(2,5-bis(3-alkylthiophen-2-yl)thieno(3,2-b)thiophene), PBTTT (**Figure 1.2,b**).<sup>6</sup> In this case, the ordered structure is obtained through the better side-chain interdigitation in the thiophene–thienothiophene units, which also accounts for improving its stability by increasing its ionization potential. Recently, high performing donor-acceptor copolymers have been reported.<sup>7,8</sup> However, despite their high performance, the synthesis of highly pure material in large amounts is not trivial. Doped organic semiconducting polymers have also been deeply investigated as conducting polymers. Among them, poly(3,4-ethylenedioxythiophene) doped with polystyrene sulfonate, PEDOT:PSS (**Figure 1.2,c**), is the most studied, exhibiting a very high conductivity up to  $4600 \text{ S cm}^{-1}$  and high stability.<sup>9</sup>

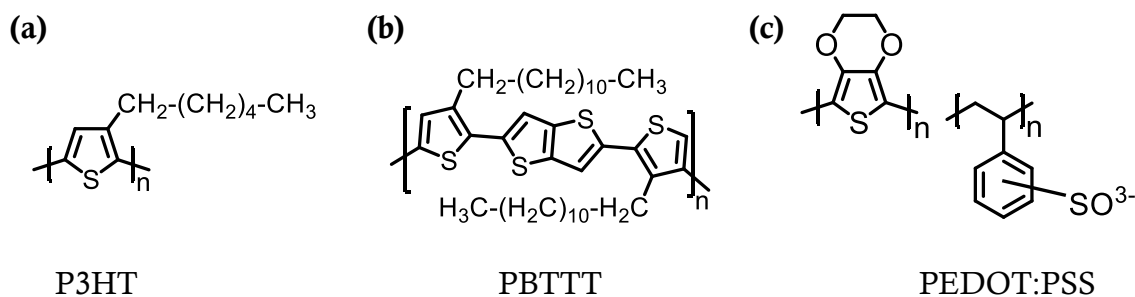


**Figure 1.2.** Molecular structure of (a,b) two organic semiconducting polymers and (c) a conducting doped polymer.

On the other hand, **small molecules** typically show lower solubility in organic solvents, increasing the difficulty of processing from solution, but show a higher degree of thin film crystallinity, through the formation of ordered molecular structures, improving their charge transport and so becoming appealing in the organic electronics

field. Acenes and thiophenes have been the most studied classes of small molecules. Organic chemists have made a great effort in synthesizing soluble derivatives, adding alkyl chains or electro-donating groups in the aromatic core, aiming at tuning both the crystal structure and the morphology of their corresponding thin films, and also facilitating their solution processability (**Figure 1.3**). An example of improved solubility is that of pentacene and its derivative, bis(triisopropylsilyl)ethynyl pentacene, TIPS-PEN. The former crystallises following a herringbone structure and it is deposited by physical vapour deposition reaching a charge carrier mobility equal to  $1 \text{ cm}^2/\text{V}\cdot\text{s}$  in OFETs.<sup>10</sup> Instead, TIPS-PEN is processed from solution and forms a 2D “bricklayer” arrangement with significant  $\pi$ - $\pi$  overlapping, achieving a charge carrier mobility of near  $1.5 \text{ cm}^2/\text{V}\cdot\text{s}$  in OFETs.<sup>11,12</sup> Regarding thiophene molecules, the most explored is [1]benzothieno[3,2-b][1]benzothiophene (BTBT), which presents a highly delocalized electronic structure along with a low-lying HOMO level. Nevertheless, this molecule is highly insoluble in organic solvents, for this reason, a lot of derivatives have been designed and synthesized to increase its solubility. In particular, alkyl chains have been added at the positions 2 and 7 of the aromatic rings. Among these derivatives the 2,7-dioctyl BTBT ( $\text{C}_8$ -BTBT- $\text{C}_8$ ) is one of the most exploited which has given an optimised performance.<sup>13,14</sup> 2,8-Difluoro-5,11-bis(triethylsilyl)ethynylanthradithiophene, diF-TES-ADT, has been also a benchmark active layer in OFETs, showing high OFET mobilities above  $1 \text{ cm}^2/\text{V}\cdot\text{s}$  when deposited employing solution-based techniques.<sup>15,16</sup>

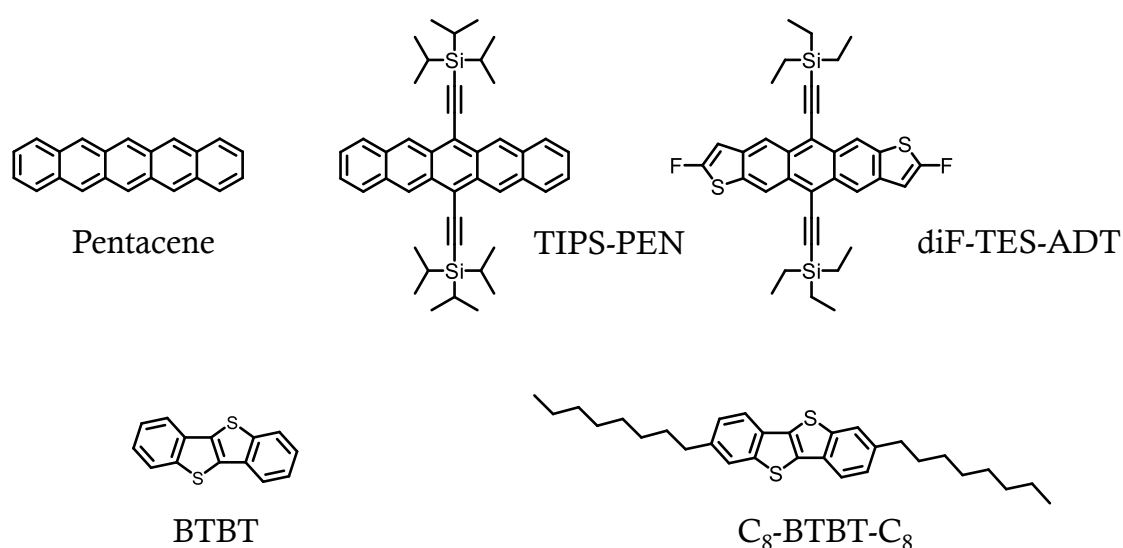


**Figure 1.3.** Molecular structures of *p*-type small molecules OSCs.

Apart from a chemical modification of the molecular structure, a technique used for improving the processability of these small molecules in solution consists in blending them with insulating polymers such as polystyrene (PS) and poly (methyl methacrylate) (PMMA).<sup>17</sup> The low viscosity of OSC solutions causes dewetting problems from the surface which leads to non-continuous and non-homogenous thin films and, thus, hampers the device-to-device reproducibility. Therefore, increasing the solution viscosity by adding insulating polymers favours the formation of more uniform thin films. In addition, during the deposition of OSC/insulating polymer blends, a vertical phase separation occurs, which promotes the crystallisation of the OSC. This process leads to the formation of bilayer (polymer:OSC) or trilayer (polymer:OSC:polymer) structures.<sup>17</sup> The mechanism of this phase separation is still not completely clear and it depends on different factors, such as the kind of substrates, the boiling point of the solvent used, the processing conditions and, most importantly, the nature of the polymer binder. In both layered structures, the insulating polymer is in contact with the gate dielectric, acting as a passivation layer and decreasing the density of charge carrier traps at the dielectric/OSC interface, typically caused by the OH groups of oxide dielectrics. On the other hand, the trilayered structure is also appealing since it self-encapsulates the OSC protecting it from the environment, which can be particularly interesting in liquid-gated transistors. Such phase separation has been demonstrated for various benchmark OSCs, such as TIPS-PEN:PS,<sup>15,18</sup> C<sub>8</sub>-BTBT-C<sub>8</sub><sup>15</sup> and diF-TES-ADT.<sup>15,19</sup>

Therefore, blending OSC molecules with insulating polymers helps to overcome the common processing limitations of small molecule OSCs allowing to, i) improve the thin films crystallinity, ii) obtain a high device-to-device reproducibility due to the formation of uniform and homogenous thin films, iii) reduce the amount of semiconductor required and iv) enhance the device stability.<sup>20–23</sup>

- **Charge transport in organic semiconductors**

A comprehensive model to describe the charge transport mechanism in organic semiconductors is still lacking, which is also influenced by the different morphologies of organic thin films, spanning from single crystals to polycrystalline and amorphous materials. In organic materials, several factors are influencing the charge carrier



mobility, among them molecular packing, disorder, temperature, impurities and charge carrier density.<sup>24</sup> To date, the most exploited transport models used to describe the transport in organic semiconductors are i) band-like transport, ii) multiple trapping and release model (MTR) and iii) hopping.

The **band-like transport** is typical of high-quality organic single-crystal films with a low density of charge traps. In such ordered crystal lattices, the highest occupied molecular orbitals (HOMO) of adjacent molecules interact to form the valence band, whereas the lowest unoccupied molecular orbitals (LUMO) generate the conduction band, thus an extended wave function over several molecular units can be achieved. As occurs for inorganic semiconductors, charge carrier mobility increases at lower temperatures.<sup>25</sup> Indeed, higher temperature increases scattering processes by lattice phonons. In organic molecular crystals, electron-phonon interactions are comparable to electronic interactions, contributing to lower the charge carrier mobility.<sup>24</sup>

**Multiple trapping and release model** is applied to describe the charge transport in polycrystalline films, in which crystalline grains are separated by amorphous phases, the so-called grain boundaries.<sup>26</sup> Impurities, structural defects and grain boundaries can induce the formation of electronic states in the band gap of OSCs, which act as charge traps.<sup>27</sup> In a polycrystalline material, the highest concentration of traps is located into the grain boundaries. Thus, according to this model, the charge carrier transport occurs in extended states, but most of the carriers remain trapped in these in-gap localized states. Indeed, this model is consistent with a thermally activated behaviour since phonons promote the release of the trapped charges.<sup>26,28</sup>

In highly disordered small molecules films or amorphous polymers, the charge transport mechanism occurs by **hopping** transport. This model is based on the presence of localized states more than extended states.<sup>29</sup> The charge carriers, holes or electrons, transfer from one molecule to the adjacent one. For this reason, the hopping transport is depicted according to Marcus theory, which was developed in 1956 to describe the electron transfer rate in redox reactions in donor-acceptor complexes. Marcus theory is extensively used by chemists to assess the charge transfer rate in weak coupling systems, in which the charge is localized prior on a donor and after the electron is transferred on the acceptor. Hopping rate is given by:<sup>29</sup>

$$k = \frac{2\pi}{\hbar} t^2 \frac{1}{\sqrt{4\pi\lambda K_B T}} e^{-\frac{\lambda}{4K_B T}} \quad (1.1)$$

where  $t$  is the transfer integral and  $\lambda$  is the reorganization energy. The transfer integral ( $t$ ) accounts for the electronic coupling between adjacent molecules, which should be maximized, whereas the reorganization energy ( $\lambda$ ) takes into account the energy required to conformational changes upon the electron transfer, which should be minimized for an efficient charge transport.<sup>24</sup>

- **Solution-processing methods**

Solution-processing deposition methods are of utmost importance for a fast, low-cost and large-scale fabrication of thin film devices. Several techniques have been developed so far, such as drop-casting, spin-coating, dip-coating, spray-coating, inkjet printing, and roll-to-roll compatible techniques, including blade coating and the bar-assisted meniscus-shearing technique (BAMS).

**Drop-casting** consists in pipetting a drop of the OSC solution on top of the substrate, waiting for the solvent to evaporate (**Figure 1.4,a**). It represents a very simple technique which does not require any particular equipment. However, drop-casting usually needs to be followed by thermal annealing to improve the thin film crystallinity and the reproducibility is low. **Spin-coating** involves application of an OSC solution to a substrate and subsequently acceleration of the substrate to a chosen rotational speed (**Figure 1.4,b**). By selecting a precise angular velocity and solution concentration it is possible to have a high control of thin film thickness and morphology. The high reproducibility, the formation of high homogeneous films over a relatively large area and the simplicity of the techniques made spin-coating deposition widely used, not only in research laboratories but also in microelectronics industries.<sup>30</sup> **Dip-coating** is employed to prepare large-area semiconducting films with low cost facilities. This process is composed of two steps, i) dipping of the substrate into the reservoir containing the OSC solution, ii) removal of the substrate at a constant speed (**Figure 1.4,c**). It is possible to tune thin films crystallization by varying the speed at which the substrate is removed, or by changing the solvent and the OSC concentration.<sup>31</sup> The

drawback of this technique is the volume of solution required, which can provoke an increase of the overall fabrication process. An example of dip-coating technique is the Langmuir-Blodgett, suitable for the formation of films with amphiphilic molecules.<sup>32</sup> Another widely employed technique, also at industrial level is **spray-coating**. The OSC solution is forced through a nozzle whereby a fine aerosol is formed. A gas carrier and/or electrostatic charging are used to help directing the aerosol onto the substrate (**Figure 1.4,d**). However, the formation of the aerosol and the evaporation of some kind of solvents can be difficult and, with respect to other methods, obtaining smooth surfaces is more complicated because the levels of the droplets into the surface is not granted.<sup>30</sup> Finally, **inkjet printing** is a promising technique for scalable thin films patterning. The printing nozzle is made of ceramic or materials resistant to a wide range of solvents. The technique is based on the formation of a droplet of semiconducting ink which is deposited on the substrate. The droplet can be formed by mechanical compression of the ink through a nozzle or by heating the ink formulation. Then, the droplet is electrostatically charged and accelerated towards the substrate by an electric field. This method offers the possibility not only to deposit the OSC, but also to print the conducting electrodes on top of it. However, there are some issues for the ink formulation which limits the application of this method, such as low viscosity, and a loss of ink droplets during the printing procedure.<sup>33</sup>

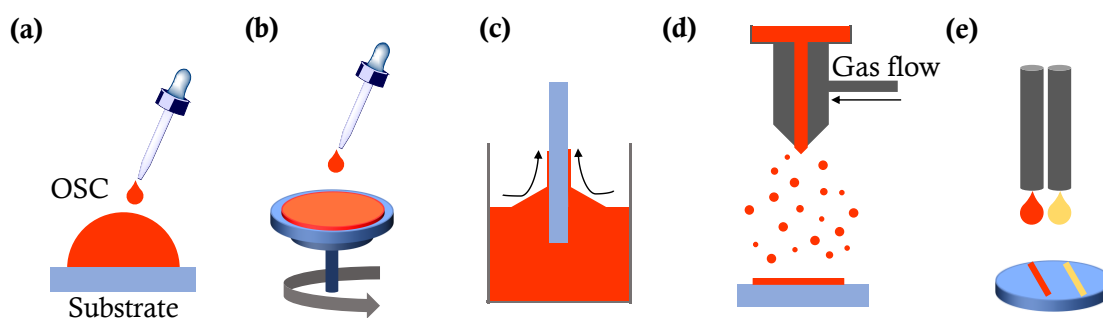


**Figure 1.4.** Schematic representation of the above-described solution-processing methods. (a) drop-casting; (b) spin-coating; (c) dip-coating; (d) spray-coating; (e) inkjet printing.

**Blade coating** can be regarded as a roll-to-roll compatible deposition method. It is widely employed for producing thin films on large area surfaces, achieving a well-defined thickness, with a poor loss of coating solution. The technique uses a blade placed on top of the substrate, at a fixed distance, which spans to 10-500  $\mu\text{m}$ . In front

of the blade is deposited the OSC solution. By moving the blade towards the solution, or the substrate in the opposite direction, a wet film is formed (**Figure 1.5**). The thickness of the films is estimated to be half of the distance between the blade and the substrate, but other factors can influence it, such as the viscosity of the solution, the surface tension or the meniscus formed between the blade and the substrate.<sup>33,34</sup>

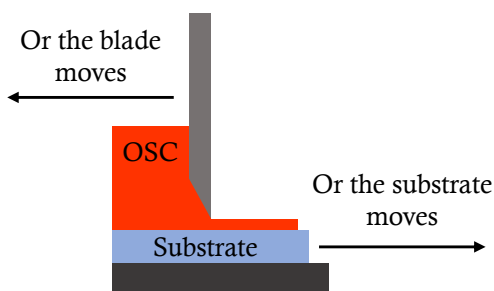


**Figure 1.5.** Schematic representation of the blade coating deposition technique.

Bar-assisted meniscus shearing technique (**BAMS**), is also a roll-to-roll compatible deposition technique, similar to blade coating. It was developed in our research group.<sup>15,35</sup> The substrate is placed on top of a hot plate, and a rounded bar is placed on top of the hot plate. A drop of OSC solution is pipetted between the bar and the substrate, in such a manner that a meniscus is formed (**Figure 1.6**). Afterwards, the bar is sheared horizontally along the substrate at a constant speed, or the hot plate is moved in the opposite direction. The meniscus is displaced and a uniform thin film is produced by convective self-assembly.<sup>35</sup> The solvent evaporates during the coating according to the hot plate temperature. The speed rate of the bar shearing can be modulated, thus tuning the morphology and crystal structure of the crystalline thin film. The temperature of the hot plate can be adapted to the boiling point of the solvent employed, to allow its instantaneous evaporation.<sup>22</sup> Furthermore, no post-coating treatments are necessary, reducing the production time and cost of the devices. This technique requires small quantity of OSC solution, with no significant loss of the materials during the coating. It has been applied extensively for the coating of OSC solutions blended with insulating polymers, obtaining thin films with a high degree of crystallinity and homogeneity. This technique resulted useful for the rapid and low-cost production of OFET and liquid-gated OFET devices.<sup>15,36</sup> BAMS has been

used in this thesis to prepare the organic semiconducting thin films for the fabrication of all the devices.

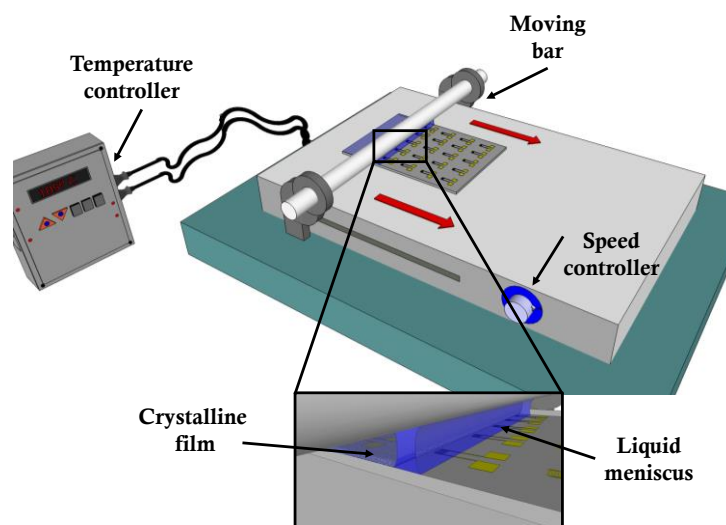


**Figure 1.6.** Schematic representation of the BAMS technique and the meniscus shearing. Extracted from ref.37.

## 1.2. Organic transistors: characteristics and operating principles

Transistors are semiconducting-based devices and represent the main components of modern electronics, due to their capacity to operate as electrical switches and electrical amplifiers. The term transistor derives from the union of the words “*transfer resistor*”, and it refers to the capacity of this device to transfer, unaltered, a variation of current from a lower resistor to a higher one, thus achieving an amplification of potential. The transistor was discovered in 1947 by Bardeen, Brattain and Shockley in Bell Laboratories and it was made of a Germanium semiconductor.<sup>38</sup> For this discovery, they were awarded the Noble Prize. A few years later, in 1954, the first Silicon-based transistor was developed by Morris Tanenbaum, in Bell Laboratories too.<sup>39</sup> Since then, they became the building block of modern electronic devices, such as radio, calculators, computers, mobile phones and so on.

The metal-oxide-semiconductor field-effect transistor (MOSFET) was developed in 1959 in Bell laboratories and it has become the most widely employed device in history. However, the first organic FET was fabricated in the 1980s. The theory elaborated for the description of the MOSFET characteristics is the starting point for the one used for the analysis of OFETs and liquid-gated OFETs. A FET device can operate in

accumulation or depletion mode and can transport electron or holes according to the type of semiconductor used, *n*-type or *p*-type, respectively. When a device works in depletion, it means that there is current flowing into the semiconducting channel when a potential is applied to the source-drain contacts, and the application of a gate voltage produces a reduction of the mobile charges. On the contrary, in the devices working in the accumulation mode, mobile charges are only produced by the application of a gate voltage. OFET devices work always in the accumulation mode.<sup>40</sup>

There are several classes of organic-based transistors, however, the discussion in this thesis manuscript will be focused on organic field-effect transistors, organic electrolyte-gated transistors and organic electrochemical transistors.

- **Organic field-effect transistors**

Organic Field-Effect Transistors (OFETs) are three-terminal devices, Source (S), Drain (D) and Gate (G), in which the semiconductor material is an organic conjugated polymer or small molecule. The gate is separated from the semiconductor by an insulator. When a potential is applied to the gate electrode, the electric field generated creates a thin layer of mobile charges in the semiconductor, precisely at the interface between the insulator and the semiconductor. In this way, the gate terminal controls the charge density in the semiconductor channel, and so its electric conductivity. The application of a potential between the drain and the source terminals, allows the charge to flow along the semiconductor channel.<sup>41</sup> In **Figure 1.7** the energy-band diagram of an ideal *p*-type OFET is illustrated. The Fermi level ( $E_F$ ) represents the energy at which the probability of occupation by an electron is exactly one-half, and it is given by the so-called Fermi-Dirac distribution. The work-function ( $\phi_{WF}$ ) of metals is defined as the energy required to extract an electron from the Fermi level to the vacuum level, whereas the ionization potential (*IP*) of an OSC is the energy required to extract an electron from the HOMO level to the vacuum level.<sup>41</sup> Considering an ideal *p*-type organic semiconductor, when no potential is applied to the gate terminal, no mobile charges accumulate and no charge transport occurs, even upon the application of a source-drain potential. However, when a negative source-gate potential is applied, holes accumulate at the semiconductor/insulator interface since the HOMO level bends upwards in energy to match the  $E_F$  of the source electrode. At this point, the

application of a negative potential to the source-drain allows the holes to move towards the drain terminal.<sup>41</sup> In the case of an *n*-type OSC, similar effects occur but involving the LUMO level and applying opposite voltages.

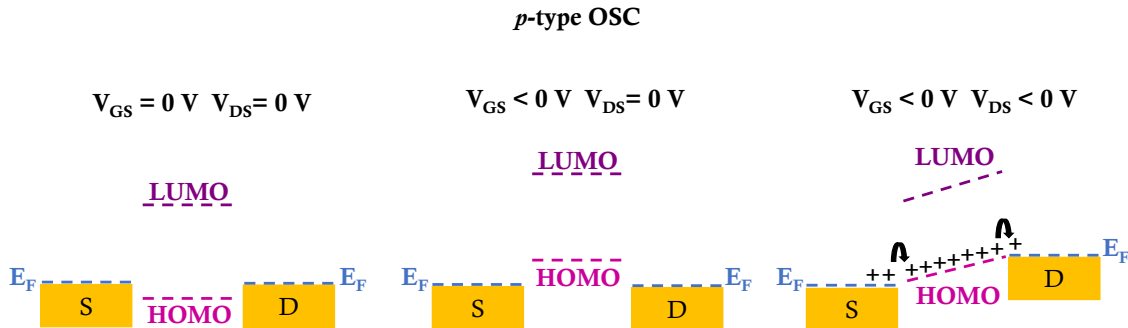


**Figure 1.7.** Energy-level diagrams of an ideal *p*-type OFET, showing the transport of positive carriers from the source through the semiconductor to the drain.

Several configurations have been developed for the OFET fabrication and are depicted in **Figure 1.8**: i) bottom-gate bottom-contact (BGBC), ii) bottom-gate top-contact (BGTC), iii) top-gate bottom-contact (TGBC) and iv) top-gate top-contact (TGTC). The nomenclature top and bottom refer to the relative position of the gate and the source and drain contacts with respect to the OSC layer. Depending on the geometry used, contact resistance between the source injecting electrode and the organic semiconductor can be affected. In top-contact devices contact resistance is usually reduced due to the penetration of some metal atoms into the OSC layers upon the physical vapor deposition process. In top-gate configuration, the OSC layer is protected from ambient air exposure. According to the layout, different microfabrication steps should be followed.

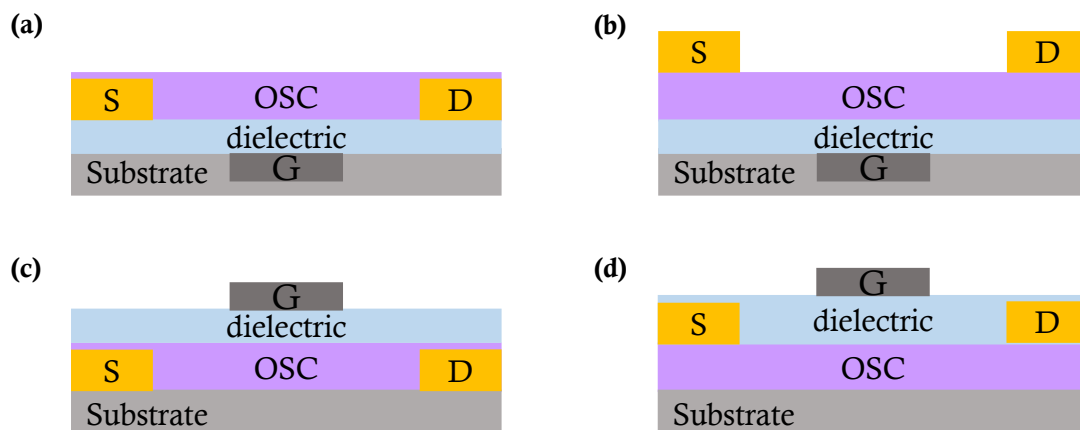


**Figure 1.8.** Schematic representation of the common geometries employed for OFET fabrication. (a) Bottom-gate, bottom-contact (BGBC); (b) Bottom-gate, top-contact (BGTC); (c) Top-gate, bottom-contact (TGBC); (d) Top-gate, top-contact (TGTC).

To describe mathematically the current-voltage characteristics of OFETs, a model developed by *Horowitz et al.* is used.<sup>40,42</sup> This theory is based on the one validated for MOSFET devices. This model relies on some assumptions that are not always strictly consistent with OFETs and thus care should be taken in handling it. It is assumed that charge carrier mobility ( $\mu$ ) is constant during the range of operation, however it has been noted that a gate-bias-dependent mobility is often encountered in OFETs, which could be attributed to the charge transport mechanism in organic molecules.<sup>42</sup> The second assumption is that the electric field along the channel, controlled by the gate electrode, is negligible with respect to the electric field across the channel, determined by the source and drain electrodes, the so-called gradual channel approximation, which is the case when the channel length ( $L$ ) is considerably larger than the insulator thickness. Lastly, the contact between the metal electrodes and the organic semiconductor are considered as pure Ohmic contacts, ignoring parasitic contact resistances.

Considering this, two operating regimes take place in an OFET, i) linear regime and ii) saturation regime.

In the linear regime, the source-drain current,  $I_{DS}$ , increases with the source-drain potential,  $V_{DS}$ , in a linear way, according to the following equation:



$$I_{DS,lin} = \frac{W}{L} \mu_{FE,lin} C_i \left[ (V_{GS} - V_{th}) V_{DS} - \frac{V_{DS}^2}{2} \right] \quad (1.2)$$

where  $I_{DS,lin}$  is the source-drain current in the linear regime,  $W$  and  $L$  are the channel width and the channel length, respectively,  $\mu_{FE}$  is the field-effect mobility,  $C_i$  is the gate capacitance per unit area,  $V_{GS}$ ,  $V_{th}$  and  $V_{DS}$  are the source-gate potential, the threshold voltage and the source-drain potential.

In the saturation regime, the source-drain current is no longer dependent on the potential applied at the source-drain terminal, and the current reaches a saturation, according to the following equation:

$$I_{DS,sat} = \frac{W}{2L} \mu_{FE,sat} C_i (V_{GS} - V_{th})^2 \quad (1.3)$$

where  $I_{DS,sat}$  is the source-drain current in the saturation regime.

The current-voltage behaviour expressed by these two equations is well depicted by the two standard measurements performed in OFETs, i) output characteristics, in which the  $V_{DS}$  is swept at constant  $V_{GS}$ , and ii) transfer characteristics, in which  $V_{GS}$  is swept at constant  $V_{DS}$ .

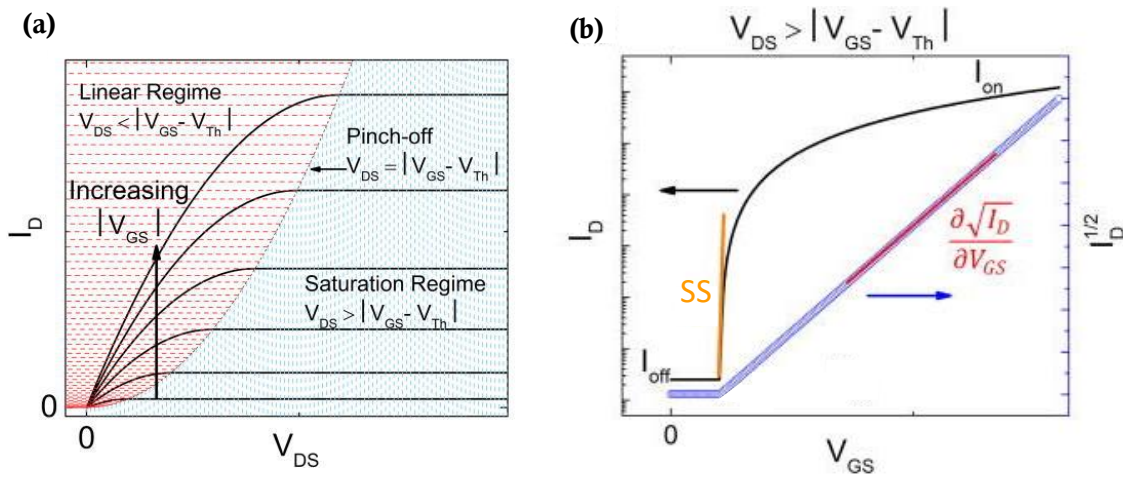


**Figure 1.9.** (a) Output characteristics and (b) transfer characteristics in saturation regime of an ideal OFET, extracted from ref. 43.

From transfer and output characteristics some parameters for the description of the device performances can be extracted, employing the OFET model above-mentioned. A brief illustration of the figures of merit used throughout this thesis manuscript will follow.

The most important parameter to define the performance of OFETs is the **field-effect mobility**,  $\mu_{FE}$ . Mobility is important for transport because it describes how strongly the motion of a charge is influenced by an applied electric field.<sup>44</sup> When a small electric field is applied to a semiconductor, each electron (or hole) will experience a force equal to  $-qE$  (where  $q$  is the elementary charge and  $E$  is the electric field), and will be accelerated along the field, with a velocity called drift velocity,  $v_D$ , to be distinguished from the one due to the thermal motion of electrons.<sup>44</sup> Mobility is related to the applied electric field through the following relation:

$$\mu_p = \frac{v_p}{E} \quad (1.4)$$

where  $\mu_p$  is the hole mobility and  $v_p$  is the drift velocity of the holes.

Field-effect mobility is extracted from the transfer characteristics, in the linear and saturation regimes, according to the equations (1.2) and (1.3), and it is expressed in  $\text{cm}^2/\text{V}\cdot\text{s}$ . It is worth noting that the mobility parameter extracted from the devices could differ from the intrinsic mobility of the semiconducting materials employed, because of the presence of trap states, defects or injection issues that could lower this value.

In the linear regime, a simple rearrangement of equation (1.2) leads to:

$$\mu_{FE,lin} = \frac{L}{W C_i |V_{DS}|} \cdot \left( \frac{\partial I_{DS,lin}}{\partial V_{GS}} \right)_{V_{DS}=const} \quad (1.5)$$

By plotting the transfer curve in the linear regime and by fitting it linearly, it is possible to insert the slope of the fitting in equation (1.5) obtaining  $\mu_{FE,lin}$ .

In the saturation regime, the following rearrangement from equation (1.3) leads to:

$$\mu_{FE,sat} = \frac{2L}{W C_i} \cdot \left( \frac{\partial \sqrt{I_{DS,sat}}}{\partial V_{GS}} \right)_{V_{DS}=const}^2 \quad (1.6)$$

By plotting the square root of the absolute source-drain current *vs* source-gate voltage curve in the saturation regime, it is possible to insert the slope obtained by fitting this curve linearly, in equation (1.6), extracting  $\mu_{FE,sat}$ .

The so-called **threshold voltage**,  $V_{th}$ , is another important parameter in OFETs and it is defined as the minimum source-gate voltage required to induce appreciable drain current. This terminology comes from MOSFET devices, indicating the gate potential needed to induce strong inversion. Nonetheless, the concept has been transferred also to OFETs working in accumulation mode.<sup>41</sup> Threshold voltage can be extracted from the transfer characteristics by a rearrangement of equations (1.2) and (1.3), as shown for the field-effect mobility calculation.

A parameter to define the general performance of a device is the so-called **subthreshold swing**,  $SS$ , which is extracted from the maximum slope of the  $\log(|I_{DS}|)$  *vs*  $V_{GS}$  curve in the subthreshold regime and is measured in V/dec.<sup>45</sup> The subthreshold region is defined as the region in the transfer curve beyond the threshold voltage. In this region drain current is due to carriers that have sufficient thermal energy to overcome the gate-voltage-controlled energy barrier.<sup>41</sup> Thus, the  $SS$  indicates how sharply the device turns on and the lower this value is, the lower is the power consumption of the device. This parameter is also a measure of the charge traps at the OSC interface since they hamper the switching on of the device.

In an OFET device the ratio between the off-current (the current measured when the device is switched off),  $I_{off}$ , and the on-current (the maximum source-drain current),  $I_{on}$ , is considered an important parameter to evaluate its performance. To be considered high-performing device the  $I_{on/off}$  **ratio** should be as high as possible. Generally, for OFET devices a good value is around  $10^6$ - $10^7$ . This value is important because it gives information about the current amplification property of the device and its switching capability.<sup>41</sup>

- **Electrolyte-gated organic field-effect transistors**

Electrolyte-gated Organic Field-Effect Transistors (EGOFETs) have been described more recently, precisely in 2010 by *Kergoat et al.*, and since then they have registered a huge interest and growth in a relatively short time period.<sup>46</sup> As suggested by the name, they are considered a sub-class of OFET, in which the dielectric is replaced with a liquid electrolyte and the gate electrode is directly immersed into it. It works in accumulation mode and it relies on the capacitive coupling between the gate electrode and the OSC layer through the electrolyte. The main advantage upon OFET devices is their low operating window potential, making them suitable for the development of low power devices. As shown in **Figure 1.10**, when a potential is applied to the gate electrode, cations or anions, according to the sign of the potential, are attracted towards the gate surface, forming an electrical double-layer at the electrolyte interface. Simultaneously, at the OSC/electrolyte interface, a second electrical double-layer builds up, due to the accumulation of charges in the OSC, opposite to the applied gate potential. Finally, the application of a potential between the source-drain terminal, allows the flow of the mobile charges along the OSC layer.

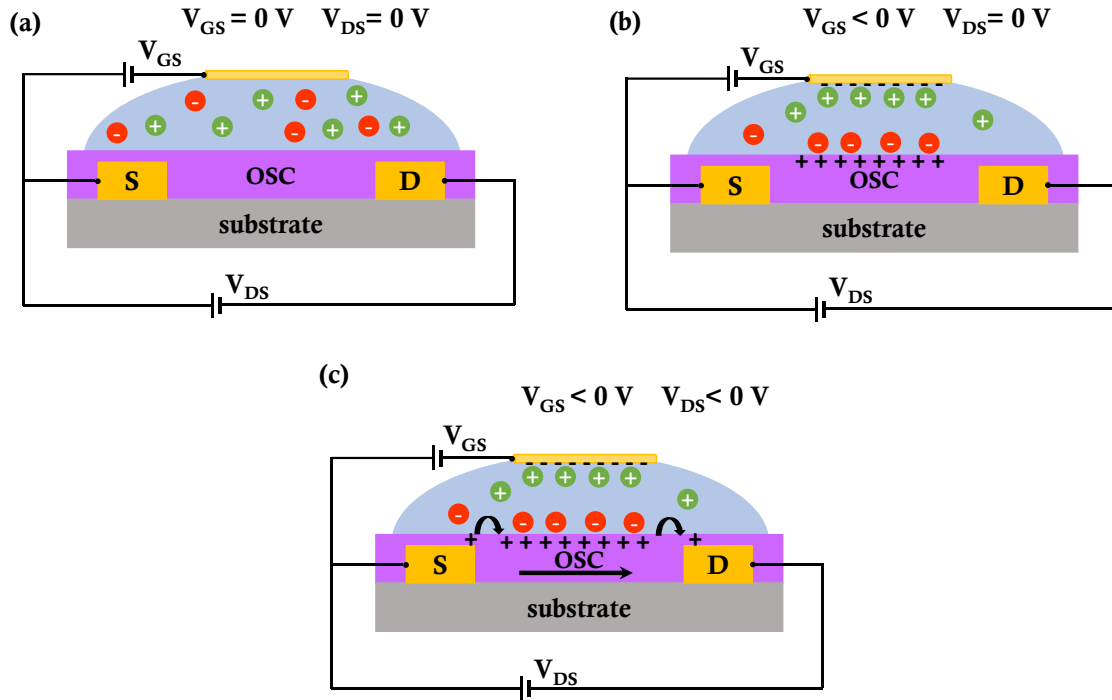


**Figure 1.10.** Schematic representation of a *p*-type EGOFET device and electrical double-layer formation. (a) No source-gate nor source-drain potential is applied to the device. (b) A negative potential applied to the gate terminal induces the formation of an electrical double-layer at both the gate/electrolyte interface and the OSC/electrolyte interface, accumulating holes at this OSC interface. (c) A negative source-drain potential allows the mobile holes flow along the active layer.

The capacitance of the electrical double-layer is a key factor to understand the low-operating voltage of these devices. It has been proved experimentally that an electrode/solution interface behaves like a capacitor.<sup>47</sup> A capacitor is a system in which two conductor plates are separated by a dielectric and it is able to storage electrical charge at the surface of the plates in contact with the dielectric, when a potential is applied to the plates. The charge is proportional to the potential applied through a coefficient of proportionality, which is called the capacitance, measured in Farad and expressed by the following relation:

$$C = \frac{Q}{V} \quad (1.7)$$

where  $C$  is the capacitance,  $Q$  is the electrical charge, and  $E$  is the potential.

Thus, at a given potential, a certain amount of charge is present to the metal surface and into the solution, in a way that:

$$q^M = -q^S \quad (1.8)$$

where  $q^M$  is the charge on the metal surface and  $q^S$  is the charge into the solution.

This separation of charges originates the electrical double-layer, characterized by a double-layer capacitance,  $C_{dl}$ , which is typically in the range of 10-40  $\mu\text{F}\cdot\text{cm}^{-2}$ .<sup>47</sup> The electrical double-layer is composed of different regions at the solution side, according to the Gouy-Chapman-Stern theory, i) the inner layer, ii) the outer layer and the iii) diffuse layer, as depicted in **Figure 1.11**. The so-called inner Helmholtz plane (IHP) defines the distance,  $x_1$ , at which ions are adsorbed into the metal surface. Solvated ions cannot approach this layer. The outer Helmholtz plane (OHP) is placed at a distant  $x_2$  from the metal surface and delimits the zone in which solvated ions can access, but they are non-specifically adsorbed. The interaction between the charged plate and the solvated ions entails only long-range electrostatic forces and is independent of the nature of the ions. The IHP and the OHP form the Stern-layer. From the OHP and the bulk of the solution extends the diffuse layer, or Gouy layer, in which solvated ions diffuse from the OHP due to thermal agitations.

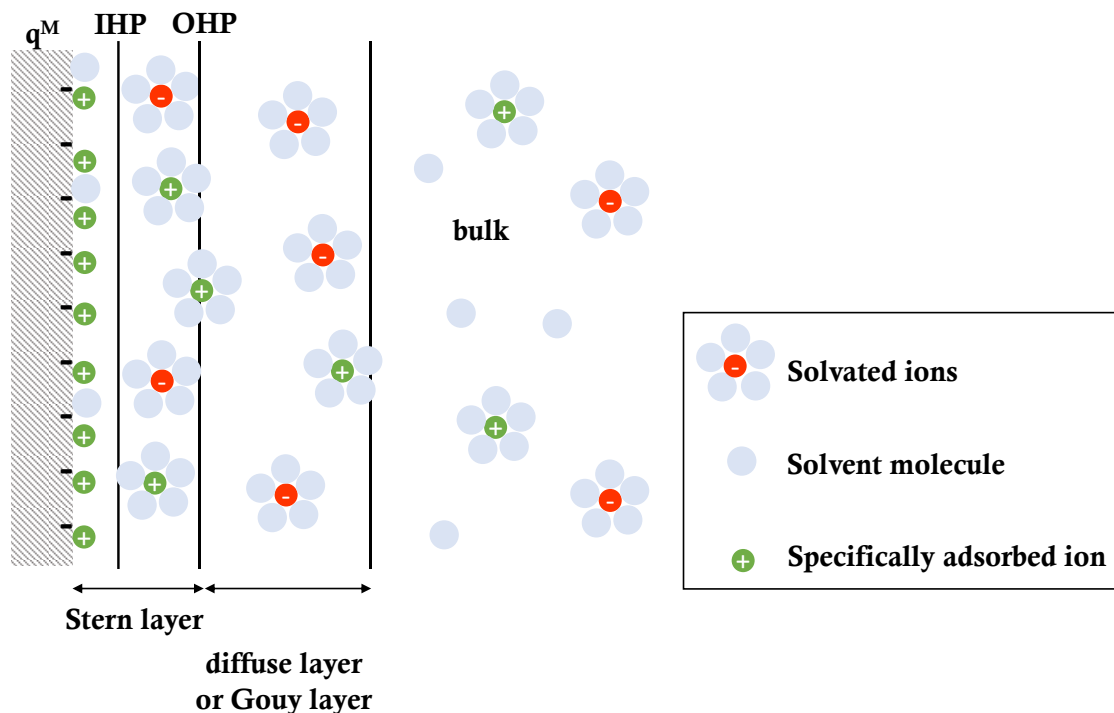


**Figure 1.11.** Model of the electrical double-layer in which cations are specifically adsorbed onto the metal surface.

The double-layer capacitance,  $C_{dl}$ , thus can be regarded as the contribution of two capacitances in series, the capacitance of the Stern layer and the capacitance of the Gouy layer as follows:

$$\frac{1}{C_{dl}} = \frac{1}{C_{Stern}} + \frac{1}{C_{Gouy}} \quad (1.9)$$

where  $C_{Stern}$  is the capacitance of the Stern layer and  $C_{Gouy}$  is the capacitance of the diffuse layer.

The thickness of diffuse layer depends on the ionic strength of the solution, and for a solution concentration higher than  $10^{-2}$  M, the thickness is less of  $100 \text{ \AA}$ .<sup>47</sup> The length between the charged metal surface and the end of the diffuse layer is indicated as Debye length ( $\lambda_D$ ), which represents the distance needed for the ions in solution to fully compensate the charge of the electrode. The Debye length is inversely proportional to the ionic strength of the solution as follows:<sup>48</sup>

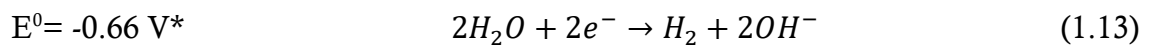
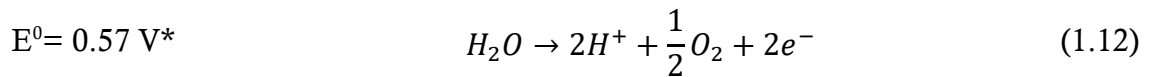
$$\lambda_D = \sqrt{\frac{\varepsilon_0 \varepsilon_r K_B T}{2 C_0 N_A e^2}} \quad (1.10)$$

where  $\varepsilon_0$  and  $\varepsilon_r$  are the vacuum and the relative permittivity, respectively,  $K_B$  is the Boltzmann constant,  $T$  is the temperature,  $C_0$  is the ionic strength of the solution,  $N_A$  is the Avogadro number and  $e$  is the elementary charge.

The Debye length is correlated to the  $C_{dl}$  by the following inverse relation:

$$C_{dl} \sim \frac{1}{\lambda_D} \quad (1.11)$$

From equations (1.10) and (1.11) it is clear that the higher the ionic strength the lower is the Debye length and the higher is the  $C_{dl}$ . As above-mentioned, a typical electrical double-layer capacitance is in the range of 10-40  $\mu\text{F}\cdot\text{cm}^{-2}$ , which is three order of magnitudes higher compared to the capacitance of the most common dielectrics used in OFETs (*i.e.*,  $\text{SiO}_2$  and polymeric dielectrics), which are in the range of  $\text{nF}\cdot\text{cm}^{-2}$ . This huge capacitance, achieved thanks to the thickness of the electrical double-layer (in the order of Å units), allows the liquid-gated transistors to operate at very low source-gate and source-drain potentials, from about 1 V to -1 V. The higher limit of potential to be applied in an EGOFET only depends on the electrolysis of the solution.<sup>49</sup> For a water-gated transistor, the electrolysis of water should be considered:



\*with respect to the Standardized Hydrogen Electrode (SHE).

Ultra-pure water shows an ionic conductivity of  $10^{-5} \text{ S}\cdot\text{cm}^{-1}$ , due to protons transfer.<sup>49</sup>

To extract the figures of merit of the EGOFETs, the same model already discussed for OFET is used, although a more comprehensive and specific theory for liquid-gated field-effect transistors should be developed. Compared to OFETs, EGOFETs display lower field-effect mobility, with the best reported mobilities around 0.1- 0.2  $\text{cm}^2/\text{V}\cdot\text{s}$ ,<sup>36,50,51</sup> as, for instance, the EGOFET based on the OSC diF-TES-ADT



blended with PS<sub>10k</sub> thin film, measured in water media, namely 0.18 cm<sup>2</sup>/V·s.<sup>36</sup> Additionally, for EGOFET devices it is more common to report the product of the mobility and the effective double-layer capacitance,  $C_{eff} \cdot \mu_{FE}$ , due to the difficulties in obtaining reliable values of the double-layer capacitance and its dependence from the potential applied ( $C_{dl}$ ). Regarding the  $I_{on/off}$  ratio, in EGOFET devices spans in the range of 10<sup>2</sup>-10<sup>3</sup>.

The low-operating potentials, the intrinsic amplification property, the possibility to fabricate them with biocompatible and flexible materials with low-cost fabrication techniques, along with the possibility to operate directly in aqueous media, makes the EGOFETs appealing for biosensing applications, as it will be discussed in the next session.

- **Organic Electrochemical Transistors**

Organic Electrochemical Transistors (OECTs) are liquid-gated transistors, but they do not work as field-effect devices. The realization of these devices date back in the mid-1980s thanks to the work of *Wrighton* and colleagues.<sup>52</sup> Like EGOFETs they are three-terminal devices in which the gate electrode is separated from the active layer by a liquid electrolyte.<sup>53</sup> Whereas for EGOFETs the current modulation is ascribed to the capacitive coupling between the gate and the OSC, in OECTs the ions from the electrolyte medium can enter the active layer modifying its doping state and consequently its conductivity.<sup>53</sup> The gate voltage governs the injection of ions into the active layers and thus the redox state (or doping state) of the organic film, while the drain voltage promotes the flow of the current, which is proportional to the mobile charges in the organic layer. OECTs share the switching and amplification properties of OFET devices. There exist *n*-type or <sup>54-56</sup> *p*-type OECTs,<sup>57,58</sup> working in accumulation or depletion regime. Depletion OECTs are the most common ones and are made of doped organic materials, which are conducting when no source-gate potential is applied and switches off upon the application of a gate voltage, which dedopes it. The sign of the gate voltage to be applied depends on the charge of the mobile carriers. On the other hand, OECTs working in the accumulation mode start to switch on upon the application of a source-gate potential.

The active layer of OECT devices is made of a semiconducting or conducting polymer which has to be permeable to ions, opposite to the materials employed for OFET and EGOFET fabrication, which ideally should be impermeable to ions. The most common conducting polymers used are based on poly(3,4-ethylenedioxythiophene), (PEDOT) and polypyrrole (PPy), which are typically porous *p*-type doped with the addition of small anions or polyanions, such as polystyrene sulfonate (PSS).<sup>53</sup> PEDOT:PSS is the most exploited because: i) it is easily synthesized by solution, vapour phase or electrochemical polymerization and it is commercially available,<sup>59</sup> ii) small ions are injected into PEDOT:PSS films from an electrolyte in a barrierless way, exhibiting a drift mobility equal to the one in bulk solution,<sup>60,61</sup> iii) it is electrochemically stable and cross-linkers can be added into the PEDOT:PSS solution before coating it in order to increase its stability in water medium,<sup>62</sup> iv) it shows a high hole conductivity, which can be increased by adding co-solvents, surfactants and by changing the processing method<sup>63</sup> and v) it exhibits a transconductance in the range of mS and a response time in the order of tens of microseconds.<sup>64</sup> However, alternative materials are being studied to improve further OECT performances. One strategy consists in attaching the sulfonate anion directly into the lateral chain of a thiophene molecule, developing an accumulation-mode OECT based on the semiconducting polythiophene sulfonate (PTHS), achieving also a high transconductance in the mS order.<sup>65</sup> Also, the development of *n*-type conducting polymers is important, and thus, *n*-type polymers such as the copolymer poly((ethoxy)ethyl 2-(2-(2-methoxyethoxy)ethoxy)acetate)-naphthalene-1,4,5,8-tetracarboxylic-diimide-co-3,3'-bis(2-(2-(2-methoxyethoxy)ethoxy)ethoxy)-(bithiophene))(p(gNDI-g2T)) is subject of study.<sup>66</sup>

To describe the physics of OECTs, the Bernardis and Mallaras model, with the name of the scientists who developed it, is widely employed.<sup>67</sup> According to this model, an organic electrochemical transistor is composed of two circuits, i) an electronic and ii) an ionic circuit. The electronic circuit accounts for the movement of mobile charges into the source-channel-drain structure and it is treated as a resistor. Thus, the mobile charges in the channel move under the influence of the source-drain potential, in a similar way as in OFETs and EGOFETs. The ionic circuit accounts for the movement of ions into the gate-electrolyte-channel structure and it is made of two capacitances and a resistance in series. The capacitances originate from both the gate/electrolyte

interface ( $C_g$ ) and the OSC/interface ( $C_{ch}$ ). The resistance expresses the resistance of the ions in solution,  $R_s$ , and it thus represents the flow of the ions in the solution (see **Figure 1.12**). This model assumes that no redox reactions occur between the electrolyte and the channel, hence excluding faradaic processes at this interface.<sup>67</sup>

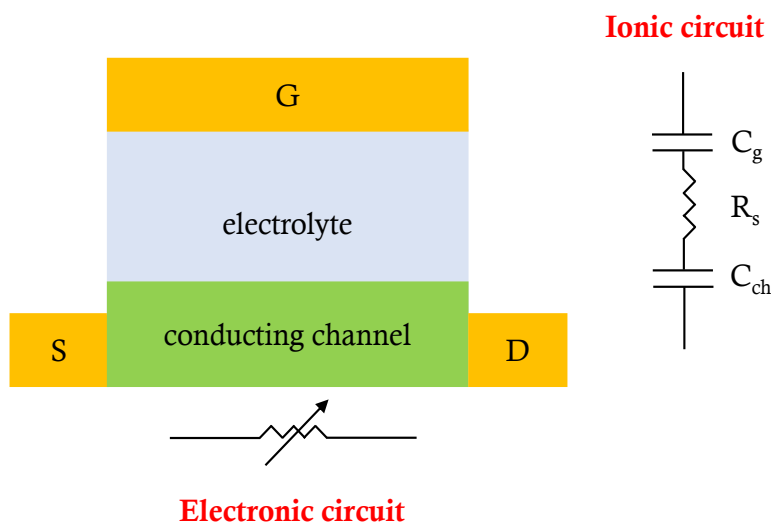


**Figure 1.12.** Scheme of the OEET layout along with the ionic circuit and the electronic circuit depicted by the Bernards model. Adapted from ref. 53.

Despite its good accordance with experimental data, the Bernards model is still lacking a comprehensive understanding of the OEET devices. For instance, a work by *Friedlein* and collaborators pointed out non-uniform mobility in OEETs channel.<sup>68</sup> Non-ideal contact<sup>69</sup> and the influence of disorder in hole transport<sup>70</sup> are other aspects to be implemented in a future model.

The most important figure of merit of an OEET device is the transconductance,  $g_m$ , expressed as the first derivative of the source-drain current profile *vs* source-gate voltage. Transconductance describes the efficiency of the transduction, that is to say, the conversion of small source-gate voltage changes in large source-drain current changes. While the transconductance values in OEET devices are in the order of mS, in EGOFET devices the transconductances are in the order of  $\mu$ S. This huge difference between these two devices is ascribed to the volumetric capacitance of OEETs in comparison to the double-layer capacitance of EGOFETs. The capacitance at the OSC/electrolyte interface in an OEET is not limited to the interface, but it extends for the entire bulk of the channel, due to the penetration of the ions throughout the

channel. According to the Bernards model, transconductance in saturation regime and for depletion-mode OECTs is given by:

$$g_m = \frac{W}{L} d \cdot \mu \cdot C^* (V_{th} - V_{GS}) \quad (1.14)$$

where  $d$  is the thickness of the channel,  $\mu$  is the charge carrier mobility and  $C^*$  is the volumetric capacitance.

The characteristics of an OECT can be tuned by changing the device geometry: increasing the channel width and thickness, the source-drain current and the transconductance increase, while when the channel length is increased, the current and transconductance decrease.<sup>71</sup>

In **Figure 1.13** an illustration of the gate dielectric/conducting channel interface behaviour is presented, for OFET, EGOFET and OECT devices, in order to give an insight into the main differences between these devices. In OFETs, as above-mentioned, the dielectric/conducting channel interface works like a capacitor, as it happens in EGOFET. However, in the latter case, the thickness of the dielectric is reduced to molecular dimensions, due to the formation of the electrical double layers (EDLs), achieving a huge capacitance and, consequently, a low-operating window potential. Lastly, in an OECT, the interface capacitance does not act as a parallel plate capacitor, but as a volumetric capacitance, due to the permeability of the active layer to ions from the electrolyte, resulting in the high transconductance values at low-operating potentials.<sup>53</sup> It is worth noting that in OECTs the thickness of the conducting layer is important in determining the volumetric capacitance because it represents the limit for ion penetration. In the bottom part of **Figure 1.13**, the gate potential profile for each device is illustrated. In OFET devices the gate potential drops linearly along the dielectric. On the contrary, in EGOFET devices, the potential drop occurs at the interface between the gate and the electrolyte, due to the formation of the electrical double-layer, which in turn is formed also at the electrolyte/OSC interface. In OECTs, the gate potential drop is similar to the EGOFETs but, at the electrolyte/OSC interface, this continues to drop throughout the bulk of the active layer, due to the penetration of ions. Thus, these interfaces are crucial in the design of sensing systems

because small modification of one of these interfaces leads to important changes in the potential drop profile, and consequently, in the device performances.

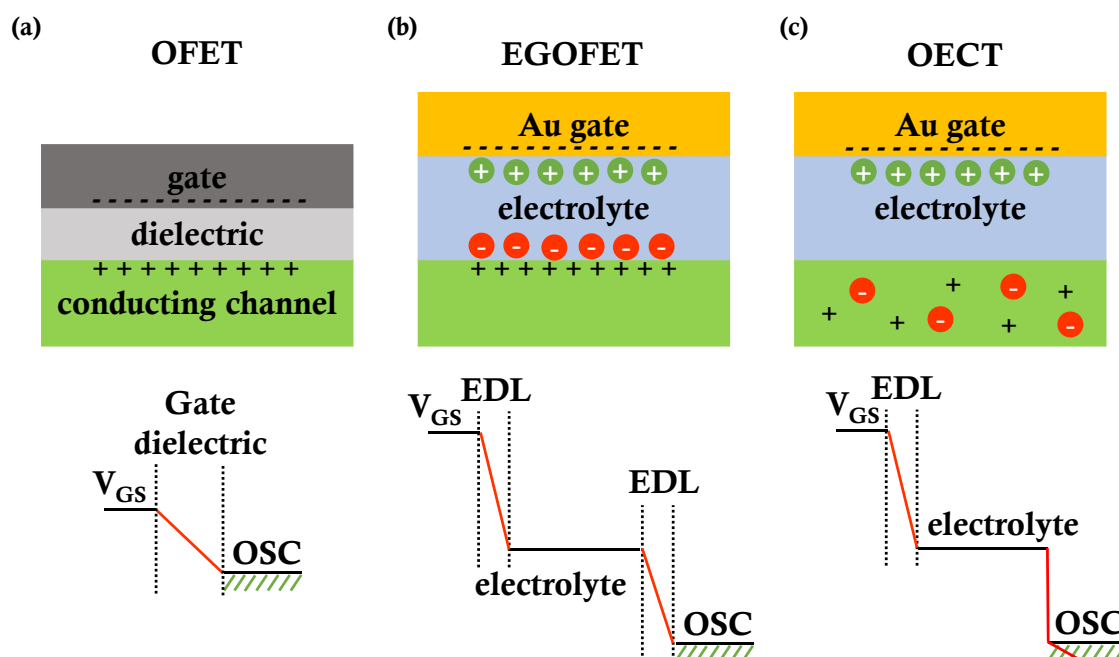


**Figure 1.13.** Schematic representation of the interface between the conducting channel and the gate dielectric in (a) OFET, (b) EGOFET and (c) OECT devices, along with the gate potential drop along the dielectric/electrolyte for each device.

While OECT has a high transconductance and hence higher amplification, the response time is lower compared to that of EGOFETs. The transconductance of OECTs starts to roll off in the kHz range of frequencies, whereas field-effect devices can be operated at higher frequencies, in the MHz range. This behaviour is ascribed to the low ion diffusion.<sup>53</sup>

### 1.3. Biosensors

The IUPAC definition of biosensors states that: “a biosensor is a device which uses specific biochemical reactions mediated by isolated enzymes, immunosystems, tissues, organelles or whole cells to detect chemical or biological compounds, usually by use of electric, thermal or optical signals”.<sup>72</sup> The first biosensor was developed in 1962 by Clark and collaborators for continuous monitoring of blood pH, oxygen, and carbon dioxide tensions and contents

for cardiovascular surgery.<sup>73</sup> Currently, they are promising analytical tools especially in the field of healthcare, environment follow-up and food industry.<sup>74</sup>

A biosensor is mainly formed by three components, i) the sensitive recognition element (or biorecognition platform), ii) the transducer and iii) the data processing. The biorecognition platform is involved in the capture of the analyte and it consists of an immobilized biocomponent for the specific detection of a target. The transducer converts the biorecognition event in an electrical, thermal or optical signal which is made readable by the data processing. A biosensor can be classified according to the receptor employed to capture the analyte or depending on the transducer used (see **Figure 1.14**).<sup>74,75</sup>

The **receptors** are selected to ensure a selective and specific binding with the analyte of interest. Antibodies and enzymes are known to be rather specific against proteins and electroactive molecules and they can discriminate even between two enantiomers.<sup>76,77</sup> DNA strands can be engineered to be selective towards a specific analyte and their easy and low-cost synthesis have spread their use.<sup>78</sup> Cells have also been exploited in biosensing, for example, to monitor their vital signs.<sup>79</sup>

Regarding the **transducer** component, one class of platform entails the **electrochemical** biosensors, which in turn, can be classified as i) amperometric, when the current resulting from the reduction or oxidation of the analyte is measured, ii) potentiometric, when a potential difference between a working electrode and a reference one is measured, iii) conductometric, when a change in the conductivity of a system is revealed, or iv) field-effect, which are mostly based on the so-called ion-selective field-effect transistor, ISFET, OFET and EGOFET devices. They will be discussed in detail in the next section.<sup>80</sup> The most important **optical** biosensors are Surface Plasmon Resonance based sensors<sup>81</sup> or fibre optic based ones.<sup>78</sup> **Calorimetric** biosensors relate to the measurement of the changes in temperature in the reaction between the biorecognition element and a suitable analyte, which can be correlated to the amount of the analyte present in the system.<sup>75</sup> Finally, **piezoelectric** biosensors are mass-based sensors, in which a change in the adsorbed mass promotes a change in the oscillation frequency of the transducer, like in the quartz-crystal microbalance based sensors.<sup>73</sup>

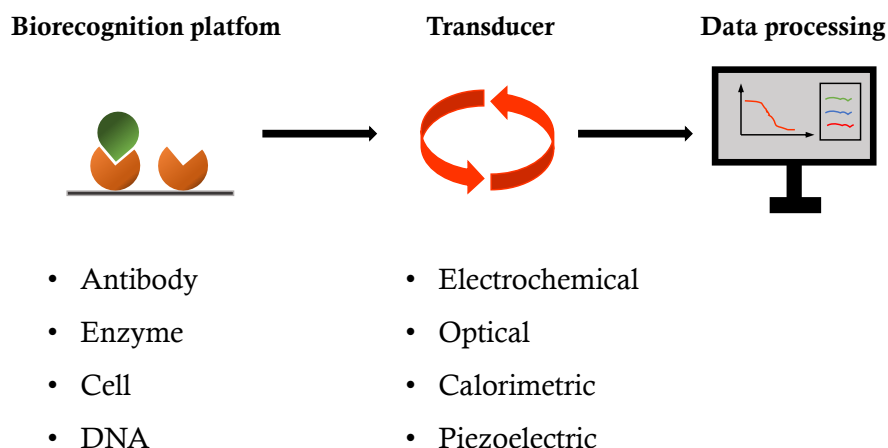


**Figure 1.14.** Scheme of the main components of biosensors. A biosensor can be classified according to the biorecognition platform and the kind of transducer.

The main focus of this thesis research was the development of organic electrolyte-gated field-effect and organic electrochemical transistors-based biosensors, thus the discussion will be centred on this kind of biosensors.

- **Ion-sensitive and chemically sensitive field-effect transistors**

In 1970 Bergveld invented the first field-effect based sensor, the so-called ion-sensitive field-effect transistor, ISFET.<sup>82</sup> The ion-sensitive FET measures the concentration of ions present in the solution, which is registered as a variation of the output current. The operating principle relies on the use of an ion-selective membrane placed on top of the gate dielectric, an electrolyte solution and a reference electrode placed into the solution, which act as the gate electrode. The ion-selective membrane allows the passage of specific ions with a small energy barrier for their transport across the membrane-solution interface, prohibiting the transport of all the other ions, which possess a large energy barrier to cross the membrane.<sup>83</sup> When the concentration of the ions of interest changes, they diffuse across the membrane, according to the concentration gradient, however, all the other ions are not allowed. Thus, an interfacial potential change occurs at the source-gate terminal, provoking a change in the conductivity of the ISFET channel. The more general variant of the ISFET is the so-called chemically-sensitive FET, CHEMFET, which is sensitive to other chemicals apart to ions. As for ISFET, the gate terminal is substituted with a chemically sensitive

membrane immersed in an electrolyte solution and in contact with the gate dielectric, and the gate potential is applied through a reference electrode, as depicted in **Figure 1.15**.

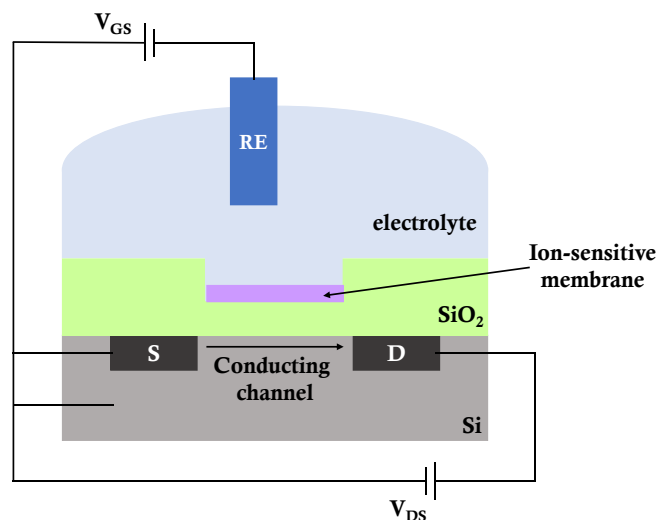


**Figure 1.15.** Schematic representation of an ISFET, adapted from ref. 84.

The above-discussed ISFET and ChemFET were initially based on inorganic materials, in particular Silicon semiconductor, but in recent years organic counterparts have been developed.<sup>85</sup> For instance, *Scarpa* and co-workers elaborated an ion-selective organic FET (ISOFET) based on the semiconducting polymer P3HT, conceived as a pH sensor.<sup>86</sup> The active layer is in direct contact with the electrolyte solution and thus the ions can penetrate the polymer and reach the interface with the dielectric, at which the conduction takes place, influencing the charge carrier mobility in the conducting channel.<sup>86</sup>

One limitation of these kind of devices is the need to use a reference electrode, being the Ag/AgCl electrode the most employed, which is fragile and difficult to miniaturize.

- **Liquid-gated transistors in the biosensing field**

Both electrolyte-gated field-effect transistors (EGOFETs) and organic electrochemical transistors (OECTs) are widely explored for biosensing applications. Among the reasons for such interest, there are i) low-cost processability, ii) possibility to use biocompatible and flexible materials for implantable and wearable systems,



iii) intrinsic signal amplification, iv) low operating voltages and v) label-free and fast response.

Regarding **EGOFET-based biosensors**, they are preferentially used to detect an analyte which does not undergo a redox reaction upon the binding with the immobilized receptors. The operating principle of the EGOFETs relies on the capacitive coupling between the gate electrode and the active layer. If a faradaic current is produced, a non-negligible gate current will arise. In general, an EGOFET biosensor can be considered as a potentiometric sensor, acting similarly as the pioneer ISFET, in which a differential potential builds up upon the analyte binding.<sup>87</sup> However, also the binding event can cause a change in the double-layer capacitance.

Two different strategies have been exploited so far for the design of the sensing platform, i) immobilization of the receptors on top of the gate electrode surface<sup>76,88–92</sup> or ii) on top of the active layer of the device,<sup>93–95</sup> as depicted in **Figure 1.16**. These two interfaces are the most sensitive to changes occurring at the gate surface or OSC surface, due to the potential drop that takes place at the electrical double layer, as mentioned in the above section.

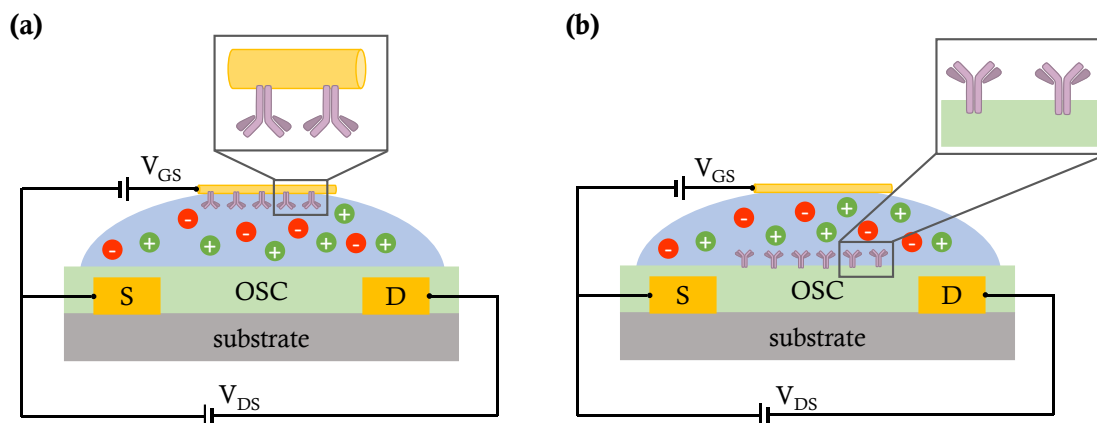


**Figure 1.16.** Schematic representation of an electrolyte-gated field-effect transistor biofunctionalized for sensing applications. (a) Biomodification of the gate electrode surface, (b) receptors immobilization on the OSC surface.

In 2013 one of the first works concerning the EGOFET gate modification for biosensing purposes was published by *Casalini* and co-workers. They employed a P3HT-based EGOFET to detect dopamine, by the immobilization of boronic acid into the gold gate surface, through a thiol-based self-assembled monolayer (**Figure 1.17,a**).

The interaction between dopamine and boronic acid promotes the formation of a negatively charged boronic ester whose charge is screened by the amino group of the dopamine, thus creating an interfacial dipole which is reflected by a shift of the transfer characteristics. They conceived an interfacial potential profile as illustrated in **Figure 1.17,b**, claiming that dopamine adsorption at the gate electrode changes both the gate capacitance and the dipole potential thus, a more negative gate voltage has to be applied to obtain the same amount of source-drain current.<sup>88</sup>

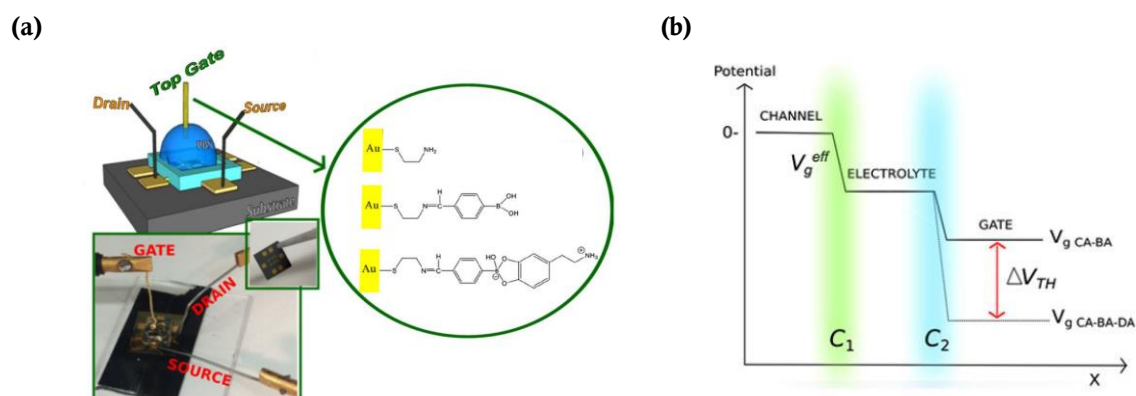


**Figure 1.17.** (a) Schematic and real picture of the system used. (b) Interfacial potential profile before and after dopamine binding. Extracted from ref. 88.

Concerning an example of the active layer modification, *Magliulo* and collaborators elaborated a P3HT-based EGOFET for protein-C detection by direct adsorption of its autoantibody on top of the P3HT active layer (**Figure 1.18**).<sup>93</sup> The receptors were physically adsorbed onto the P3HT layer, without the need of any polymer pre-treatment. They obtained a reduction of the source-drain current upon the binding with the analyte, but no appreciable  $V_{th}$  variation was observed. Thus, the reduction of the current was ascribed to a reduction in the capacitance of the gating system after the biomolecules binding.

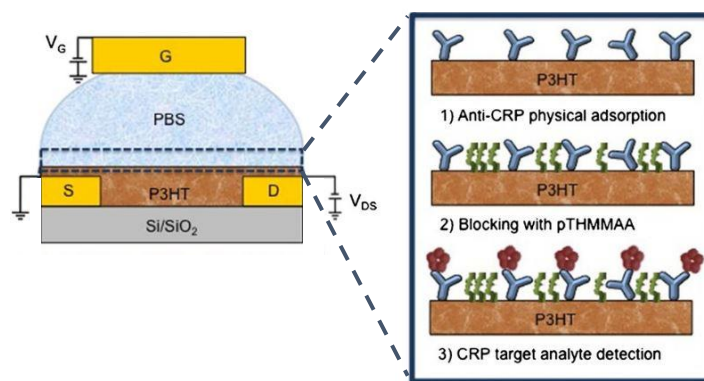


**Figure 1.18.** Biofunctionalization of the OSC surface of an EGOFET, extracted from ref. 93.

In both cases, the biofunctionalization of one of the two sensitive interfaces of an EGOFET, namely the gate/electrolyte and the electrolyte/OSC interfaces, promotes a variation of the effective potential drop at that interface and also of its capacitance, which is reflected by a variation of the electrical performance of the device, in terms of  $V_{th}$  or in terms of source-drain current caused by a change in the slope of the transfer curves.

A debated aspect among the scientific community is whether is possible or not to detect a recognition event which happens beyond the above-discussed Debye length. Some scientists assert that beyond the Debye length the screening effect of the ions impedes accurate sensing because the interfacial potential created by the biomolecule binding exponentially decays towards zero with distance.<sup>96,97</sup> There are two possible solutions to try to overcome this problem, i) use of simple and short receptors directly anchored at the surface, such as aptamers or affimers, ii) use of diluted electrolyte solution, as the Debye length is inversely proportional to the ionic strength of the electrolyte. Aptamers and affimers are emerging ligands because of their small size, simple preparation procedure and thermal stability, which makes them suitable for label-free and sensitive analyte detection. Aptamers are oligonucleotide sequences, whereas affimers are oligopeptide sequences which recognize a specific antigen. Some other works, instead, claimed a possible detection far beyond the Debye length.<sup>92,98</sup>

A huge effort in the biosensing field has been dedicated to exploring **OECT devices**, especially for detecting electroactive species. Most OECT biosensors in literature exploit enzymatic-mediated redox reactions, which promote a variation of the diffusion of ions into the permeable active channel. While EGOFETs are employed

mainly as potentiometric sensors, OECTs can be used also as amperometric sensor. In the case of an EGOFET, a faradaic current promoted by the binding of the analyte would cause a non-negligible source-gate current, the so-called leakage current, which would interfere with the proper operating of the device itself. In OECT devices, however, a faradaic current generated by the analyte would help in the modification of the doping state of the conducting channel by providing additional ions to diffuse into it. Nevertheless, the distinction between the two operating regimes in OECT biosensors is not always straightforward.<sup>87</sup> However, having a clear understanding of the sensing mechanism, amperometric or potentiometric, is of utmost importance for the rationalization and quantification of the sensor itself.

As it happens for EGOFET devices, also for OECTs there are examples in which the biorecognition event occurs at the gate surface or at the active layer surface. Different metabolites have been sensed with OECT devices, such as ascorbic acid,<sup>99</sup> dopamine,<sup>100</sup> acetylcholine,<sup>101</sup> glutamate<sup>101</sup> and gallic acid<sup>102</sup> and also to monitor in *real-time* the glucose level on plants,<sup>103</sup> paving the way towards the so-called electronics plants field (*e-plants*).

An OECT-based glucose sensor was reported by *Yang* and coworkers.<sup>104</sup> In this case an ionic liquid was exploited for the encapsulation of the glucose oxidase, and placed on top of the PEDOT:PSS gate electrode and conducting channel, both sites acting as sensing platform (**Figure 1.19**). The addition of the glucose in the ionic liquid electrolyte, promotes its oxidation and the subsequent production of H<sub>2</sub>O<sub>2</sub>. At the same time the enzymes are reduced: electrons move towards the gate and cations enter the conducting channel, de-doping it and thus decreasing the source-drain current. Due to the intrinsic amplification of OECTs, the source-drain current variation is much larger than the source-gate current.

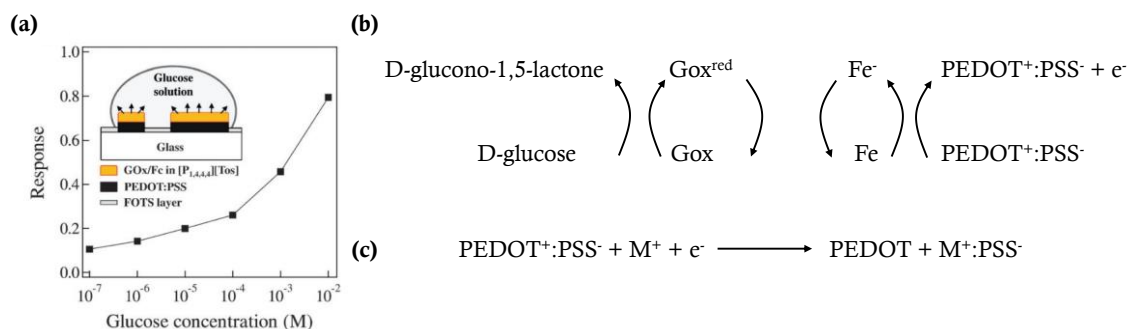


**Figure 1.19.** (a) Calibration curve obtained for different glucose concentrations; in the inset a schematic representation of the OECS is illustrated: the ionic liquid embedded with the enzymes is placed on top of the PEDOT:PSS conducting channel and PEDOT:PSS gate electrode. (b) Reaction occurring at the gate electrode; (c) reaction occurring at the conducting channel. Extracted from ref. 104.

A more recent example of a plant glucose biosensor was described by *Diacci* and coworkers.<sup>103</sup> In this case the sensing platform relies on the gate electrode. In **Figure 1.20** the gate functionalization with glucose oxidase cross-linked within a chitosan matrix is reported. Upon the oxidation of glucose, a faradaic current is generated, changing the effective gate potential, and subsequently, decreasing the source-drain current.<sup>103</sup>

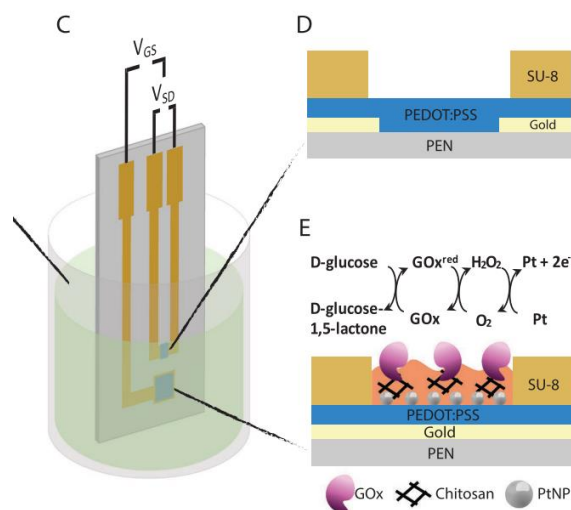


**Figure 1.20.** Structure of an OECS with the gate surface functionalized with glucose oxidase, extracted from ref. 103.

In literature there are also examples of OEET-based biosensors in which no redox reactions are involved in the sensing mechanism. For instance, very recently a sensor for the detection of the aggregated form of amyloids protein was developed. The biorecognition platform was placed here on top of the active layer and consisted of a nanostructured membrane displaying a high affinity for these amyloid aggregates (**Figure 1.21**). Upon adsorption of the oligopeptides the penetration of ions from the electrolyte solution is impeded due to steric hindrance, and consequently, the doping and de-doping of the active layer is hampered.

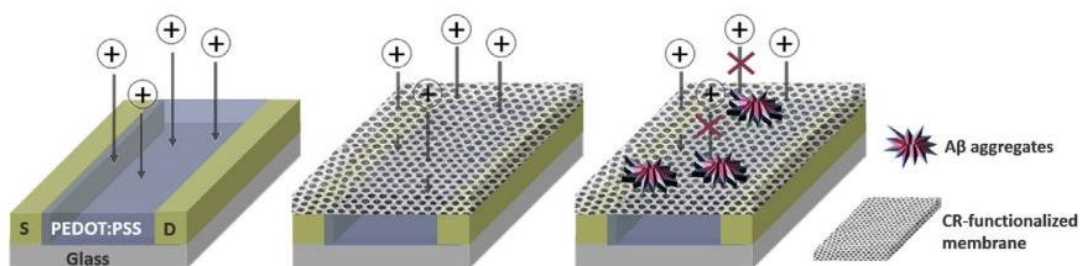


**Figure 1.21.** OEET in which the amyloid-selective membrane is placed between the channel and the electrolyte solution (middle). Cation drift into the PEDOT:PSS channel is impaired because of the A $\beta$  aggregates adsorbed on the membrane (right). Extracted from ref. 105.

Only a few examples of non-electroactive targets for immunosensing are reported in literature for OEETs. In immunosensing, there are no redox reactions involved, thus no electrons are transferred to the gate electrode and the change in the source-drain current can be attributed solely to a variation in the potential drop at one of the two interfaces, the so-called surface potential modulation.<sup>106</sup> In chapter 3, this will be discussed in more detail.

In this thesis manuscript, both EGOFET and OEET devices have been investigated for the detection of an important biomarker for neurodegenerative diseases,  $\alpha$ -synuclein.

## 1.4. General objectives

This thesis is focused on the fabrication of high-performance electrolyte-gated field-effect transistors (EGOFETs), employing *p*-type small molecules blended with insulating polymers and deposited by a solution-processed technique, Bar-Assisted Meniscus-Shearing (BAMS). The main goals of this thesis are the development of a biosensor for the detection of a Parkinson's disease biomarker, *viz.*  $\alpha$ -synuclein, and the study of an all-flexible liquid-gated transistor. The manuscript is divided into three experimental chapters (from chapter 2 to chapter 4) and a final chapter containing all the experimental details (chapter 6). Particularly, the thesis is centred on the following objectives:

1. Development of a label-free immunosensor for the detection of  $\alpha$ -synuclein, based on diF-TES-ADT:PS<sub>10k</sub> EGOFET device by designing and comparing two different approaches for the autoantibody immobilization on the gold gate surface electrode. Implementation of these biorecognition EGOFET platforms into a microfluidic system aiming at a more applicative interface.
2. Development of an OECT device based on PEDOT:PSS as label-free immunosensor for the detection of  $\alpha$ -synuclein, aiming at a deep understanding of the sensing response.
3. Study of the C<sub>8</sub>O-BTBT-OC<sub>8</sub> organic semiconductor as active layer in EGOFET devices. Comparison of the electric performances of the bare OSC and the polystyrene blended OSC deposited by BAMS. Fabrication of the devices on flexible substrates and evaluation of the electrical performances under mechanical strain.

## Bibliography

- (1) Anderson, P. W.; Lee, P. A. Remarks on Giant Conductivity in TTF-TCNQ. *Solid State Communications* **1973**, *13* (1), 595–598.
- (2) Shirakawa, H.; Louis, E. J.; MacDiarmid, A. G.; Chiang, C. K.; Heeger, A. J. Synthesis of Electrically Conducting Organic Polymers: Halogen Derivatives of Polyacetylene, (CH)<sub>x</sub>. *Journal of the Chemical Society, Chemical Communications* **1977**, No. 16, 578–580.
- (3) Sirringhaus, H. 25th Anniversary Article : Organic Field-Effect Transistors : The Path Beyond Amorphous Silicon. *Advanced Materials* **2014**, *26*, 1319–1335.
- (4) Heeger, A. J. Semiconducting Polymers: The Third Generation. *Chemical Society Reviews* **2010**, *39* (7), 2354–2371.
- (5) Sirringhaus, H.; Brown, P. J.; Friend, R. H.; Nielsen, M. M.; Bechgaard, K.; Langeveld-Voss, B. M. W.; Spiering, A. J. H.; Janssen, R. A. J.; Meijer, E. W.; Herwig, P.; et al. Two-Dimensional Charge Transport in Self-Organized, High-Mobility Conjugated Polymers. *Nature* **1999**, *401*, 685–688.
- (6) Hamadani, B. H.; Gundlach, D. J.; McCulloch, I.; Heeney, M. Undoped Polythiophene Field-Effect Transistors with Mobility of  $1 \text{ cm}^2 \text{ V}^{-1} \text{ s}^{-1}$ . *Applied Physics Letters* **2007**, *91* (24), 243512.
- (7) Yun, H. J.; Cho, J.; Chung, D. S.; Kim, Y. H.; Kwon, S. K. Comparative Studies on the Relations between Composition Ratio and Charge Transport of Diketopyrrolopyrrole-Based Random Copolymers. *Macromolecules* **2014**, *47*(20), 7030–7035.
- (8) Leonardi, F.; Zhang, Q.; Kim, Y. H.; Mas-Torrent, M. Solution-Sheared Thin Films of a Donor-Acceptor Random Copolymer/Polystyrene Blend as Active Material in Field-Effect Transistors. *Materials Science in Semiconductor Processing* **2019**, *93*, 105–110.
- (9) Groenendaal, L.; Jonas, F.; Freitag, D.; Pielartzik, H.; Reynolds, J. R. Poly(3,4-Ethylenedioxythiophene) and Its Derivatives: Past, Present, and Future.



*Advanced Materials* **2000**, *12* (7), 481–494.

- (10) Stadlober, B.; Zirkl, M.; Beutl, M.; Leising, G.; Bauer-Gogonea, S.; Bauer, S. High-Mobility Pentacene Organic Field-Effect Transistors with a High-Dielectric-Constant Fluorinated Polymer Film Gate Dielectric. *Applied Physics Letters* **2005**, *86* (24), 242902.
- (11) Park, S. K.; Kuo, C. C.; Anthony, J. E.; Jackson, T. N. High Mobility Solution-Processed OTFTs. *IEEE International Electron Devices Meeting, 2005. IEDM Technical Digest* **2005**, 105–108.
- (12) Giri, G.; Park, S.; Vosgueritchian, M.; Shulaker, M. M.; Bao, Z. High-Mobility, Aligned Crystalline Domains of Tips-Pentacene with Metastable Polymorphs through Lateral Confinement of Crystal Growth. *Advanced Materials* **2014**, *26* (3), 487–493.
- (13) Ruzie, C.; Karpinska, J.; Laurent, A.; Sanguinet, L.; Hunter, S.; Anthopoulos, T. D.; Lemaur, V.; Cornil, J.; Kennedy, A. R.; Fenwick, O.; et al. Design, Synthesis, Chemical Stability, Packing, Cyclic Voltammetry, Ionisation Potential, and Charge Transport of [1]Benzothieno[3,2-b]-[1]Benzothiophene Derivatives. *Journal of Materials Chemistry C* **2016**, *4*, 4863–4879.
- (14) Karpinska, J.; Chattopadhyay, B.; Schweicher, G.; Richard, A.; Lemaur, V.; Kennedy, A. R.; Diao, Y.; Lee, W.; Mannsfeld, S.; Bao, Z.; et al. Thienoacene Dimers Based on the Thieno[3,2-b] Thiophene Moiety: Synthesis, Characterization and Electronic Properties. *Journal of Materials Chemistry C* **2015**, *3*, 674–685.
- (15) Temiño, I.; Del Pozo, F. G.; Ajayakumar, M. R.; Galindo, S.; Puigdollers, J.; Mas-Torrent, M. A Rapid, Low-Cost, and Scalable Technique for Printing State-of-the-Art Organic Field-Effect Transistors. *Advanced Materials Technologies* **2016**, *1* (5), 1–7.
- (16) Pitsalidis, C.; Pappa, A. M.; Hunter, S.; Laskarakis, A.; Kaimakamis, T.; Payne, M. M.; Anthony, J. E.; Anthopoulos, T. D.; Logothetidis, S. High Mobility Transistors Based on Electrospray-Printed Small-Molecule/Polymer Semiconducting Blends. *Journal of Materials Chemistry C* **2016**, *4* (16), 3499–3507.

- (17) Riera-Galindo, S.; Leonardi, F.; Pfattner, R.; Mas-Torrent, M. Organic Semiconductor/Polymer Blend Films for Organic Field-Effect Transistors. *Advanced Materials Technologies* **2019**, 1900104.
- (18) Teixeira da Rocha, C.; Haase, K.; Zheng, Y.; Löffler, M.; Hamsch, M.; Mannsfeld, S. C. B. Solution Coating of Small Molecule/Polymer Blends Enabling Ultralow Voltage and High-Mobility Organic Transistors. *Advanced Electronic Materials* **2018**, 4 (8), 1–9.
- (19) Niazi, M. R.; Li, R.; Qiang Li, E.; Kirmani, A. R.; Abdelsamie, M.; Wang, Q.; Pan, W.; Payne, M. M.; Anthony, J. E.; Smilgies, D. M.; et al. Solution-Printed Organic Semiconductor Blends Exhibiting Transport Properties on Par with Single Crystals. *Nature Communications* **2015**, 6, 8598.
- (20) Stingelin-Stutzmann, N.; Smits, E.; Wondergem, H.; Tanase, C.; Blom, P.; Smith, P.; De Leeuw, D. Organic Thin-Film Electronics from Vitreous Solution-Processed Rubrene Hypereutectics. *Nature Materials* **2005**, 4 (8), 601–606.
- (21) Lee, W. H.; Park, Y. D. Organic Semiconductor/Insulator Polymer Blends for High-Performance Organic Transistors. *Polymers* **2014**, 6 (4), 1057–1073.
- (22) Riera-Galindo, S.; Tamayo, A.; Mas-Torrent, M. Role of Polymorphism and Thin-Film Morphology in Organic Semiconductors Processed by Solution Shearing. *ACS Omega* **2018**, 3 (2), 2329–2339.
- (23) Paterson, A. F.; Singh, S.; Fallon, K. J.; Hodsden, T.; Han, Y.; Schroeder, B. C.; Bronstein, H.; Heeney, M.; McCulloch, I.; Anthopoulos, T. D. Recent Progress in High-Mobility Organic Transistors: A Reality Check. *Advanced Materials* **2018**, 1801079.
- (24) Coropceanu, V.; Demetrio, A.; Filho, S.; Olivier, Y.; Silbey, R.; Bre, J. Charge Transport in Organic Semiconductors. *Chemical Reviews* **2007**, 107, 926–952.
- (25) Minder, N. A.; Ono, S.; Chen, Z.; Facchetti, A.; Morpurgo, A. F. Band-like Electron Transport in Organic Transistors and Implication of the Molecular Structure for Performance Optimization. *Advanced Materials* **2012**, 24 (4), 503–508.
- (26) Verlaak, S.; Arkhipov, V.; Heremans, P. Modeling of Transport in

- Polycrystalline Organic Semiconductor Films. *Applied Physics Letters* **2003**, *82*, 745.
- (27) Haneef, H. F.; Zeidell, A. M.; Jurchescu, O. D. Charge Carrier Traps in Organic Semiconductors: A Review on the Underlying Physics and Impact on Electronic Devices. *Journal of Materials Chemistry C* **2020**, *8* (3), 759–787.
- (28) Horowitz, G.; Hajlaoui, M. E.; Hajlaoui, R. Temperature and Gate Voltage Dependence of Hole Mobility in Polycrystalline Oligothiophene Thin Film Transistors. *Journal of Applied Physics* **2000**, *87*, 4456.
- (29) Olivier, Y.; Lemaire, V.; Brédas, J. L.; Cornil, J. Charge Hopping in Organic Semiconductors: Influence of Molecular Parameters on Macroscopic Mobilities in Model One-Dimensional Stacks. *Journal of Physical Chemistry A* **2006**, *110* (19), 6356–6364.
- (30) Chilvery, A.; Das, S.; Guggilla, P.; Brantley, C.; Sunda-Meya, A. A Perspective on the Recent Progress in Solution-Processed Methods for Highly Efficient Perovskite Solar Cells. *Science and Technology of Advanced Materials* **2016**, *17* (1), 650–658.
- (31) Qin, M. Z.; Wang, X. H.; Yuan, M.; Lv, S. C.; Gu, X. Dip-Coating of Patterned Organic Semiconductor Films. *Applied Mechanics and Materials* **2015**, *748*, 29–37.
- (32) Xu, G.; Bao, Z.; Groves, J. T. Langmuir-Blodgett Films of Regioregular Poly(3-Hexylthiophene) as Field-Effect Transistors. *Langmuir* **2000**, *16* (4), 1834–1841.
- (33) Krebs, F. C. Fabrication and Processing of Polymer Solar Cells: A Review of Printing and Coating Techniques. *Solar Energy Materials and Solar Cells* **2009**, *93* (4), 394–412.
- (34) Berni, A.; Mennig, M.; Schmidt, H. Doctor Blade BT - Sol-Gel Technologies for Glass Producers and Users; Aegerter, M. A., Mennig, M., Eds.; Springer US: Boston, MA, 2004; pp 89–92.
- (35) Del Pozo, F. G.; Fabiano, S.; Pfattner, R.; Georgakopoulos, S.; Galindo, S.; Liu, X.; Braun, S.; Fahlman, M.; Veciana, J.; Rovira, C.; et al. Single Crystal-like Performance in Solution-Coated Thin-Film Organic Field-Effect Transistors. *Advanced Functional Materials* **2016**, *26* (14), 2379–2386.

- (36) Zhang, Q.; Leonardi, F.; Casalini, S.; Temiño, I.; Mas-Torrent, M. High Performing Solution-Coated Electrolyte-Gated Organic Field-Effect Transistors for Aqueous Media Operation. *Scientific Reports* **2016**, *6* (November), 1–10.
- (37) Leonardi, F.; Casalini, S.; Zhang, Q.; Galindo, S.; Gutiérrez, D.; Mas-Torrent, M. Electrolyte-Gated Organic Field-Effect Transistor Based on a Solution Sheared Organic Semiconductor Blend. *Advanced Materials* **2016**, *28* (46), 10311–10316.
- (38) Bardeen, J.; Brattain, W. H. The Transistor, A Semi-Conductor Triode. *Physical Review* **1948**, *74* (2), 230–231.
- (39) Tanenbaum, M.; Valdes, L. B.; Buehler, E.; Hannay, N. B. Silicon N-p-n Grown Junction Transistors. *Journal of Applied Physics* **1955**, *26* (6), 686–692.
- (40) Horowitz, B. G. Organic Field-Effect Transistors. *Advanced Materials* **1998**, *10* (5), 365–377.
- (41) Klauk, H. Organic Thin-Film Transistors. *Chemical Society Reviews* **2010**, *39* (7), 2643–2666.
- (42) Horowitz, B. G.; Hajlaoui, R.; Bouchriha, H. The Concept of “Threshold Voltage” in Organic Field-Effect Transistors. *Advanced Materials* **1998**, *10*, 923–927.
- (43) Lamport, Z. A.; Haneef, H. F.; Anand, S.; Waldrip, M.; Jurchescu, O. D. Tutorial: Organic Field-Effect Transistors: Materials, Structure and Operation. *Journal of Applied Physics* **2018**, *124* (7), 071101.
- (44) Sze, S. M. *Semiconductor Devices, Physics and Technology*, 2nd editio.; Jonh Wiley & Sons, Inc.
- (45) Gamota, D.; Paul Brazis, J. *The Authoritative Dictionary of IEEE Standards Terms*, 7th editio.; Institute of Electrical and Electronics Engineers, I., Ed.; New York, 2008.
- (46) Kergoat, L.; Herlogsson, L.; Braga, D.; Piro, B.; Pham, M. C.; Crispin, X.; Berggren, M.; Horowitz, G. A Water-Gate Organic Field-Effect Transistor. *Advanced Materials* **2010**, *22* (23), 2565–2569.

- (47) Bard, A. J.; Faulkner, L. R. *Electrochemical Methods. Fundamentals and Applications*; 2001.
- (48) Melzer, K.; Brändlein, M.; Popescu, B.; Popescu, D.; Lugli, P.; Scarpa, G. Characterization and Simulation of Electrolyte-Gated Organic Field-Effect Transistors. *Faraday Discussions* **2014**, *174*, 399–411.
- (49) Cramer, T.; Campana, A.; Leonardi, F.; Casalini, S.; Kyndiah, A.; Murgia, M.; Biscarini, F. Water-Gated Organic Field Effect Transistors – Opportunities for Biochemical Sensing and Extracellular Signal Transduction. *Journal of Materials Chemistry B* **2013**, *1*, 3728–3741.
- (50) Mulla, M. Y.; Tuccori, E.; Magliulo, M.; Lattanzi, G.; Palazzo, G.; Persaud, K.; Torsi, L. Capacitance-Modulated Transistor Detects Odorant Binding Protein Chiral Interactions. *Nature Communications* **2015**, *6*, 6010.
- (51) Kergoat, L.; Battaglini, N.; Miozzo, L.; Piro, B.; Pham, M.-C.; Yassar, A.; Horowitz, G. Use of Poly(3-Hexylthiophene)/Poly(Methyl Methacrylate) (P3HT/PMMA) Blends to Improve the Performance of Water-Gated Organic Field-Effect Transistors. *Organic Electronics* **2011**, *12* (7), 1253–1257.
- (52) Kittlesen, G. P.; White, H. S.; Wrighton, M. S. Chemical Derivatization of Microelectrode Arrays by Oxidation of Pyrrole and N-Methylpyrrole: Fabrication of Molecule-Based Electronic Devices. *Journal of the American Chemical Society* **1984**, *106* (24), 7389–7396.
- (53) Rivnay, J.; Inal, S.; Salleo, A.; Owens, R. M.; Berggren, M.; Malliaras, G. G. Organic Electrochemical Transistors. *Nature Reviews Materials* **2018**, *3*, 17086.
- (54) Sun, H.; Vagin, M.; Wang, S.; Crispin, X.; Forchheimer, R.; Berggren, M.; Fabiano, S. Complementary Logic Circuits Based on High-Performance n-Type Organic Electrochemical Transistors. *Advanced Materials* **2018**, *30*, 1704916.
- (55) Pappa, A. M.; Ohayon, D.; Giovannitti, A.; Maria, I. P.; Savva, A.; Uguz, I.; Rivnay, J.; McCulloch, I.; Owens, R. M.; Inal, S. Direct Metabolite Detection with an N-Type Accumulation Mode Organic Electrochemical Transistor. *Science Advances* **2018**, *4*, 1–8.
- (56) Bischak, C. G.; Flagg, L. Q.; Yan, K.; Li, C. Z.; Ginger, D. S. Fullerene Active

- Layers for N-Type Organic Electrochemical Transistors. *ACS Applied Materials and Interfaces* **2019**, *11* (31), 28138–28144.
- (57) M. Demelas, E. Scavetta, L. Basiricò, R. Rogani, A. B. A Deeper Insight into the Operation Regime of All-Polymeric Electrochemical Transistors. *Applied Physics Letters* **2013**, *102* (193301), 1–4.
- (58) Schmode, P.; Ohayon, D.; Reichstein, P. M.; Savva, A.; Inal, S.; Thelakkat, M. High-Performance Organic Electrochemical Transistors Based on Conjugated Polyelectrolyte Copolymers. *Chemistry of Materials* **2019**, *31* (14), 5286–5295.
- (59) Elschner, A., Kirchmeyer, S., Lovenich, W., Merker, U., Reuter, K. *PEDOT Principles and Applications of an Intrinsically Conductive Polymer*, CRC Press, 2010.
- (60) Inal, S.; Malliaras, G. G.; Rivnay, J. Optical Study of Electrochromic Moving Fronts for the Investigation of Ion Transport in Conducting Polymers. *Journal of Materials Chemistry C* **2016**, *4* (18), 3942–3947.
- (61) Rivnay, J.; Inal, S.; Collins, B. A.; Sessolo, M.; Stavriniidou, E.; Strakosas, X.; Tassone, C.; Delongchamp, D. M.; Malliaras, G. G. Structural Control of Mixed Ionic and Electronic Transport in Conducting Polymers. *Nature Communications* **2016**, *7*, 11287.
- (62) Håkansson, A.; Han, S.; Wang, S.; Lu, J.; Braun, S.; Fahlman, M.; Berggren, M.; Crispin, X.; Fabiano, S. Effect of (3-Glycidioxypropyl)Trimethoxysilane (GOPS) on the Electrical Properties of PEDOT:PSS Films. *Journal of Polymer Science, Part B: Polymer Physics* **2017**, *55* (10), 814–820.
- (63) Wang, Y.; Zhu, C.; Pfattner, R.; Yan, H.; Jin, L.; Chen, S.; Molina-Lopez, F.; Lissel, F.; Liu, J.; Rabiah, N. I.; et al. A Highly Stretchable, Transparent, and Conductive Polymer. *Science Advances* **2017**, *3* (3), e1602076.
- (64) Khodagholy, D.; Rivnay, J.; Sessolo, M.; Gurfinkel, M.; Leleux, P.; Jimison, L. H.; Stavriniidou, E.; Herve, T.; Sanaur, S.; Owens, R. M.; et al. High Transconductance Organic Electrochemical Transistors. *Nature Communications* **2013**, *4*, 2133.
- (65) Inal, S.; Rivnay, J.; Leleux, P.; Ferro, M.; Ramuz, M.; Brendel, J. C.; Schmidt, M. M.; Thelakkat, M.; Malliaras, G. G. A High Transconductance

- Accumulation Mode Electrochemical Transistor. *Advanced Materials* **2014**, *26* (44), 7450–7455.
- (66) Giovannitti, A.; Nielsen, C. B.; Sbircea, D. T.; Inal, S.; Donahue, M.; Niazi, M. R.; Hanifi, D. A.; Amassian, A.; Malliaras, G. G.; Rivnay, J.; et al. N-Type Organic Electrochemical Transistors with Stability in Water. *Nature Communications* **2016**, *7*, 13066.
- (67) Bernardis, B. D. A.; Malliaras, G. G. Steady-State and Transient Behavior of Organic Electrochemical Transistors. *Advanced Functional Materials* **2007**, *17*, 3538–3544.
- (68) Friedlein, J. T.; Shaheen, S. E.; Malliaras, G. G.; McLeod, R. R. Optical Measurements Revealing Nonuniform Hole Mobility in Organic Electrochemical Transistors. *Advanced Electronic Materials* **2015**, *1* (11), 1500189.
- (69) Kaphle, V.; Liu, S.; Al-Shadeedi, A.; Keum, C. M.; Lüssem, B. Contact Resistance Effects in Highly Doped Organic Electrochemical Transistors. *Advanced Materials* **2016**, *28* (39), 8766–8770.
- (70) Friedlein, J. T.; Rivnay, J.; Dunlap, D. H.; McCulloch, I.; Shaheen, S. E.; McLeod, R. R.; Malliaras, G. G. Influence of Disorder on Transfer Characteristics of Organic Electrochemical Transistors. *Applied Physics Letters* **2017**, *111* (2), 023301.
- (71) Simon, D. T.; Gabrielsson, E. O.; Tybrandt, K.; Berggren, M. Organic Bioelectronics: Bridging the Signaling Gap between Biology and Technology. *Chemical Reviews* **2016**, *116*, 13009–13041.
- (72) A. D. McNaught and A. Wilkinson. *IUPAC. Compendium of Chemical Terminology, 2nd Ed*; Oxford, 1992; Vol. 64, p 143.
- (73) Pohanka, M. The Piezoelectric Biosensors: Principles and Applications, a Review. *International Journal of Electrochemical Science* **2017**, *12* (1), 496–506.
- (74) Wang, D.; Noël, V.; Piro, B. Electrolytic Gated Organic Field-Effect Transistors for Application in Biosensors—A Review. *Electronics* **2016**, *5* (1), 9.
- (75) Malhotra, B. D.; Pandey, C. M. *Book-Biosensors : Fundamentals and Applications*;

- Smithers Rapra Technology Ltd, 2017.
- (76) Diacci, C.; Berto, M.; Di Lauro, M.; Bianchini, E.; Pinti, M.; Simon, D. T.; Biscarini, F.; Bortolotti, C. A. Label-Free Detection of Interleukin-6 Using Electrolyte Gated Organic Field Effect Transistors. *Biointerphases* **2017**, *12* (5), 05F401.
- (77) Berto, M.; Di Lauro, M.; Biscarini, F.; Bortolotti, C. A.; Diacci, C.; Theuer, L.; Simon, D. T.; Berggren, M.; Beni, V. Label Free Urea Biosensor Based on Organic Electrochemical Transistors. *Flexible and Printed Electronics* **2018**, *3* (2), 024001.
- (78) Ranallo, S.; Porchetta, A.; Ricci, F. DNA-Based Scaffolds for Sensing Applications. *Analytical Chemistry* **2019**, *91*, 44–59.
- (79) Kyndiah, A.; Leonardi, F.; Tarantino, C.; Cramer, T.; Garreta, E.; Mas-torrent, M.; Gomila, G. Bioelectronic Recordings of Cardiomyocytes with Accumulation Mode Electrolyte Gated Organic Field Effect Transistors. *Biosensors and Bioelectronics* **2019**, *150*, 111844.
- (80) Thevenot, D.; Toth, K.; Durst, R.; Wilson, G. Electrochemical Biosensors : Recommended Definitions and Classification. *Biosensors and Bioelectronics* **2001**, *16*, 121–131.
- (81) Homola, J. *Surface Plasmon Resonance Based Sensors*; Springer, Ed.; Springer, 2006.
- (82) Bergveld, P. Development of an Ion-Sensitive Solid-State Device for Neurophysiological Measurements. *IEEE Transactions on Biomedical Engineering* **1970**, *BME-17*(1), 70–71.
- (83) Turner, A. P. F.; Karube, I.; Wilson, G. S.; Worsfold, P. J. *Biosensors: Fundamentals and Applications*; 1987; Vol. 201.
- (84) Kharitonov, A. B.; Zayats, M.; Lichtenstein, A.; Katz, E.; Willner, I. Enzyme Monolayer-Functionalized Field-Effect Transistors for Biosensor Applications. *Sensors and Actuators, B: Chemical* **2000**, *70* (1–3), 222–231.
- (85) Roberts, M. E.; Mannsfeld, S. C. B.; Queraltó, N.; Reese, C.; Locklin, J.; Knoll,



- W.; Bao, Z. Water-Stable Organic Transistors and Their Application in Chemical and Biological Sensors. *Proceedings of the National Academy of Sciences of the United States of America* **2008**, *105* (34), 12134–12139.
- (86) Scarpa, G.; Idzko, A. L.; Yadav, A.; Thalhammer, S. Organic ISFET Based on Poly (3-Hexylthiophene). *Sensors* **2010**, *10* (3), 2262–2273.
- (87) Picca, R. A.; Manoli, K.; Macchia, E.; Sarcina, L.; Franco, C. Di; Cioffi, N.; Blasi, D.; Österbacka, R.; Torricelli, F.; Scamarcio, G. Ultimately Sensitive Organic Bioelectronic Transistor Sensors by Materials and Device Structure Design. *Advanced Funtional Materials* **2020**, *30*, 1904513.
- (88) Casalini, S.; Leonardi, F.; Cramer, T.; Biscarini, F. Organic Field-Effect Transistor for Label-Free Dopamine Sensing. *Organic Electronics* **2013**, *14* (1), 156–163.
- (89) Casalini, S.; Dumitru, A. C.; Leonardi, F.; Bortolotti, C. A.; Herruzo, E. T.; Campana, A.; Oliveira, R. F. De; Cramer, T.; Garcia, R.; Biscarini, F. Multiscale Sensing of Antibody À Antigen Interactions by Organic Transistors and Single-Molecule Force Spectroscopy. *ACS Nano* **2015**, *9* (5), 5051–5062.
- (90) Berto, M.; Vecchi, E.; Baiamonte, L.; Condò, C.; Sensi, M.; Di Lauro, M.; Sola, M.; De Stradis, A.; Biscarini, F.; Minafra, A.; et al. Label Free Detection of Plant Viruses with Organic Transistor Biosensors. *Sensors and Actuators, B: Chemical* **2019**, *281*, 150–156.
- (91) Macchia, E.; Manoli, K.; Holzer, B.; Di Franco, C.; Ghittorelli, M.; Torricelli, F.; Alberga, D.; Mangiatordi, G. F.; Palazzo, G.; Scamarcio, G.; et al. Single-Molecule Detection with a Millimetre-Sized Transistor. *Nature Communications* **2018**, *9* (1).
- (92) Chu, C.; Sarangadharan, I.; Regmi, A.; Chen, Y.; Hsu, C. Beyond the Debye Length in High Ionic Strength Solution : Direct Protein Detection with Field-Effect Transistors (FETs) in Human Serum. *Scientific Reports* **2017**, *7*, 5256.
- (93) Magliulo, M.; De Tullio, D.; Vikholm-Lundin, I.; Albers, W. M.; Munter, T.; Manoli, K.; Palazzo, G.; Torsi, L. Label-Free C-Reactive Protein Electronic Detection with an Electrolyte-Gated Organic Field-Effect Transistor-Based

- Immunosensor. *Analytical and Bioanalytical Chemistry* **2016**, 408 (15), 3943–3952.
- (94) Torsi, L.; Farinola, G. M.; Marinelli, F.; Tanese, M. C.; Omar, O. H.; Valli, L.; Babudri, F.; Palmisano, F.; Zambonin, P. G.; Naso, F. A Sensitivity-Enhanced Field-Effect Chiralsensor. *Nature Materials* **2008**, 7 (5), 412–417.
- (95) Knopfmacher, O.; Hammock, M. L.; Appleton, A. L.; Schwartz, G.; Mei, J.; Lei, T.; Pei, J.; Bao, Z. Highly Stable Organic Polymer Field-Effect Transistor Sensor for Selective Detection in the Marine Environment. *Nature communications* **2014**, 5, 2954.
- (96) Kergoat, L.; Piro, B.; Berggren, M.; Pham, M. C.; Yassar, A.; Horowitz, G. DNA Detection with a Water-Gated Organic Field-Effect Transistor. *Organic Electronics* **2012**, 13 (1), 1–6.
- (97) Hammock, M. L.; Knopfmacher, O.; Naab, B. D.; Tok, J. B. H.; Bao, Z. Investigation of Protein Detection Parameters Using Nanofunctionalized Organic Field-Effect Transistors. *ACS Nano* **2013**, 7 (5), 3970–3980.
- (98) Palazzo, G.; De Tullio, D.; Magliulo, M.; Mallardi, A.; Intranuovo, F.; Mulla, M. Y.; Favia, P.; Vikholm-Lundin, I.; Torsi, L. Detection beyond Debye's Length with an Electrolyte-Gated Organic Field-Effect Transistor. *Advanced Materials* **2015**, 27 (5), 911–916.
- (99) Gualandi, I.; Marzocchi, M.; Scavetta, E.; Calienni, M.; Bonfiglio, A.; Fraboni, B. A Simple All-PEDOT:PSS Electrochemical Transistor for Ascorbic Acid Sensing. *Journal of Materials Chemistry B* **2015**, 3 (33), 6753–6762.
- (100) Tang, H.; Lin, P.; Chan, H. L. W.; Yan, F. Highly Sensitive Dopamine Biosensors Based on Organic Electrochemical Transistors. *Biosensors and Bioelectronics* **2011**, 26 (11), 4559–4563.
- (101) Kergoat, L.; Piro, B.; Simon, D. T.; Pham, M. C.; Noël, V.; Berggren, M. Detection of Glutamate and Acetylcholine with Organic Electrochemical Transistors Based on Conducting Polymer/Platinum Nanoparticle Composites. *Advanced Materials* **2014**, 26 (32), 5658–5664.
- (102) Xiong, C.; Wang, Y.; Qu, H.; Zhang, L.; Qiu, L.; Chen, W.; Yan, F.; Zheng, L. Highly Sensitive Detection of Gallic Acid Based on Organic Electrochemical

- Transistors with Poly(Diallyldimethylammonium Chloride) and Carbon Nanomaterials Nanocomposites Functionalized Gate Electrodes. *Sensors and Actuators, B: Chemical* **2017**, 246, 235–242.
- (103) Diacci, C.; Lee, J. W.; Janson, P.; Dufil, G.; Méhes, G.; Berggren, M.; Simon, D. T.; Stavriniidou, E. Real-Time Monitoring of Glucose Export from Isolated Chloroplasts Using an Organic Electrochemical Transistor. *Advanced Materials Technologies* **2019**, 1900262 (August), 1–6.
- (104) Yang, S. Y.; Cicoira, F.; Byrne, R.; Benito-Lopez, F.; Diamond, D.; Owens, R. M.; Malliaras, G. G. Electrochemical Transistors with Ionic Liquids for Enzymatic Sensing. *Chemical Communications* **2010**, 46 (42), 7972–7974.
- (105) Wustoni, S.; Wang, S.; Alvarez, J. R.; Hidalgo, T. C.; Nunes, S. P.; Inal, S. An Organic Electrochemical Transistor Integrated with a Molecularly Selective Isoporous Membrane for Amyloid- $\beta$  Detection. *Biosensors and Bioelectronics* **2019**, 143 (July), 111561.
- (106) Wang, N.; Yang, A.; Fu, Y.; Li, Y.; Yan, F. Functionalized Organic Thin Film Transistors for Biosensing. *Accounts of Chemical Research* **2019**, 52, 277–287.

# CHAPTER 2

## *Label-free immunosensing of $\alpha$ -synuclein\**

---

### 2.1. Introduction

The incidence of neurodegenerative diseases is increasing lately, according to the *World Alzheimer's report 2019*.<sup>1</sup> The ageing of the population is the principal factor taken into account in the projections. In fact, the occurrence of dementia is strictly correlated to increasing age and the number of people living with dementia worldwide is estimated to double every 20 years, arriving at above 152 million in 2050.<sup>1,2</sup>

Parkinson's disease, for instance, represents the 15% of all dementia cases affecting, only in the UK, the 0.2% of the population, with an overall cost on the National Health Service (NHS) of about £212 million per year.<sup>3</sup> Accordingly, developing low-cost and reliable devices for the early diagnosis of this pathology is becoming of utmost importance.

- **$\alpha$ -synuclein: physiological and pathological role**

$\alpha$ -synuclein is emerging as a biomarker for a broad range of neurodegenerative disorders, known as *synucleinopathies*, including Parkinson's disease, dementia with Lewy Bodies and Multiple System Atrophy.<sup>4</sup>

---

\*This work was carried out under the co-supervision and collaboration of Dr. Stefano Casalini.

$\alpha$ -synuclein is predominantly expressed in the cytosol of cells, but it is also present in the cerebrospinal fluid (CSF), blood and plasma.<sup>5</sup> Its physiological role is not completely understood yet, but it is involved in neurotransmission and vesicle budding.<sup>3</sup> Its structure can be divided into three portions: i) N-terminal part, responsible for lipid membrane-binding, ii) C-terminal part, rich in acid amino acidic residues, making this protein negatively charged at physiological pH, and iii) the non-amyloid- $\beta$  component (NAC), a hydrophobic central core liable for protein-protein interactions. Due to dysfunctional regulation,  $\alpha$ -synuclein can undergo aggregation processes, which lead to the formation of soluble oligomers in the first place, and progressively insoluble protofibrils and fibrils. Different factors have pointed to promote aggregation, such as oxidative stress, metal ions, or fatty acid concentration. These aggregations result to produce protein-based inclusions, like Lewy Bodies, located in the brain and associated with the manifestation of dementia symptoms.<sup>5</sup>

- **$\alpha$ -synuclein biosensing state of the art**

In the last decade, great efforts have been dedicated to the development of  $\alpha$ -synuclein biosensors. In the work by *Zhang et al.* a description of the principal devices conceived in the last decade is reported, as summarized in **Table 2.1**.<sup>6</sup>

**Table 2.1.** Comparison of the analytical performance of the currently available  $\alpha$ -synuclein biosensors.

<b>Probe</b>	<b>Sensor</b>	<b>Limit of Detection/sample</b>	<b>Ref</b>
<b>Polysaccharide</b>	Optical sensor	70 nM/Gly-NaOH buffer	7
<b>Chemical</b>	Microcantilever array	6 ng/PBS buffer	8
<b>Aptamer</b>	Electrochemical sensor	10 pM/serum sample	9
<b>Antibody</b>	ELISA	1 ng/mL/human sample	10
<b>Peptide</b>	Surface Plasmon Resonance	Serum sample	11
<b>Antibody</b>	Single-molecule technology	Serum sample	12
<b>Antibody</b>	Western blot analysis	Gut sample	13
<b>Indirect</b>	Ultrasonication method	Cerebrospinal fluid	14
<b>Antibody</b>	ELISA	Plasma	15
<b>Aptamer</b>	Colorimetric	1 nM/PBS buffer	16
<b>Aptamer</b>	Surface Plasmon Resonance	10 pM/PBS buffer	16
<b>Antibody</b>	Voltammetry	1 fM/PBS buffer	6

The limit of detection (LOD) achieved spans from  $10^{-12}$  M to  $10^{-9}$  M of  $\alpha$ -synuclein, except for the very recent work of *Zhang et al.*, who achieved a LOD equal to  $10^{-15}$  M, developing a voltammetric sensor through gold-nanourchin conjugated anti- $\alpha$ -synuclein antibody seeded on single-walled carbon nanotube (SWCN) integrated interdigitated electrode (IDE).<sup>6</sup> Different sensing probes have been

employed to trap the analyte, being the anti-( $\alpha$ -synuclein) antibody the most frequent one. Besides, the samples analysed vary from physiological phosphate buffer saline (PBS) going to *in-vivo* samples, *viz.* serum, gut, plasma or cerebrospinal fluid. Regarding the transducer component of the sensing devices, electrochemical, optical, colorimetric and the classic ELISA have been investigated. Western blot analysis and ELISA tests are well-known techniques in biochemistry for the detection of specific proteins in complex samples, at concentrations down to picomolar levels. However, they usually require a completed equipped chemistry laboratories and very specialized technicians to be performed. Electrochemical and optical methodologies have gained a lot of interest due to easy read-out interfaces, fast analysis and possibility to integrate the biosensing systems into point-of-care (POC) chips. In this regard, electrolyte-gated organic field-effect transistors (EGOFETs), represent a promising tool for label-free immunosensing, also thanks to their intrinsic amplification property.<sup>17-19</sup> To our knowledge, no field-effect transistor-based transducer has been explored for  $\alpha$ -synuclein detection yet.

- **Au surface engineering for immunosensing platforms**

There are various methodologies to immobilize biomolecules onto Au surfaces. In this work, the attention is focused on the chemisorption of antibodies molecules on polycrystalline Au.

Antibodies (Abs), also known as Immunoglobulins (Ig), are Y shaped proteins having a molecular weight (MW) equal to 150 kDa approximatively. The two arms of the Y backbone in the end region are specific for the binding with the antigen (Ag) and they are referred to as fragment antigen-binding portions,  $F_{ab}$ . The aminoacidic composition of the  $F_{ab}$  portions varies depending on the type of antigen and on the function of the Ab itself. On the contrary, the stem of the Y shape is less variable in the aminoacidic sequence and it is common to different Ig classes. This portion is known as  $F_c$ , *viz.* crystallizable fragment, and it is devoted to the binding with receptors or cells.<sup>20</sup>

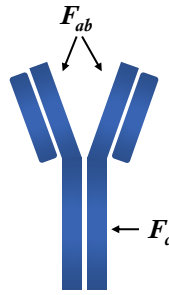


**Figure 2.1.** Schematic representation of an antibody protein.

The most common way to modify Au surfaces is to exploit molecules functionalized with a thiol group capable to organize into Self-Assembled Monolayers (SAMs) through the formation of a S-Au bond. The molecules used for this purpose are typically constituted of three parts: i) a head group, ii) a tail and iii) a terminal functional group. The head group corresponds to a thiol moiety and is needed for the binding with Au. The tail is usually made by an alkyl or pegylated chain and it can be of different lengths. The composition of the tail is crucial for the packing of the SAM, being governed by weak interactions, mostly Van der Waals forces. Lastly, the terminal group allows to introduce a surface functionality or to introduce a chemical group that permits to perform further chemical reactions on the surface. The two most frequently chemicals moieties employed to carry out further reactions are carboxylic or amino groups because they can be easily activated towards the binding with primary amines. Since Ab backbones contain lysine residues with accessible primary amines, this route can thus be applied to graft Abs on Au surfaces.

Another manner to immobilize Abs on Au surfaces is to take advantage of protein G (PG). PG is an antibody-binding protein. The formation of the PG-Ab complex is in a certain way regiospecific. PG interacts preferentially with the  $F_c$  portion of Ab, allowing the  $F_{ab}$  moieties to be accessible for the interaction with the Ag. In turn, there are two main kinds of recombinant PG commercially available: i) tailored with a cysteine tag, for covalent binding with Au, and ii) customized with a histidine tag, for the deposition onto both Au or Ni surfaces.

Supramolecular chemistry resulted to be also a useful strategy for surfaces modification. Calixarenes are molecules with a cavity able to give rise to host-guest



interactions. In literature, there are examples of calixarenes used for biological applications.<sup>21-24</sup> Specifically, *Chen et al.* studied the orientation and activity of Abs attached on a calixarene-based monolayer on Au surface.<sup>25</sup>

DNA strands have also been engineered for Ab immobilization onto metal surfaces in different applications.<sup>26-29</sup> In particular, *Chen. et al.* anchored an Ab on Au surface using a DNA nanostructured scaffold.<sup>30</sup> The advantage of this technique is that DNA strands synthesis is easy and cost-effective, and the interaction with the Ab could be tuned to have a well-oriented Ab monolayer. The drawback is that the Ab has to be chemically modified.

## 2.2. Objectives

This chapter is focused on the design, fabrication and characterization of an electrolyte-gated organic field-effect transistor (EGOFET)-based immunosensor for the detection of  $\alpha$ -synuclein in solution. To achieve this, the following sub-objectives were planned:

1. Testing of two different strategies for tethering the anti-( $\alpha$ -synuclein) antibody. i) **Approach I** exploited a thiol-based SAM to covalently attach the Ab on a Au electrode surface, and ii) **Approach II** was based on PG to anchor the Ab on the Au surface. These two sensing platforms were characterized and tested towards the effective binding with the analyte employing complementary techniques.
2. Implementation of the sensing platform into top-gated EGOFET devices and the realization of their corresponding calibration curves.
3. Design of a coplanar gate configuration with an integrated microfluidics system to achieve a more applicative interface.

### **2.3. Design and preparation of engineered Ab functionalised Au surfaces**

The first step of the work consisted in the design and characterization of the  $\alpha$ -synuclein capturing platform. For this aim, two different methodologies for the tethering of anti-( $\alpha$ -synuclein) Ab on polycrystalline Au were conceived, namely **Approach I** and **Approach II**.

- **Approach I**

Approach I relies on an amino-terminated pegylated thiol SAM, namely HS-C<sub>11</sub>-EG<sub>6</sub>-NH<sub>2</sub> (**Figure 2.2**). This molecule was selected because:

1. Based on previous works, pegylated chains are supposed to have antifouling properties.<sup>31</sup> This was accounted by the fact that a network of water molecules is formed at the interface, which repels the hydrophobic proteins.<sup>31</sup> However, it should be mentioned that some works have shown that not only the pegylated unit is necessary to prevent protein adsorption, but also neutrality of the total charges of the terminal groups. In the case of amino-terminated or carboxy-terminated thiols, they stated that local electrostatic interactions between these groups and proteins are stronger than repulsion induced by structured interfacial water, reducing the antifouling effect of the pegylated units.<sup>32</sup>
2. The primary amino groups react easily with glutaraldehyde (Gl), a quite common cross-linker, according to the reaction shown in **Figure 2.2**.

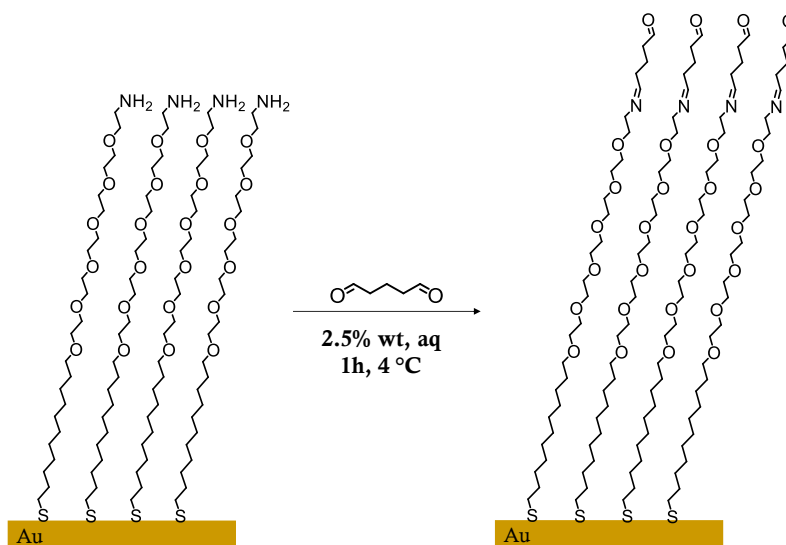


**Figure 2.2.** Activation of the terminal amino group by glutaraldehyde in a HS-C<sub>11</sub>-EG<sub>6</sub>-NH<sub>2</sub> SAM on Au through a nucleophilic addition reaction to the aldehydic moiety.

Accordingly, the resulting surface contains aldehydic moieties that can further react with the primary amine of a lysine residue present in the backbone of the Ab. In **Figure 2.3** all the steps followed for the immobilization of the Ab through Approach I are summarized together with the reaction conditions employed (see Experimental Chapter for further details). Thus, Approach I leads to covalently attached Abs but randomly oriented on the surface.

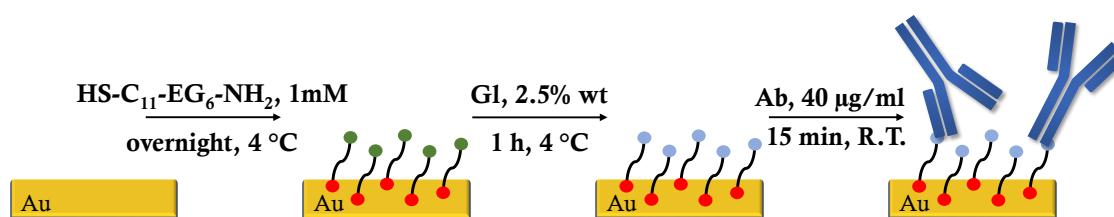


**Figure 2.3.** Schematic representation of the functionalization steps carried out in Approach I.

- **Approach II**

The second strategy is based on protein G (PG). As mentioned before, Abs bind to PG preferentially with the *F<sub>c</sub>* portions. Accordingly, Abs are adsorbed on the Au surface

by exposing their  $F_{ab}$  arms towards the electrolyte solution. For our purpose, a recombinant histidine-tag protein G was employed. This PG has been engineered in a way to retain only the portions specific for the Ab binding, and each PG can attach from 3 to 5 Ab molecules. Histidine contains an imidazole ring in its lateral chain (see **Figure 2.4**). Imidazole ring has two coordination sites, i)  $\epsilon$ -N whose lone pair is in a  $2p$  orbital being part of the aromatic sextet and thus having less basic character than ii)  $\delta$ -N, whose lone pair lies in a  $sp^2$  orbital, being available for metal coordination.<sup>33</sup>

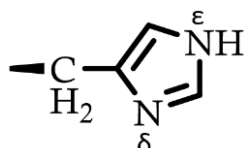


**Figure 2.4.** Lateral chain of histidine, underlying the  $\delta$ -N and the  $\epsilon$ -N of the imidazole ring.

All the steps and experimental conditions employed for the functionalization process are illustrated in **Figure 2.5** (see further details in the Experimental Chapter).

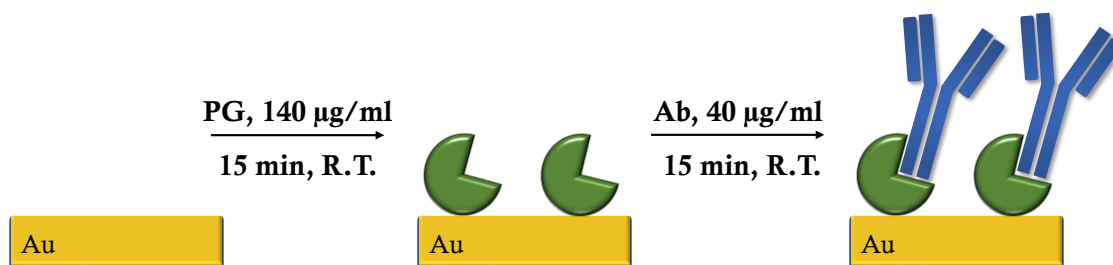


**Figure 2.5.** Schematic representation of the functionalization steps carried out in Approach II.

PG-Ab complex is characterized by non-covalent interactions, but the strength of this approach consists in the proper orientation of the Abs.

## 2.4. Characterization of the bio-engineered Au surfaces

- **Approach I**

The correct formation of the HS-C<sub>11</sub>-EG<sub>6</sub>-NH<sub>2</sub>-based SAM on gold wire surface was assessed through different techniques, namely electrochemistry, X-ray photoelectron spectroscopy (XPS) and Kelvin probe force microscopy (KPFM). Regarding SAM formation, Au wire was incubated in an Eppendorf containing 1 mM HS-C<sub>11</sub>-EG<sub>6</sub>-NH<sub>2</sub> solution in EtOH and stored at 4 °C overnight, to guarantee a high degree of molecular packing.

First of all, a pH dependency study was carried out by Electrochemical Impedance Spectroscopy (EIS) (see Experimental Chapter for further details). The terminal amino-group can be protonated or deprotonated according to the pH of the solution. A negatively charged redox probe, specifically K<sub>3</sub>[Fe(CN)<sub>6</sub>], was exploited aiming at qualitatively determining the degree of Au coverage. Indeed, when the Au electrode surface is hindered by materials deposited on top of it, the redox probe hardly exchanges its electrons with it, resulting in a greater impedance signal. This is the case of the HS-C<sub>11</sub>-EG<sub>6</sub>-NH<sub>2</sub>-coated Au. Furthermore, varying the pH of the electrolyte solution used for the electrochemical measurement, the overall charge of the SAM is changed, due to the basic properties of the terminal amino group. As it is shown in **Figure 2.6**, a more basic pH entails an increase in the charge transfer resistance values,  $R_{ct}$ . This can be explained by the electrostatic interactions occurring between the SAM and the negatively charged redox probe, which become more repulsive at basic pHs, indicating deprotonation of the amino groups. On the contrary, the  $R_{ct}$  values of a bare Au does not show any dependency from the pH of the electrolyte solution. Thus, this method allowed us to assess the correct formation of the SAM and also approximatively the  $pK_a$  of the amino-terminal groups.

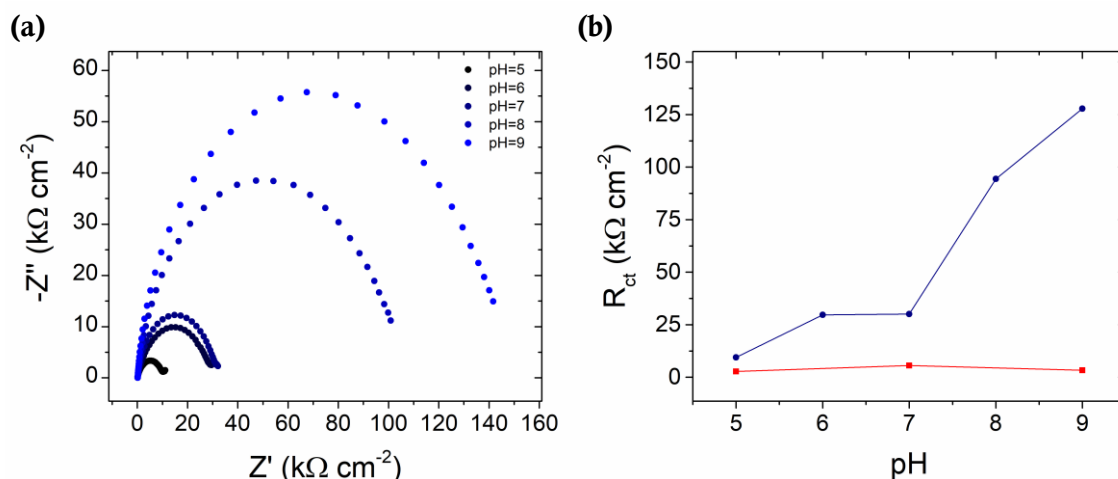
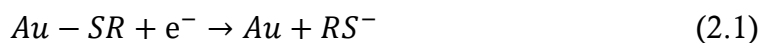


**Figure 2.6.** pH dependency behaviour of the terminal amino group: (a) Nyquist plot of the HS- C<sub>11</sub>- EG<sub>6</sub>-NH<sub>2</sub>-coated Au wire recorded in different pH solutions, (b) comparison of the  $R_{ct}$  values of the HS-C<sub>11</sub>-EG<sub>6</sub>-NH<sub>2</sub>-coated Au wire (blue curve) and the bare Au (red curve) at different pH.  $R_{ct}$  values are extracted by fitting with a *Randles* equivalent circuit (see experimental section). A three-electrode cell has been employed: Pt wire as the counter electrode, Ag/AgCl as the reference electrode and Au wire as the working electrode. Electrolyte used: 5 mM K<sub>3</sub>[Fe(CN)<sub>6</sub>], 100 mM KCl and 50 mM sodium phosphate salt at pH= 5, 6, 7, 8, 9.

Electrochemistry was also employed for the quantitative determination of Au coverage. It is known that thiols attached on Au can be removed by electrochemical desorption.<sup>34</sup> In fact, by applying a negative potential to Au electrode, a redox reaction occurs. The sulphur atom is reduced restoring the thiol group and Au-S bond is oxidized to Au(0) as follows:



For our purpose, Differential Pulse Voltammetry (DPV) resulted to be the best technique to follow this process. As it is shown in **Figure 2.7**, two peaks appeared in the voltammogram. They can be ascribed to the desorption of thiol molecules from different faces of polycrystalline gold, namely Au(111) and Au(110), as reported in literature.<sup>34</sup> The quantity of adsorbed thiol was calculated through Faraday's law:

$$Q = z F n \quad (2.2)$$

where  $Q$  is the overall charge (in C),  $z$  is the number of electrons involved in the reaction,  $F$  is the Faraday's constant equal to 96,485 C/mol, and  $n$  is the number of moles of reactants. By substituting  $n$  with  $A\Gamma_m$ , where  $A$  is the electrode surface area (in  $\text{cm}^2$ ) and  $\Gamma_m$  is the monolayer coverage for unit area (in  $\text{mol}\cdot\text{cm}^{-2}$ ), the following rearrangement is obtained:

$$\Gamma_m = Q / z F A \quad (2.3)$$

Finally, multiplying by Avogadro constant, the number of molecules per  $\text{cm}^2$  is extrapolated. It is worth noting that, to extract  $Q$ , the area obtained by the integration of the reductive peak was divided for the scan rate used during the measurement, namely  $0.1 \text{ V}\cdot\text{s}^{-1}$ . A mean surface coverage equal to  $4.74(\pm 1.9)\cdot 10^{14} \text{ molecules}\cdot\text{cm}^{-2}$  was calculated from 6 different experiments, which is in agreement with values reported in literature for *n*-alkanethiol SAMs, *viz.*  $\sim 5.6\cdot 10^{14} \text{ molecules}\cdot\text{cm}^{-2}$ .<sup>34,35</sup>

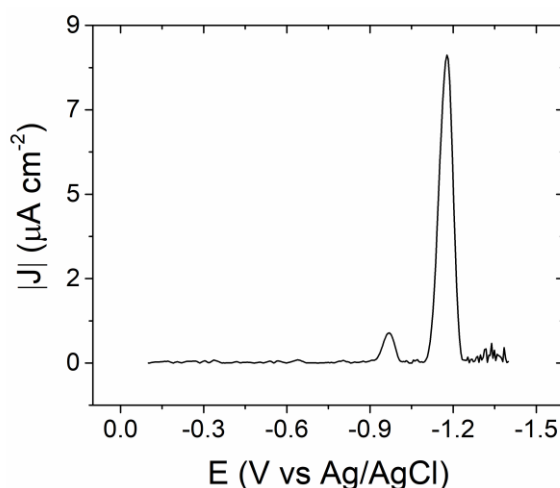


**Figure 2.7.** Reductive desorption of HS-C<sub>11</sub>-EG<sub>6</sub>-NH<sub>2</sub> molecules from a Au wire surface. DPV performed in NaOH 1 M, at a scan rate equal to  $0.1 \text{ V}\cdot\text{s}^{-1}$ .

XPS is a useful technique for surfaces characterization.<sup>36</sup> XPS is based on the photoelectron effect. The sample is irradiated with X-ray photons of known energy in vacuum. When the photon interacts with an atomic orbital electron, it can transfer completely its energy so that the electron is extracted from the atom with a certain kinetic energy, which is recorded by the instrument. The difference between the incident photon's energy and the measured kinetic energy represents the binding

energy (*B.E.*) of the electrons. *B.E.* are specific for each element. The sampling depth in XPS is in the range of 20-100 Å. XPS spectra of bare Au and HS-C<sub>11</sub>-EG<sub>6</sub>-NH<sub>2</sub>-coated Au wire are compared in **Figure 2.8**. Carbon (1s) and oxygen (1s) peaks intensity increases for the SAM-coated Au sample and, on the contrary, the intensity of the gold (4f) signal decreases, confirming the adsorption of the thiol molecules on top of it. It is worth noting that the shape of the carbon spectrum gives also some information about the packing of the SAM.<sup>37</sup> In fact, two peaks appear at slightly different *B.E.* This difference in *B.E.* can be attributed to the different type of carbon atoms present in the molecules, namely the ones of the alkyl chains and the ones of the pegylated chain directly bound to oxygen atoms. Furthermore, the intensity ratio of these peaks fit with the ratio of the two types of carbon in the molecule. The fact that also the carbon atoms of the alkyl chain are detected with the same intensity of the pegylated ones, could be an indication that the molecules are slightly tilted and not strongly compacted, as it is reported in a previous work of *Harder et al.*<sup>31</sup> In their work, they claim that when the SAM is well packed, pegylated moieties attenuate the signal C (1s) of the underlying alkyl chain, resulting in an asymmetric peak splitting. On the other hand, when the pegylated units are not layered, the peak splits according to the stoichiometric proportion of the alkyl chain and the pegylated units, as occurs in our case.



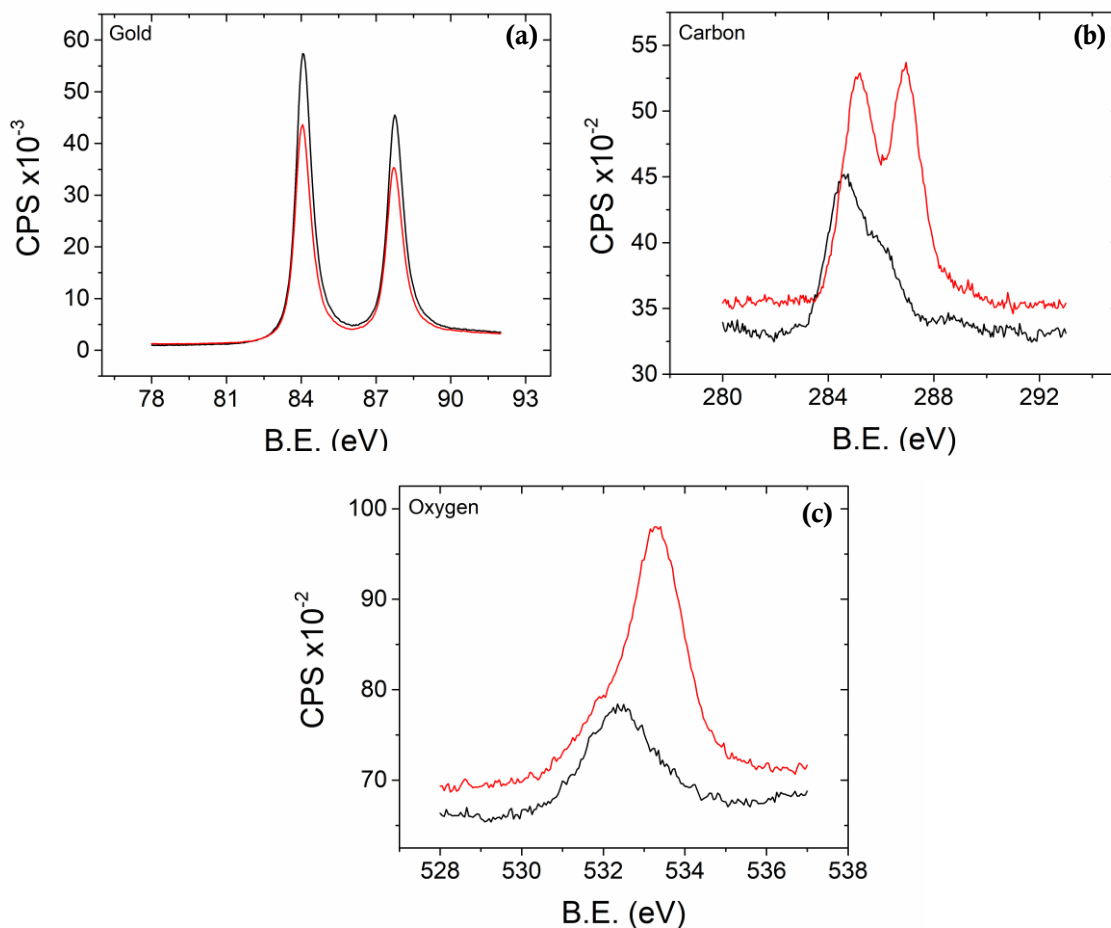


**Figure 2.8.** XPS spectra: red curves represent HS-C<sub>11</sub>-EG<sub>6</sub>-NH<sub>2</sub>-coated Au wire, and pristine Au wire signals are shown in black. (a) Au signal (4f). (b) Carbon signal (1s). (c) Oxygen signal (1s).

Among other techniques for surface characterization, KPFM allows for the mapping of the surface potential or work function of the sample. It measures the Contact Potential Difference (CPD) between the tip of the instrument and the sample.<sup>38</sup> In **Figure 2.9** the CPD measurement of a pristine Au surface and HS-C<sub>11</sub>-EG<sub>6</sub>-NH<sub>2</sub>-coated Au surface is shown. A dramatic negative shift in the CDP is observed, safely deducing a variation in the surface potential promoted by the adsorption of the SAM.

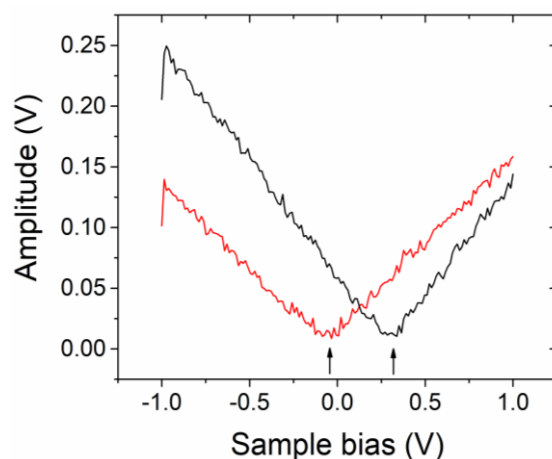


**Figure 2.9.** KPFM measurements of pristine Au surface (black line) and HS-C<sub>11</sub>-EG<sub>6</sub>-NH<sub>2</sub>-coated Au wire (red line). The difference between the minima of these curves (highlighted with arrows correspond to the difference in work functions).

To get a deep insight into the biofunctionalization process, Surface Plasmon Resonance (SPR) technique was employed. SPR is an optical technique, well developed for the study of biomolecules interactions on Au surfaces. It can detect changes on the refractive index in the vicinity of metal surfaces based on the Au plasmonic resonance effect.<sup>39</sup> Resonance occurs when the mobile electrons of a thin metallic layer interact with a *p*-polarized light at a precise angle. Surface mobile electrons oscillate creating waves that propagate towards the parallel direction of the metal/dielectric interface, called indeed, surface plasmons. At a certain angle, the incident *p*-polarized light vector couples with the surface plasmons created by the mobile electrons, resulting in a resonance effect.<sup>40</sup> This coupling promotes a loss of energy of the incident photons because of the transfer of part of its energy to the plasmon. When the refractive index of the metal surface is changed, the angle at which resonance occurs changes accordingly. Thus, biomolecules adsorbed on Au surfaces are detected as a change in the resonance angle, as illustrated in **Figure 2.10**.

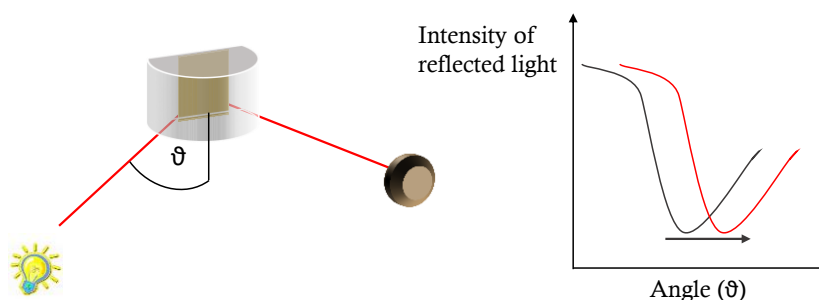


**Figure 2.10.** Schematic illustration of the basic principle of the SPR technique: at the angle at which light incidence resonates with surface plasmons, a decrease of the reflected light is observed. Changes in the refractive index of the surface results in a change of the resonance angle.

To assess the proper immobilization protocol of the anti-( $\alpha$ -synuclein) Ab and its subsequent ability to capture  $\alpha$ -synuclein, SPR experiments were carried out (See experimental section for further details of the instrument employed). SPR technique allowed us to monitor adsorption processes occurring on the Au surface in *real-time*. The data are shown in the so-called sensorgrams, in which the reflected light variation,  $\Delta R(\%)$ , is plotted *vs* time. Firstly, a carrier solution is flown into the cell and subsequently, the solution containing the ligand or analyte of interest is injected (flow rate equal to 25  $\mu\text{L}/\text{min}$ ). At this point, a variation of  $\Delta R(\%)$  is produced, due to the different refractive index of the solutions. Afterwards, the carrier solution is flown again to remove any physisorbed material. The variation between the initial and the final reflectivity,  $\Delta R$ , is an indication of the Au refractive index modification caused by the biomolecule's deposition. When no adsorption occurs, the initial and the final reflectivity matches exactly, because the carrier solution is the same and so the gold surface. Interestingly, **in Figure 2.11** the sensorgram relative to the glutaraldehyde activation of the terminal amino-group of the HS-C<sub>11</sub>-EG<sub>6</sub>-NH<sub>2</sub>-based SAM is shown. The SAM formation was carried out *ex-situ* because of the incompatibility of the microfluidics tubes with EtOH solutions as required for the SAM preparation. The addition of glutaraldehyde moieties on the surface promotes a visible change in the refractive index of the surface, as highlighted by the red dashed lines in the figure. This result expresses the sensitivity of this technique even for detecting very little changes taking place on the gold surface.

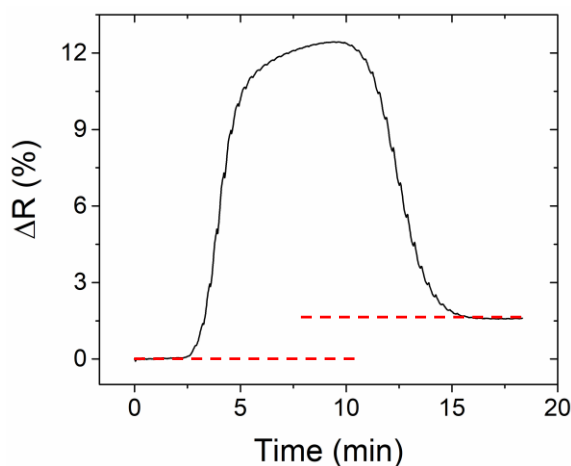


**Figure 2.11.** Sensorgram relative to the activation of the HS-C<sub>11</sub>-EG<sub>6</sub>-NH<sub>2</sub>-coated Au by glutaraldehyde.

Encouraged by this result, we proceeded with the immobilization of the Abs. Different solutions at different concentrations of Ab were tested and their corresponding sensorgrams are shown in **Figure 2.12**. Firstly, water medium was investigated at a low Ab concentration, namely 1  $\mu\text{L}/\text{mL}$ . Small adsorption was observed and, thus, the Ab concentration was increased up to 10  $\mu\text{L}/\text{mL}$ . A great shift was then detected. Accordingly, a more standard solution for biomolecules was employed, *viz.* PBS 1x at physiological pH. The optimum condition was found to be 40  $\mu\text{g}/\text{mL}$  of Ab in PBS 1x, achieving a  $\Delta R$  variation as high as 7. Despite the slightly higher variation in terms of  $\Delta R$  noticed in water media at 10  $\mu\text{g}/\text{mL}$  of Ab, almost equal to 8, the curve in PBS medium exhibits a clearer shape and no desorption occurs when the carrier solution is finally flown.

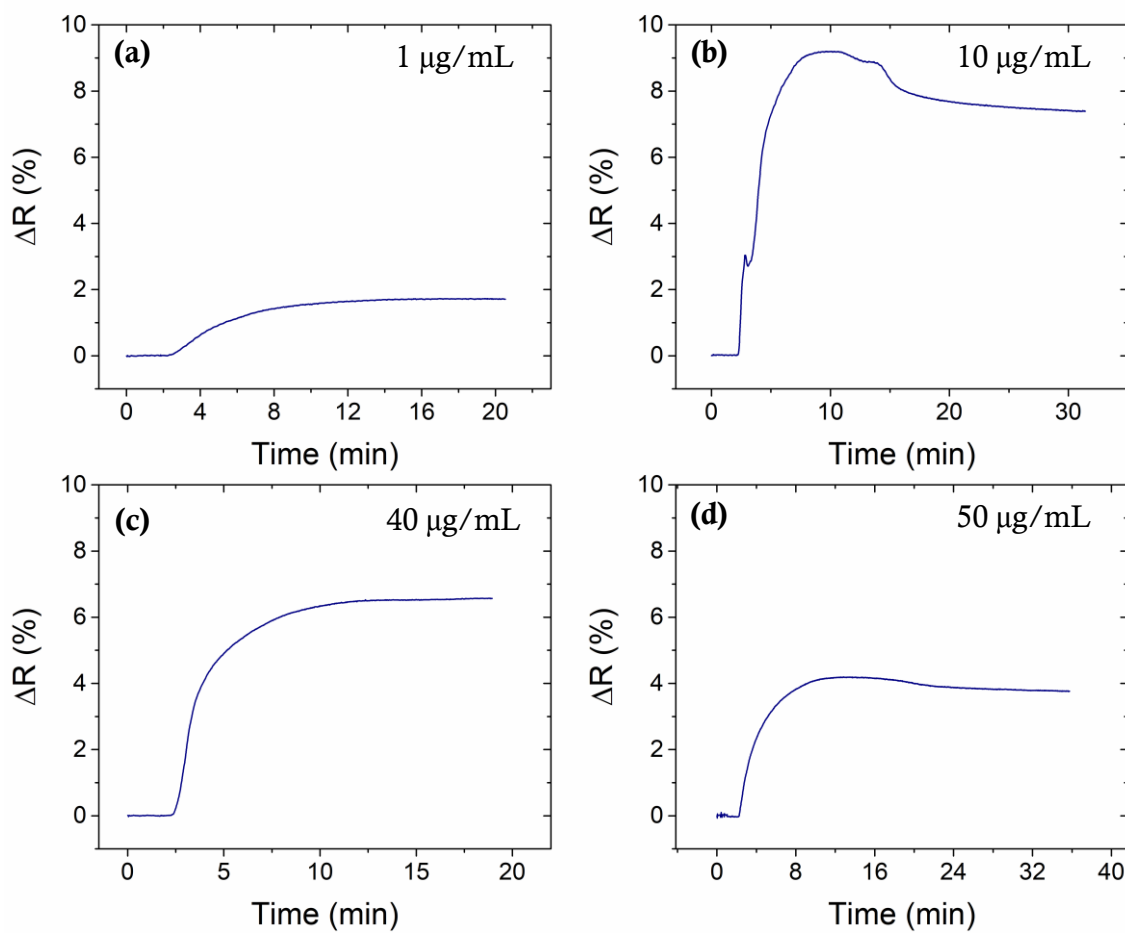


**Figure 2.12.** Ab immobilization study on the activated HS-C<sub>11</sub>-EG<sub>6</sub>-NH<sub>2</sub>-coated Au surface by SPR in different carrier solutions and at different Ab concentrations. (a) Water media, 1  $\mu\text{g/mL}$ . (b) Water media, 10  $\mu\text{g/mL}$ . (c) PBS 1x, 40  $\mu\text{g/mL}$ . (d) PBS 1x, 50  $\mu\text{g/mL}$ . The flow rate of the microfluidics system was equal to 25  $\mu\text{L/min}$ .

The Ab-coated surface was subsequently tested towards  $\alpha$ -synuclein capturing ability in PBS 1x. An appreciable signal was observed for an antigen concentration as low as 10 nM, showing a  $\Delta R(\%)$  equal to  $\approx 0.1$ . No changes in  $\Delta R(\%)$  were noticed for lower  $\alpha$ -synuclein concentration. When the concentration was increased up to 250 nM a more defined sensorgram was obtained ( $\Delta R(\%)$  almost equal to  $\approx 0.3$ ) and no desorption processes occurred when the carrier solution was flown, indicating a strong affinity between the ligand (Ab) and the analyte (**Figure 2.13**). Protein and buffer solutions were streamed applying a flow rate equal to 25  $\mu\text{L/min}$ .

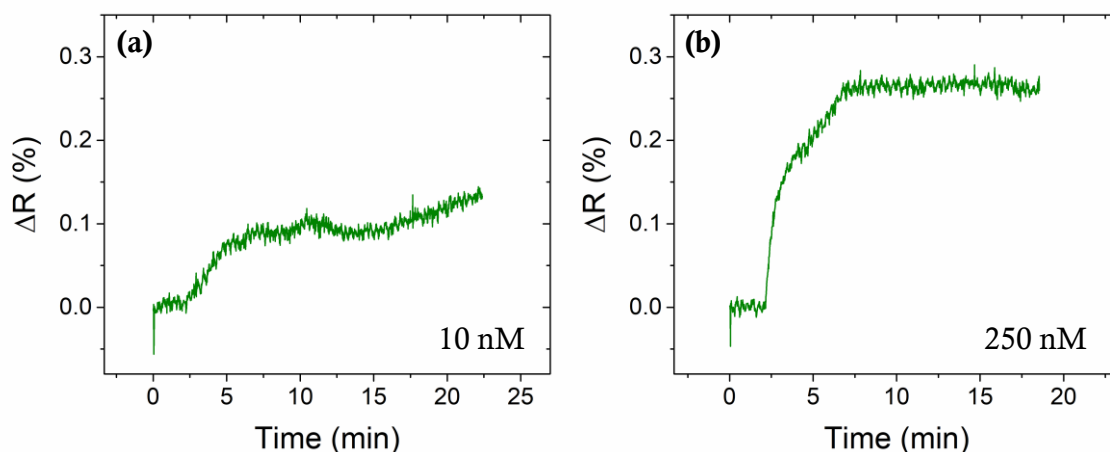


**Figure 2.13.** Sensorgram of the  $\alpha$ -synuclein interaction with Ab-coated surface, in PBS 1x at physiological pH at two different concentrations: (a) 10 nM and (b) 250 nM.

As mentioned above, SPR is an optical technique, thus we decided to carry out the preliminary characterization of the sensing platform also through electrochemistry. Specifically, EIS and DPV were carried out in a three-electrode standard cell. Thus, impedance signal and current profile of a redox probe, namely  $K_3[Fe(CN)_6]$ , were monitored, respectively, for each functionalization step to assess the degree of coverage of the Au surface and the ability of the sensing platform to bind the analyte. HS- $C_{11}$ -EG $_6$ -NH $_2$ -coated Au wire was activated by incubation in an Eppendorf containing GI solution, stored at 4 °C for 1 h. Regarding the protein immobilization and the sensing tests, Ab and  $\alpha$ -synuclein solutions were prepared in PBS 1x at physiological pH and the Au wire was immersed in these solutions 15 minutes at R.T. Before electrical measurements, the Au surface was rinsed with PBS 1x to remove physisorbed materials. In **Figure 2.14** the Nyquist plot is depicted in which the signals relative to the different biofunctionalization steps were compared. As expected, the more hindered the Au surface, the more is the impedance signal measured. Furthermore, the Ab-coated surface was exposed to 250 nM  $\alpha$ -synuclein solution (green dots in **Figure 2.14,a**). The impedance signal shows a dramatic further increase, demonstrating a good capacity of the sensing platform to recognise the antigen. Specifically, charge transfer resistances,  $R_{ct}$ , were extrapolated by fitting the Nyquist curves with *Randles* circuit (details are reported in the experimental section) and it was found that  $R_{ct}$  passes from 133  $k\Omega \cdot cm^{-2}$  for the SAM-coated Au, to 855  $k\Omega \cdot cm^{-2}$  for the

Ab-coated Au and finally to  $1296 \text{ k}\Omega\cdot\text{cm}^2$  for the Ab-coated Au exposed to  $250 \text{ nM}$   $\alpha$ -synuclein. The same behaviour is observed in the DPV measurements, from which is clear how the redox peak of the ferricyanide decreases significantly upon the SAM formation and disappear completely upon the biofunctionalization of the Au surface, due to the steric hindrance (**Figure 2.14,b**).

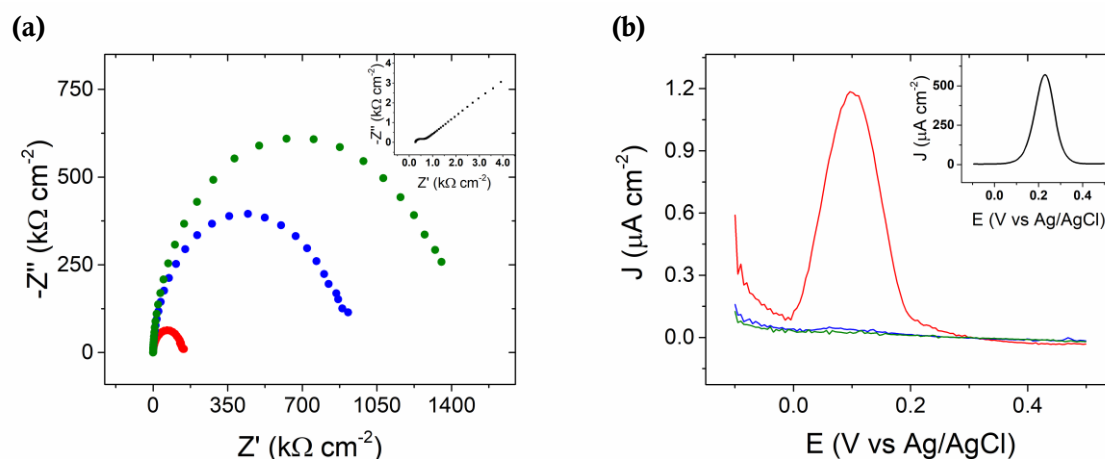


**Figure 2.14.** Electrochemical plots of the functionalization steps followed in Approach I, employing a standard three-electrode cell, Pt wire as the counter electrode, Ag/AgCl as the reference and Au wire as the working in  $5 \text{ mM K}_3[\text{Fe}(\text{CN})_6]$ ,  $100 \text{ mM KCl}$  and  $50 \text{ mM}$  sodium phosphate salt, at  $\text{pH}= 7.2$ . (a) EIS, Nyquist plot. The red symbols refer to HS-C<sub>11</sub>-EG<sub>6</sub>-NH<sub>2</sub>-coated Au, blue symbols to Ab-coated Au and green symbols to  $250 \text{ nM}$  of  $\alpha$ -synuclein. In the inset the curve relative to bare Au is shown. (b) DPV recorded in the same conditions of EIS.

- **Approach II**

Concerning Approach II, SPR and electrochemistry tools were selected for the characterization of the resulting biofunctionalized surfaces.

First of all, the adsorption of PG was monitored by SPR, carrying out a screening of the PBS solution pH to define the optimum conditions for its immobilization on the Au surface (see **Figure 2.15**). PG adsorption promotes a dramatic variation in  $\Delta R(\%)$ , namely  $\Delta R(\%) = 15\text{-}20$ , indicating a high change in the Au surface optical properties. Interestingly, the coordination between his-tag PG and Au resulted to be very stable even under constant solution flowing, being the flow rate equal to  $25 \mu\text{L}/\text{min}$ . The pH 5.5 and pH 6.5 were selected as optimised parameters and were also tested for the subsequent immobilization of the Ab.

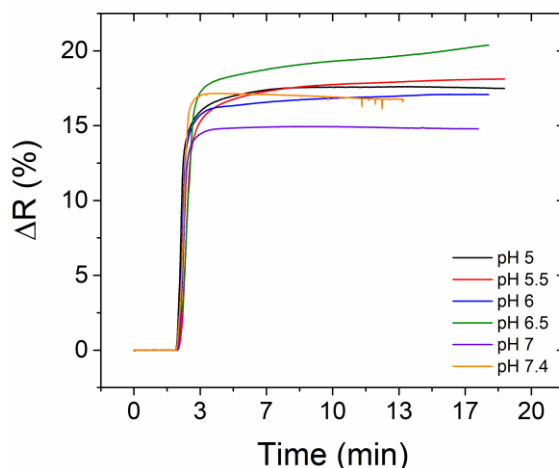


**Figure 2.15.** Overlap of the sensorgrams relative to PG (140  $\mu\text{g}/\text{mL}$ ) adsorption at different pH (PBS 1x). The baseline has been corrected for each curve.

As shown in **Figure 2.16**, it is quite evident that the interplay between PG and Ab is higher and more stable in PBS solution respect to distilled water, displaying a  $\Delta R(\%) \approx 20$  and  $\Delta R(\%) \approx 10$ , respectively. A more saline solution, in fact, stabilizes the intermolecular interactions, which are the driving forces of the recognition process. Combining the evidence collected from PG adsorption and Ab immobilization, PBS 1x at pH 5.5 was selected for the immobilization of both PG and Ab in the next experiments.

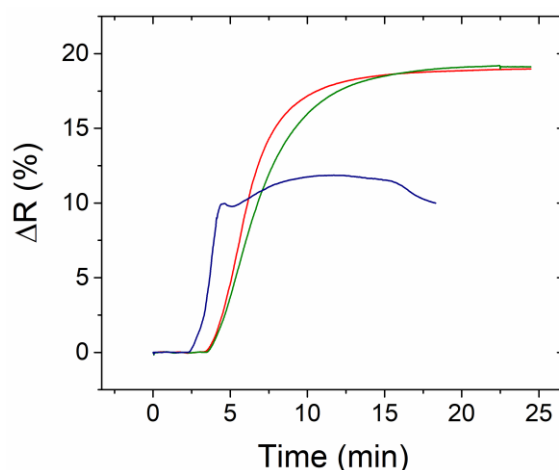


**Figure 2.16.** Overlap of Ab adsorption onto PG-coated Au surface with different solutions: PBS 1x pH=5.5 (red line), PBS 1x pH=6.5 (green curve), distilled water (blue line).



Afterwards, the ability of the Ab to interact with  $\alpha$ -synuclein was explored. First,  $\alpha$ -synuclein solutions were prepared in PBS 1x at physiological pH, in order to produce a more suitable environment for the Ab-Ag complex formation. In **Figure 2.17** the sensorgrams relative to 10 nM and 250 nM  $\alpha$ -synuclein concentrations are reported. The shifts in the reflectivity,  $\Delta R(\%)$ , were equal to  $\approx 0.5$  and  $\approx 0.8$ , respectively.

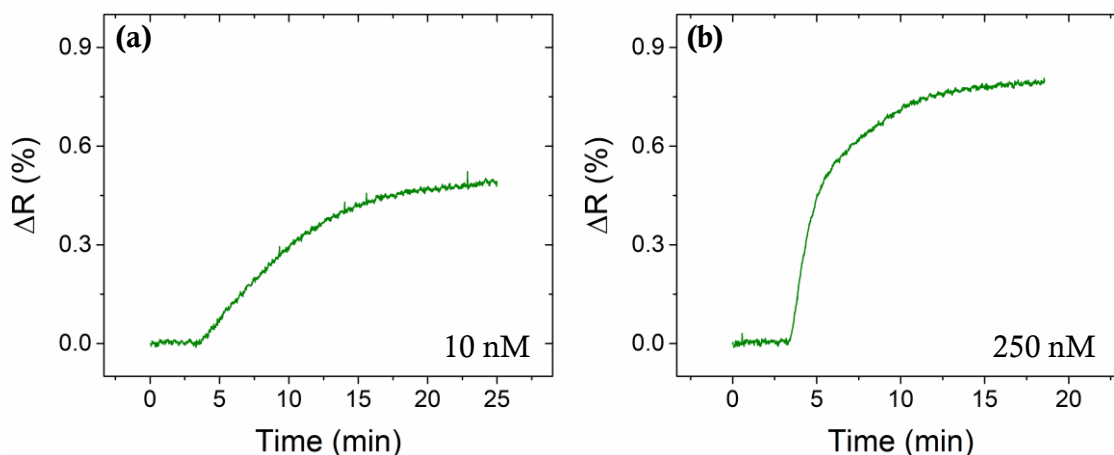


**Figure 2.17.** Sensorgrams of the  $\alpha$ -synuclein interaction with Ab-coated surface (Approach II), in PBS 1x at pH= 5.5 at two different concentrations: (a) 10 nM and (b) 250 nM.

Comparing the SPR results obtained for Approach I and Approach II, it can be observed that a higher amount of Ab is immobilized through Approach II, since  $\Delta R(\%)$  is approximately equal to 20 in Approach II and 7 in Approach I (**Figure 2.12** and **Figure 2.16**). This could be ascribed to the fact that each PG can entice up to three Ab moieties. Furthermore, as mentioned above, PG allows a better exposure of the  $F_{ab}$  portions of the Ab towards the Ag containing solutions. Thus, the more amount of Abs adsorbed along with their proper orientation, can be responsible for the better curves achieved for the Ag binding in Approach II.

Similarly to Approach I, electrochemistry was also used as a complementary technique for the characterization of the sensing platform for Approach II. Au wire was dipped in an Eppendorf containing PG solution (140  $\mu\text{g}/\text{mL}$ , pH 5.5) for 15 minutes at R.T. Afterwards, the surface was rinsed with PBS solution and the wire was immersed in the Ab solution (40  $\mu\text{g}/\text{mL}$ , pH 5.5). Finally, the Ab-coated Au wire was incubated in a 250 nM  $\alpha$ -synuclein solution. In **Figure 2.18** electrochemistry results are reported. From Nyquist plots,  $R_{ct}$  values were calculated.  $R_{ct}$  resulted equal

to  $21 \text{ k}\Omega\cdot\text{cm}^{-2}$  for PG-coated Au, equal to  $17 \text{ k}\Omega\cdot\text{cm}^{-2}$  for Ab-coated Au and to  $6 \text{ k}\Omega\cdot\text{cm}^{-2}$  for the Ab-coated Au exposed to  $250 \text{ nM}$   $\alpha$ -synuclein. It is worth noting that, from the EIS data, PG layer is much less resistive towards the redox probe electron transfer in comparison to the thiol-based SAM, indicating that the monolayer formed by PG is less compact than the one formed by the thiol molecules. DPV measurements (**Figure 2.18,b**) are in agreement with the EIS results, showing an increase of the redox peak passing from PG-coated gold to Ab and (Ab-Ag)-coated gold. The other important difference between the two approaches is the opposite trend promoted by  $\alpha$ -synuclein binding. Indeed, while the impedance signal increased for approach I, in the second case the impedance signal decreased. A detachment of PG from Au surface could safely be excluded according to the results achieved by SPR. SPR demonstrated, indeed, strong adsorption of PG and  $\alpha$ -synuclein despite the dynamic modality of the measurements. Thus, this behaviour must be ascribed to a different organization and packing of the surface which leads, accordingly, to a different overall surface charge.

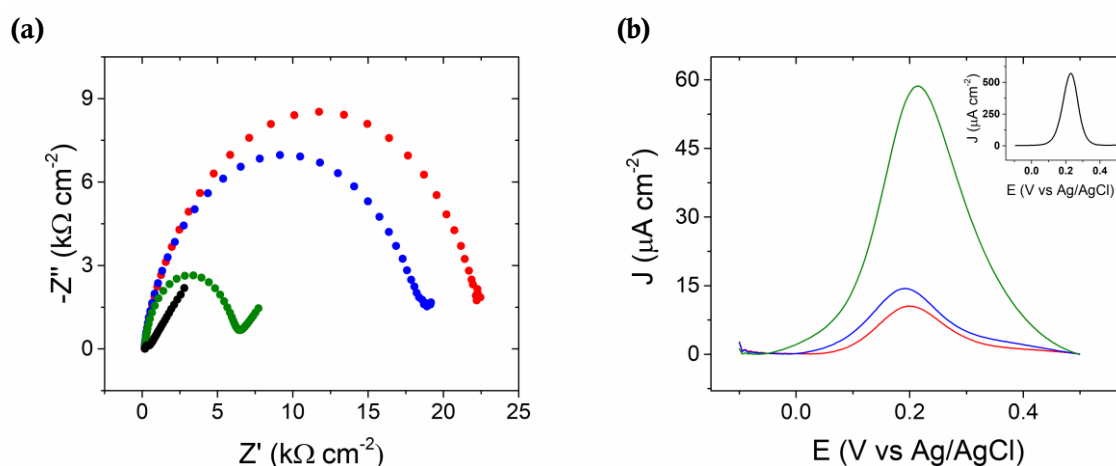


**Figure 2.18.** Electrochemical plots of the functionalization steps followed in Approach II employing a standard three-electrode cell, Pt wire as the counter electrode, Ag/AgCl as the reference and Au wire as working in  $5 \text{ mM K}_3[\text{Fe}(\text{CN})_6]$ ,  $100 \text{ mM KCl}$  and  $50 \text{ mM}$  sodium phosphate salt, at  $\text{pH} = 7.2$ . (a) EIS, Nyquist plot. The black symbols refer to pristine Au, the red symbols to PG-coated Au, blue symbols to Ab-coated Au, green symbols to  $250 \text{ nM}$  of  $\alpha$ -synuclein. (b) DPV recorded in the same condition of EIS, in the inset is shown the measurement relative to pristine Au.

To investigate PG monolayer characteristics in terms of uniformity, AFM images were acquired (see **Figure 2.19**). From the results, it seems that PG forms a quasi-homogeneous monolayer on the Au surface, but such monolayer is not very compact.

Hence, a great portion of Au surface remains uncovered. This can explain the less resistive character of PG monolayer observed by electrochemistry.

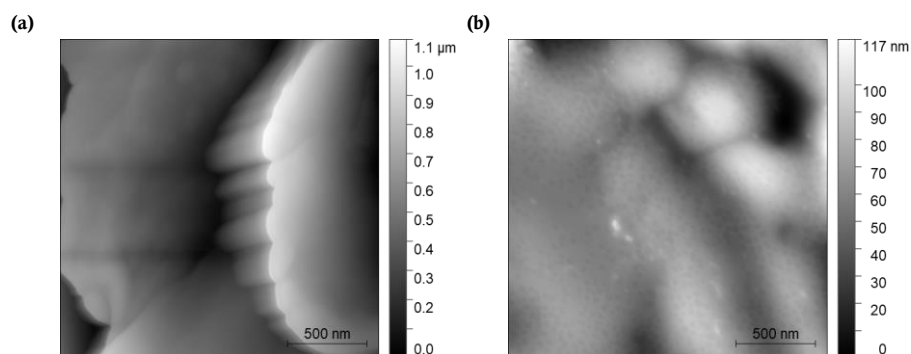


**Figure 2.19.** Topography AFM images of (a) bare Au and (b) PG-coated Au. The images are relative to different Au wires.

Concluding the first part of this work, the characterization of the surfaces achieved following Approach I and Approach II was successfully fulfilled. As expected, these two methodologies for Ab immobilisation are suitable for  $\alpha$ -synuclein detection and the results obtained allowed us to proceed with the implementation of these sensing platforms into EGOFET devices.

## 2.5. Immunosensing with top-gated EGOFETs

- **EGOFETs characteristics**

The second part of the work was focused on the study and development of a transistor-based biosensor for  $\alpha$ -synuclein detection. The sensing platform relies on the bio-functionalisation of the gate terminal of an Electrolyte-Gated Field-Effect Transistor, EGOFET. *Kapton*<sup>®</sup> foils (75  $\mu\text{m}$  thick) were employed as the substrate of the devices, interdigitated Au source (S) and drain (D) electrodes were patterned through a photolithography process (**Figure 2.20**), and a bio-functionalized polycrystalline Au wire was employed as the gate electrode. Characteristics of the active channel layout are the following: channel length ( $L$ ) equal to 30  $\mu\text{m}$  and channel width ( $W$ ) equal to 18000  $\mu\text{m}$ , with a  $W/L= 600$ .

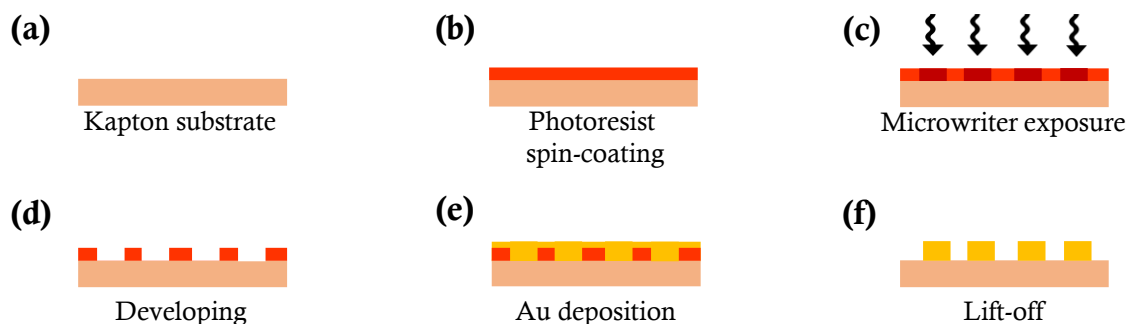


**Figure 2.20.** Gold Source (S) and Drain (D) interdigitated electrodes patterning process on *Kapton*<sup>®</sup> foils by photolithography. (a) Kapton substrate 75  $\mu\text{m}$  thick; (b) spin-coating of the positive photoresist; (c) exposure of the photoresist-coated substrate to the microwriter laser; (d) developing step; (e) Au evaporation (40 nm of gold on top of 5 nm of chromium adhesive layer); (f) lift-off in acetone to remove the residual photoresist.

The semiconductor molecule employed as the active layer consisted of 2,8-difluoro-5,11-bis(triethylsilylethynyl)anthradithiophene, diF-TES-ADT (see **Figure 2.21,a**). This OSC has been well studied as the active layer in OFETs and previously investigated in our group.<sup>41,42</sup> The deposition technique selected to deposit the OSC layer was the Bar-Assisted Meniscus-Shearing technique, which is a fast and low-cost technique that leads to high crystalline thin films.<sup>43,44</sup> The OSC was coated by moving the Bar at 10 mm/s and by setting the plate temperature to 105 C.<sup>41</sup> The OSC was blended with an insulating polymer (ratio 4:1), namely polystyrene (MW= 10000 Da), PS<sub>10k</sub>, in chlorobenzene (CB) at 2% wt.<sup>41</sup> The use of blends of OSCs improves the crystallization of the films and the stability of the electrical performances, especially for the devices operating in liquid. In fact, it has been claimed that a vertical phase separation occurs during the deposition, *i.e.* the organic semiconductor crystallizes sandwiched between a bottom PS layer and a top thin skin PS layer.<sup>42,43,45–47</sup> However, little investigation on this phenomenon has been reported for diF-TES-ADT:PS blend yet.

Before OSC deposition, gold S and D interdigitated electrodes were functionalized with a self-assembled monolayer of 2,3,4,5,6-pentafluorothiophenol (PFBT). In the case of diF-TES-ADT molecules, the formation of a PFBT-based SAM on the electrodes has a double role. Firstly, it is known that SAMs on Au can modify its work-function, thus lowering the gap between the Au work-function and the HOMO level

of the OSC, reducing the contact resistance. Secondly, PFBT molecules improve the ordering of diF-TES-ADT through F-F interaction, achieving higher electrical performances.<sup>48</sup>

A polydimethylsiloxane (PDMS) gasket was placed on top the S and D interdigitated electrodes (IDEs) to confine the liquid gate dielectric. During electrical measurements, the gate electrode, consisting of a polycrystalline Au wire ( $\varnothing = 0.5$  mm) was immersed into the PDMS pool and connected to the potentiostat with banana connectors (see **Figure 2.21,b**).

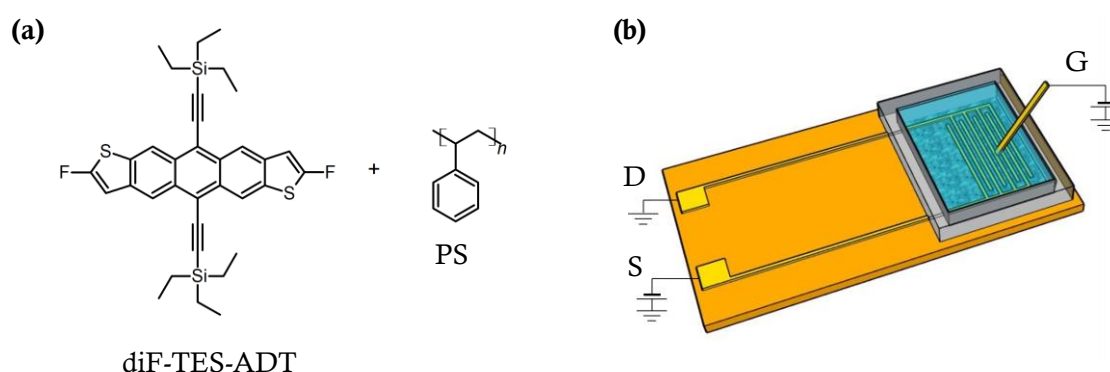


**Figure 2.21.** (a) Molecular structure of the organic semiconductor (diF-TES-ADT) and polystyrene (PS). (b) Representation of the EGOFET configuration.

In **Figure 2.22** the polarized optical microscopy images of the thin films are shown. A high degree of crystallinity and homogeneity was achieved.

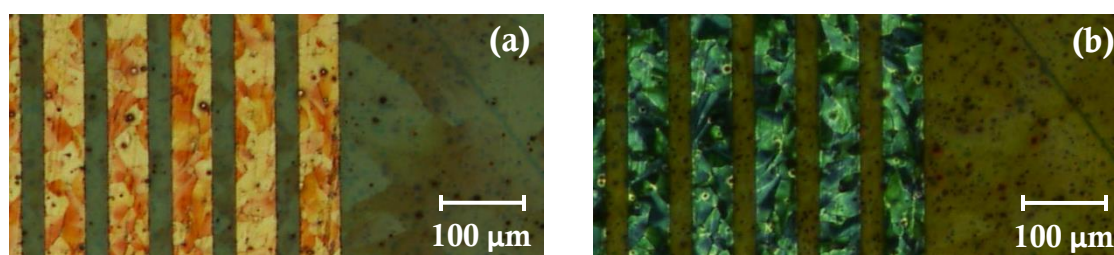


**Figure 2.22.** Cross-polarized optical microscopy images of diF-TES-ADT:PS<sub>10k</sub> (4:1) thin film. (a) polarizer/analyser= 0°, (b) polarizer/analyser= 90°.

Before the sensing experiment, the working regime and the stability of the device were tested in distilled water and in saline solutions, employing a Au gate and

Ag/AgCl electrodes. The material of the gate electrode is of utmost importance. Indeed, the basic principle of the EGOFETs relies on the capacitive coupling between the gate and the active layer. Upon the application of a potential to the gate electrode, the accumulation of charges promotes the formation of an electrical double-layer (EDL), both at the gate/electrolyte interface and at the OSC/electrolyte interface. Depending on the nature of the gate material, the potential drop occurring at the gate/electrolyte interface will be affected, influencing the effective potential on the active layer. Au electrode is regarded as a polarizable electrode thus a significant potential drop takes place at the interface with the electrolyte. On the contrary, Ag/AgCl is a non-polarizable electrode. Indeed, due to the following reaction occurring at the surface of the electrode, a steady-state current continuously flows, preventing the formation of the electrical double layer at its interface (**Figure 2.23**).<sup>49</sup>

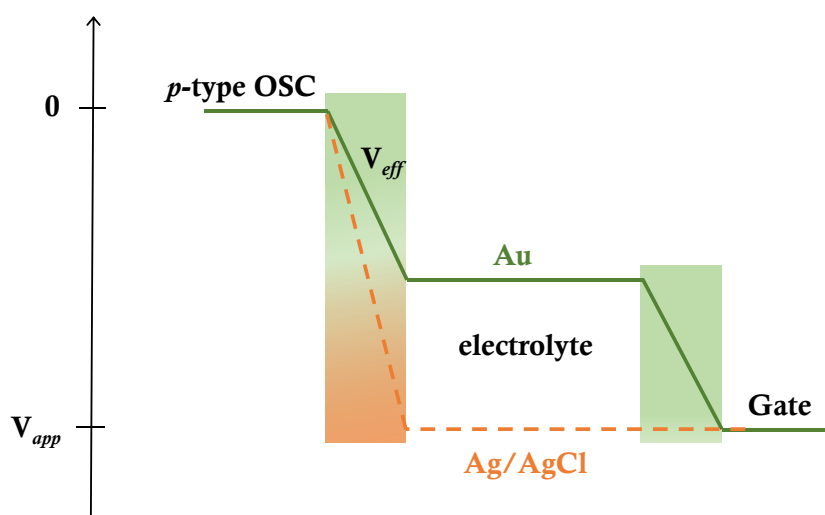
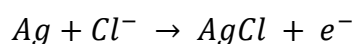


**Figure 2.23.** Scheme of the potential drop at the interfaces of the gate/electrolyte and OSC/electrolyte, for Ag/AgCl gate electrode (orange dashed line) and Au electrode (green solid line).

In **Figure 2.24** the electrical characterization of diF-TES-ADT:PS<sub>10k</sub> thin film EGOFET employing Au and Ag/AgCl as gate electrodes is shown. Devices present a *p*-type behaviour with negligible hysteresis and the parameters extrapolated are comparable with the ones already reported in a previous work of our group.<sup>41</sup> As expected, the threshold voltage,  $V_{th}$ , is quite different, namely, it is equal to 0.2 V for

the device measured with the gold gate, and equal to  $-0.2$  V for the device measured with Ag/AgCl gate electrode. This can be ascribed to the different work-function of the two electrodes. As it is clear from the transfer plots, the device is switched on faster when the gold gate is used, exhibiting a subthreshold swing,  $SS$  of  $0.7$  V/dec for the gold gate, while for the device with Ag/AgCl gate this value is  $1.7$  V/dec. This could be attributed to a better capacitive coupling between the gold gate and the active layer. Accordingly, the product of  $C_{eff}\mu$  is equal to  $0.15 \mu\text{S}\cdot\text{V}^{-1}$  and  $0.45 \mu\text{S}\cdot\text{V}^{-1}$ , for the Ag/AgCl and Au gate, respectively.

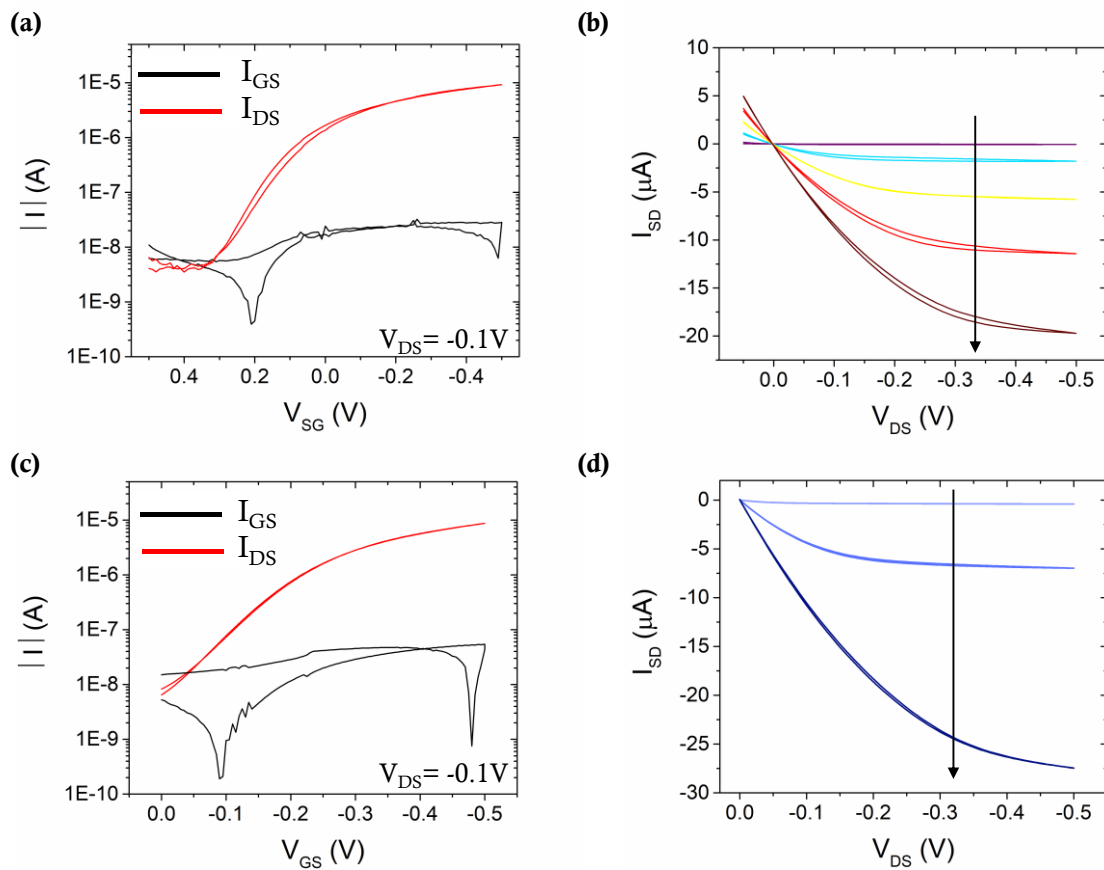


**Figure 2.24.** Transfer and output characteristics of diF-TES-ADT:PS<sub>10k</sub> thin film EGOFETs. (a)  $I$ - $V$  measurement recorded with Au gate by sweeping  $V_{GS}$  from 0.5 V to -0.5 V at a constant  $V_{DS} = -0.1$  V. (b) Output measured with Au gate by sweeping  $V_{DS}$  from 0.05 V to -0.5 V at the following constant  $V_{GS}$  applied in this order (following the arrow in the figure): 0.3 V, 0.1 V, -0.1 V, -0.3 V, -0.5 V. (c)  $I$ - $V$  measurement recorded with Ag/AgCl gate electrode by sweeping  $V_{GS}$  from 0 V to -0.5 V at a constant  $V_{DS} = -0.1$  V. (d) Output measured with Ag/AgCl gate electrode by sweeping  $V_{DS}$  from 0 V to -0.5 V applying the following  $V_{GS}$  applied in this order (following the arrow in the figure): -0.1 V, -0.3 V and -0.5 V. Phosphate buffer (5 mM) was used as the electrolyte in all measurements, pH = 7.2.

- **Immunosensing based on Approach I**

The sensing of  $\alpha$ -synuclein with the EGOFET devices was carried out by *ex-situ* functionalization of Au gate electrode, as explained before. Gold wire was dipped in an Eppendorf containing the protein solutions, for 15 min at R.T. and subsequently connected to the EGOFET device to act as the gate electrode. Protein solutions were prepared in PBS 1x at physiological pH to guarantee the best conditions for the protein-protein interactions. However, the gate dielectric employed was PBS 0.01x at physiological pH, to decrease the concentration of the ions, which can be detrimental for the device. First of all, a cleaned gold wire was employed to characterize the device and to stabilize it. At this aim, a constant  $V_{GS}$  and  $V_{DS}$  (equal to -0.1 V) were applied to the device and the current was monitored as a function of time. The measurement was stopped when a steady-state current was reached, approximatively after 30 minutes. Afterwards, at least five transfers were recorded to be sure on the reliability of the measurements. At this stage, the device was employed as the transducer of our biosensor, exploiting the functionalized Au wire as the gate electrode.

In **Figure 2.25** the  $I$ - $V$  transfer characteristics recorded after each functionalization step of the Au gate electrode, following Approach I are shown. The transfers are measured in the linear regime, specifically, at  $V_{DS} = -0.1$  V. The deposition of the SAM promotes a decrease in the measured  $I_{DS}$ , along with a slight change in the slope of the curve obtained by plotting the absolute values of  $I_{DS}$  vs  $V_{GS}$  in a semilogarithmic scale. This result suggests a variation of the double-layer capacitance,  $C_{dl}$ , if one assumes that the OSC mobility keeps constant during the experimental session. The immobilization of the Ab provokes a dramatic shift of the  $V_{th}$  towards more negative values. This means that the Ab layer induces a quite high potential screening at the gate/electrolyte interface so that higher energy is required to switch on the device. On the other hand, no appreciable variation of the slope is observed, hint that no significant variation of the  $C_{dl}$  is occurring upon the Ab attachment on the surface. The Ab-coated Au surface was exposed to increasing concentration of antigen, in a range which spans from pM to nM. The binding of  $\alpha$ -synuclein causes, in turn, a shift of the  $V_{th}$  towards more positive values with no great variation in the slope of the curves. Two different observations can arise from this result. First of all, the biggest change in the device



response to  $\alpha$ -synuclein is achieved for the less concentrated solution. Afterwards, when increasing further the concentration of  $\alpha$ -synuclein smaller shifts are observed. The binding of an antigen to its autoantibody is always accompanied by a conformational change of the Ab. Accordingly, the exposure of the Ab-coated Au to the first  $\alpha$ -synuclein aliquot redefines greatly the organization of the surface. Secondly,  $\alpha$ -synuclein has a pI equal to 4.67, bearing an overall negative charge at physiological pH (*viz.* pH > pI). This negative charge can explain the positive shift of the  $V_{th}$ . A greater accumulation of negative charge at the gate/electrolyte interface, leads to an extra-accumulation of positive charge at the OSC/electrolyte interface, resulting in a sort of *p*-doping effect.

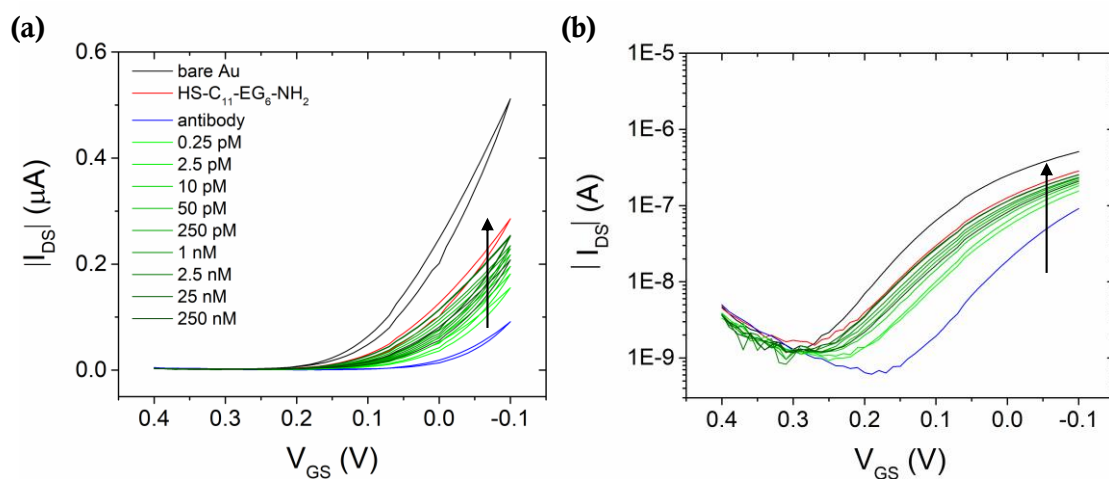


**Figure 2.25.** *I-V* transfer characteristics recorded sweeping  $V_{GS}$  from 0.4 V to -0.1 V under a constant  $V_{DS} = -0.1$  V. (a) Back and forward scans in the linear scale. (b) Representation of the  $\log(I_{DS})$  vs  $V_{GS}$ , forward scans. The black transfer is relative to a bare Au gate, the red one refers to HS-C<sub>11</sub>-EG<sub>6</sub>-NH<sub>2</sub>-coated Au, the blue one corresponds to the Ab-coated Au, and the green ones are recorded upon the exposure of the Ab-coated gate to increasing concentration of  $\alpha$ -synuclein (from light to darker green shades), namely 0.25 pM, 2.5 pM, 10 pM, 50 pM, 250 pM, 1 nM, 2.5 nM, 25 nM, 250 nM. Electrolyte: PBS 0.01x, pH=7.2.

The sensing experiment was repeated three times, recording at least three transfers for each functionalization step, to ensure the stability of the system under the application of an electric potential. To obtain a dose-response relationship which is not affected by device-to-device variation, a mathematical elaboration suggested by *Ishikawa et al.*,<sup>50-52</sup> was applied. In their work, the absolute response of the biosensor is correlated to the change in the effective gate potential induced by the binding of the

biomolecule, in the following way. According to the general MOSFET model, the  $I_{DS}$  in the linear regime is given by:

$$I_{before} = \mu_{FE,lin} \frac{W}{L} C V_{DS} (V_{GS} - V_{T1}) \quad (2.4)$$

where  $\mu_{FE,lin}$  is the electron mobility,  $W$  and  $L$  are geometric parameters, respectively the width and the length of the active channel,  $C$  is the dielectric capacitance,  $V_{DS}$  is the constant source-drain potential,  $V_{GS}$  is the source-gate potential and  $V_{T1}$  is the initial threshold voltage.

After the binding of the biomolecule, the equation is transformed into:

$$I_{after} = \mu_{FE,lin} \frac{W}{L} C V_{DS} (V_{GS} - (V_{T1} + \Delta V)) \quad (2.5)$$

where  $\Delta V$  is the gating voltage change induced by the biomolecule binding. Taking into account electrostatic factors as the main sensing driving force and that  $\mu_{FE,lin}$  and  $C$  are considered constant during the experiment, the following approximation is derived:

$$B = \frac{dI}{dV_{GS}} = \mu_{FE,lin} \frac{W}{L} C V_{DS} = g_m \quad (2.6)$$

where  $g_m$  is the maximum transconductance of the device.

The normalized response is defined as:

$$\frac{\Delta I}{I_0} = \frac{(B (V_{GS} - V_{T1}) - B (V_{GS} - (V_{T1} + \Delta V)))}{B (V_{GS} - V_{T1})} = \frac{\Delta V}{V_{GS} - V_{T1}} \quad (2.7)$$

The calibrated response results:

$$\frac{\Delta I}{\frac{dI}{dV_{GS}}} = \frac{(B (V_{GS} - V_{T1}) - B (V_{GS} - (V_{T1} + \Delta V)))}{B} = \frac{\Delta I}{g_m} = \Delta V \quad (2.8)$$

Finally, the calibrated response, taking into account the transconductance ( $g_m$ ) of the device, which is an intrinsic property, is no longer dependent from  $V_{TI}$ , but only from the variation of the effective potential,  $\Delta V$ , promoted by the biomolecules binding. On the contrary, the normalized response is still affected by the device parameter  $V_{TI}$ .

In **Figure 2.26,a**  $\Delta V$  is reported *vs*  $\alpha$ -synuclein concentration. To calculate this parameter,  $g_m$  values corresponding to the maximum ones were selected. Indeed, in the maximum of transconductance the EGOFET devices display the highest sensitivity.<sup>53</sup> In **Figure 2.26,b** the data are reported in logarithmic scale. A linear fitting was carried out, obtaining a sensitivity equal to  $21(\pm 2)$  mV/dec. The range of concentrations used spans from 0.25 pM to 250 nM, but the system saturated at 1 nM of  $\alpha$ -synuclein. Above this value, a plateau is reached. Approach I yields an overall  $\Delta V$  shift of  $+111(\pm 20)$  mV. The limit of detection (LOD) reached was at the sub-picomolar level.

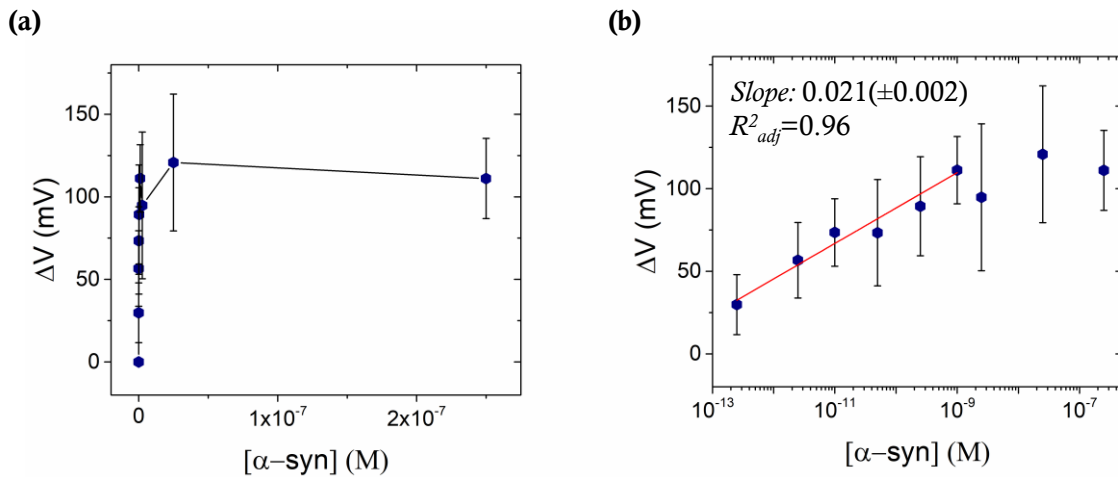


**Figure 2.26.** (a) Sensing response calculated as  $\Delta V$  *vs*  $\alpha$ -synuclein concentration. The error bars are relative to three different experiments (different devices and biofunctionalized Au gates). (b) Plot of  $\Delta V$  *vs* the log of the  $\alpha$ -synuclein concentration (blue symbols). These data have been linearly fitted (red line).

The stability of the device was assured by measuring it before and after the sensing experiment with a bare Au wire. In **Figure 2.27** the comparison between the starting and final device performance is presented. A slight negative shift of  $V_{th}$  occurs, but the overall performance of the device is not compromised.

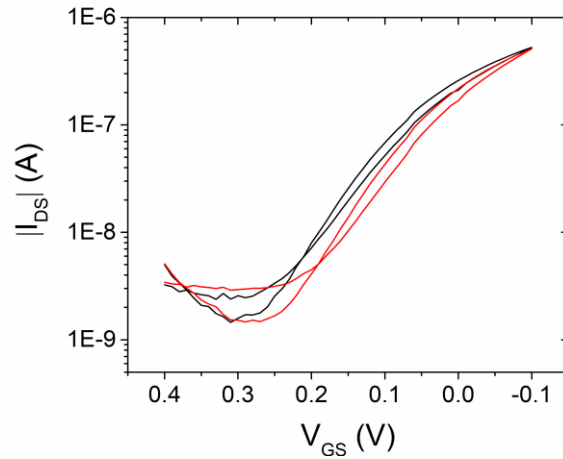


**Figure 2.27.**  $I/V$  transfer characteristics recorded with a bare Au gate before the beginning of the sensing experiment (black curve) and at the end of the sensing experiment (red curve) at a constant  $V_{DS} = -0.1$  V. Electrolyte: PBS 0.01x, pH = 7.2.

- **Immunosensing based on Approach II**

The same procedure was carried out for Approach II. As above-mentioned for Approach I, gold gate surface was modified *ex-situ* and transfer characteristics were recorded for each functionalization step. In **Figure 2.28** transfers characteristics are reported. PG-coated Au promotes a dramatic positive shift of the  $V_{th}$ . The PG has a pI = 4.5, so at the pH at which the measurements are performed, it bears an overall negative charge density, resulting in a strong positive charge accumulation at the OSC/electrolyte interface. Thus, the effective potential in the active channel is increased. From the slope of the transfer plotted in semi-logarithmic scale, it is clear that also a change in the  $C_{dl}$  is likely to occur. The PG-Ab complex formation is responsible for a negative shift of the  $V_{th}$ . It is known that Ab molecules have a dipolar moment which should be oriented towards the  $F_c$  portion of PG. Thus, the  $F_{ab}$  moieties carry a positive charge density. As explained above, thanks to the regioselectivity of PG-Ab complex,  $F_{ab}$  portions are exposed towards the electrolyte solution. As a result, the negative shift registered can be explained by a combination of two factors: from one hand the screening of the negative charge carried by PG and from the other hand an accumulation of a positive charge density on the surface due to the intrinsic dipole of the Ab molecules.

On the contrary, the binding of  $\alpha$ -synuclein cannot be understood only in terms of simply electrostatic interactions.  $\alpha$ -synuclein binding provokes a negative shift of the  $V_{th}$ . If only the pI of this protein is taken into account, one would expect the opposite trend, like the one obtained for Approach I. Apparently there are competitive effects that contribute to the final results. Firstly, respect to Approach I, PG does not form a homogenous monolayer on Au surface, as demonstrated by electrochemistry and by AFM images. Thus, a considerable portion of the Au surface is still exposed to the analyte solution. Secondly,  $\alpha$ -synuclein binding exerts a screening effect on PG, decreasing the above-mentioned  $p$ -doping effect due to the negative charge of the first monolayer.

Considering all the above, the results observed with EGOFETs are coherent with the ones obtained with electrochemistry, according to which, two opposite trends occurred. These differences are most likely ascribable to differences in the overall charge density of the surface.

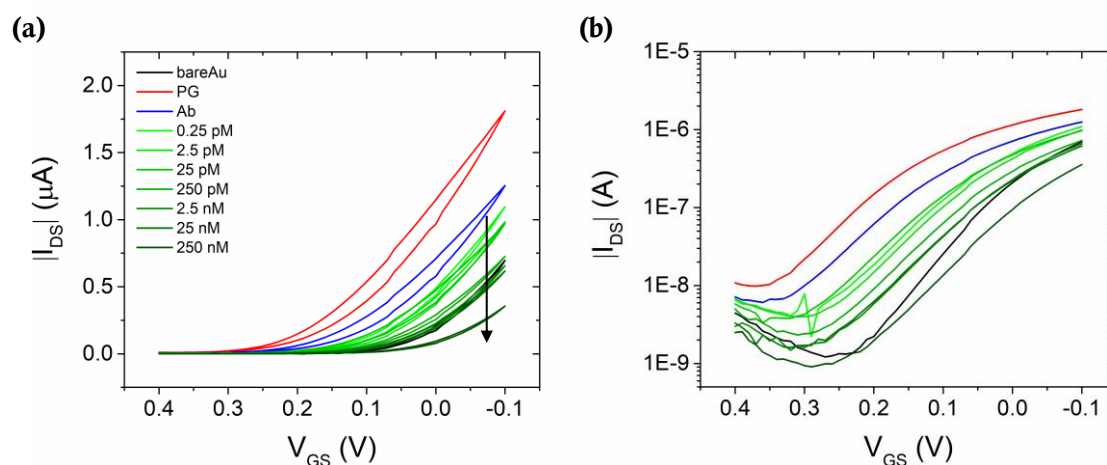


**Figure 2.28.**  $I/V$  transfer characteristics recorded sweeping  $V_{GS}$  from 0.4 V to -0.1 V under a constant  $V_{DS} = -0.1$  V. (a) Back and forward curves plotted in the linear scale. (b) Representation of the  $\log(I_{DS})$  vs  $V_{GS}$ , forward scans. The black transfer is relative to a bare Au gate, the red one refers to PG-coated Au, the blue one corresponds to the Ab-coated Au, and the green ones are recorded upon the exposure of the Ab-coated gate to an increasing concentration of  $\alpha$ -synuclein (from lighter to darker green shades), namely 0.25 pM, 2.5 pM, 25 pM, 250 pM, 2.5 nM, 25 nM and 250 nM. Electrolyte: PBS 0.01x, pH= 7.2.

The mathematical elaboration described above for Approach I, was also adopted for Approach II and the results are shown in **Figure 2.29**. The overall shift reached is equal to  $-111(\pm 29)$  mV and the sensitivity achieved is equal to  $-16(\pm 2)$  mV/dec. These

values are similar to the ones obtained for Approach I. However, in the case of Approach II, the plateau of the response is fulfilled at higher concentrations of  $\alpha$ -synuclein, namely at around 250 nM. This is in agreement with the outcomes obtained by SPR measurements, that is to say, more Ab moieties are available for the antigen-binding, compared to Approach I. The LOD, in this case, is also set at the sub-picomolar level.

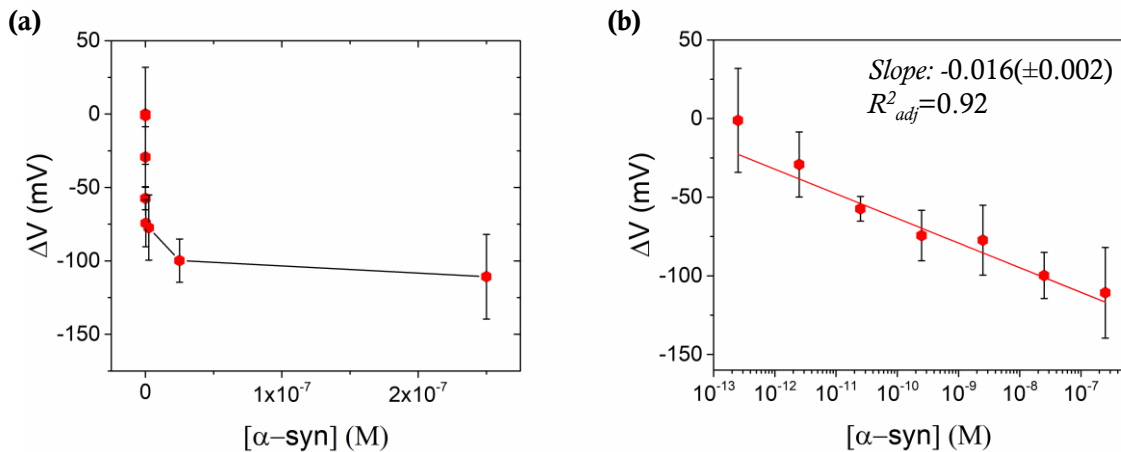


**Figure 2.29.** (a) Sensing response calculated as  $\Delta V$  vs  $\alpha$ -synuclein concentration. The error bars are relative to three different experiments. (b) Plot of  $\Delta V$  vs the log of the  $\alpha$ -synuclein concentration (red symbols). These data have been fitted linearly (red line).

In **Figure 2.30** the transfer curves measured before and after the sensing experiment are reported. Similar to in the previous case, only a slight negative shift of the  $V_{th}$  occurs, without altering the overall performance of the device, confirming its stability during the experiments.

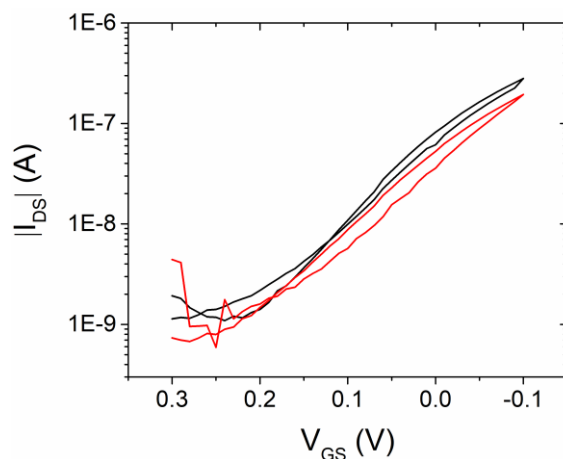


**Figure 2.30.**  $I/V$  transfer characteristics recorded with a bare Au gate before the beginning of the sensing experiment (black curve) and at the end of the sensing experiment (red curve) at a constant  $V_{DS} = -0.1$  V. Electrolyte: PBS 0.01x, pH = 7.2.

## 2.6. Towards a self-standing chip

Taking into account the promising results achieved in the detection of  $\alpha$ -synuclein with top-gated configuration, a more compact platform comprising a planar gate architecture and a microfluidics cell fixed on top of the substrate was conceived.

The microfluidics cell is illustrated in **Figure 2.31** and consists of two separated chambers, each containing a coplanar gold gate, i) chamber 1, in which gold S and D IDEs are patterned together with a so-called reference gate (RG) and ii) chamber 2 which contains the so-called sensing gate (SG), in which the sensing platform relies on. The RG was designed aiming at guaranteeing a straightforward check of the electrical performance of the device before, during and after the experiment session. Chamber 1 and chamber 2 are linked through a narrow channel, which is indicated as connecting channel. This channel has a double function, i) to allow electrical connection between the SG and the IDEs, ii) to minimise cross-contamination between the two chambers, as it is explained below. The microfluidics cell was moulded by 3D pre-printed plastic stamps by PDMS curing (further details are reported in the experimental section) and finally, 3D-printed plastic support was fabricated to fix all the components (**Figure 2.31,b**). The top support was equipped with three openings, one on top of the sensing gate, one on top of the connecting channel and one on top of chamber 1, in order to have the chance to check the streaming of the liquid once the device is mounted. Furthermore, a plastic cap was printed to cover the opening of chamber 1 during

electrical measurements. The device was designed with two inlets, i) *Inlet1* to introduce the liquid gate dielectric from chamber 1 and ii) *Inlet2* to introduce the solutions containing the biological materials directly via chamber 2. Chamber 2 was also embedded with an *Outlet* to allow the stream of the liquids out. Liquids were pumped in and out by peristaltic pumps.

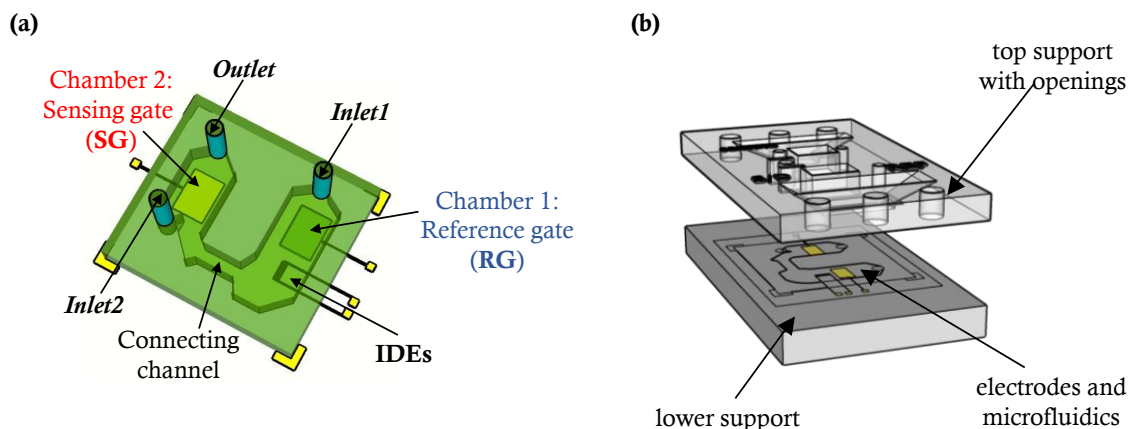


**Figure 2.31.** (a) 3D scheme of the microfluidic setup in which chamber 1, chamber 2 and the connecting channel are indicated, along with Inlet1, Inlet2 and the Outlet. (b) 3D view of the plastic support used to fix the electrical components and the PDMS microfluidic cell.

The great advantage of the envisioned device respect to the above discussed top-gated configuration relies on the possibility to functionalize the gate electrode *in-situ* avoiding electrical fluctuations arising from water evaporation and, more important, adventitious contamination of the aqueous medium in direct contact with the OSC during the time-scale of the whole experiment.

The effective segregation of the electrolyte in the two chambers was assessed using coloured dyes. A blue dye was flown from *Inlet1* until all the microfluidics cell was filled up completely. Afterwards, a red dye was flown from *Inlet2*. As it is illustrated in **Figure 2.32**, no cross-contamination between the two chambers occur. In fact, the thin channel impedes the electrolyte to flow towards chamber 1. In this way, no screw was necessary to close mechanically the channel, avoiding also the possible formation of over-pressures which could favour liquid leakages.



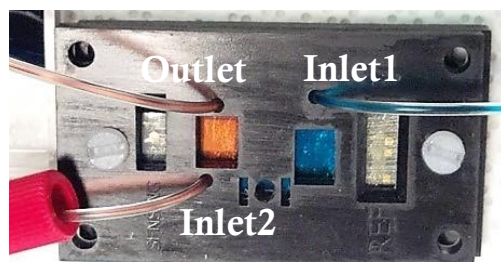


**Figure 2.32.** A real picture of the dye chambers filling test.

In the first place, the RG electrode was conceived smaller respect to the SG and placed in between the SG and the IDEs (**Figure 2.33,a**). Nevertheless, by electrically measuring the device, it was noticed that this was not the optimal solution. The device performance recorded with the RG was affected by a previous measurement recorded with the SG, namely a shift of the  $V_{th}$  was observed. The  $V_{th}$  recovered repeating the measurement. This was probably due to the polarization of the Au surface of the RG by the electric field generated by the SG. Furthermore, for a better comparison, it was decided to pattern the gates with the same geometric area. The definitive layout used is shown in **Figure 2.33b**. Employing this latter layout, the measurements recorded with RG were no longer affected by previous measurements with SG electrode.

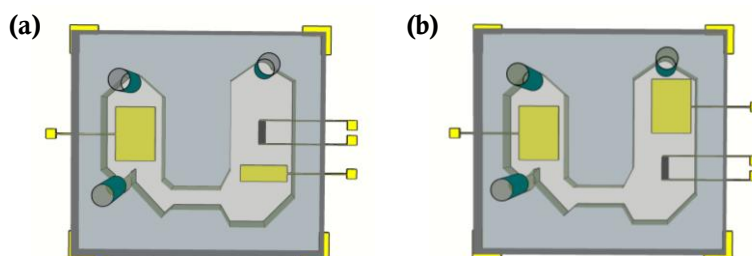


**Figure 2.33.** Electrodes geometry used for the microfluidics. (a) RG smaller than SG and placed in between SG and IDEs. (b) Definitive layout employed, in which SG and RG are separated by the IDEs and have the same geometric area.

The active layer employed was the same used in the top-gated configuration, namely diF-TES-ADT:PS<sub>10k</sub> deposited on *Kapton*<sup>®</sup>. However, oppositely to the top-gated configuration, previously to the OSC deposition, a sacrificial layer of dextran was deposited on top of the RG surface before the functionalisation of the source and drain electrodes and deposition of the OSC on the IDEs area. Afterwards, the substrate was dipped in PFBT solution avoiding the contact of the SG area with the solution.

Then, the OSC was coated by BAMS exclusively on the portion of IDEs and RG. Finally, dextran was removed from the RG surface by water rinsing. The steps followed are depicted in **Figure 2.34**.

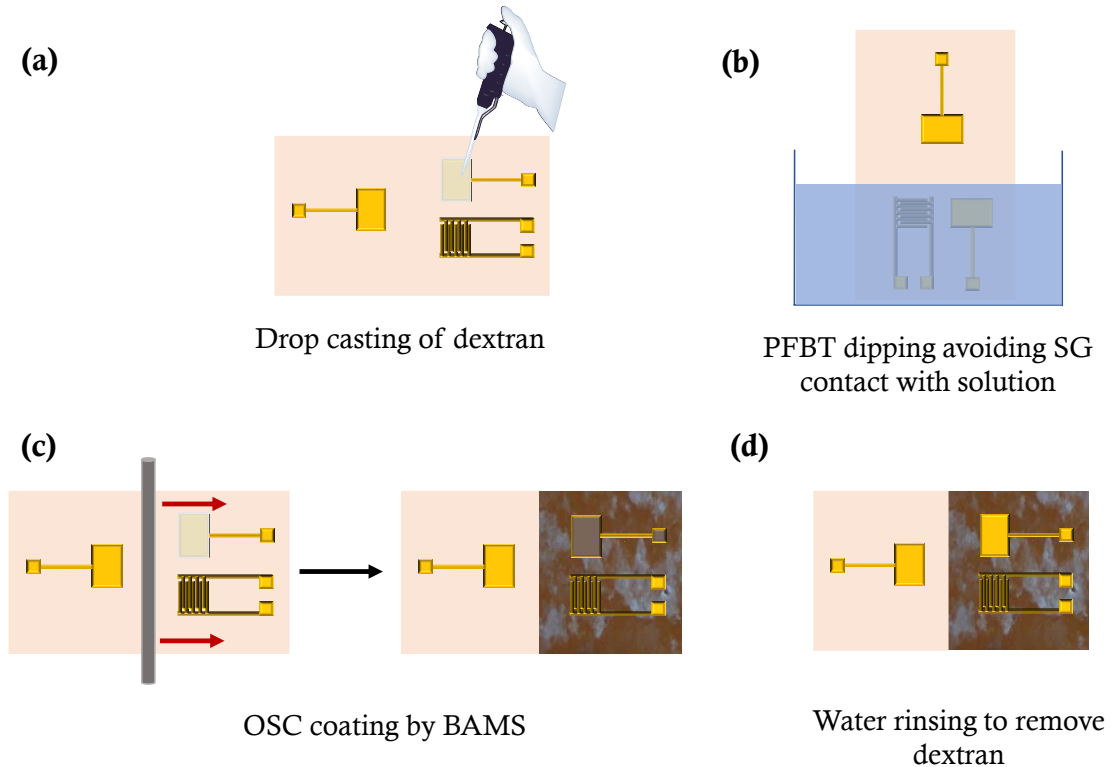


**Figure 2.34.** Scheme of diF-TES-ADT:PS<sub>10k</sub> coating protocol by BAMS on *Kapton*<sup>®</sup> foil (75  $\mu$ m thick). (a) drop casting of a sacrificial layer of dextran on top of the RG; (b) dipping of the IDEs and RG on PFBT solution to functionalise the source and drain electrodes; (c) BAMS coating; (d) removal of the sacrificial layer by water rinsing.

It is worth noting that, employing the coplanar gate layout, the operational voltage of the active channel is shifted towards more negative potential values (**Figure 2.35**). Specifically,  $I$ - $V$  transfer characteristics were recorded sweeping the  $V_{GS}$  from +0.1 V to -0.4 V, whereas before with the Au wire gate, the potential window selected ranged from +0.4 V to -0.1 V. This significant shift could be ascribed to a combination of i) the differences in the cleaning protocol of Au surfaces and the ii) variation of the gate geometry. Both modifications could lead to a change in the surface potential of Au, consequently changing the effective potential at the OSC/electrolyte interface, affecting the performance of the device. Furthermore, the hysteresis measured with the

SG is higher respect to the one measured with the RG. This could be ascribed to the fact that the SG is more distant to the active layer compared to the RG, affecting the rate at which the double-layer is formed. A comparison of the transfers obtained from the two gate electrodes is shown in **Figure 2.35**.

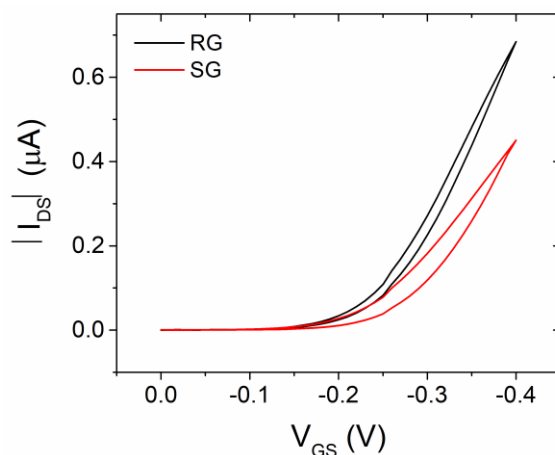


**Figure 2.35.**  $I$ - $V$  transfers characteristics of diF-TES-ADT:PS<sub>10k</sub>-based EGOFETs in the microfluidics layout. Measurements were recorded with the reference gate (black curve) and with the sensing gate (red curve), by sweeping  $V_{GS}$  from 0 V to -0.4 V at a constant  $V_{DS} = -0.1$  V. Electrolyte: PSB 0.01x, pH= 7.2.

- **Approach I based  $\alpha$ -synuclein sensing by coplanar gating and *in-situ* functionalization**

To immobilize the HS-C<sub>11</sub>-EG<sub>6</sub>-NH<sub>2</sub> based SAM onto the coplanar sensing gate, microcontact printing ( $\mu$ CP) technique was exploited and its effectiveness assessed by electrochemistry.  $\mu$ CP technique was firstly reported by *Wilbur et al.*<sup>54</sup> It consists of dropping the solution of the thiol molecules on a PDMS stamp and pushing it, gently, onto the Au film. It is proven that, in this way, the SAM is formed rapidly at the interface between the two surfaces. Finally, the PDMS stamp is removed and the SAM is transferred to the Au surface. For our purpose, the PDMS stamp was maintained over the planar Au gate approximately 15 minutes at 4 °C. Afterwards, the surface was washed with EtOH and distilled water, paying attention not to rinse the OSC thin film too. Electrochemistry experiments were carried out employing Au thin film (40 nm thick, 1 cm<sup>2</sup> area) on *Kapton*<sup>®</sup> substrate with a standard three-electrode cell. As it is evident from the Nyquist plot and the differential pulse voltammogram (**Figure 2.36**), the surface of the evaporated Au is more resistive respect to the polycrystalline

wire used above. This is probably due to the different cleaning protocol followed for the two surfaces, electropolish and sonication in organic solvents, respectively. After  $\mu$ CP, SAM-coated Au reduces the impedance signal and the redox peak of the ferricyanide probe is shifted. This result was unexpected on the base of the previous one achieved with the Au wire, but the experiment was repeated three times, and the same behaviour was obtained. One difference between the two methodologies, apart from the SAM formation, *viz.* overnight dipping of the wire gold in one case, and  $\mu$ CP in the other, resides on the gold cleaning procedures employed. Gold wire was cleaned by electropolishing in mildly acidic conditions (see Experimental chapter), whereas the surface of the planar gate was cleaned by sonication in acetone and isopropanol, following the protocol used for the device fabrication. This could be the cause of the higher impedance signal observed for the gold thin film, compared with the electropolished gold wire. The exposure of the planar gold surface to the thiol solution in ethanol might have reduced the eventual oxides on the surface, reducing, accordingly the impedance signal and displacing the redox peak of the ferricyanide, as shown in the DPV plot (**Figure 2.36,b**). The amino-terminal group was subsequently activated by dropping glutaraldehyde solution for 10 minutes at 4 °C. Afterwards, Ab solution was cast on top for 10 minutes at R.T. Electrochemistry measurements showed a dramatic increase of the impedance signal and the disappearance of the redox peak in the voltammogram, confirming the successful covalent grafting of the Ab to the underneath SAM.

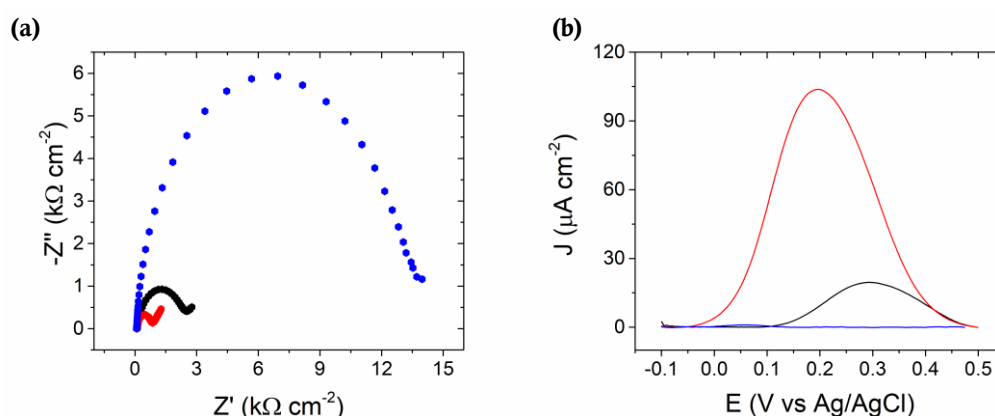


**Figure 2.36.** Electrochemistry of functionalized Au surface (40 nm thick) on Kapton substrate. (a) EIS recorded applying a DC voltage equal to 0.3 V, in a range of frequency from  $10^5$  Hz to 0.1 Hz. (b) DPV plot. Electrolyte used:  $\text{K}_3[\text{Fe}(\text{CN})_6]$  5 mM, KCl 100 mM, phosphate buffer 50 mM at pH 7.2. Black symbols: bare Au, red symbols: HS-C<sub>11</sub>-EG<sub>6</sub>-NH<sub>2</sub>-coated Au, blue symbols: Ab-coated Au.

As mentioned above, the microfluidics allows an *in-situ* functionalization of the SG. To achieve it, solutions containing the reagents required for the gold gate modification were injected from *Inlet2*, helping the fluid to be pumped out by a second peristaltic pump operating at the *Outlet*, at the same flow rate, namely  $10 \mu\text{L}/\text{min}$  (further details are reported in the experimental section). First of all, glutaraldehyde ( $100 \mu\text{L}$ , 2.5% wt. (aqueous), flow rate equal to  $10 \mu\text{L}/\text{min}$ ) was injected to activate the amino groups of the SAM. Subsequently, Ab solution was injected ( $50 \mu\text{L}$ ,  $40 \mu\text{g}/\text{mL}$ , 5 minutes flowing continuously at  $10 \mu\text{L}/\text{min}$ ) and finally PBS was streamed approximatively for three minutes to remove physisorbed molecules. At this stage, the flow was stopped and at least three transfers were recorded employing the SG. This protocol was repeated for the  $\alpha$ -synuclein solutions, which were injected at increasing concentrations, namely 0.25 pM, 2.5 pM, 25 pM, 250 pM, 2.5 nM, 25 nM and 250 nM ( $50 \mu\text{L}$  aliquots at a flow rate equal to  $10 \mu\text{L}/\text{min}$ ), for 5 minutes each followed by a 3-minute rinse with the PBS solution. In **Figure 2.37** the transfers recorded with the SG at each functionalization stage are reported. The results obtained are coherent with the ones achieved with the top-gated configuration, that is to say, that the binding of the analyte promotes an increase of the current, proportional to its concentration.

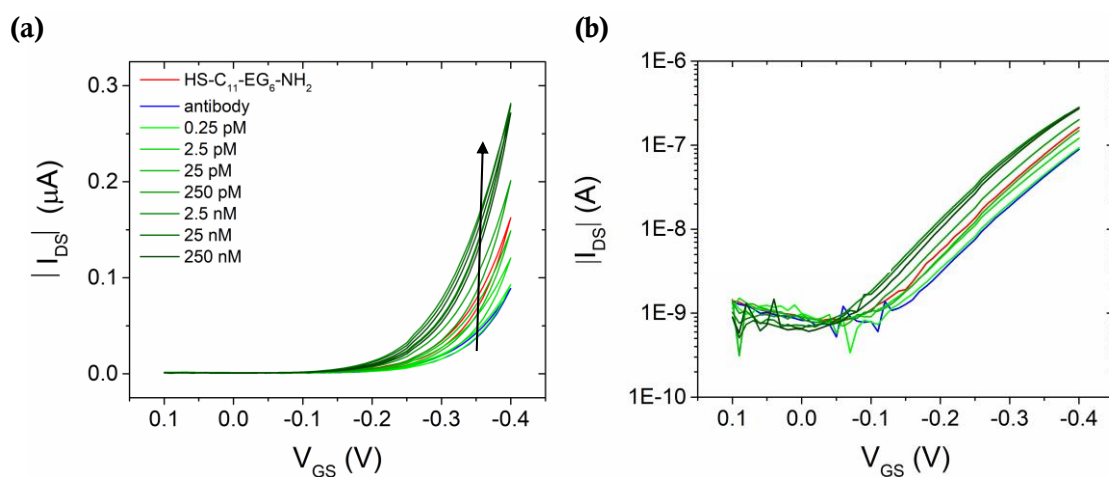


**Figure 2.37.**  $I$ - $V$  transfer characteristics recorded sweeping  $V_{GS}$  from 0.4 V to -0.1 V under a constant  $V_{DS} = -0.1$  V. (a) Back and forward curves in the linear scale. (b) Representation of the  $\log(I_{DS})$  vs  $V_{GS}$ , forward scans. The red transfer refers to HS-C<sub>11</sub>-EG<sub>6</sub>-NH<sub>2</sub>-coated Au, the blue one corresponds to the Ab-coated Au, and the green ones are recorded after the exposure of the Ab-coated gate to an increasing concentration of  $\alpha$ -synuclein (from lighter to darker green shades), namely 0.25 pM, 25 pM, 250 pM, 2.5 nM, 25 nM and 250 nM. Recorded biasing was performed with the so-called sensing gate. Electrolyte: PBS 0.01x, pH= 7.2.

In **Figure 2.38** the dose-response curve, calculated with the above-mentioned mathematical elaboration, is reported. The maximum  $\Delta V$  reached is  $+166(\pm 52)$  mV, higher compared to the top-gated configuration. The linear fitting shows also a slight increase in sensitivity, equal to  $37(\pm 5)$  mV/dec. The sensitivity range spans from 0.25 pM to 25 nM  $\alpha$ -synuclein concentration. A LOD at the sub-picomolar level is confirmed also in the coplanar arrangement.

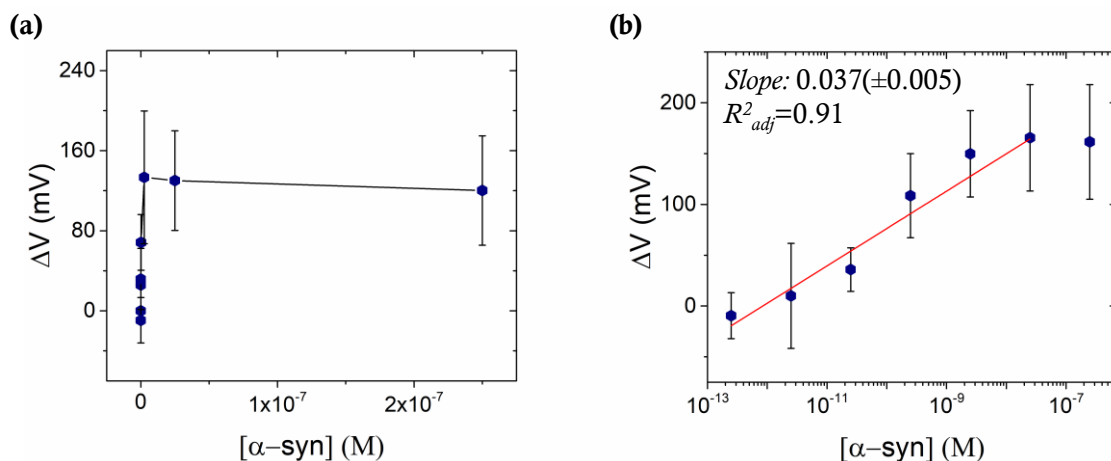


**Figure 2.38.** (a) Sensing response calculated as  $\Delta V$  vs  $\alpha$ -synuclein concentration (blue symbols). (b) Plot of the sensing response vs the log of  $\alpha$ -synuclein concentrations (0.25 pM, 2.5 pM, 25 pM, 250 pM, 2.5 nM, 25 nM, 250 nM) and the relatively linear fitting (red line). The error bars are relative to three different experiments.

In **Figure 2.39** transfer characteristics recorded with the RG electrode, before and after the sensing experiment, are shown, confirming the high stability of the device.

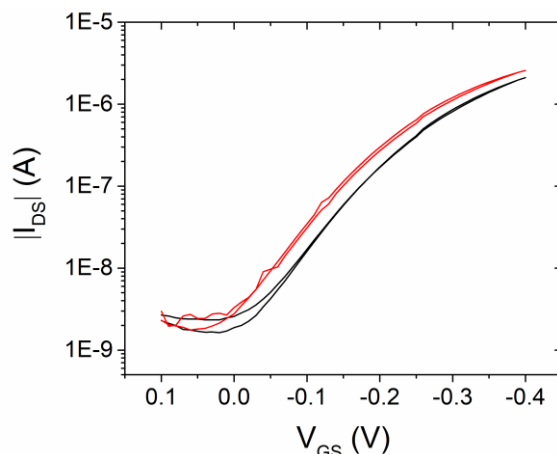


**Figure 2.39.**  $I$ - $V$  transfer characteristics recorded with the reference gate before the beginning of the sensing experiment (black curve) and at the end of the sensing experiment (red curve) at a constant  $V_{DS} = -0.1$  V. Electrolyte: PBS 0.01x, pH= 7.2.

- **Approach II based  $\alpha$ -synuclein sensing by coplanar gating and *in-situ* functionalization**

It is important to point out that microfluidics setup was also tested for Approach II. Unfortunately, it was not possible to reproduce the results obtained with the top-gated configuration as for Approach I. The hypothesis of a detachment of the protein due to the microfluidics flow was discarded based on the previous results achieved by SPR. As shown above, PG assembly resulted to be very stable under streaming, furthermore, the rate used was as low as 10  $\mu\text{L}/\text{min}$ . The main difference between top-gated configuration and the coplanar one relies on the operational window potential. In the former case, an almost entirely positive potential is applied on the gate. However, in the devices embedded in the microfluidics an entirely negative potential should be applied on the gate to operate the devices.

It is reported in literature that the potential applied on a surface, could promote conformational changes to the proteins adsorbed on top of it.<sup>55</sup> Thus, to give a deeper insight into the problem, capacitance measurements were performed, for both approaches, at negative and positive DC potentials. The results are presented in **Figure 2.40** as phase angle variation along with frequency scanning. Phase angle values indicate the behaviour of a metal/electrolyte interface. Specifically, when the phase angle is equal to  $90^\circ$  the interface can be considered as an ideal capacitor, when it is equal to  $0^\circ$  it behaves as a pure resistor, when it is in between, an intermediate situation

occurs.<sup>56</sup> In the case of Approach I, the SAM influences dramatically the interface behaviour. In fact, independently on the voltage applied a quasi-ideal capacitor is created. The deposition of the additional biological molecules on top of it apparently does not affect the interface. On the contrary, regarding Approach II, the character of the interface resulted not to be independent from the sign of the voltage applied. In fact, when a negative potential is used, at low frequencies, the phase angle almost reaches 0°. This resistive behaviour could be the reason of the irreproducibility of Approach II based sensing with the coplanar configuration. As mentioned above, the potential applied on the surface of the electrode can influence the proteins adsorbed on top of it, causing conformational changes. Furthermore, PG has a negative pI, so a negative voltage could cause a detachment of it from the surface. Anyway, the origin of this result needs further *ad hoc* investigation.

Concluding, it is conceivable that the negative operational window potential applied with the microfluidics setup is not compatible with Approach II, but it is still functional for Approach I.



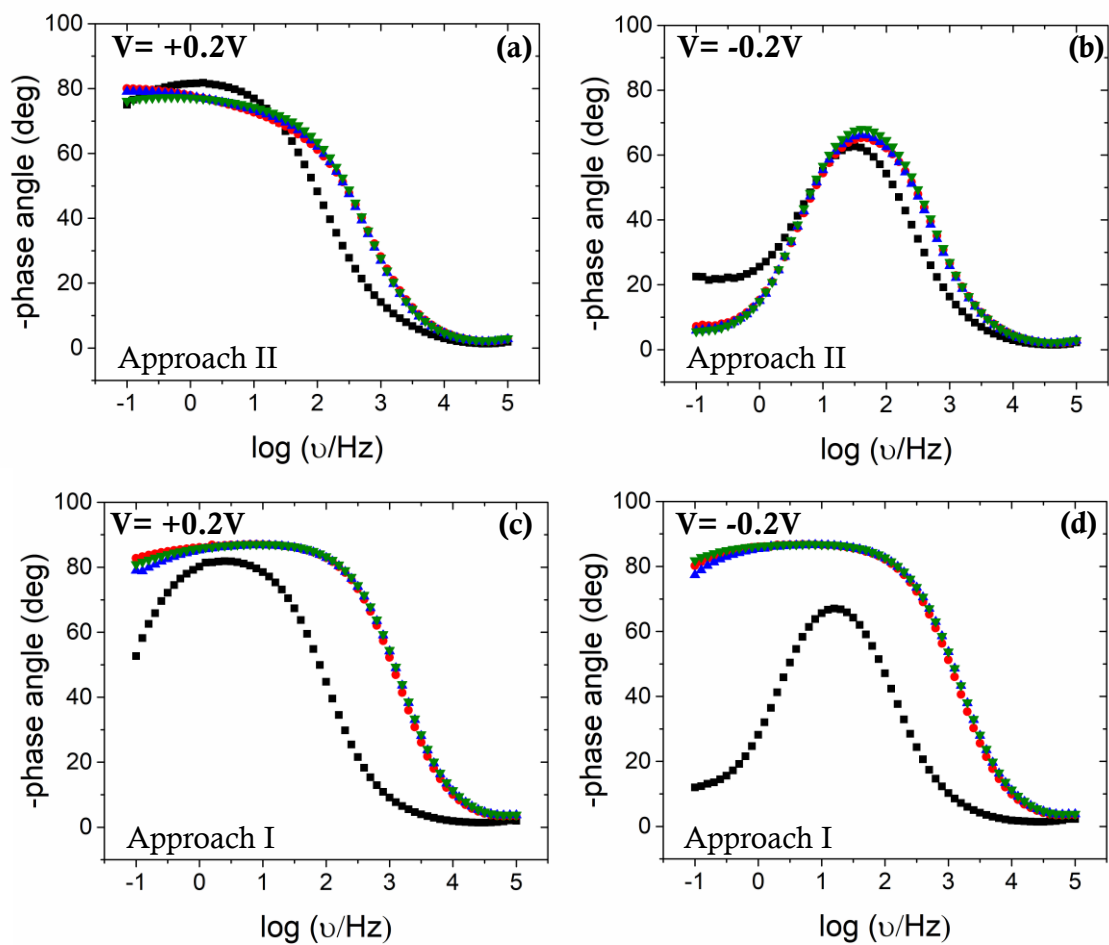


**Figure 2.40.** Bode plots: phase angle *vs* frequency. Three-electrode standard cell, Pt wire as the counter electrode, Ag/AgCl as the reference electrode, gold wire as the working electrode. Electrolyte: KCl 10 mM, PBS 50 mM at pH= 7.2. Black symbols: bare Au; red symbols: PG-coated Au in (a) and (b), HS-C<sub>11</sub>-EG<sub>6</sub>-NH<sub>2</sub>-coated Au in (c) and (d); Green symbols:  $\alpha$ -synuclein 25 nM. DC potentials set at +0.2 V in (a) and (c) and at -0.2 V in (b) and (d).

## 2.7. Summary

In summary, this chapter was focused on the design, study and development of a biosensor based on an electrolyte-gated field-effect transistor (EGOFET) for the detection of  $\alpha$ -synuclein, an important biomarker for neurodegenerative diseases such as Parkinson's disease. The optimum immuno-detection strategy based on anti- ( $\alpha$ - synuclein) monoclonal antibody was inferred by a comparative study of two surface functionalization routes of the gate electrode, referred to as Approach I and Approach II. Both showed similar sensitivities, namely  $21(\pm 2)$  mV/dec and  $-16(\pm 2)$  mV/dec respectively, and similar limit of detection (LOD) values, down at the sub-picomolar level. However, they exhibited different response range, that is to say, approach II had a wider range than approach I (*viz.* 0.25 pM - 250 nM versus 0.25 pM - 1 nM, respectively).

In a second step, a dual gate coplanar EGOFET in a microfluidic chamber was designed. The microfluidics layout has been conceived to avoid cross-contamination between the sensing gate and the active layer. Such methodology allowed us both the *in-situ* functionalization of the sensing gate and in-line electrical tests with reference solutions of  $\alpha$ -synuclein. Approach I was successfully tested, confirming the trend obtained with the top-gated configuration and displaying a slightly higher sensitivity, namely  $37(\pm 5)$  mV/dec and a LOD at the sub-picomolar level.

These devices showed excellent potential for the prognostics and diagnosis of *synucleinopathies* such as Parkinson's disease, and also can provide a promising label-free tool for gaining insights into the role of  $\alpha$ -synuclein and its aggregation mechanism, which is pivotal for a comprehensive understanding of such neurodegenerative diseases.

## Bibliography

- (1) World Alzheimer Report. *Alzheimer's Disease International* **2019**.
- (2) World Alzheimer Report. *Alzheimer's Disease International* **2015**.
- (3) Meade, R. M.; Fairlie, D. P.; Mason, J. M. Alpha-Synuclein Structure and Parkinson ' s Disease – Lessons and Emerging Principles. *Molecular Neurodegeneration* **2019**, *14*, 29.
- (4) Goedert, M.; Jakes, R.; Spillantini, M. G. The Synucleinopathies: Twenty Years On. *Journal of Parkinson's Disease* **2017**, *7*, S51–S69.
- (5) Atik, A.; Stewart, T.; Zhang, J. Alpha-Synuclein as a Biomarker for Parkinson's Disease. *Brain Pathology* **2016**, *26* (3), 410–418.
- (6) Zhang, R.; Wang, S.; Huang, X.; Yang, Y.; Fan, H.; Yang, F.; Li, J.; Dong, X.; Feng, S.; Anbu, P.; et al. Gold-Nanourchin Seeded Single-Walled Carbon Nanotube on Voltammetry Sensor for Diagnosing Neurogenerative Parkinson's Disease. *Analytica Chimica Acta* **2020**, *1094*, 142–150.
- (7) Khatri, A.; Punjabi, N.; Ghosh, D.; Maji, S. K.; Mukherji, S. Detection and Differentiation of Alpha-Synuclein Monomer and Fibril by Chitosan Film Coated Nanogold Array on Optical Sensor Platform. *Sensors and Actuators, B: Chemical* **2018**, *255*, 692–700.
- (8) Jensen, J.; Farina, M.; Zuccheri, G.; Grange, W.; Hegner, M. Quantitative, Label-Free Detection of the Aggregation of  $\alpha$ -Synuclein Using Microcantilever Arrays Operated in a Liquid Environment. *Journal of Sensors* **2012**, *2012*.
- (9) Taghdisi, S. M.; Danesh, N. M.; Nameghi, M. A.; Ramezani, M.; Alibolandi, M.; Hassanzadeh-Khayat, M.; Emrani, A. S.; Abnous, K. A Novel Electrochemical Aptasensor Based on Nontarget-Induced High Accumulation of Methylene Blue on the Surface of Electrode for Sensing of  $\alpha$ -Synuclein Oligomer. *Biosensors and Bioelectronics* **2019**, *123* (September 2018), 14–18.
- (10) Tinsley, R. B.; Kotschet, K.; Modesto, D.; Ng, H.; Wang, Y.; Nagley, P.; Shaw, G.; Horne, M. K. Sensitive and Specific Detection of  $\alpha$ -Synuclein in Human

- Plasma. *Journal of Neuroscience Research* **2010**, *88* (12), 2693–2700.
- (11) Gao, H.; Zhao, Z.; He, Z.; Wang, H.; Liu, M.; Hu, Z.; Cheng, O.; Yang, Y.; Zhu, L. Detection of Parkinson's Disease through the Peptoid Recognizing  $\alpha$ -Synuclein in Serum. *ACS Chemical Neuroscience* **2019**, *10* (3), 1204–1208.
- (12) Ng, A. S. L.; Tan, Y. J.; Lu, Z.; Ng, E. Y. L.; Ng, S. Y. E.; Chia, N. S. Y.; Setiawan, F.; Xu, Z.; Tay, K. Y.; Prakash, K. M.; et al. Plasma Alpha-Synuclein Detected by Single Molecule Array Is Increased in PD. *Annals of Clinical and Translational Neurology* **2019**, *6* (3), 615–619.
- (13) Preterre, C.; Corbillé, A. G.; Balloy, G.; Letournel, F.; Neunlist, M.; Derkinderen, P. Optimizing Western Blots for the Detection of Endogenous  $\alpha$ -Synuclein in the Enteric Nervous System. *Journal of Parkinson's Disease* **2015**, *5* (4), 765–772.
- (14) Kakuda, K.; Ikenaka, K.; Araki, K.; So, M.; Aguirre, C.; Kajiyama, Y.; Konaka, K.; Noi, K.; Baba, K.; Tsuda, H.; et al. Ultrasonication-Based Rapid Amplification of  $\alpha$ -Synuclein Aggregates in Cerebrospinal Fluid. *Scientific Reports* **2019**, *9* (1), 1–10.
- (15) El-Agnaf, O. M. A.; Salem, S. A.; Paleologou, K. E.; Curran, M. D.; Gibson, M. J.; Court, J. A.; Schlossmacher, M. G.; Allsop, D. Detection of Oligomeric Forms of  $\alpha$ -Synuclein Protein in Human Plasma as a Potential Biomarker for Parkinson's Disease. *FASEB Journal* **2006**, *20* (3), 419–425.
- (16) Sun, K.; Xia, N.; Zhao, L.; Liu, K.; Hou, W.; Liu, L. Aptasensors for the Selective Detection of Alpha-Synuclein Oligomer by Colorimetry, Surface Plasmon Resonance and Electrochemical Impedance Spectroscopy. *Sensors and Actuators, B: Chemical* **2017**, *245*, 87–94.
- (17) Macchia, E.; Manoli, K.; Holzer, B.; Di Franco, C.; Ghittorelli, M.; Torricelli, F.; Alberga, D.; Mangiatordi, G. F.; Palazzo, G.; Scamarcio, G.; et al. Single-Molecule Detection with a Millimetre-Sized Transistor. *Nature Communications* **2018**, *9* (1).
- (18) Casalini, S.; Leonardi, F.; Cramer, T.; Biscarini, F. Organic Field-Effect

- Transistor for Label-Free Dopamine Sensing. *Organic Electronics* **2013**, *14* (1), 156–163.
- (19) Kergoat, L.; Piro, B.; Berggren, M.; Horowitz, G.; Pham, M. C. Advances in Organic Transistor-Based Biosensors: From Organic Electrochemical Transistors to Electrolyte-Gated Organic Field-Effect Transistors. *Analytical and Bioanalytical Chemistry* **2012**, *402* (5), 1813–1826.
- (20) Charles A Janeway, J.; Travers, P.; Walport, M.; Mark J Shlomchik. *Immunobiology: The Immune System in Health and Disease. 5th Edition*; Garland Science: New York, 2001.
- (21) Pinalli, R.; Pedrini, A.; Dalcanale, E. Biochemical Sensing with Macrocyclic Receptors. *Chemical Society Reviews* **2018**, *47* (18), 7006–7026.
- (22) Oh, S. W.; Moon, J. D.; Lim, H. J.; Park, S. Y.; Kim, T.; Park, J. B.; Han, M. H.; Snyder, M.; Choi, E. Y. Calixarene Derivative as a Tool for Highly Sensitive Detection and Oriented Immobilization of Proteins in a Microarray Format through Noncovalent Molecular Interaction. *FASEB Journal* **2005**, *19* (10), 1335–1337.
- (23) Rodik, R. V; Boyko, V. I.; Kalchenko, V. I. Calixarenes in Bio-Medical Researches. *Current Medicinal Chemistry* **2009**, *16*, 1630–1655.
- (24) Nimse, S. B.; Kim, T. Biological Applications of Functionalized Calixarenes. *Chemical Society Reviews* **2013**, *42* (1), 366–386.
- (25) Chen, H.; Huang, J.; Lee, J.; Hwang, S.; Koh, K. Surface Plasmon Resonance Spectroscopic Characterization of Antibody Orientation and Activity on the Calixarene Monolayer. *Sensors and Actuators, B: Chemical* **2010**, *147* (2), 548–553.
- (26) Boozer, C.; Ladd, J.; Chen, S.; Jiang, S. DNA-Directed Protein Immobilization for Simultaneous Detection of Multiple Analytes by Surface Plasmon Resonance Biosensor. *Analytical Chemistry* **2006**, *78* (5), 1515–1519.
- (27) Jung, Y.; Jeong, M. L.; Jung, H.; Bong, H. C. Self-Directed and Self-Oriented Immobilization of Antibody by Protein G-DNA Conjugate. *Analytical Chemistry* **2007**, *79* (17), 6534–6541.

- (28) Bailey, R. C.; Kwong, G. A.; Radu, C. G.; Witte, O. N.; Heath, J. R. DNA-Encoded Antibody Libraries: A Unified Platform for Multiplexed Cell Sorting and Detection of Genes and Proteins. *Journal of the American Chemical Society* **2007**, *129* (7), 1959–1967.
- (29) Wacker, R.; Schröder, H.; Niemeyer, C. M. Performance of Antibody Microarrays Fabricated by Either DNA-Directed Immobilization, Direct Spotting, or Streptavidin-Biotin Attachment: A Comparative Study. *Analytical Biochemistry* **2004**, *330* (2), 281–287.
- (30) Chen, X.; Zhou, G.; Song, P.; Wang, J.; Gao, J.; Lu, J.; Fan, C.; Zuo, X. Ultrasensitive Electrochemical Detection of Prostate-Specific Antigen by Using Antibodies Anchored on a DNA Nanostructural Scaffold. *Analytical Chemistry* **2014**, *86* (15), 7337–7342.
- (31) Harder, P.; Grunze, M.; Dahint, R.; Whitesides, G. M.; Laibinis, P. E. Molecular Conformation in Oligo(Ethylene Glycol)-Terminated Self-Assembled Monolayers on Gold and Silver Surfaces Determines Their Ability To Resist Protein Adsorption. *The Journal of Physical Chemistry B* **2002**, *102* (2), 426–436.
- (32) Hayashi, T.; Tanaka, Y.; Koide, Y.; Tanaka, M.; Hara, M. Mechanism Underlying Bioinertness of Self-Assembled Monolayers of Oligo(Ethyleneglycol)-Terminated Alkanethiols on Gold: Protein Adsorption, Platelet Adhesion, and Surface Forces. *Physical Chemistry Chemical Physics* **2012**, *14* (29), 10196–10206.
- (33) Atkins; Overton; Rourke; Weller; Armstrong. *Shriver and Atkin's Inorganic Chemistry, Fifth Edition*; 2010.
- (34) Widrig, C. A.; Chung, C.; Porter, M. D. The Electrochemical Desorption of N-Alkanethiol Monolayers from Polycrystalline Au and Ag Electrodes. *Journal of Electroanalytical Chemistry* **1991**, *310* (1–2), 335–359.
- (35) Gorman, C. B.; Williams, J. A. Alkanethiol Reductive Desorption from Self-Assembled Monolayers on Gold, Platinum, and Palladium Substrates. *Journal*

- of Physical Chemistry C* **2007**, *111* (34), 12804–12810.
- (36) Andrade, J. D. Surface and Interfacial Aspects of Biomedical Polymers. *Surface and Interfacial Aspects of Biomedical Polymers* **1985**.
- (37) Bourg, M. C.; Badia, A.; Bruce Lennox, R. Gold-Sulfur Bonding in 2D and 3D Self-Assembled Monolayers: XPS Characterization. *Journal of Physical Chemistry B* **2000**, *104* (28), 6562–6567.
- (38) Melitz, W.; Shen, J.; Kummel, A. C.; Lee, S. Kelvin Probe Force Microscopy and Its Application. *Surface Science Reports* **2011**, *66* (1), 1–27.
- (39) Tudos, A. J.; Schasfoort, R. B. M. *Handbook of Surface Plasmon Resonance*; Royal Society of Chemistry, 2008.
- (40) Daghestani, H. N.; Day, B. W. Theory and Applications of Surface Plasmon Resonance, Resonant Mirror, Resonant Waveguide Grating, and Dual Polarization Interferometry Biosensors. *Sensors* **2010**, *10*, 9630–9646.
- (41) Zhang, Q.; Leonardi, F.; Casalini, S.; Temiño, I.; Mas-Torrent, M. High Performing Solution-Coated Electrolyte-Gated Organic Field-Effect Transistors for Aqueous Media Operation. *Scientific Reports* **2016**, *6* (November), 1–10.
- (42) Leonardi, F.; Casalini, S.; Zhang, Q.; Galindo, S.; Gutiérrez, D.; Mas-Torrent, M. Electrolyte-Gated Organic Field-Effect Transistor Based on a Solution Sheared Organic Semiconductor Blend. *Advanced Materials* **2016**, *28* (46), 10311–10316.
- (43) Temiño, I.; Del Pozo, F. G.; Ajayakumar, M. R.; Galindo, S.; Puigdollers, J.; Mas-Torrent, M. A Rapid, Low-Cost, and Scalable Technique for Printing State-of-the-Art Organic Field-Effect Transistors. *Advanced Materials Technologies* **2016**, *1* (5), 1–7.
- (44) Del Pozo, F. G.; Fabiano, S.; Pfattner, R.; Georgakopoulos, S.; Galindo, S.; Liu, X.; Braun, S.; Fahlman, M.; Veciana, J.; Rovira, C.; et al. Single Crystal-like Performance in Solution-Coated Thin-Film Organic Field-Effect Transistors. *Advanced Functional Materials* **2016**, *26* (14), 2379–2386.
- (45) Pérez-Rodríguez, A.; Temiño, I.; Ocal, C.; Mas-Torrent, M.; Barrena, E.

- Decoding the Vertical Phase Separation and Its Impact on C8-BTBT/PS Transistors Properties. *ACS Applied Materials & Interfaces* **2018**, *10*, 7296–7303.
- (46) Paterson, A. F.; Treat, N. D.; Zhang, W.; Fei, Z.; Wyatt-Moon, G.; Faber, H.; Vourlias, G.; Patsalas, P. A.; Solomeshch, O.; Tessler, N.; et al. Small Molecule/Polymer Blend Organic Transistors with Hole Mobility Exceeding  $13 \text{ cm}^2 \text{ V}^{-1} \text{ s}^{-1}$ . *Advanced Materials* **2016**, *28* (35), 7791–7798.
- (47) Campos, A.; Riera-Galindo, S.; Puigdollers, J.; Mas-Torrent, M. Reduction of Charge Traps and Stability Enhancement in Solution-Processed Organic Field-Effect Transistors Based on a Blended n-Type Semiconductor. *ACS Applied Materials and Interfaces* **2018**, *10* (18), 15952–15961.
- (48) Ward, J. W.; Loth, M. A.; Kline, R. J.; Coll, M.; Ocal, C.; Anthony, E.; Jurchescu, O. D. Tailored Interfaces for Self-Patterning Organic Thin-Film Transistors. *Journal of Materials Chemistry* **2012**, *22*, 19047–19053.
- (49) Melzer, K.; Br, M.; Popescu, B.; Popescu, D.; Lugli, P.; Scarpa, G. Characterization and Simulation of Electrolyte-Gated Organic Field-Effect Transistors. *Faraday Discussions* **2014**, *174*, 399–411.
- (50) Ishikawa, F. N.; Curreli, M.; Chang, H.; Chen, P.; Zhang, R.; Cote, R. J.; Thompson, M. E.; Zhou, C. A Calibration Method for Nanowire Biosensors to Suppress Device-to-Device Variation. *ACS Nano* **2009**, *3* (12), 3969–3976.
- (51) Duan, X.; Li, Y.; Rajan, N. K.; Routenberg, D. A.; Modis, Y.; Reed, M. A. Quantification of the Affinities and Kinetics of Protein Interactions Using Silicon Nanowire Biosensors. *Nature Nanotechnology* **2012**, *7* (6), 401–407.
- (52) Lee, B. Y.; Sung, M. G.; Lee, J.; Baik, K. Y.; Kwon, Y. K.; Lee, M. S.; Hong, S. Universal Parameters for Carbon Nanotube Network-Based Sensors: Can Nanotube Sensors Be Reproducible? *ACS Nano* **2011**, *5* (6), 4373–4379.
- (53) Cramer, T.; Campana, A.; Leonardi, F.; Casalini, S.; Kyndiah, A.; Murgia, M.; Biscarini, F. Water-Gated Organic Field Effect Transistors – Opportunities for Biochemical Sensing and Extracellular Signal Transduction. *Journal of Materials Chemistry B* **2013**, *1*, 3728–3741.



- (54) Wilbur, J. L.; Whitesides, G. M.; Kumar, A.; Biebuyck, H. A.; Kim, E. Microcontact Printing of Self-Assembled Monolayers: Applications in Microfabrication. *Nanotechnology* **2002**, 7 (4), 452–457.
- (55) Ghisellini, P.; Caiazzo, M.; Alessandrini, A.; Eggenhöfner, R.; Vassalli, M.; Facci, P. Direct Electrical Control of IgG Conformation and Functional Activity at Surfaces. *Nature Publishing Group* **2016**, 6, 3–10.
- (56) Bard, A. J.; Faulkner, L. R. *Electrochemical Methods. Fundamentals and Applications*; 2001.

# CHAPTER 3

## *Organic Electrochemical Transistors: $\alpha$ -synuclein immunosensing\**

---

### 3.1. Introduction

Organic Electrochemical Transistors (OECTs) were developed consequently to the discover of conductive polymers by *Wrighton* and colleagues in the mid-1980s,<sup>1</sup> and they have gained a lot of interest recently, especially in the field of bioelectronics.

- **Conductive polymers: special focus on PEDOT:PSS**

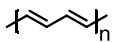
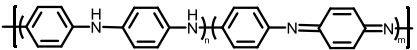
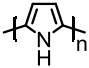
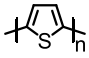
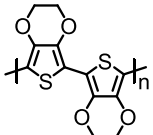
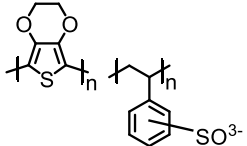
In 2000 three scientists, Hideki Shirakawa, Alan Heeger and Alan MacDiarmid were awarded the Noble Prize for their pioneering study and discovery of a new class of materials, intrinsic conducting polymers.<sup>2</sup> Indeed, before their work, polymers were known for their insulating properties. Conductive polymers (CPs) exhibit good electrical conductivity along with mechanical properties typical of plastics.<sup>3</sup> For these reasons, the field of CPs has been exploited in different fields, among them OFETs,<sup>4-6</sup> LEDs,<sup>7,8</sup> solar cells,<sup>9</sup> electrochromic displays<sup>10</sup> and sensors.<sup>11</sup>

---

\*This work was carried out in collaboration with Dr. Simone Fabiano, Dr. Valerio Beni and Chiara Diacci during a three-months secondment at Linköping University, in the Laboratory of Organic Electronics.

The ability to conduct current is given by the presence of conjugated double bonds throughout the polymeric chain coupled by the presence of dopants, usually oxidizing (*p*-dopant) or reducing (*n*-dopants) agents, which generate free charge carriers through the  $\pi$ -backbone of the polymer. The main conductive polymers studied up to now along with their main characteristics are summarized in **Table 3.1**.<sup>11-14</sup>

**Table 3.1.** Main conductive polymers.

Name and structure	Characteristics
<p style="text-align: center;"><b>Polyacetylene</b></p> 	$10^4$ - $10^5$ S cm <sup>-1</sup>
<p style="text-align: center;"><b>Polyaniline (PANI)</b></p> 	$30$ - $200$ S cm <sup>-1</sup> Doping: <i>n</i> , <i>p</i>
<p style="text-align: center;"><b>Polypyrrole</b></p> 	$10$ - $7.5 \cdot 10^3$ S cm <sup>-1</sup> Doping: <i>p</i>
<p style="text-align: center;"><b>Polythiophene</b></p> 	$10$ - $10^3$ S cm <sup>-1</sup> Doping: <i>p</i>
<p style="text-align: center;"><b>Poly(3,4-ethylenedioxythiophene)</b></p> 	$0.4$ - $400$ S cm <sup>-1</sup> Doping: <i>n</i> , <i>p</i>
<p style="text-align: center;"><b>PEDOT:PSS</b></p> 	Up to $4600$ S cm <sup>-1</sup> Doping: <i>p</i>

Poly(3,4-ethylenedioxythiophene), abbreviated as PEDOT was developed for the first time in the Bayer AG research laboratories in the second half of the 1980s.<sup>15</sup> The polymer exhibited interesting features, such as high conductivity, up to  $300 \text{ S}\cdot\text{cm}^{-1}$ , and stability in its oxidized form, but very poor solubility. The solubility issue was overcome by employing a water-soluble polyelectrolyte dopant, namely poly(styrene sulfonic acid), PSS.<sup>16</sup> Poly(3,4-ethylenedioxythiophene):poly(styrenesulfonate), PEDOT:PSS, is the most explored conductive polymer at the moment, because of its outstanding properties, such as stability, flexibility, high conductivity, compatibility with solution-processing techniques, along with commercial availability.<sup>16,17</sup> PEDOT:PSS has become the key polymeric conductor for the fabrication of Organic Electrochemical Transistors, OEETs.<sup>18,19</sup>

- **OEETs: applications in bioelectronics**

Due to the operating principle of this kind of devices combined with their properties (*i.e.*, low-cost processability, high stability, low-voltage operating, inherent flexibility of the materials employed, etc.) the development of OEET in the bioelectronics field has attracted a lot of attention in the last few years.<sup>20-25</sup>

They have been employed in electrophysiology to record cell activity in electrically active tissues and organs.<sup>26,27</sup> For instance, *in vivo* recording of brain activity with an OEET was demonstrated in 2013, achieving a better signal-to-noise ratio compared to the standard probes, due to the intrinsic amplification of the transistor.<sup>28</sup> Cutaneous applications have been explored for the recording of an electrocardiogram, by placing the device directly in contact with human skin, thanks to their inherent flexibility.<sup>29</sup> OEETs have been employed not only to detect electrical signals from cells but also to monitor cell coverage. By growing a monolayer of cells on top of the active layer, a physical barrier is created and the ions penetration is hampered, promoting, in turn, a modification on the source-drain current.<sup>30</sup> Furthermore, enzymatic biosensors have been developed and employed for the detection of electroactive metabolites, thanks to the ability of OEETs to amplify the ionic signals originating by enzymatic events into electronic signals.<sup>20,31-33</sup>

The OECTs have been studied, albeit to a less extent, for the sensing of non-electroactive molecules, such as for the detection of DNA,<sup>34</sup> bacteria<sup>35</sup> and as immunosensors.<sup>36,37</sup> *Macchia* and collaborators claimed the development of an OECT sensor for the detection of immunoglobulin G (IgG) in solution, reaching the femtomolar limit of detection (LOD).<sup>36</sup> The gold gate electrode was functionalized with anti-IgG antibodies as the biorecognition platform. Further, the work by *Gentili* and co-workers demonstrated the label-free detection of interleukin-6 (IL-6) with an OECT device, through antibody-antigen recognition.<sup>37</sup> Also in this study the gold gate acted as the sensing platform, in which anti-IL-6 antibodies were immobilized (**Figure 3.1**). Upon the functionalization of the gold gate, the source-drain current modulation decreased. This behaviour was ascribed to a decrease of the electrical double-layer capacitance at the gate/electrolyte interface, due to the increase of the double-layer thickness.

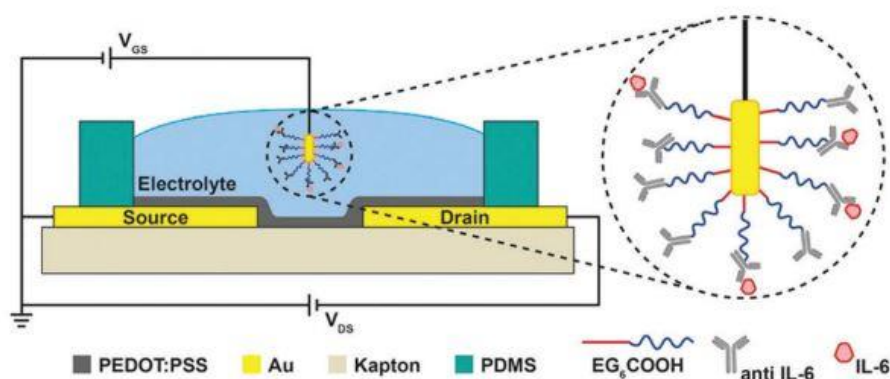


**Figure 3.1.** Scheme of the gate biofunctionalization for the detection of IL-6, extracted from ref. 37.

However, due to the volumetric capacitance of the active layer in OECT devices, the sensing of non-electroactive molecules, including immunosensing, has been less exploited. It has been claimed, indeed, that they display less sensitivity with respect to other liquid-gated transistors such as EGOFETs, in potentiometric based sensing.<sup>38</sup>

In this chapter, an OECT immunosensor for the detection of  $\alpha$ -synuclein is conceived, to give a further contribution in this field. It has been reported that, at physiological concentrations, which is estimated to be approximately 70 pM in the cerebrospinal fluid (CSF), this protein protects neurons against toxic insults.<sup>39</sup> But, when its expression level increases up to the  $\mu$ M range, it exerts a cytotoxic effect on

neurons, originating neurodegenerative disorders, known as *synucleopathies*.<sup>39</sup> However, the pathological role of this protein is under investigation yet, and in literature there is confusing information about the concentration ranges which discriminate between physiological and pathological conditions, due also to the lack of reliable ultra-sensitive biosensors for  $\alpha$ -synuclein.<sup>40-43</sup>

### 3.2. Objectives

In this chapter the attention is focused on the fabrication and characterization of Organic Electrochemical Transistors based on PEDOT:PSS conductive polymer, aiming at the study and development of a diagnostic tool for  $\alpha$ -synuclein risk level detection. To achieve that, the following sub-objectives were planned:

1. Design and electrochemical characterization of the  $\alpha$ -synuclein capturing platform, by grafting the anti-( $\alpha$ -synuclein) antibody on a Au surface, through a mixed alkylthio-based Self-Assembled Monolayer.
2. Study of the OECT devices response upon Au gate bio-functionalization. Two strategies were conceived: i) *in-situ* antigen binding under *real-time* current monitoring, ii) *ex-situ* gate modification and subsequent *I-V* transfer measurements.

### 3.3. OECTs microfabrication and characterization

The first part of the work consisted in the microfabrication of the OECTs. A summarized scheme of the fabrication protocol is illustrated in **Figure 3.2** and **Figure 3.3**. More details are reported in the experimental section (chapter 6). Devices were manufactured on polyethylene naphthalate (PEN, 125  $\mu\text{m}$  thick). First of all, the gold electrode contacts were patterned. For this aim, 50 nm of Au were evaporated by physical vapour deposition (PVD) technique. Afterwards, a photolithography process followed by wet etching of the metals with a solution of  $\text{I}_2/\text{KI}$  defined the electrodes pattern, which included the S, D and the coplanar G electrodes (**Figure 3.2**). The area of the gate electrode was equal to 0.25  $\text{mm}^2$ , while the channel length was equal to 20  $\mu\text{m}$  and the channel width to 100  $\mu\text{m}$ . Importantly, the gate area was 100 or 250 times larger with respect to the channel length in order to guarantee an appropriate gating of the device.

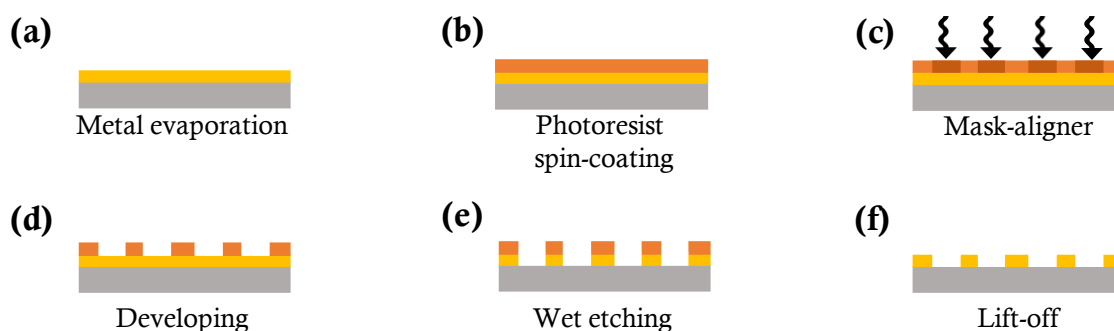


**Figure 3.2.** Gold contact patterning scheme. (a) Cr (2 nm) and Au (50 nm) evaporation on a PEN substrate; (b) Spin-coating of a positive photoresist; (c) Laser exposure with mask-aligner; (d) Exposed photoresist developing; (e) Wet etching of Au and Cr. (f) Removal of unexposed photoresist with acetone rinsing.

Once gold contacts were fabricated, a formulation of PEDOT:PSS was spin-coated and subsequently annealed at 110  $^{\circ}\text{C}$  for 2 h. In the PEDOT:PSS formulation ethylene glycol (EG, 5% v/v) and 3-glycidyloxypropyl (GOPS, 0.5% v/v) were added to increase its conductivity<sup>44</sup> and to cross-link the polymer chain,<sup>45</sup> improving its resistance to delamination when exposed to liquid media,<sup>18</sup> respectively. Then, a second photolithography process was carried out, to pattern the conductive layer only in the region between S and D electrodes and on top of the coplanar Au gate (**Figure 3.3**).

Finally, gold contact electrodes were protected by the deposition of an encapsulation layer, made of SU-8, which is an epoxy-based negative photoresist. The patterning of the encapsulation layer was performed by another photolithography process and it is needed to ensure that no liquid is in contact with gold electrodes during the operation of the device.

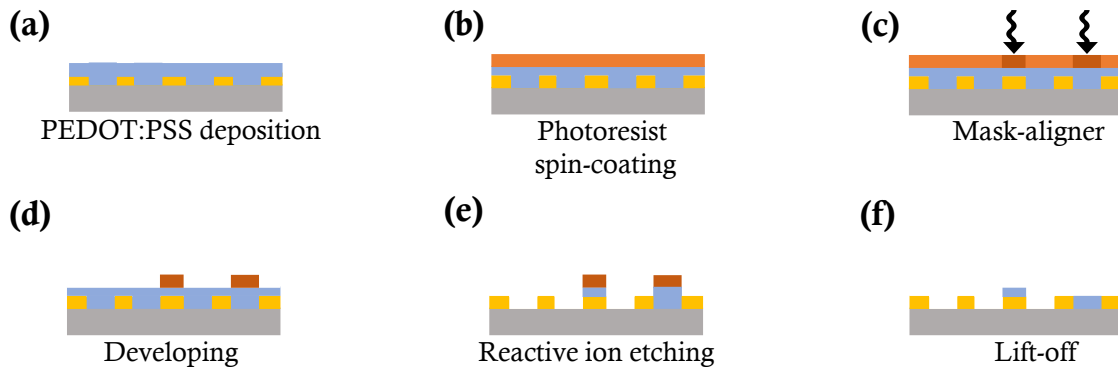


**Figure 3.3.** OECT microfabrication scheme. (a) PEDOT:PSS spin-coating and subsequent 2 h annealing at 110 °C; (b) Positive photoresist spin-coating; (c) Laser exposure with mask-aligner; (d) Exposed photoresist developing; (e) PEDOT:PSS dry etching; (f) Residual photoresist removal by acetone rinsing.

In **Figure 3.4** the final layout obtained is shown.

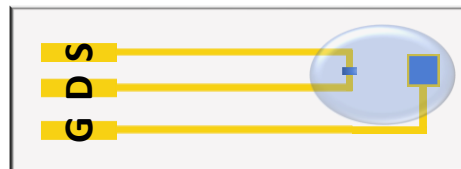


**Figure 3.4.** Scheme of the final device obtained. PEDOT:PSS layer is represented by the blue coloured zone, between S and D electrodes and on top of G electrode.

Once the devices were fabricated, electrical characterization was carried out, in order to assess the operating potential window of the transistor. Electrical measurements were performed employing the PEDOT:PSS gate and the Au gate (disk,  $\varnothing = 1.6$  mm). OECTs can operate in Faradaic regime, when the oxidative de-doping of the conducting layer is coupled to a reduction occurring at the gate electrode, or in non-Faradaic regime, *i.e.* capacitive regime, when de-doping is coupled to the



formation of an electrical-double layer at the gate/electrolyte interface.<sup>46,47</sup> The predominance of one of these regimes depends in particular on the gate composition. Au electrode is a polarizable electrode, thus, a double-layer is formed at the interface with the electrolyte. On the other hand, PEDOT:PSS gate/electrolyte interface behaves as a supercapacitor, that is to say, upon the application of a potential, electron transfer processes occur, accompanied by a potential-dependent change of the oxidation state that produces a capacitive effect.<sup>47</sup> As explained above, in fact, PEDOT:PSS manifests a volumetric capacitance, which is formed not only at the interface but also in the entire bulk of the material.<sup>19,47</sup>

Taking in mind this, in **Figure 3.5** and **Figure 3.6** the electrical characterization of the OECT is reported, using both the PEDOT:PSS gate and gold gate, respectively. The measurements were carried out by placing a PDMS pool on the region of the channel and coplanar PEDOT:PSS gate and adding inside a drop of the electrolyte solution, as it is shown in the insets of the figures. For the gold gate, a gold disk electrode was immersed into the electrolyte solution. Phosphate buffer saline (PBS) solutions at neutral pH and increasing concentrations, namely 1 mM (PBS 0.01x), 10 mM (PBS 0.1x) and 100 mM (PBS 1x) were used as the electrolyte to assess the effect of the ion concentration on the  $I_{DS}$  modulation. In these figures, the  $I$ - $V$  transfer characteristics are reported along with the plot of the transconductance,  $g_m$ , which is the main figure of merit of OECT devices. Also, the gate current plot as a function of the  $V_{GS}$  is shown, in order to figure out what processes are happening in the gate. The device switches off when a positive gate voltage is applied and starts to turn on when a more negative gate voltage is applied since the conductive layer is doped.

The devices display the same current modulation and also a similar value of maximum  $g_m$  with both kinds of gate electrodes. However, it is worth noting how the dependence of the ion concentration on  $I_{DS}$  is found only when PEDOT:PSS gate is employed. This is coherent with the volumetric capacitance of PEDOT:PSS, both at the active layer/electrolyte interface and the gate/electrolyte interface. On the contrary, when Au gate is employed, only double-layer charging is occurring at the gate interface, so the drain current modulation is not affected by ions concentration, but only by the potential drop occurring at the gate. Looking at the gate currents, it is difficult to say if faradaic and/or capacitive processes are occurring.

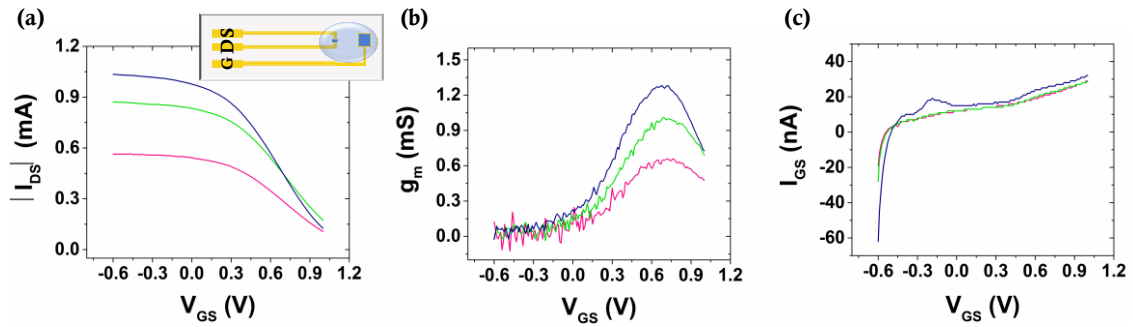


**Figure 3.5.** Electrical characterization employing PEDOT:PSS gate. (a)  $I$ - $V$  transfer characteristics recorded sweeping  $V_{GS}$  from  $-0.6$  V to  $+1$  V at a constant  $V_{DS} = -0.5$  V. (b) Transconductance plots at a constant  $V_{DS} = -0.5$  V; (c) Gate currents plots at a constant  $V_{DS} = -0.5$  V. Measurements were recorded in PBS solution (pH= 7.2) at different concentrations: PBS 0.01x (pink curves), PBS 0.1x (green curves), PBS 1x (blue curves).

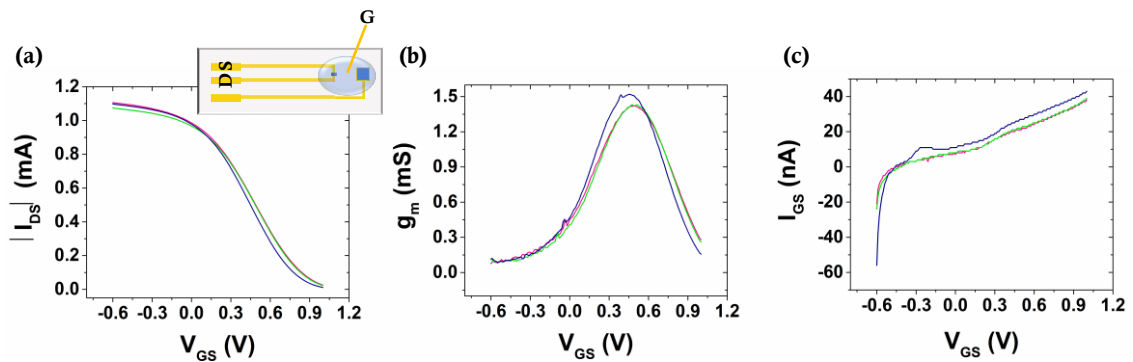


**Figure 3.6.** Electrical characterization employing Au gate. (a)  $I$ - $V$  transfer characteristics recorded sweeping  $V_{GS}$  from  $-0.6$  V to  $+1$  V at a constant  $V_{DS} = -0.5$  V. (b) Transconductance plots at a constant  $V_{DS} = -0.5$  V; (c) Gate currents plots at a constant  $V_{DS} = -0.5$  V. Measurements were recorded in PBS solution (pH= 7.2) at different concentrations: PBS 0.01x (pink curves), PBS 0.1x (green curves), PBS 1x (blue curves).

Along with transfer characteristics, also output measurements were recorded and are shown in **Figure 3.7**. The device exhibits the same  $p$ -type behaviour with both electrodes, but the gold gate electrode demonstrated to be more efficient in modulating the drain current.

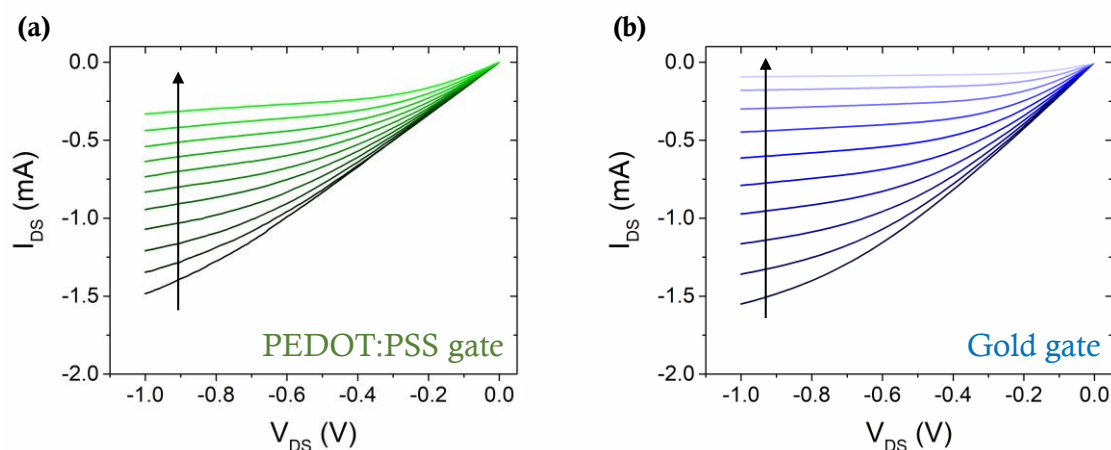


**Figure 3.7.** Output characteristics recorded in PBS 0.1x by sweeping  $V_{DS}$  from 0 V to -1 V at constant  $V_{GS}$ : 0 V, 0.1 V, 0.2 V, 0.3 V, 0.4 V, 0.5 V, 0.6 V, 0.7 V, 0.8 V, 0.9 V, 1 V, according to the arrows in the graphs. (a) PEDOT:PSS gate was employed; (b) Au disk gate was used.

### 3.4. Sensing platform design and electrochemical characterization

The sensing platform of the designed  $\alpha$ -synuclein biosensor relies on the Au gate of the OECT device. To sense  $\alpha$ -synuclein it was decided to employ the anti-( $\alpha$ -synuclein) antibody (Ab), as in the case of the previously reported EGOFET-based immunosensor, since this approach resulted to be successful. However, it was decided to avoid the use of large molecules for grafting the Ab onto the surface, such as protein G or long alkylthiols, in order to have the biomolecules as close as possible to the double-layer formed at the gate/electrolyte interface. For this reason, the formation of self-assembled monolayers (SAMs) of 8-amino-1-octanethiol ( $\text{HS-C}_8\text{-NH}_2$ ) on the gold gate electrode were selected to functionalise it with the Ab. The thiol moiety is required for the binding with Au surface, whereas the amino functionality is needed for the binding of the Ab, upon its activation with glutaraldehyde (Gl).

For the surface Ab immobilization, it was also decided to form a mixed SAM, to homogenise the Abs distribution on the surface. The use of mixed SAMs for Ab grafting was already reported in literature.<sup>37,48</sup> For this aim, 6-mercapto-1-hexanol ( $\text{HS-C}_6\text{-OH}$ ) was chosen, because it has a slightly shorter alkyl chain with respect to  $\text{HS-C}_8\text{-NH}_2$ , and it has an alcoholic termination which is unreactive towards Gl. Repulsion of terminal groups, especially when they can bear a charge, as in the case of

amino-groups, cause a not optimal packing of the SAM. Thus, employing a second thiol molecule, with different alkyl chain length and with a different terminal moiety, allows a better-organized SAM formation, achieving a sensing platform with a higher recognition capacity due to a less steric hindrance of the Abs on the surface. Three different mixing ratios were tested:  $[\text{HS-C}_8\text{-NH}_2]:[\text{HS-C}_6\text{-OH}]$  1:1, 1:10 and 1:100.

In **Figure 3.8** the Au surface modification steps carried out are illustrated. Thiols solution were prepared in EtOH at 1 mM concentrations and, subsequently, mixed to obtain the desired ratio. Au disk electrode was incubated overnight at 4 °C in order to achieve a good coverage. Gl was used to cross-link the amino group of the thiols with a primary amine of the Ab backbone, as previously explained. The Ab immobilization was carried out by dipping the electrode in a 10  $\mu\text{g}/\text{mL}$  Ab solution in PBS 1x, for 1 h at R.T. Finally, to deactivate the unreacted glutaraldehyde groups, the Ab-coated Au disk was immersed in a 2-Amino-2-hydroxymethyl-propane-1,3-diol solution (TRIS buffer at physiological pH), for 15 minutes at R.T.

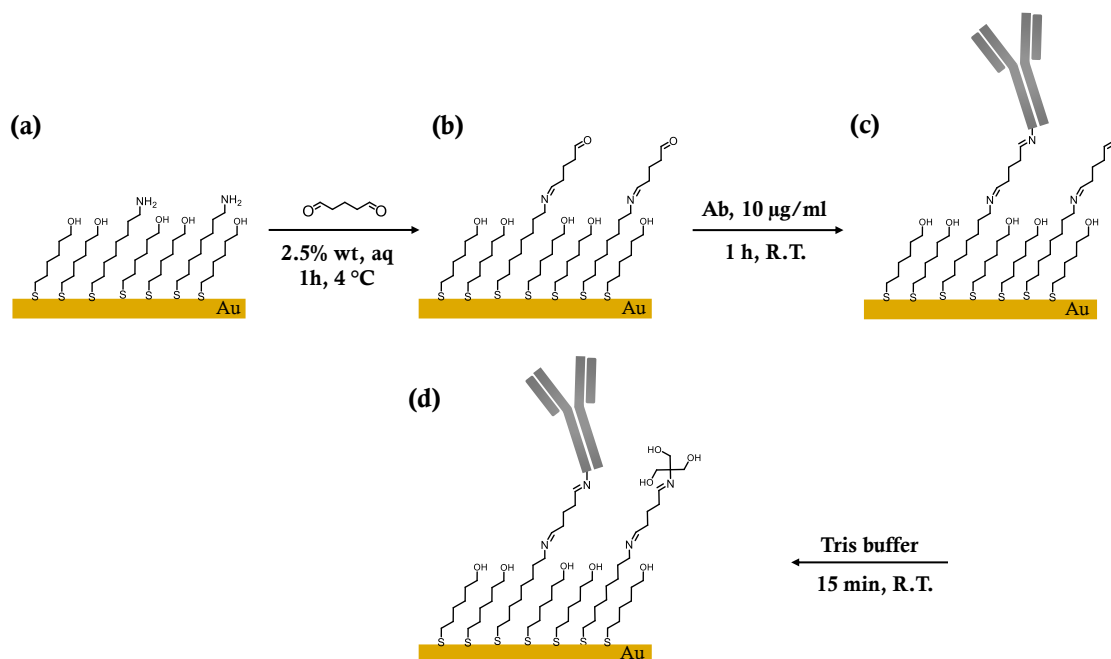


**Figure 3.8.** Sensing platform preparation steps: (a) SAM formation, (b) amino group activation by Gl, (c) Ab grafting and (d) unreacted Gl moieties deactivation.

The correct immobilization of the Abs on the Au surface and the subsequent response of the Ab-coated Au surface towards  $\alpha$ -synuclein were assessed by electrochemistry (*i.e.*, DPV and EIS), aiming also at selecting the best mixing ratio of the SAM for an optimal response. The Ab-coated Au disk was immersed in 500 nM  $\alpha$ -synuclein solution in PBS 1x at physiological pH for 1 h at R.T. The obtained results are reported in **Figure 3.9**.

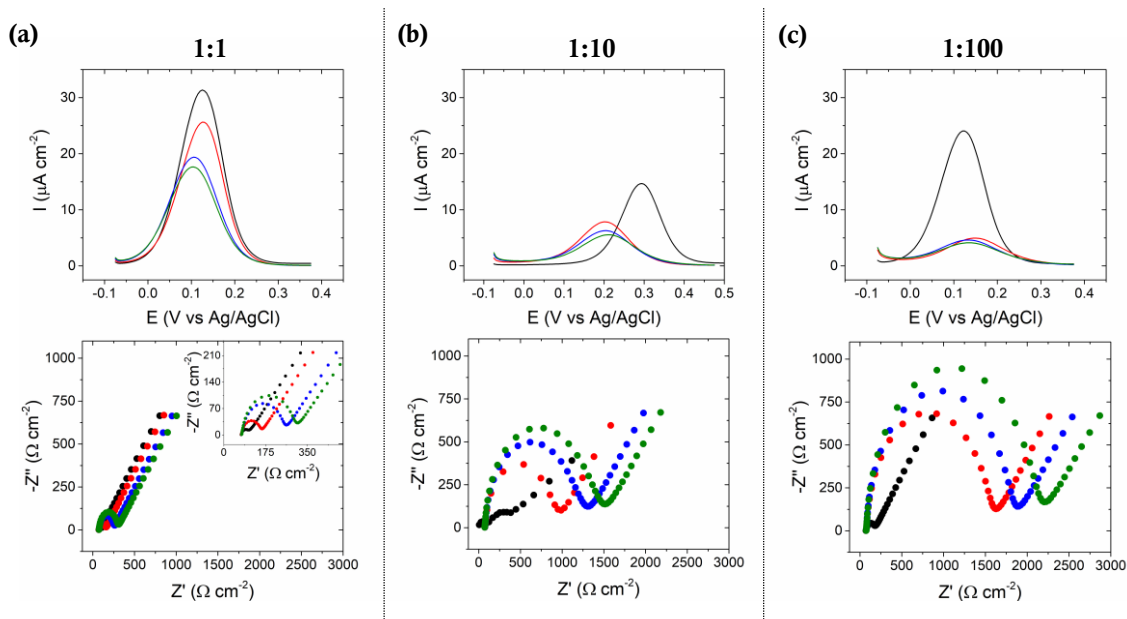


**Figure 3.9.** Electrochemical characterization of the sensing platform. On the top part of the figure, DPV is reported and on the bottom EIS measurements. SAM mixing  $[\text{HS-C}_8\text{-NH}_2]:[\text{HS-C}_6\text{-OH}]$  ratio is equal to (a) 1:1, (b) 1:10, (c) 1:100. Black curves refer to pristine Au, red curves to SAM-coated Au, blue curves to Ab-SAM-coated Au and green curves to  $\alpha$ -synuclein (500 nM) detection step. Three-electrode cell was employed: Pt wire as the counter electrode, Ag/AgCl as the reference electrode and Au disk as the working electrode. Electrolyte: 50 mM sodium phosphate salt, 100 mM KCl and 5 mM  $\text{K}_3[\text{Fe}(\text{CN})_6]$ , at pH= 7.2. For EIS analysis DC potential was set to the open circuit potential (OCP).

In all cases, a decrease of the current and an increase of the impedance signal is registered for each functionalization step of the Au electrode, suggesting a correct immobilization of the biomolecules. However, the degree of Au coverage appears to be slightly different in the case of the 1:1 mixing ratio SAM, compared to the 1:10 or 1:100 ones. Charge transfer resistance,  $R_{ct}$ , was evaluated by fitting the Nyquist plots by the *Randles* circuit (chapter 6 contains a detailed description of the method), aiming at having a more quantitative assessment. Regarding the 1:1 case,  $R_{ct}$  moves from 30  $\Omega$  for pristine Au to 80  $\Omega$  for SAM-coated Au, whereas  $R_{ct}$  moves from above 150  $\Omega$  for

pristine Au to 850  $\Omega$  and from 100  $\Omega$  for pristine Au to 1500  $\Omega$ , for 1:10 and 1:100 SAM mixing ratios, respectively. In the case of 1:1 mixing ratio, more SH-C<sub>8</sub>-NH<sub>2</sub> molecules are supposed to be present on the surface, bearing bulky amino groups which increase the disorganization of the SAM. Furthermore, as it has been assessed in the case of HS-C<sub>11</sub>-EG<sub>6</sub>-NH<sub>2</sub> molecules in the previous thesis chapter, at physiological pH some amino groups bear a positive charge. For these reasons, the SAM formed at 1:1 mixing ratio is probably less packed and more disordered with respect to the 1:10 and 1:100 mixed SAMs due to the higher amount of the bulky and positively charged amino groups, which makes the surface more accessible to the negative redox probe employed in the experiment. Thus, a combination of both factors, *i.e.*, less packed SAM and overall positive surface charge, are coherent with the resulting decrease on the impedance signal. Furthermore, the DPV measurements are in agreement with EIS experiments, there is a decrease in the redox peak intensity of the ferricyanide probe due to the gold surface functionalization. The reduction of the redox peaks is higher for the 1:10 and 1:100 mixing ratios because of the same above-mentioned explanations.

Comparing the 1:10 and 1:100 mixing ratios, no significative differences were observed in terms of the surface coverage and also in terms of  $\alpha$ -synuclein detection. Thus, it was decided to select the 1:10 mixing ratio for the study of the detection response with OECT devices, to guarantee a sufficient number of Abs grafted onto the surface.

### 3.5. $\alpha$ -synuclein detection: OECTs approach

Once having characterized the OECTs operating window potential and the sensing platform ability to capture the antigen, the Ab functionalized gold electrode was integrated into the transistor to conduct sensing experiments. Two experimental approaches were tested:

- i) *in-situ*  $\alpha$ -synuclein detection coupled with *real-time* current monitoring.
- ii) *ex-situ* gate sensing and subsequent transfers recording.

Before starting the measurement of a device, conditioning of PEDOT:PSS active layer was carried out by a pulsed gate sweeping, as reported in **Figure 3.10**. A gate potential pulse was applied cyclically with a step of +0.4 V. In this way, ions enter and exit the active layer, recovering the equilibrium of ions. The measurement was stopped when  $I_{on}$  and  $I_{off}$  values reached a steady-state.

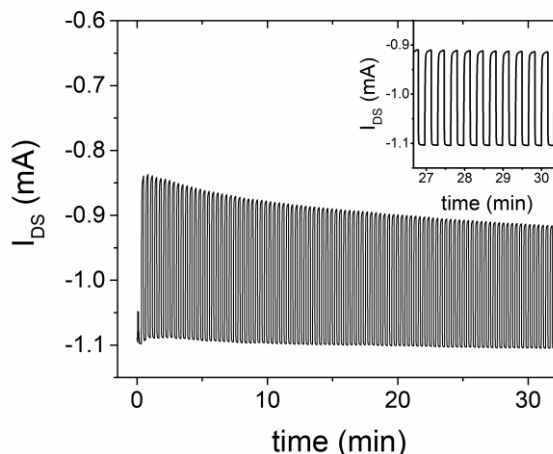


**Figure 3.10.** Pulsed measurement of an as-prepared OECT device recorded with PEDOT: PSS gate electrode and by pulsing  $V_{GS}$  from 0 V to +0.4 V with an interval time equal to 10 s, at a constant  $V_{DS} = -0.3$  V, in PBS 0.01x, pH= 7.2.

- **Real-time current monitoring**

In the case of continuous monitoring of the current *vs* time sensing experiment, Ab immobilization on the Au gate surface was performed *ex-situ*, following the procedure described previously. Once the OECT was stabilised after the application of  $V_{GS}$  pulses with the PEDOT:PSS coplanar gate,  $I$ - $V$  transfer characteristics were measured employing a bare Au disk and, subsequently, the Au disk functionalized with the SAM and eventually, with the Ab-coated Au disk. Then, drain current was recorded continuously employing PBS 0.01x as gate dielectric, applying  $V_{GS} = +0.3$  V and  $V_{DS} = -0.5$  V and employing the Ab-coated gate. When a steady-state current was reached, a drop of  $\alpha$ -synuclein solution was added into the vial containing the sensing system (see **Figure 3.11**), in order to achieve the desired concentration.

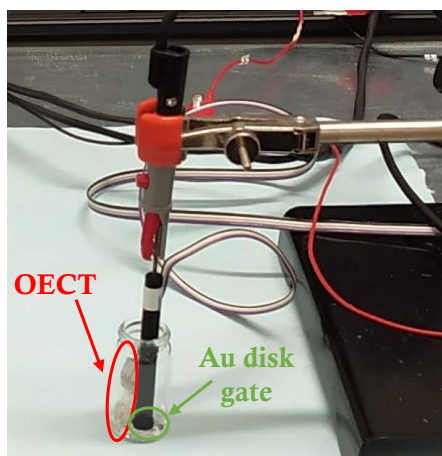


**Figure 3.11.** Real picture of the measurement setup. The device and the Au disk gate are immersed in a vial containing the electrolyte solution and the analyte.

Increasing concentrations of  $\alpha$ -synuclein (previously aliquots were prepared in PBS at physiological pH) were added, to achieve progressively the total concentration of 0.05 nM, 0.25 nM, 5 nM, 100 nM, 270 nM, respectively, at interval of 30 minutes to a maximum of 60 minutes. The results are shown in **Figure 3.12**. A change in the current magnitude was expected after the  $\alpha$ -synuclein binding. However, a quasi-constant decrease of the source-drain current was observed, not correlated to the addition of the analyte in the electrolyte, but more likely due to some bias-stress. Once the current monitoring was stopped, a transfer was recorded and compared to the ones measured before (**Figure 3.12,b**). It can be noticed that, when the gold electrode is modified with the Ab biomolecules, there is a better modulation of the device with respect to the one with bare gold gate, as it is clear from the transfers and the transconductance profiles. The increase of the current in absolute value registered in the  $I_{DS}$  vs time is coherent with the transfers recorded at the end of the experiment. In fact, the transfer measured with Ab-coated gate after exposure to  $\alpha$ -synuclein exhibits a less gating capacity, which results in a lower decrease of the current as the gate potential increases. That is to say, the same de-doping level occurs at higher potentials. A possible explanation is that the potential drop at the gate/electrolyte interface increases when the antigen is present on the Au surface.



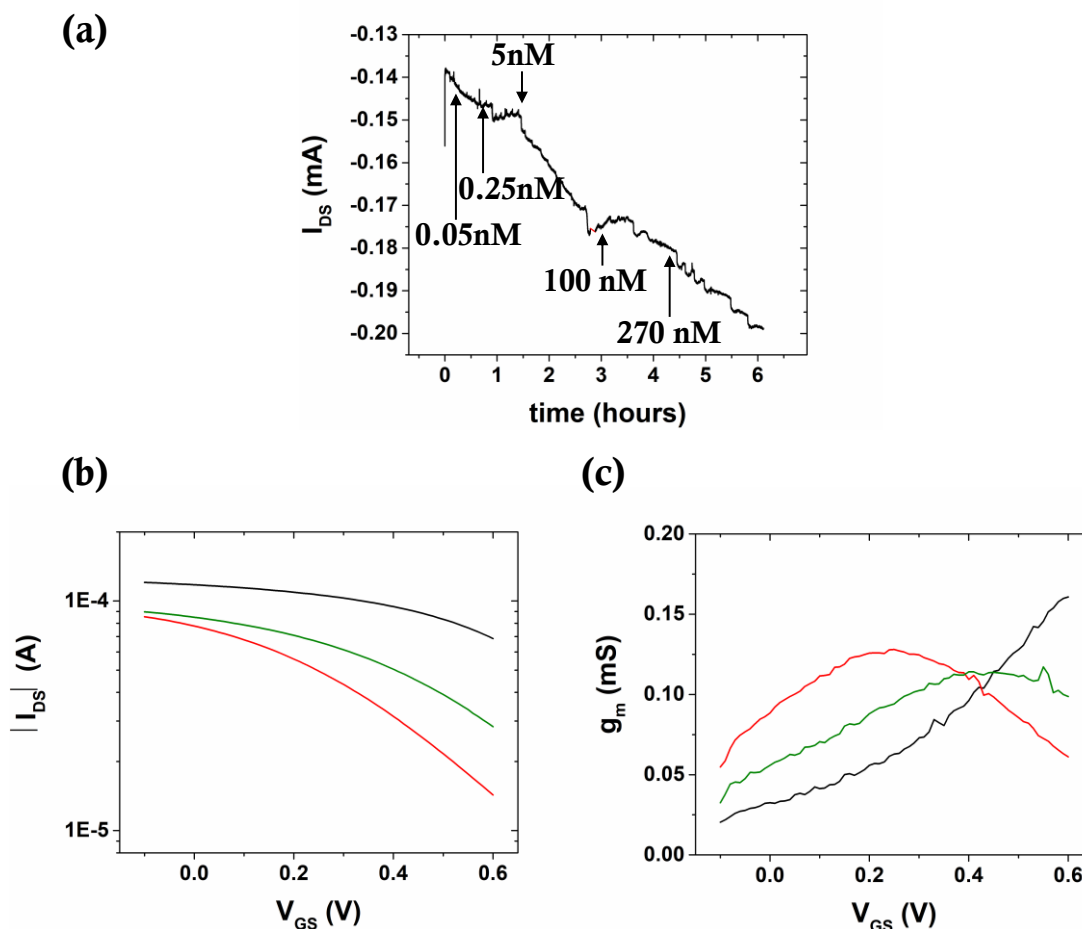


**Figure 3.12.** *In-situ* and *real-time* detection of  $\alpha$ -synuclein. (a)  $I_{DS}$  vs time profile, recorded at  $V_{GS} = +0.3$  V and  $V_{DS} = -0.5$  V, with the Ab-coated gold electrode, in PBS 0.01x, at pH= 7.2. The arrows indicate the additions of  $\alpha$ - synuclein obtaining the following final concentrations in solution: 0.05 nM, 0.25 nM, 5 nM, 100 nM, 270 nM. (b) Transfers plotted in semilogarithmic scale recorded applying a constant  $V_{DS} = -0.1$  V and sweeping  $V_{GS}$  from - 0.1 V to 0.6 V. The black line refers to pristine gold gate, the red line to the Ab-coated Au gate measured before the current monitoring, and the green curve corresponds to the device measured with the Ab-coated Au after the current monitoring sensing experiment. (c) Corresponding transconductance plots, at  $V_{DS} = -0.1$  V.

A control experiment was carried out following the same procedure, but without grafting the Ab on the SAM-coated Au. The results are reported in **Figure 3.13**. From the  $I_{DS}$  vs time profile, an increase of the current (in absolute value) was registered initially and after the first hour of measurement, no significant changes occurred, even after further  $\alpha$ -synuclein additions. From the transfer characteristics, we observe that the SAM-coated Au gate promotes a better current modulation than the bare gold gate, as in the case of Ab-coated gate (**Figure 3.13,b**). Even in the control experiment, the exposure of the SAM-coated Au gate to the electrolyte containing the antigen (Ag),

promotes a slightly less de-doping effect. This could be ascribed to some physisorption of biomolecules on the gate surface.

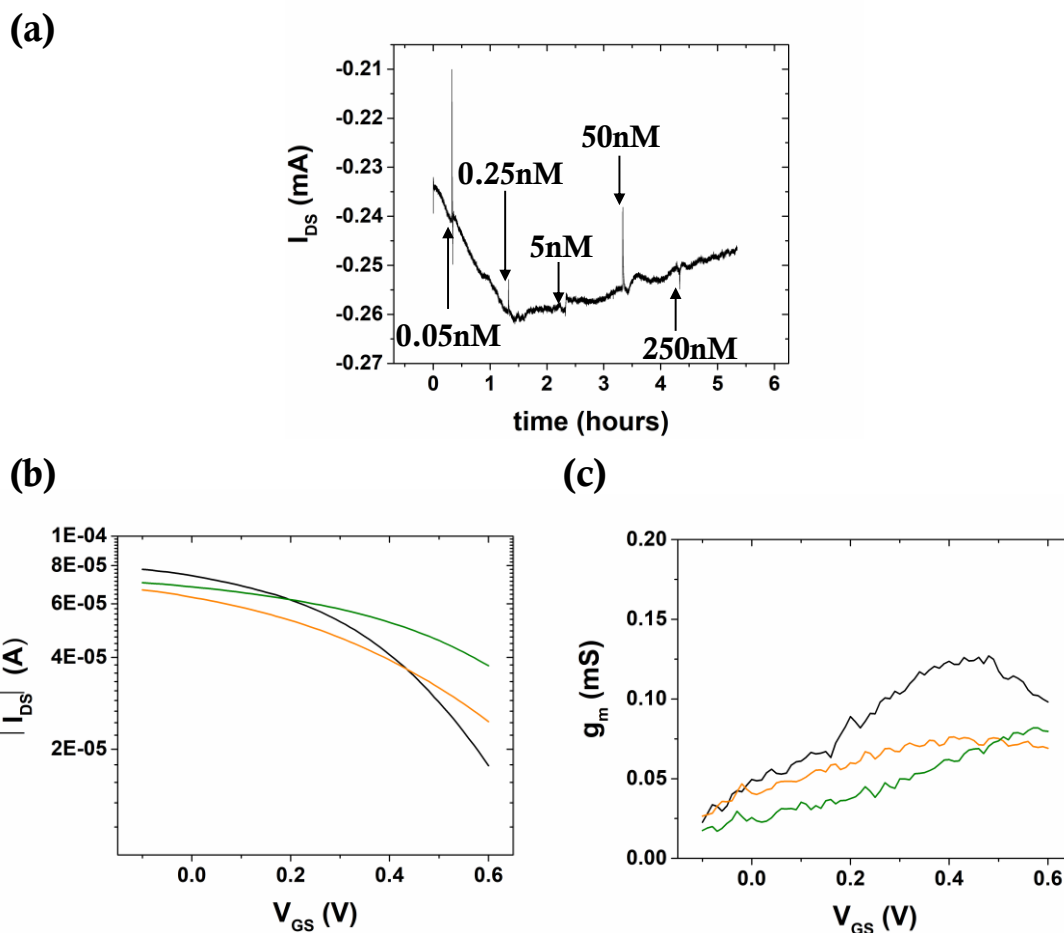


**Figure 3.13.** *In-situ* and *real-time* control experiment. (a)  $I_{DS}$  vs time profile, recorded at  $V_{GS} = +0.3$  V and  $V_{DS} = -0.5$  V, with the SAM-coated gold electrode, in PBS 0.01x, at pH= 7.2. The arrows indicate adding of  $\alpha$ -synuclein obtaining the following final concentrations in solution: 0.05 nM, 0.25 nM, 5 nM, 50 nM, 250 nM. (b) Transfers plotted in semilogarithmic scale recorded applying a constant  $V_{DS} = -0.1$  V and sweeping  $V_{GS}$  from -0.1 V to 0.6 V. The black line refers to the pristine gold gate and the orange line to the SAM-coated Au gate and were measured before the current monitoring, the green curve was measured after the current monitoring. (c) Transconductance plot, at  $V_{DS} = -0.1$  V.

These results were promising in the sense that we could observe different responses between the control experiment and the one with the Au gate functionalised with Ab after exposure to  $\alpha$ -synuclein. However, it was difficult to reproduce the experiments to get a significant and reliable change in the modulation of the output current in *real-time* to be correlated with the amount of  $\alpha$ -synuclein. For this reason, an *ex-situ*  $\alpha$ -synuclein detection was envisioned.

- ***Ex-situ* sensing**

In this second strategy, each step of the functionalization of the gold electrode was performed *ex-situ*, and transfers were recorded for each one, in two different approaches, i) linear sweeping of  $V_{GS}$  and ii) pulsed sweeping of  $V_{GS}$ . Two  $\alpha$ -synuclein concentration values were selected, a low level one, namely 50 pM, and a high level one, namely 500 nM. Ab-coated Au disk was immersed into the increasing concentration solutions containing  $\alpha$ -synuclein in PBS at physiological pH for 1 h at R.T. Afterwards, the electrode surface was rinsed with water to remove physisorbed materials and the Au disk was used as gate contact in the OECT device. The results of the *ex-situ* detection experiment are illustrated in **Figure 3.14**. SAM-coated Au disk and Ab-coated Au disk gates show a better source-drain current modulation capability respect to pristine Au disk and, as it is clear from **Figure 3.14,b**, a great shift of the transconductance peak occurs. Furthermore,  $\alpha$ -synuclein binding promotes an additional decrease of the  $I_{on}$  and  $I_{off}$  current, which is an indication of a better de-doping of the conducting polymer. The peaks of transconductance corresponding to the biomodified gate are shifted at lower  $V_{GS}$  potential with respect to pristine Au, indicating that the potential drop at the gate/electrolyte interface is quite different (**Figure 3.14,b**). Gate currents are reported (**Figure 3.14,c**) and it is apparent that  $I_{GS}$  varies with the gate potential, especially in the Au gold coated gate and after exposure to the antigen. However, it is not straightforward to discriminate between a capacitive or faradaic process at the gate surface.

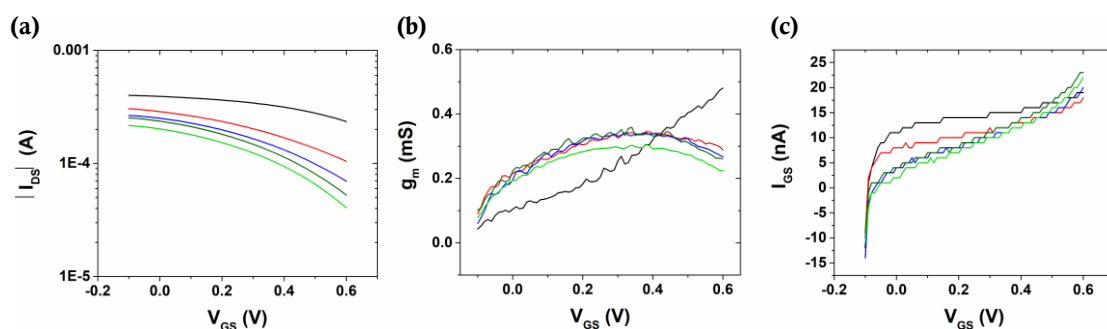


**Figure 3.14.** *Ex-situ*  $\alpha$ -synuclein detection experiment. (a)  $I_{DS}$ - $V$  transfer measurements recorded at  $V_{DS} = -0.1$  V sweeping  $V_{GS}$  from -0.1 V to 0.6 V, plotted in semilogarithmic scale. (b) Transconductance plot at  $V_{DS} = -0.1$  V. (c) Gate currents,  $I_{GS}$  vs  $V_{GS}$  plot at  $V_{DS} = -0.1$  V. Black curves refer to pristine Au, red curves to SAM-coated Au, blue curves to Ab-coated Au, dark green curves to Ab-coated Au exposed to 50 pM of  $\alpha$ -synuclein solution and light green curves to 500 nM  $\alpha$ -synuclein. Electrolyte: PBS 0.01x, pH= 7.2.

A control experiment consisting of exposing the SAM-coated Au disk (without the Ab) directly to  $\alpha$ -synuclein solutions, namely 50 pM and 500 nM, was carried out, to prove the specificity of the Ab-coated Au towards the Ag. The results are shown in **Figure 3.15**. When Abs are not immobilized onto the Au surface, a small change occurs after the dipping of the SAM-coated Au into the first aliquot of  $\alpha$ -synuclein, 50 pM, but no change is registered after the exposure to the second aliquot, 500 nM. This could be ascribed to a reorganization of the SAM molecules or limited unspecific physisorption of  $\alpha$ -synuclein.

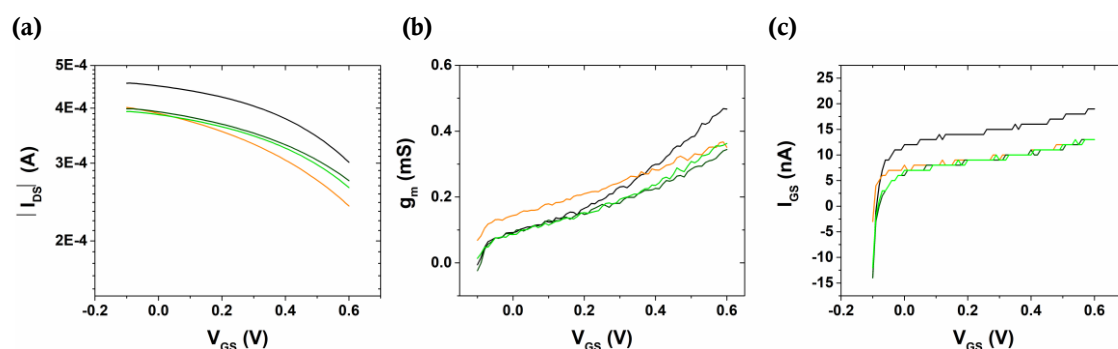


**Figure 3.15.** *Ex-situ*  $\alpha$ -synuclein detection control experiment. (a)  $I_{DS}$ - $V$  transfer measurements recorded at  $V_{DS} = -0.1$  V sweeping  $V_{GS}$  from -0.1 V to 0.6 V, plotted in semilogarithmic scale. (b) Transconductance plot at  $V_{DS} = -0.1$  V. (c) Gate currents,  $I_{GS}$  vs  $V_{GS}$  plot. Black curves refer to pristine Au, orange curves to SAM-coated Au, dark green curves to Ab-coated Au exposed to 50 pM  $\alpha$ -synuclein solution and light green curves to 500 nM  $\alpha$ -synuclein. Electrolyte: PBS 0.01x, pH= 7.2.

A response was calculated by normalizing the current values obtained for 50 pM and 500 nM  $\alpha$ -synuclein concentrations with respect to the current recorded without the presence of  $\alpha$ -synuclein, extrapolated by the respective transfer curves at fixed  $V_{DS} = -0.1$  V and  $V_{GS} = +0.3$  V, for the sensing experiment, and  $V_{DS} = -0.1$  V and  $V_{GS} = +0.5$  V for the control experiment. The gate potential at which the response was calculated was selected taking into account the maximum of the transconductance reached for each experiment. As it is clear from **Table 3.2**, the response obtained from the experiment in which Abs were immobilized on the gate, is opposite with respect to the one obtained when no receptors are immobilized. Specifically, the exposure to the first aliquot of Ag promotes a comparable current shift, but opposite in sign. However,

the 500 nM  $\alpha$ -synuclein, provokes a significative further variation in the case of the Ab-coated gold disk and a considerable smaller variation for the SAM-coated gate.

**Table 3.2.** Response towards  $\alpha$ -synuclein binding for Ab-coated Au and SAM-coated Au.

Experiment performed	50 pM	500 nM
<b>Sensing experiment</b> ( $V_{DS} = -0.1$ V, $V_{GS} = +0.3$ V)	-0.11	-0.25
<b>Control experiment</b> ( $V_{DS} = -0.1$ V, $V_{GS} = +0.5$ V)	+0.11	+0.08

These results are promising but they present some limitations of our system. The control experiment shows an opposite but still non-negligible response with respect to the sensing experiment, likely due to protein physisorption. Thus, the following approach was followed.

The *ex-situ*  $\alpha$ -synuclein detection experiment was repeated measuring the OECT devices by applying a pulsed gate potential ramp at a constant  $V_{DS}$ . The pulse was maintained for 10 s, for each voltage applied to the gate. In this way the source-drain current can reach an electrical equilibrium and the sensitivity of the response is expected to improve. From this kind of measurement, it is possible to observe more clearly the  $I_{on}$  recover when  $V_{GS}$  is set again to the initial value, *i.e.*  $V_{GS} = 0$  V. Furthermore, it is possible to observe how fast the  $I_{DS}$  reaches a steady-state under constant  $V_{GS}$ . The results are shown in **Figure 3.16**. Firstly, it is worth noting that the values of  $I_{DS}$  at  $V_{GS} = 0$  V change according to the different functionalization steps, namely source-drain current corresponding to a gate potential equal to 0 V decreases (in absolute terms) when the gold gate is functionalized with the SAM. The further immobilization of the Abs and then  $\alpha$ -synuclein on the surface promotes a further decrease (in absolute terms) of the source-drain current at zero gate potential. This result is coherent with the previous experiments and is an indication of a variation of the local surface gate potential due to the coating with the SAM and the biomolecules, which probably creates a change of the surface dipoles. When the  $I_{DS}$  is normalized with respect to the baseline (**Figure 3.16,b**), it is observed that not only  $I_{DS}$  at  $V_{GS} = 0$  V is decreasing (in absolute terms), but also at different applied gate potential, the absolute value of the source-drain current decreases with the gate biofunctionalization.

Overall, the  $I_{on/off}$  ratio increases with the functionalization and the binding with increasing concentrations of  $\alpha$ -synuclein, which means that the de-doping process of the conducting layer of the device is more efficient when the biomolecules are adsorbed on the gate. The response to  $\alpha$ -synuclein is more significant for the highest concentration employed, namely 500 nM, whereas a slighter change is appreciable for  $\alpha$ -synuclein 50 pM. Additionally, as the Au surface is coated with bio-molecules, the current stabilizes slightly faster, as it is possible to appreciate from the shape of the current pulses. The perfect operating of the OECT device after the sensing experiment was assessed by measuring the device with the coplanar PEDOT:PSS gate electrode, before and after the sensing experiment, as shown in **Figure 3.16,c**.

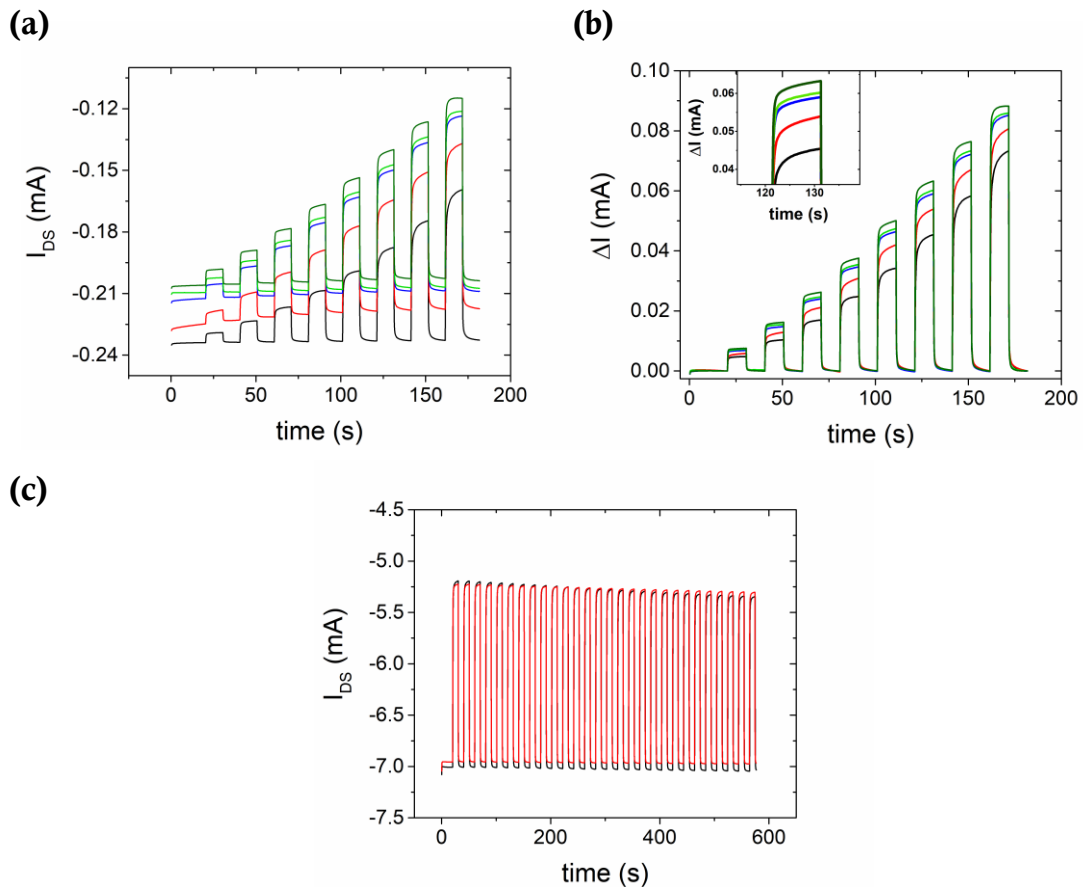


**Figure 3.16.** (a) Electrical measurements carried out in PBS 0.01x at pH= 7.2 with modified Au disk as gate electrode. A constant  $V_{DS} = -0.1$  V and a pulsed from 0 V to +0.4 V with a step of +0.05 V and an interval time equal to 10 s was applied. The black curve is relative to pristine Au, the red one to the SAM-coated Au, the blue curve is referred to the Ab-coated curve and the green ones to the  $\alpha$ -synuclein (50 pM light green, 500 nM dark green). (b) Baseline normalization. In the inset the current modulation at  $V_{GS} = +0.3$  V is reported. (c) Current stabilization of the device before (black line) and after the sensing experiment (red line), recorded with PEDOT:PSS gate electrode, by applying a constant  $V_{DS} = -0.3$  V and a pulsed  $V_{GS}$  with a step equal to +0.4 V and an interval time equal to 20 s.

Thus, the response can be rationalized in terms of a variation in the gate surface potential due to the adsorption of the analyte, which in this case is a protein bearing a negative charge at physiological pH. The variation of the effective gate potential can determine a change in the source-drain current modulation. As stated above, OECTs are mainly used as amperometric sensor, for the detection of electroactive species. The volumetric capacitance of the active layer along with the slower response with respect to EGOFET devices, has limited the use of OECTs for the detection of proteins. However, our system was capable to tune the source-drain current by functionalization of the gold gate surface with proteins, demonstrating the potential of these devices as immunosensors. Nevertheless, the sensitivity of this system seems to be lower with respect to the sensor previously developed with the EGOFET.

As future work, more control experiments with non-specific proteins are needed to assess the selectivity of our sensing platform and also experiments in more complex samples, such as blood serum and cerebrospinal fluid, along with theoretical calculation in order to give a deeper insight into the sensing mechanism.

### 3.6. Summary

In summary, microfabrication of Organic Electrochemical Transistors based on PEDOT:PSS as active layer on flexible PEN substrate, was carried out. The devices were characterized electrically, showing good electrical performance and stability, with a transconductance in the range of mS.

An immunosensing platform for the detection of  $\alpha$ -synuclein, discriminating low and high concentration levels, was designed and characterized by electrochemistry. It consisted on the immobilization of antibodies against  $\alpha$ -synuclein onto the surface of a gold electrode, to be subsequently implemented successfully into the OECT, to act as gate electrode. The response of the OECT was measured by means of i) *in-situ* detection measurements and ii) *ex-situ* functionalization of the gold gate. A control experiment was conceived to assess the specificity of our sensing platform. The response obtained with the sensing and control experiments was different and well defined. The adsorption of the biomolecules into the gate surface promoted an increase of the current modulation, reflected in an increase of the  $I_{on/off}$  ratio. The devised system was able to distinguish between two significative levels of the analyte, i) pM range and ii) nM range, paving the way towards a low-cost, low-power and fast early diagnostic tool.

Despite the promising results, more experiments are needed for the development of a biosensor against  $\alpha$ -synuclein.



## Bibliography

- (1) White, H. S.; Kittlesen, G. P.; Wrighton, M. S. Chemical Derivatization of an Array of Three Gold Microelectrodes with Polypyrrole: Fabrication of a Molecule-Based Transistor. *Journal of American Chemical Society* **1984**, *106* (24), 5375–5377.
- (2) Levi, B. G. Nobel Prize in Chemistry Salutes the Discovery of Conducting Polymers. *Physics Today* **2000**, *53* (12), 19–22.
- (3) Balint, R.; Cassidy, N. J.; Cartmell, S. H. Conductive Polymers: Towards a Smart Biomaterial for Tissue Engineering. *Acta Biomaterialia* **2014**, *10* (6), 2341–2353.
- (4) Schrödner, M.; Sensfuss, S.; Roth, H. K.; Stohn, R. I.; Clemens, W.; Bernds, A.; Fix, W. Plastic Electronics Based on Semiconducting Polymers. *First International IEEE Conference on Polymers and Adhesives in Microelectronics and Photonics: Incorporating POLY, PEP and Adhasives in Electronics* **2001**, 91–94.
- (5) Tsumura, A., Koezuka, H., Ando, T. Polythiophene Field-Effect Transistor: Its Characteristics and Operation Mechanism. *Synthetic Metals* **1988**, *25*, 11–23.
- (6) Koezuka, H.; Tsumura, A. Field-Effect Transistor Utilizing Conducting Polymers. *Synthetic Metals* **1989**, *28* (1–2), 753–760.
- (7) Gustafsson, G., Cao Y., Treacy G. M., Klavetter F., Colaneri N., H. A. J. Flexible Light-Emitting Diodes Made from Soluble Conducting Polymers. *Nature* **1992**, *357*, 477–479.
- (8) Braun, D. Semiconducting Polymer LEDs. *Materials Today* **2002**, *5* (6), 32–39.
- (9) Zachmann, H. G. *Photoresponsive Polymers II*; 2008; Vol. 99.
- (10) Mortimer, R. J.; Dyer, A. L.; Reynolds, J. R. Electrochromic Organic and Polymeric Materials for Display Applications. *Displays* **2006**, *27* (1), 2–18.
- (11) Nair, S. S.; Mishra, S. K.; Kumar, D. Recent Progress in Conductive Polymeric Materials for Biomedical Applications. *Polymers for Advanced Technologies*. 2019,

- pp 2932–2953.
- (12) Kaur, G.; Adhikari, R.; Cass, P.; Bown, M.; Gunatillake, P. Electrically Conductive Polymers and Composites for Biomedical Applications. *RSC Advances* **2015**, *5*, 37553–37567.
  - (13) Wang, Y.; Liu, A.; Han, Y.; Li, T. Sensors Based on Conductive Polymers and Their Composites : A Review. *Polymer International* **2020**, *69*, 7–17.
  - (14) Saberi, A.; Jabbari, F.; Zarrintaj, P.; Saeb, M. R. Electrically Conductive Materials : Opportunities and Challenges in Tissue Engineering. *Biomolecules* **2019**, *9*, 448.
  - (15) Bayer AG. European Patent, 339 340, 1988.
  - (16) Groenendaal, L.; Jonas, F.; Freitag, D.; Pielartzik, H.; Reynolds, J. R. Poly(3,4-Ethylenedioxythiophene) and Its Derivatives: Past, Present, and Future. *Advanced Materials* **2000**, *12* (7), 481–494.
  - (17) Shi, H.; Liu, C.; Jiang, Q.; Xu, J. Effective Approaches to Improve the Electrical Conductivity of PEDOT:PSS: A Review. *Advanced Electronic Materials* **2015**, *1* (4), 1–16.
  - (18) Marzocchi, M.; Gualandi, I.; Calienni, M.; Zironi, I.; Scavetta, E.; Castellani, G.; Fraboni, B. Physical and Electrochemical Properties of PEDOT : PSS as a Tool for Controlling Cell Growth. *ACS Applied Materials & Interfaces* **2015**, *7*, 17993–18003.
  - (19) Rivnay, J.; Inal, S.; Salleo, A.; Owens, R. M.; Berggren, M.; Malliaras, G. G. Organic Electrochemical Transistors. *Nature Reviews Materials* **2018**, *3*, 17086.
  - (20) Pappa, A. M.; Ohayon, D.; Giovannitti, A.; Maria, I. P.; Savva, A.; Uguz, I.; Rivnay, J.; McCulloch, I.; Owens, R. M.; Inal, S. Direct Metabolite Detection with an N-Type Accumulation Mode Organic Electrochemical Transistor. *Science Advances* **2018**, *4*, 1–8.
  - (21) Bernards, D. A.; Macaya, D. J.; Nikolou, M.; Defranco, J. A.; Takamatsu, S.; Malliaras, G. G. Enzymatic Sensing with Organic Electrochemical Transistors.

*Journal of Materials Chemistry* **2008**, *18*, 116–120.

- (22) Strakosas, X.; Bongo, M.; Owens, R. M. The Organic Electrochemical Transistor for Biological Applications. *Journal of Applied Polymer Science* **2015**, *132* (15), 1–14.
- (23) Wustoni, S.; Wang, S.; Alvarez, J. R.; Hidalgo, T. C.; Nunes, S. P.; Inal, S. An Organic Electrochemical Transistor Integrated with a Molecularly Selective Isoporous Membrane for Amyloid- $\beta$  Detection. *Biosensors and Bioelectronics* **2019**, *143* (July), 111561.
- (24) Gualandi, I.; Marzocchi, M.; Scavetta, E.; Calienni, M.; Bonfiglio, A.; Fraboni, B. A Simple All-PEDOT:PSS Electrochemical Transistor for Ascorbic Acid Sensing. *Journal of Materials Chemistry B* **2015**, *3* (33), 6753–6762.
- (25) Rivnay, J.; Ramuz, M.; Leleux, P.; Hama, A.; Huerta, M.; Owens, R. M. Organic Electrochemical Transistors for Cell- Based Impedance Sensing. *Applied Physics Letters* **2015**, *106*, 043301.
- (26) Rivnay, J.; Leleux, P.; Ferro, M.; Sessolo, M.; Williamson, A.; Koutsouras, D. A.; Khodagholy, D.; Ramuz, M.; Strakosas, X.; Owens, R. M.; et al. High-Performance Transistors for Bioelectronics through Tuning of Channel Thickness. *Science Advances* **2015**, *1*, 11400251.
- (27) Braendlein, M.; Lonjaret, T.; Leleux, P.; Badier, J.; Malliaras, G. G. Voltage Amplifier Based on Organic Electrochemical Transistor. *Advanced Science* **2017**, *4*, 1600247.
- (28) Bernard, C.; Ghestem, A.; Ismailova, E.; Herve, T.; Malliaras, G. G. In Vivo Recordings of Brain Activity Using Organic Transistors. *Nature Communications* **2013**, *4*, 1575.
- (29) Campana, A.; Cramer, T.; Simon, D. T.; Berggren, M.; Biscarini, F. Electrocardiographic Recording with Conformable Organic Electrochemical Transistor Fabricated on Resorbable Bioscaffold. *Advanced Materials* **2014**, *26* (23), 3874–3878.
- (30) Faria, G. C.; Duong, D. T.; Salleo, A.; Polyzoidis, C. A.; Logothetidis, S.; Rivnay, J.; Owens, R.; Malliaras, G. G. Organic Electrochemical Transistors as

- Impedance Biosensors. *MRS Communications* **2014**, 4 (4), 189–194.
- (31) Pappa, A.; Parlak, O.; Scheiblin, G.; Mailley, P.; Salleo, A.; Owens, R. M. Organic Electronics for Point-of-Care Metabolite Monitoring. *Trends in Biotechnology* **2018**, 36 (1), 45–59.
- (32) Bai, L.; Elósegui, C. G.; Li, W.; Yu, P.; Fei, J. Biological Applications of Organic Electrochemical Transistors: Electrochemical Biosensors and Electrophysiology Recording. *Frontiers in Chemistry* **2019**, 7 (May), 313.
- (33) Piro, B.; Mattana, G.; Zrig, S.; Anquetin, G.; Battaglini, N.; Capitaio, D.; Maurin, A.; Reisberg, S. Fabrication and Use of Organic Electrochemical Transistors for Sensing of Metabolites in Aqueous Media. *Applied Sciences* **2018**, 8, 928.
- (34) Lin, P.; Luo, X.; Hsing, I. M.; Yan, F. Organic Electrochemical Transistors Integrated in Flexible Microfluidic Systems and Used for Label-Free DNA Sensing. *Advanced Materials* **2011**, 23 (35), 4035–4040.
- (35) He, R. X.; Zhang, M.; Tan, F.; Leung, P. H. M.; Zhao, X. Z.; Chan, H. L. W.; Yang, M.; Yan, F. Detection of Bacteria with Organic Electrochemical Transistors. *Journal of Materials Chemistry* **2012**, 22 (41), 22072–22076.
- (36) Macchia, E.; Ghittorelli, M.; Torricelli, F.; Torsi, L. Organic Electrochemical Transistor Immuno-Sensor Operating at the Femto-Molar Limit of Detection. *IEEE* **2017**, 68–72.
- (37) Gentili, D.; Angelo, P. D.; Militano, F.; Mazzei, R.; Poerio, T.; Tarabella, G.; Bonetti, S.; Marasso, S. L.; Cocuzza, M.; Giorno, L.; et al. Integration of Organic Electrochemical Transistors and Immuno-Affinity Membranes for Label-Free Detection of Interleukin-6 in the Physiological Concentration Range through Antibody–Antigen Recognition. *Journal of Materials Chemistry B* **2018**, 6, 5400–5406.
- (38) Picca, R. A.; Manoli, K.; Macchia, E.; Sarcina, L.; Franco, C. Di; Cioffi, N.; Blasi, D.; Österbacka, R.; Torricelli, F.; Scamarcio, G. Ultimately Sensitive Organic Bioelectronic Transistor Sensors by Materials and Device Structure

- Design. *Advanced Funtional Materials* **2020**, *30*, 1904513.
- (39) Olivares, D.; Huang, X.; Branden, L.; Greig, N. H.; Rogers, J. T. Physiological and Pathological Role of Alpha-Synuclein in Parkinson ' s Disease Through Iron Mediated Oxidative Stress ; The Role of a Putative Iron-Responsive Element. *International Journal of Molecular Sciences* **2009**, *10*, 1226–1260.
- (40) Atik, A.; Stewart, T.; Zhang, J. Alpha-Synuclein as a Biomarker for Parkinson's Disease. *Brain Pathology* **2016**, *26* (3), 410–418.
- (41) Goedert, M.; Jakes, R.; Spillantini, M. G. The Synucleinopathies: Twenty Years On. *Journal of Parkinson's Disease* **2017**, *7*, S51–S69.
- (42) Xu, Q.; Evetts, S.; Hu, M.; Talbot, K.; Wade-martins, R.; Davis, J. J. An Impedimetric Assay of a -Synuclein Autoantibodies in Early Stage Parkinson' s Disease. *RSC Advances* **2014**, *4*, 58773.
- (43) Zhang, R.; Wang, S.; Huang, X.; Yang, Y.; Fan, H.; Yang, F.; Li, J.; Dong, X.; Feng, S.; Anbu, P.; et al. Gold-Nanourchin Seeded Single-Walled Carbon Nanotube on Voltammetry Sensor for Diagnosing Neurogenerative Parkinson's Disease. *Analytica Chimica Acta* **2020**, *1094*, 142–150.
- (44) Crispin, X.; Marciniak, S.; Osikowicz, W.; Zotti, G.; Gon, a W. D. V. a N. D. E. R.; Louwet, F.; Fahlman, M.; Groenendaal, L.; Schryver, F. D. E.; Salaneck, W. R. Stability of Poly ( 3 , 4-Ethylene Dioxythiophene )– Poly ( Styrene Sulfonate ): A Photoelectron Spectroscopy Study. *Polymer* **2003**, *41* (21), 2561–2583.
- (45) Håkansson, A.; Han, S.; Wang, S.; Lu, J.; Braun, S.; Fahlman, M.; Berggren, M.; Crispin, X.; Fabiano, S. Effect of (3-Glycidyoxypropyl)Trimethoxysilane (GOPS) on the Electrical Properties of PEDOT:PSS Films. *Journal of Polymer Science, Part B: Polymer Physics* **2017**, *55* (10), 814–820.
- (46) Lin, F.; Lonergan, M. C. Gate Electrode Processes in an Electrolyte- Gated Transistor : Non-Faradaically versus Faradaically Coupled Conductivity Modulation of a Polyacetylene Ionomer. *Applied Physics Letters* **2006**, *88*, 133507.
- (47) M. Demelas, E. Scavetta, L. Basiricò, R. Rogani, A. B. A Deeper Insight into the Operation Regime of All-Polymeric Electrochemical Transistors. *Applied*

- Physics Letters* **2013**, *102* (193301), 1–4.
- (48) Soler, M.; Estevez, M.; Lourdes, M. De; Cebolla, A.; Lechuga, L. M. Label-Free SPR Detection of Gluten Peptides in Urine for Non-Invasive Celiac Disease Follow-Up. *Biosensors and Bioelectronics* **2016**, *79*, 158–164.



# CHAPTER 4

## *Flexible (C<sub>8</sub>O-BTBT-OC<sub>8</sub>)-based EGOFET: stability and properties under mechanical stress\**

---

### 4.1. Introduction

- **Flexible electronics: mechanical stress and electronic properties**

The development of devices which are incorporated into materials able to stand mechanical deformations is known as flexible electronics. At the beginning of this research field, it was referred to describe only bendable versions of rigid electronics. At present not only bendable but also stretchable, foldable and twistable deformations are being studied.<sup>1,2</sup> The interest in flexible devices spans from electronics as in the case of bendable displays, health care such as medical devices for diagnosis or therapy, energy storage and generation, to *e*-textile. Thin film transistors (TFTs),<sup>3-6</sup> Organic Light-Emitting Diodes (OLEDs),<sup>7-11</sup> organic solar cells (OPV),<sup>12-16</sup> memory devices,<sup>17,18</sup> batteries<sup>19-23</sup> and capacitors<sup>24-26</sup> are the major classes of devices investigated for this aim.

The main components of the flexible devices are the substrates, conductors, insulators and semiconductor materials. Regarding the **substrates**, there are three main categories, i) polymeric films, ii) metal foils, iii) fibrous materials.<sup>1</sup>

---

\*This work was carried out with the collaboration of Dr. Tommaso Salzillo, Dr. Raphael Pfattner and Sara Ruiz.



Polymeric films are quite inexpensive, lightweight and suitable for bendable devices. The most common used are polyethylene naphthalate (PEN), polyethylene terephthalate (PET), polycarbonate (PC) and polyimide (PI). They display different physical properties thus one can choose the most suitable according to the required processing conditions. When stretchability feature is required, elastomers are employed, such as polydimethylsiloxane (PDMS).<sup>1,27</sup> Concerning metal foils, they are convenient for high-temperature processing, being stainless steel the most exploited material.<sup>1</sup> Fibrous materials, such as paper sheets have gained a lot of interest recently. Indeed, they are even less expensive than plastic films and more biodegradable. The drawback of paper substrates is its ability to absorb liquid electrolyte, which makes them not suitable for liquid-gated transistors.<sup>1</sup>

Regarding **electrical conductors**, metallic films have been the best solutions up to now. However, in order to achieve more compliant materials, liquid conductors have been explored, like the so-called *eGaIn*, a mix of gallium/indium in proportions near the eutectic point. This metal is liquid at room temperature, making it appropriate for applications that require a large degree of bending and/or stretching.<sup>1,28,29</sup> Apart from metals, conductive polymers have gained a lot of attention in this area of research, due to their intrinsic strain-tolerant mechanical behaviour. Further to their mechanical properties, polymeric materials can also be chemically tuned to obtain additional functionalities.<sup>1,30</sup> Lastly, graphene has also been exploited in flexible electronics, combining its excellent electrical properties with its remarkable mechanical features, such as strength and intrinsic flexibility. Furthermore, graphene can be easily doped to increase its performance.<sup>31</sup>

**Dielectrics** are one of the most relevant components in the fabrication of field-effect transistors. SiO<sub>2</sub> is the classic inorganic dielectric, but polymer-based insulators are required for flexible purposes and they are also being more employed since they represent a better choice for lowering the processing cost. Indeed, they can be mostly deposited from solution by spin-coating or by printing techniques. Parylene-C has been extensively exploited lately as substrate, dielectric and also encapsulation layer. However, despite its excellent properties, Parylene-C requires chemical vapor deposition to be coated into the needed substrates, increasing the total cost of fabrication.<sup>1</sup> Other dielectrics that have been used which are compatible with solution-processing are cross-linked insulating polymers. Among them, we find poly(4-vinyl

phenol-co-methyl methacrylate) (PVP-co-PMMA) thermally cross-linked with p-tolyltrimethoxysilane (TTMS),<sup>32</sup> or poly(vinyl alcohol) (PVA) thin films cross-linked by N,N'-methylene bisacrylamide (MBA).<sup>33</sup> The polymer cross-linking is often needed to improve the dielectric properties of the polymeric thin films. This process improves the performance and stability of the dielectric and reduces the presence of free hydroxyl groups on the surface, thus allowing a better coating of the organic semiconductor (OSC) and decreasing charge-traps at the dielectric/semiconductor interface.<sup>34-36</sup> Natural biopolymers, such as silk fibroin, which is constituted of repeated amino acid alternating sequence of glycine and alanine, has also been employed as gate dielectric in a flexible Organic TFT.<sup>37</sup>

Finally, concerning **semiconducting components**, organic counterparts, *viz.* small molecules or  $\pi$ -conjugated polymers, offer many advantages respect to Silicon based electronics. Indeed, they can be processed under ambient conditions by means of solution processed techniques with an overall low-cost fabrication and they are intrinsically flexible, due to the weak van der Waals interactions between organic molecules.<sup>38</sup> Furthermore, regarding the best Organic Field-Effect Transistors (OFETs) developed up to now, electrical performances comparable to that of amorphous Silicon have been reached.<sup>39</sup> However, dealing with organic molecules can be challenging due to their poor solubility in organic solvents.

Depending on the type of application, tolerance to one-time strain or to small but repetitive strain cycles has to be assessed. Mechanical deformations under evaluation are bending, stretching and twisting. Deformation of a material induces a stress that results in a strain, which can be classified as tensile, compressive or shearing strain. The relation between stress and strain is the following:

$$E = \sigma/\varepsilon \quad (4.1)$$

where  $E$  is the elastic modulus of the material,  $\sigma$  is the applied stress and  $\varepsilon$  is the resulting strain. From equation (4.1) is evident that larger  $E$  values correspond to stiffer materials, whereas smaller  $E$  values are typical of more compliant materials.

Regarding OFETs, flexibility is a key feature in sensing applications, above all in biomedicine, robotic fields or wearable systems. Specifically, some applications require

mechanical strain sensitivity and some other to operate normally even when exposed to mechanical stress.<sup>40</sup> For this reason, understanding the correlation between mechanical stress and electrical properties of the active layer is fundamental. Despite a comprehensive model has not already been assessed, a few works have been devoted to gaining insights into the driving mechanisms. In literature, it has been observed that typically compressive strains produce an increase of the output current, whereas tensile strains promote a decrease of the current.<sup>38,41–45</sup> In thin films, this effect has been often attributed to the modification of intergrain distances that impacts on the hopping charge carrier transport mechanism. Indeed, when a compressive strain is produced, the intergrain distance is reduced, and consequently, the hopping barrier decreases, and the mobility increases. The contrary effect takes place under tensile strain.<sup>40,42,43</sup> However, other works have also ascribed this effect to deformation effects on the crystal lattice upon mechanical strain. In particular, in an extensive study on a rubrene single-crystal OFET, the authors found that the dependence of the intrinsic mobility on the applied bending strain was caused by a change in the phonon modes of the crystal lattice, as demonstrated by a shift of the low-frequency Raman peaks.<sup>41</sup>

However, when a device is exposed to mechanical stress, not only the active layer is involved. It has been shown that strain sensitivity is also dependent on contact resistance. In fact, under mechanical stress, source and drain electrodes can be damaged, affecting the parasitic resistance and so the injection barrier.<sup>46</sup> The contribution of contact resistance can be tuned by modifying the channel length. Considering that the total resistance between source and drain is given by:

$$R = R_{ch} + R_c \quad (4.2)$$

where  $R_{ch}$  represents the channel resistance and  $R_c$  the contact resistance, when the channel length is decreased, channel resistance decreases, and contact resistance becomes the dominant one. Thus, modifying the channel length can modulate the effect of the variation of contact resistance under bending.<sup>38</sup>

A great effort has been dedicated to the development of all flexible OFET devices, spanning from sensors to wearable systems, but to our knowledge, no studies on flexible EGOFET devices have been performed. It could be interesting to dispose of a

liquid-gated transistor, combining good electrical performances and flexible properties, envisioning implantable devices for the monitoring of vital signs or wearable systems.

- **$C_8O$ -BTBT- $OC_8$  molecule and its application in OFET devices**

[1]benzothieno[3,2-b]benzothiophene (BTBT) derivatives have been extensively studied as organic semiconductor. BTBT crystalline films show high stability and performance when used as active layer in OFETs. This molecule displays also a high contact resistance, due to its low-lying HOMO level, *viz.* - 5.5 eV, against Au work function, which is equal to around 5.1 eV. Consequently, derivatives of the BTBT core have been designed and synthesized, to increase the HOMO level, but also to increase the solubility for solution-processing. A strategy adopted by Prof. *Y. Geerts et al.* consisted on the addition of alkyloxy moieties into the benzo groups to obtain the 2,7 - dioctyloxy[1]benzothieno[3,2,b]benzothiophene ( $C_8O$ -BTBT- $OC_8$ ), depicted in **Figure 4.1**.<sup>47</sup> In a previous work of our group, a thorough study regarding the morphology and polymorphic composition of crystalline thin films, formed by blending  $C_8O$ -BTBT- $OC_8$  with polystyrene (PS) of different molecular weight, deposited by bar-assisted meniscus shearing (BAMS) technique, was reported and correlated to the OFET performance in bottom-gate top-contact (BGBC) configuration.<sup>48</sup> The best conditions found were employing a solution of PS<sub>100k</sub> in a ratio of 4:1 ( $C_8O$ -BTBT- $OC_8$ :PS) in chlorobenzene (CB) at 2% wt, and depositing it by BAMS at a shearing speed equal to 10 mm/s and setting the hot plate temperature to 105 °C. The mobility obtained was close to 1 cm<sup>2</sup>/V·s and the devices showed a shelf-stability that exceeded one year. In contrast, the devices prepared using the same methodology but based only on the semiconductor (*i.e.*, without the PS) exhibited a mobility of almost one order of magnitude lower and the films suffered dewetting and a polymorphic transformation with time.

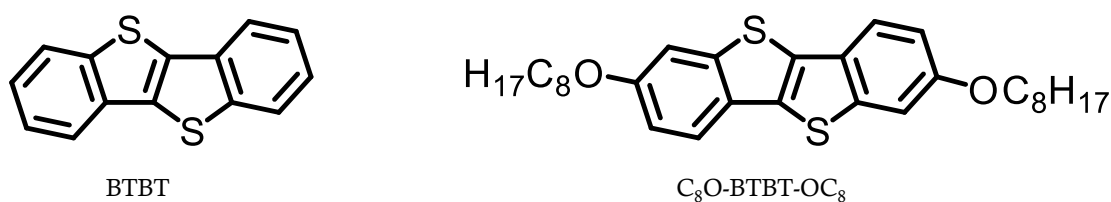


**Figure 4.1.** Molecular structure of BTBT and  $C_8O$ -BTBT- $OC_8$ .

It has been observed that C<sub>8</sub>O-BTBT-OC<sub>8</sub> molecules present two different phases, the bulk and the surface-induced phase (SIP). The SIP phase has been claimed in previous works to turn into the bulk structure by ageing or by solvent vapour annealing (SVA).<sup>49</sup> Recently, our group demonstrated that the blending the organic semiconductor with high molecular weight polystyrene (> 100 kg/mol) resulted in the stabilization of the SIP phase with time, preserving thus the device performance.<sup>48</sup>

Despite the encouraging results achieved with BTBT derivatives in OFET devices, the implementation of BTBT-based semiconductors as active layers in EGOFET devices has hardly been explored. *Di Lauro* and collaborators, developed a liquid-gated OFET based on 2,7-dioctyl BTBT.<sup>50</sup> The obtained device displayed promising electrical performances such as transconductance,  $g_m$ , equal to 45(±32) μS and an average  $C_{eff} \cdot \mu = 0.11(\pm 0.08) \mu\text{S} \cdot \text{V}^{-1}$ .

In this chapter, C<sub>8</sub>O-BTBT-OC<sub>8</sub>-based EGOFET device has been investigated as all-flexible liquid-gated OFET.

### 4.2. Objectives

This chapter is focused on the fabrication of C<sub>8</sub>O-BTBT-OC<sub>8</sub>-based EGOFETs and on the study of their mechanical and electrical properties under compressive or tensile stress. To achieve this goal the following tasks were planned:

1. Preparation and characterization of C<sub>8</sub>O-BTBT-OC<sub>8</sub> thin films by BAMS on Si/SiO<sub>2</sub> and implementation of the films as active layers in EGOFETs along with the assessment of their performance.
2. Preparation of C<sub>8</sub>O-BTBT-OC<sub>8</sub> thin film EGOFETs on two flexible substrates: *Kapton*<sup>®</sup> and PEN foils.
3. Examination of the mechanical response of the flexible devices by measuring the electrical performance under compressive and tensile stress.

### 4.3. Fabrication and characterization of C<sub>8</sub>O-BTBT-OC<sub>8</sub>-based EGOFETs

- EGOFETs on Si/SiO<sub>2</sub> substrates.

#### Preparation and characterization of the thin films

Interdigitated Source (S) and Drains (D) electrodes, along with the coplanar Gate (G), were patterned by photolithography and subsequently, Au was evaporated, achieving the following geometry: channel length,  $L = 50 \mu\text{m}$ , channel width,  $W = 18000 \mu\text{m}$  and  $W/L = 360$ . Before OSC deposition, gold S and D contacts were functionalized with a self-assembled monolayer (SAM) of 2,3,4,5,6-pentafluorothiophenol (PFBT). The formation of SAMs on Au it is known to modify its work-function, decreasing the gap between Au work-function and the HOMO level of the OSC.<sup>51</sup> For solution-processing techniques, it has been noticed that SAMs can also have an influence on the crystallization of the film, acting as nucleation sites.<sup>52</sup> In order to avoid both the formation of the SAM on top of the G electrode and later its coverage with the OSC, a sacrificial layer of dextran was drop casted on the gate before dipping the substrate into the PFBT solution.<sup>53</sup> After the SAM formation, we proceeded to deposit the OSC. Thin films of pure C<sub>8</sub>O-BTBT-OC<sub>8</sub> and blended with polystyrene of molecular weight 100 kg/mol (PS<sub>100k</sub>) were fabricated by BAMS on Si/SiO<sub>2</sub> substrates. The solutions were prepared in CB (2% wt) according to the previous work conducted in our group.<sup>48</sup> The OSC and polymer were mixed in a 4:1 ratio. The temperature of the BAMS plate was set to 105 °C and the speed rate to 10 mm/s. Finally, the sacrificial dextran layer was removed by water rinsing.

To assess the morphology and crystallinity of the semiconducting layer, polarized optical microscopy (POM) images of the thin films were taken and are shown in **Figure 4.2**. As expected, PS improves the homogeneity of the coatings. Pristine C<sub>8</sub>O-BTBT-OC<sub>8</sub> thin films exhibit a higher degree of defects and inhomogeneity, which should be detrimental for the electrical performance and stability of these devices, especially when operating in liquid media. In contrast, when PS is included in the semiconducting ink, the solution becomes more viscous, helping the wetting of the substrates during the coatings and promoting the formation of a uniform and continuous crystalline layer.

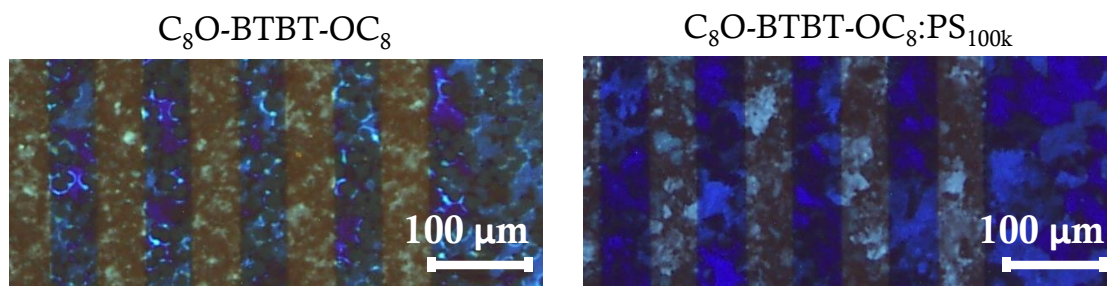


**Figure 4.2.** Polarized optical microscopy images of  $C_8O$ -BTBT- $OC_8$ -based thin films on Si/SiO<sub>2</sub> substrate.

Along with polarized optical microscopy, X-Ray diffraction (XRD) and polarization modulation infrared reflection-absorption spectroscopy (PM-IRRAS) were used for characterizing the thin films.

XRD measurements demonstrated the high crystallinity of the films. In fact, as it is shown in **Figure 4.3**, the XRD diffractograms exhibit only the peaks corresponding to the (0 0 n) family due to the stand-up configuration of the molecules with respect to the substrate surface.

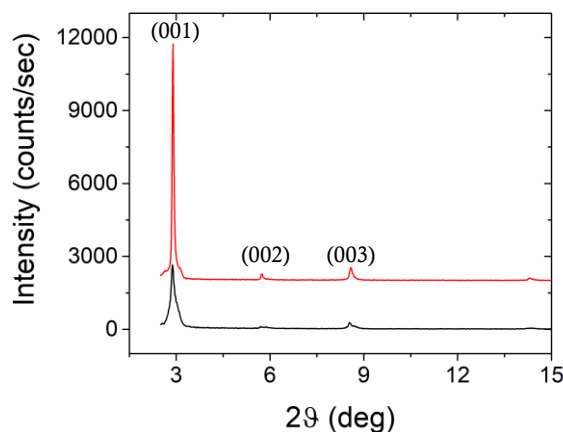


**Figure 4.3.** X-Ray diffractograms of the thin films fabricated by BAMS on Si/SiO<sub>2</sub>: red line is relative to pristine  $C_8O$ -BTBT- $OC_8$ , black line is relative to  $C_8O$ -BTBT- $OC_8$ :PS<sub>100k</sub>.

As mentioned above, it has been previously reported that  $C_8O$ -BTBT- $OC_8$  molecule displays two different crystalline phases, a so-called surface-induced phase (SIP) and a bulk phase. Understanding the polymorphic composition of the thin film devices obtained is very important to have a deeper insight into the electrical properties of the

semiconducting layer, especially in terms of charge mobility.<sup>54</sup> Both polymorphs show similar lattice parameters with two molecules per unit cell. Nevertheless, the two polymorphs of  $C_8O$ -BTBT- $OC_8$  exhibit significant differences in the molecular packing (**Figure 4.4**). The bulk phase presents a slipped  $\pi$ - $\pi$  cofacial stacking motif, whereas the SIP phase shows a 2D herringbone structure, which is in principle the best configuration for charge transport in thin film devices. In thin film, both polymorphs are arranged in a stand-up configuration, making it difficult to recognise the two structures by the classical specular X-ray diffraction. A recent work by *Schrode* and co-workers, demonstrated that by lattice phonon Raman or by IR spectroscopy it is possible to distinguish between these polymorphic species.<sup>49</sup> For the characterization of our thin film devices, PM-IRRAS was exploited. In fact, this technique helps in the analysis of films in the nanometric range thickness enhancing the IR signal.

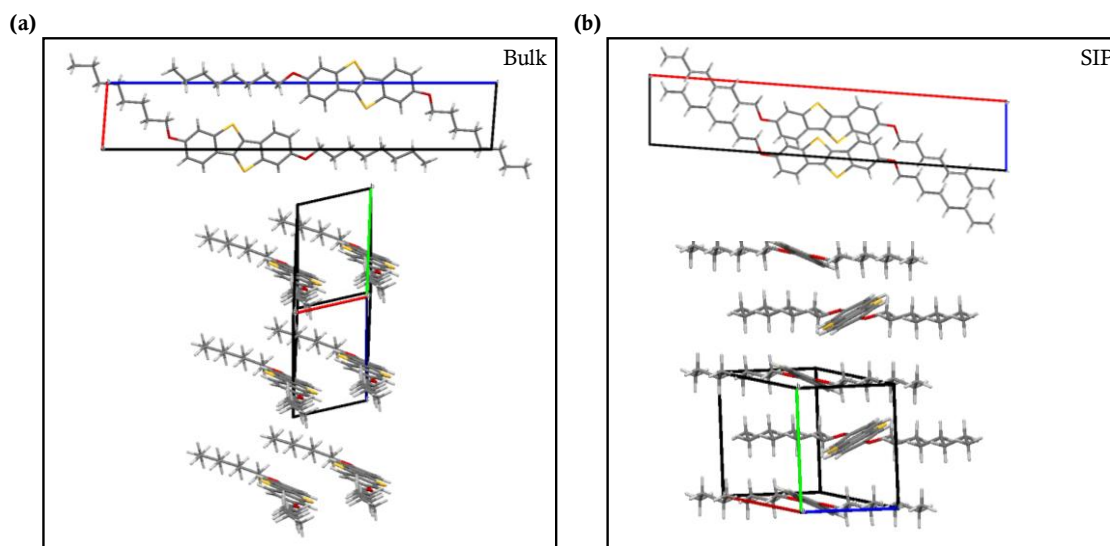


**Figure 4.4.** (a) Distinct view of the slipped  $\pi$ - $\pi$  stacking of the bulk phase and (b) herringbone stacking arrangement of the SIP phase.

For the two formulations tested (with and without PS), similar PM-IRRAS spectra were achieved. In **Figure 4.5** the spectrum of a representative  $C_8O$ -BTBT- $OC_8$ :PS<sub>100k</sub> thin film is shown and compared with reported spectra of the bulk and SIP phase. The band corresponding to the aromatic core stretching is slightly shifted for the two polymorphs. In the SIP phase, this peak is centred at  $\nu = 1605 \text{ cm}^{-1}$ , whereas in the bulk phase is shifted at higher wavenumber,  $\nu = 1611 \text{ cm}^{-1}$ . These results confirm that our films prepared by BAMS display the SIP phase, as already reported.<sup>49</sup>



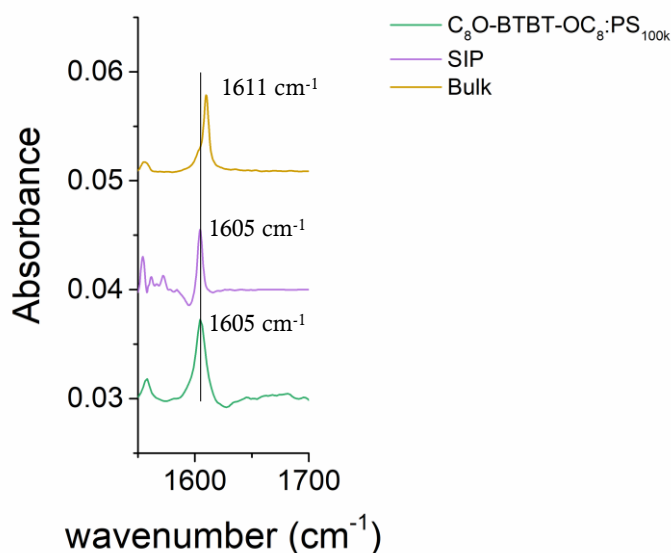


**Figure 4.5.** Comparison of the PM-IRRAS spectrum of a representative  $C_8O$ -BTBT- $OC_8$ : $PS_{100k}$  thin-film prepared by BAMS on Si/SiO<sub>2</sub> with the reported spectra of the Bulk and the SIP phase of  $C_8O$ -BTBT- $OC_8$ .<sup>49</sup>

### Devices electrical characterisation

At this point the electrical characterization of the crystalline thin films of  $C_8O$ -BTBT- $OC_8$  and  $C_8O$ -BTBT- $OC_8$ : $PS_{100k}$  as active layers in OFET devices was performed. Electrical characterization consisted of measuring transfers and output characteristics to extract the figures of merit of the devices. Transfer measurements are shown in **Figure 4.6**.  $C_8O$ -BTBT- $OC_8$ -based thin films exhibit *p*-type field-effect behaviour, with some degree of hysteresis, probably due to charge traps at the OSC/gate dielectric interface. The blended OSC showed better performances, as

expected from the previous work carried out in our group, increasing the field-effect mobility,  $\mu_{FE,sat}$ , from  $0.09(\pm 0.03) \text{ cm}^2/\text{V}\cdot\text{s}$  to  $0.92(\pm 0.02) \text{ cm}^2/\text{V}\cdot\text{s}$ .<sup>48</sup>

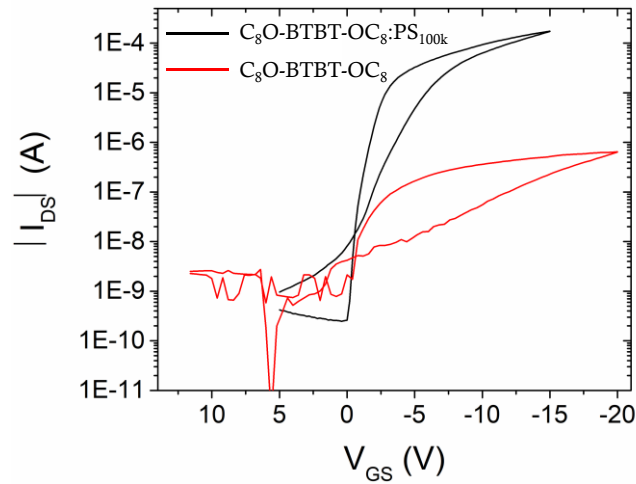


**Figure 4.6.**  $I$ - $V$  transfer characteristics of  $C_8O$ -BTBT- $OC_8$ -based thin films on Si/SiO<sub>2</sub> substrates, plotted in semilogarithmic scale in forwards and backwards directions. Black curve is relative to a  $C_8O$ -BTBT- $OC_8$ :PS<sub>100k</sub> thin film, measured by sweeping  $V_{GS}$  from 5 V to -15 V at  $V_{DS} = -16$  V. Red curve corresponds to bare  $C_8O$ -BTBT- $OC_8$  thin film, measured by sweeping  $V_{GS}$  from 12 V to -20 V at  $V_{DS} = -20$  V.

Afterwards, a systematic fabrication and electrical characterization of pristine and blended  $C_8O$ -BTBT- $OC_8$ -based EGOFETs was carried out. Electrical characterization of EGOFET devices was performed by confining the liquid electrolyte in the region of the interdigitated electrodes (IDEs) and of the coplanar gate, with the aid of a polydimethylsiloxane (PDMS) gasket. In **Figure 4.7** and **Figure 4.8**  $I$ - $V$  transfer and output characteristics are reported, respectively. From the transfer measurements, the main figures-of-merit were calculated. Due to the difficulties in obtaining reliable values for double layer capacitances ( $C_{dl}$ ), it has been decided to evaluate the device performances by the product  $C_{eff}\mu_{FE,lin}$ , as it is common for describing EGOFET devices in literature. This product is extracted from the slope of the fitting curve (see Experimental Chapter). The other key parameter calculated is the maximum transconductance, referred to as  $g_m$ , which is the first derivative of  $I_{DS}$  vs  $V_{GS}$  curves in the linear regime ( $V_{DS} = -0.05$  mV) and is an indication of how sensitive the device response is to the applied potential. Accordingly, EGOFETs displaying high transconductance are desirable in sensors applications.<sup>50</sup>

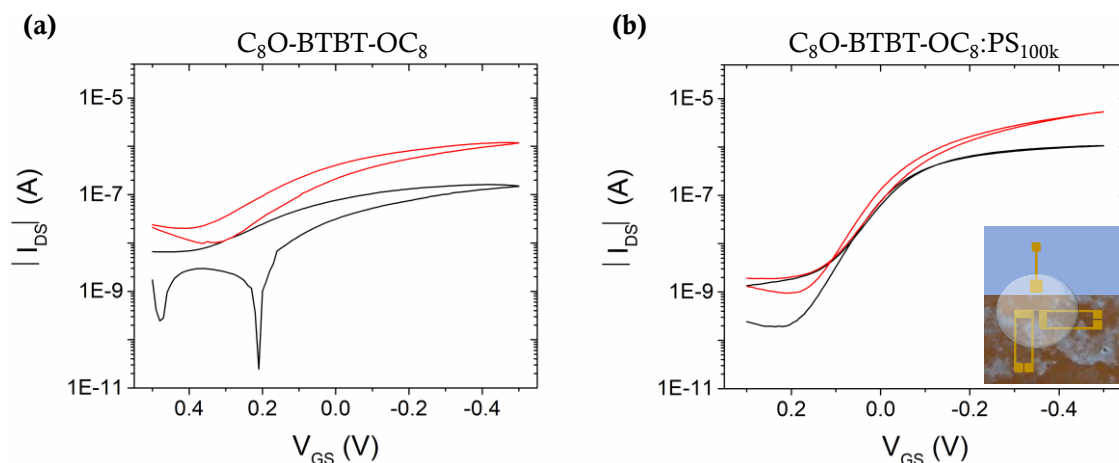


**Figure 4.7.**  $I$ - $V$  transfer characteristics of (a) pristine  $C_8O$ -BTBT- $OC_8$ -based EGOFET and (b)  $C_8O$ -BTBT- $OC_8:PS_{100k}$ . Black curves refer to measurements recorded at  $V_{DS} = -0.05$  V (linear regime), red curves were measured at  $V_{DS} = -0.4$  V (saturation regime). Au coplanar gate was employed, and MilliQ water acted as gate dielectric. In the inset illustration of the EGOFET device and water confinement.

In **Table 4.1** the EGOFET figures of merit extracted in the linear regime ( $V_{DS} = -0.05$  V) for the two types of thin films are summarized. Considering the measured curves and the extrapolated parameters, OSC blended with PS active layers exhibit better performances with respect to pristine OSC thin films, even in EGOFET configuration. In particular,  $C_{eff}\mu_{FE,lin}$  improves from  $0.09(\pm 0.06) \mu S \cdot V^{-1}$  to  $0.16(\pm 0.02) \mu S \cdot V^{-1}$ . The former value is comparable with the one found for the only BTBT-based EGOFET device reported in the literature, which is claimed to be equal to  $0.112(\pm 0.080) \mu S \cdot V^{-1}$ . When the OSC is blended with PS, this value further increases. On the other hand, transconductance,  $g_m$ , is also increased for the blended thin film, but it is lower with respect to the one reported in the literature for the BTBT-based EGOFET, namely  $45(\pm 32) \mu S$ .<sup>50</sup> Finally, the  $I_{on/off}$  ratio improves almost one order of magnitude for the blended OSC, reaching competitive values in the same range of other state-of-the-art EGOFET devices.<sup>50,55</sup>

**Table 4.1.** EGOFET figures of merit relative to pristine  $C_8O$ -BTBT- $OC_8$  and to  $C_8O$ -BTBT- $OC_8$ :PS<sub>100k</sub> thin films on Si/SiO<sub>2</sub>, recorded with the coplanar Au gate in MilliQ water. Extracted in the linear regime:  $V_{DS} = -0.05$  V.

Thin film composition	$C_{eff} \cdot \mu_{FE,lin}$ ( $\mu S \cdot V^{-1}$ )	$g_m$ ( $\mu S$ )	$V_{th}$ (mV)	$I_{on/off}$
$C_8O$ -BTBT- $OC_8$	0.09( $\pm 0.06$ )	1.5( $\pm 1.0$ )	-30( $\pm 150$ )	$\approx 10^2$
$C_8O$ -BTBT- $OC_8$ :PS <sub>100k</sub>	0.16( $\pm 0.02$ )	2.5( $\pm 0.3$ )	70( $\pm 40$ )	$10^2$ - $10^3$

In **Figure 4.8** output characteristics for the pristine thin film and the thin film blended with PS are illustrated. It is clear how the current modulation improves for the blended active layer, achieving an almost ideal MOSFET behaviour. No hysteresis is present and also no contact resistance appears, as it is deducible from the perfect linearity in the low-voltage region. Thus, from this part, it can be concluded that EGOFET devices based on  $C_8O$ -BTBT- $OC_8$ :PS<sub>100k</sub> thin film deposited by BAMS technique exhibits promising electrical properties.

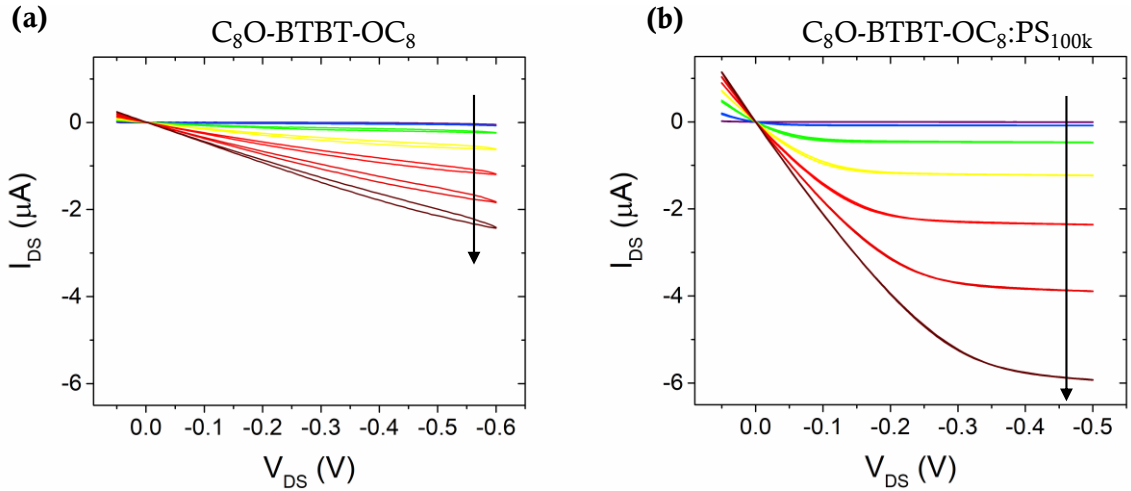


**Figure 4.8.** Output characteristics recorded with coplanar polycrystalline Au. (a) pristine  $C_8O$ -BTBT- $OC_8$  and (b)  $C_8O$ -BTBT- $OC_8$ :PS<sub>100k</sub> thin film.  $V_{DS}$  was swept from 0.05 V to -0.6 V and from 0.05 V to -0.5 V respectively, in the forward and backward directions. Constant  $V_{GS}$  applied were equal to: 0.35 V, 0.20 V, 0.05 V, -0.1 V, -0.25 V, -0.40 V, -0.55 V (in the direction of the arrows) and MilliQ water acted as gate dielectric.

### Stability assessment

Proven the good electrical properties of these devices, their stability in liquid media for a longer period was assessed. In particular, i) shelf-stability, ii) current monitoring and iii) bias stress measurements were carried out.

Regarding **shelf-stability** experiments, a pure C<sub>8</sub>O-BTBT-OC<sub>8</sub> thin film EGOFET and two blended with PS thin film EGOFETs were prepared. PDMS pools were placed on top of the device, to confine the liquid media in the region of the coplanar gate and IDEs. MilliQ water was used as gate dielectric for the C<sub>8</sub>O-BTBT-OC<sub>8</sub> device and one of the devices with the blended film. Further, a more complex electrolyte media, a phosphate buffer saline (PBS), was also used for the other blended film device. Transfer and output characteristics were recorded for the as-prepared devices. Afterwards, devices were stored at 4 °C, to avoid liquid evaporation. Electrical measurements were recorded once a day at room temperature during the first two weeks, and then three times per week, during two months. *I-V* transfers are shown in **Figure 4.9**. With time, a significant shift of the  $V_{th}$  occurred, but the hysteresis did not increase dramatically and the devices were still operating well. It is the first time, as far as we know, that an EGOFET device capable to stand two months in liquid media has been reported.

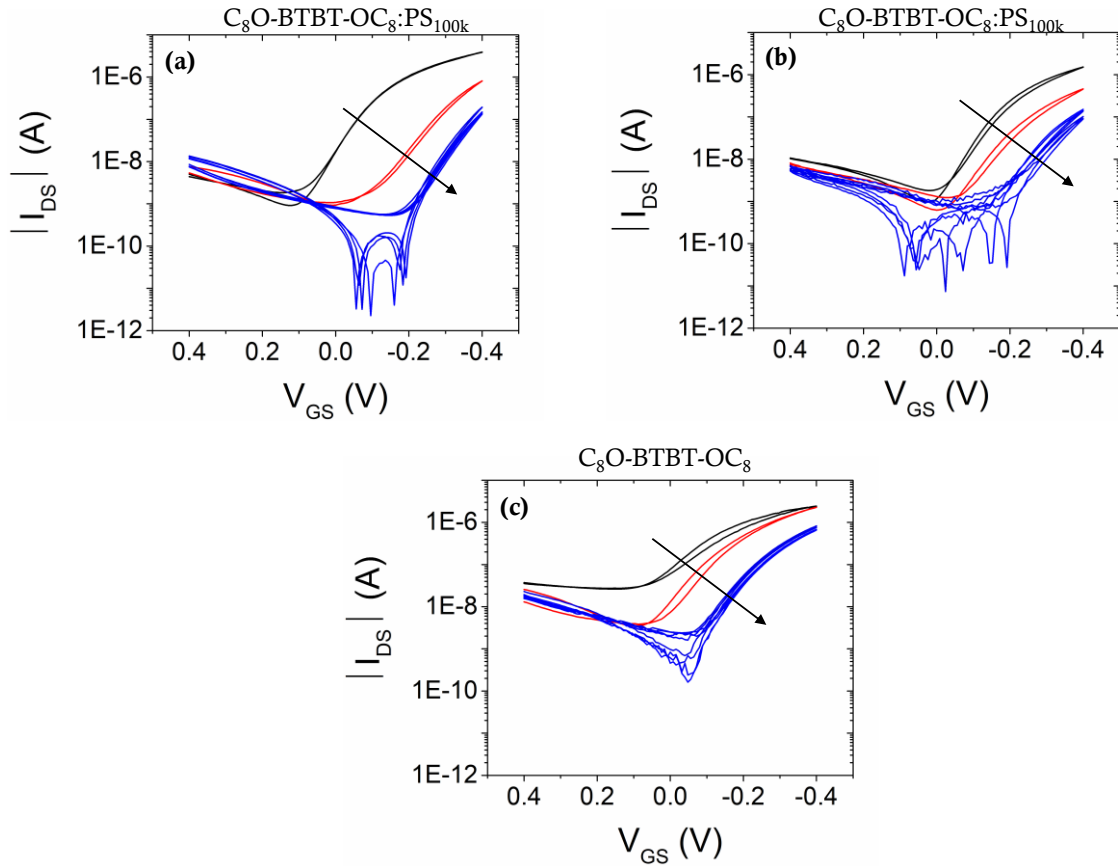


**Figure 4.9.** Shelf-stability experiment.  $I$ - $V$  transfers characteristics recorded in saturation regime,  $V_{DS} = -0.4$  V and plotted in semilogarithmic scale. The black curves are referred to the as-prepared devices, the red curves correspond to the transfers recorded after 15 days and the blue curves are the measurements in a period that spans from 52 to 59 days after the sample preparation. (a) and (c) were measured in MilliQ water and (b) in PBS 1x, at pH=7.2.

Continuous **current monitoring** of  $C_8O$ -BTBT- $OC_8$  device in MilliQ medium was performed and the results are reported in **Figure 4.10**. A constant  $V_{GS} = -0.4$  V and a constant  $V_{DS}$  as low as  $-0.05$  V were applied during the measurements. A decrease in the initial current occurred immediately, and it continued decreasing without reaching a steady-state. Before and after the current monitoring,  $I$ - $V$  transfer characteristics were recorded. From the comparison of these  $I$ - $V$  transfer characteristics (**Figure 4.10,b**), it is evident that some changes are occurring in the OSC thin film layer, considering the dramatic shift of the  $V_{th}$  towards more negative values. As we will discuss later, the

inhomogeneity of the OSC layer due to the absence of the polymeric binder agent forms defect sites, from which deterioration caused by the liquid media can start easier.

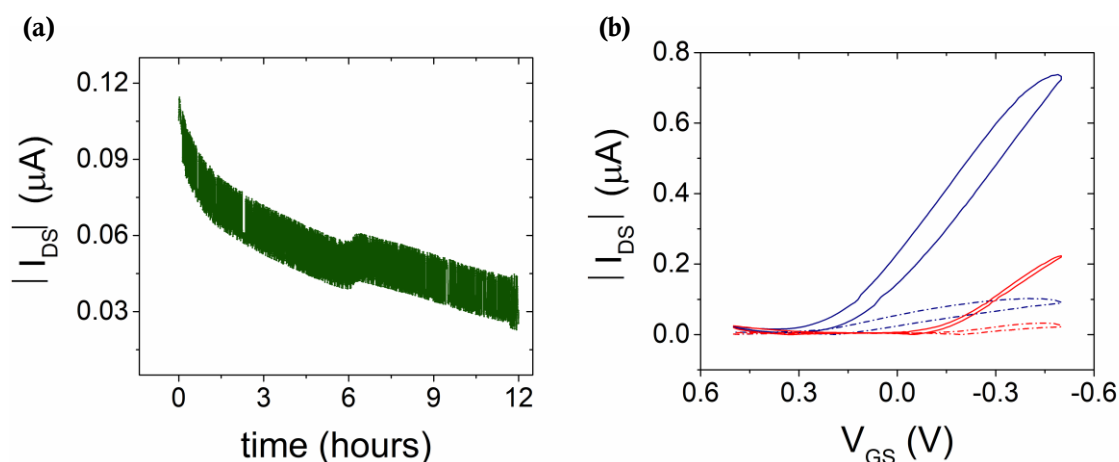


**Figure 4.10.** Stability under electrical stress of  $\text{C}_8\text{O-BTBT-OC}_8$  thin film. (a) Current vs time profile:  $V_{DS} = -0.05$  V,  $V_{GS} = -0.4$  V. (b)  $I$ - $V$  transfer characteristics recorded before the current monitoring experiment (blue lines) and after it (red lines) in linear regime (dashed lines)  $V_{DS} = -0.05$  V, and saturation regime (solid line),  $V_{DS} = -0.4$  V. Gate dielectric: MilliQ water.

The same typology of experiment was carried out for  $\text{C}_8\text{O-BTBT-OC}_8\text{:PS}_{100\text{k}}$  thin film devices (**Figure 4.11**). In this case, during the first hour of measurement, current increases, reaching a quasi-steady-state for the subsequent 8 hours, after which a slow, but constant decrease of the current is noticed. In the transfer characteristics recorded after the continuous monitoring measurements, an increase of the hysteresis is observed, but no significant variation in terms of  $V_{th}$  or current is found (**Figure 4.11, b**). The hysteresis could be ascribed to an increase of surface defects due to the long exposition of the OSC to water under electrical stress. This high stability during current monitoring is very promising for the application of these EGOFET devices in sensing, where changes in the current have to be ascribed solely to the presence of an analyte and, hence, the possible changes coming from device deterioration or instability could importantly interfere in the response.

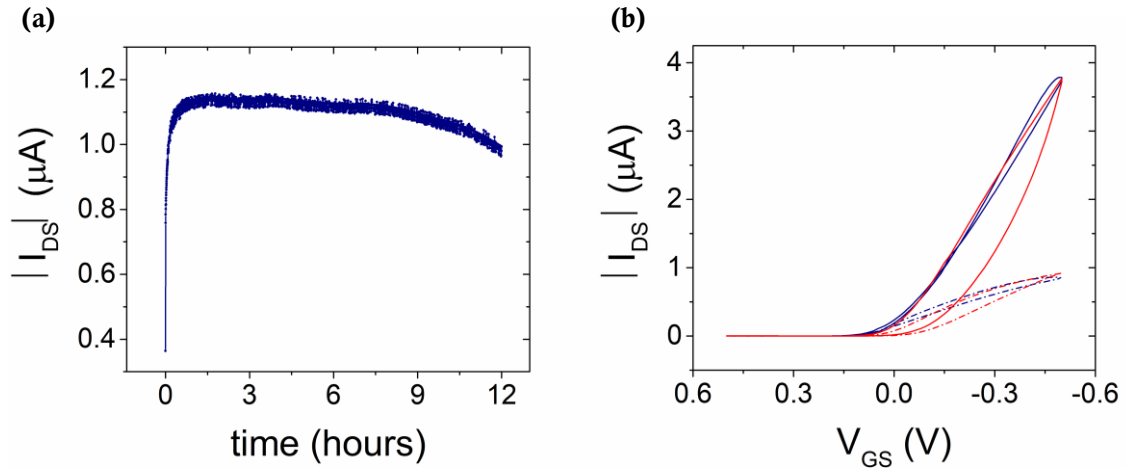


**Figure 4.11.** Stability under electrical stress of  $C_8O$ -BTBT- $OC_8$ : $PS_{100k}$ . (a) Current vs time profile:  $V_{DS} = -0.05$  V,  $V_{GS} = -0.4$  V. (b)  $I$ - $V$  transfer characteristics recorded before the current monitoring experiment (blue lines) and after it (red lines) in linear regime (dashed lines)  $V_{DS} = -0.05$  V, and saturation regime (solid line),  $V_{DS} = -0.4$  V. Gate dielectric: MilliQ water.

Apart from current monitoring, a **bias-stress** stability study was performed for devices based on the thin film blends. During this experiment, devices were measured under harder stress, namely applying a constant  $V_{GS} = -0.4$  V and a constant  $V_{DS} = -0.4$  V, and simultaneously recording the output current. The recording of the current was interrupted every ten minutes to measure transfers in linear and saturation regime. In this way, one can have a better understanding of what is happening during electrical stress. The overlap of all the transfers recorded, in linear and saturation regime, are reported in **Figure 4.12**. Slight but constant decrease of the current is registered, but after 10 hours of continuous measurements, the device is still working properly.



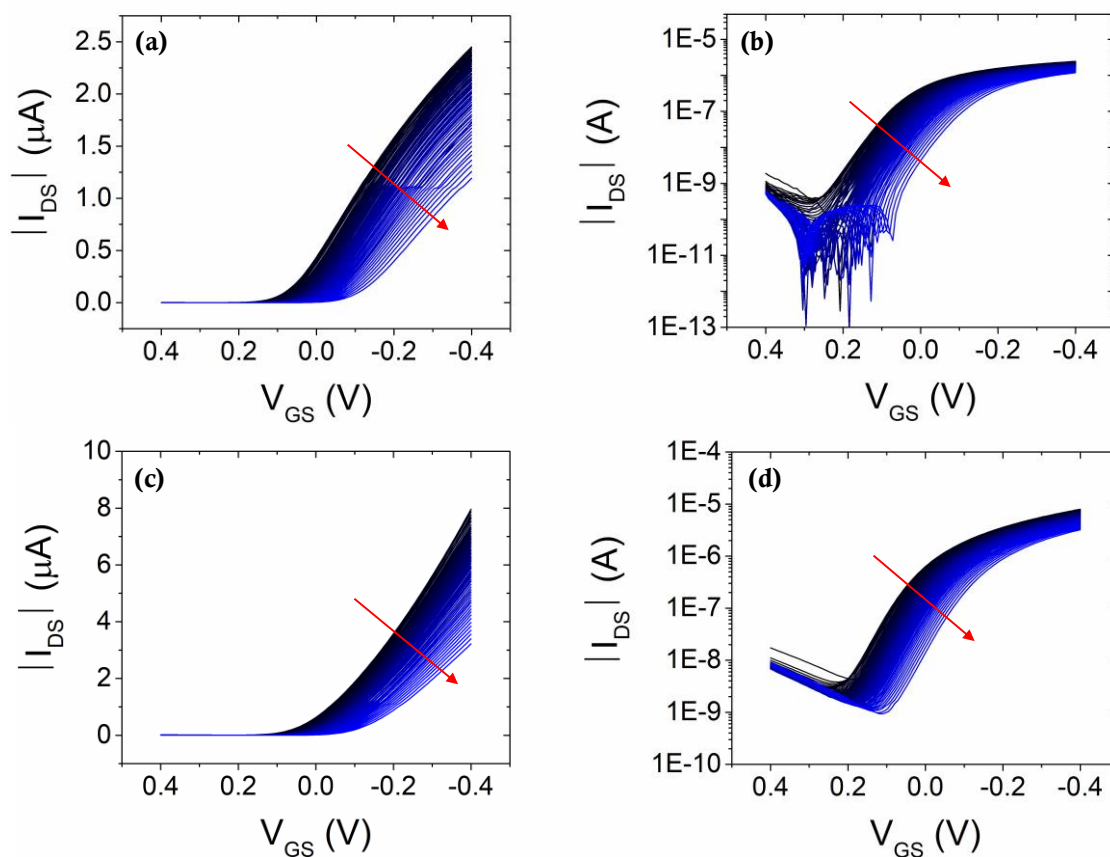


**Figure 4.12.**  $I$ - $V$  transfer characteristics recorded during bias-stress of  $C_8O$ -BTBT- $OC_8$ : $PS_{100k}$  thin film in MilliQ water.  $I$ - $V$  transfers were measured after 10 minutes of current monitoring ( $V_{DS} = -0.4$  V,  $V_{GS} = -0.4$  V), repeating this cycle during ten hours. (a)  $V_{DS} = -0.05$  V, (b) semilogarithmic plot,  $V_{DS} = -0.05$  V. (c)  $V_{DS} = -0.4$  V, (d) semilogarithmic plot,  $V_{DS} = -0.4$  V.

In **Figure 4.13** the curve relative to the current monitoring during the bias stress experiment is reported. As in the previous experiment, the current increases during the initial minutes, and then it reaches a sort of steady-state. However, in this experiment, after one hour, the current starts to decrease continuously. Interestingly, in the inset, it is displayed the shape of the current  $\nu s$  time after each transfer recording. It seems that some time is required for the current to recover. This can probably be ascribed to the double-layer formation.

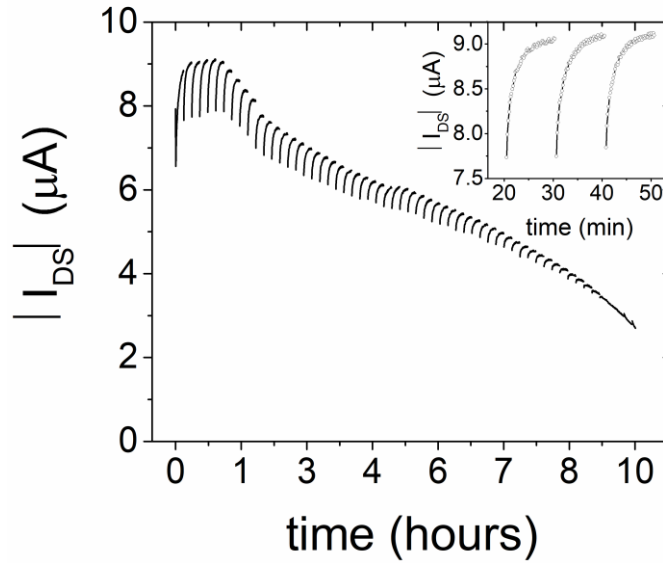


**Figure 4.13.** Current monitoring under bias-stress of  $C_8O$ -BTBT- $OC_8$ : $PS_{100k}$  thin film:  $V_{DS} = -0.4$  V,  $V_{GS} = -0.4$  V. In the inset a zoom of the  $I$ -time profile curve during the 1<sup>st</sup> hour of measurement is reported. Electrolyte: MilliQ water.

The same experiment was also carried out in phosphate buffer saline (PBS) medium and the results are illustrated in **Figure 4.14** and **Figure 4.15**. As expected, PBS resulted to be more detrimental for the device performance. The decrease of the current is dramatic during the first minutes of the measurement and, after the whole bias stress test, the device is not working well anymore. It is worth noting that the behaviour of the current *vs* time plot, is opposite to the one registered in MilliQ water. In fact, current decreases continuously, reaching a steady-state. This phenomenon could be indicative of ions penetration that favours the decrease of the current.

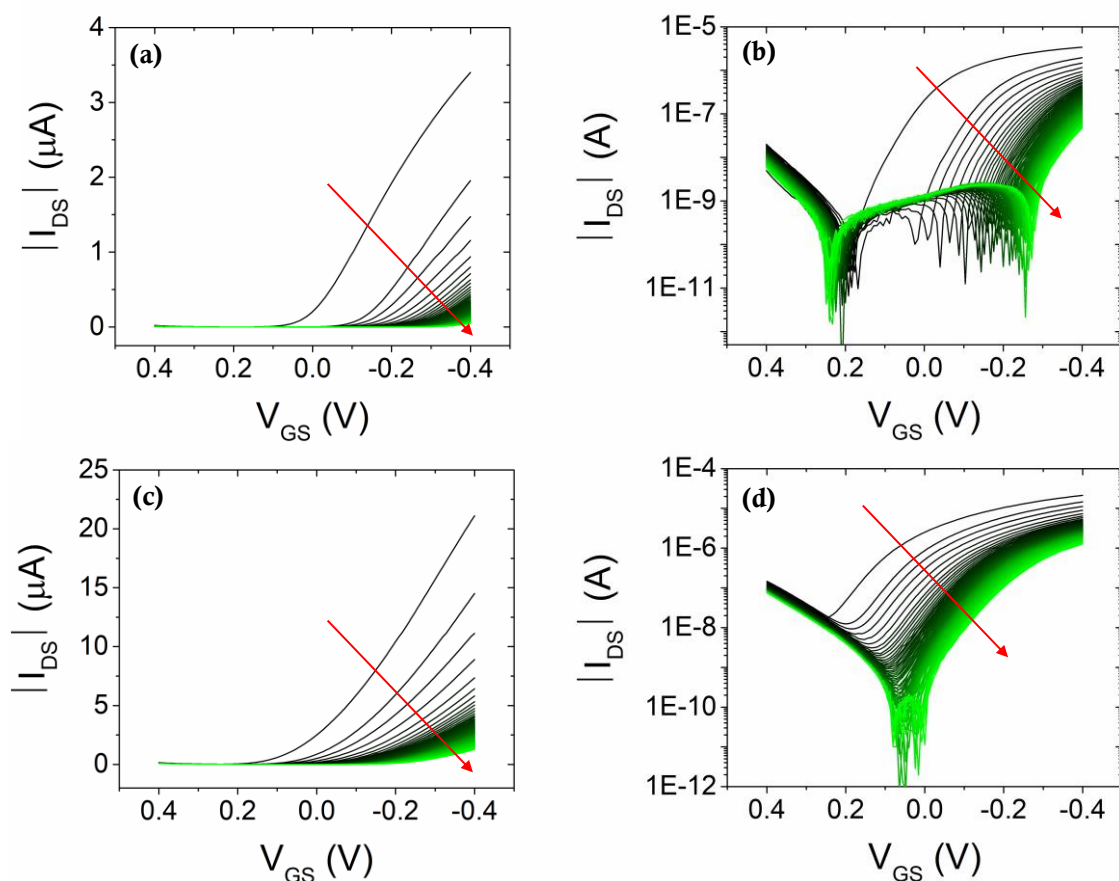


**Figure 4.14.**  $I$ - $V$  transfer characteristics recorded every 10 minutes during 10 hours during bias-stress of  $C_8O$ -BTBT- $OC_8$ : $PS_{100k}$  thin film in PBS 1x. (a)  $V_{DS} = -0.05$  V, (b) semilogarithmic plot,  $V_{DS} = -0.05$  V. (c)  $V_{DS} = -0.4$  V, (d) semilogarithmic plot,  $V_{DS} = -0.4$  V.

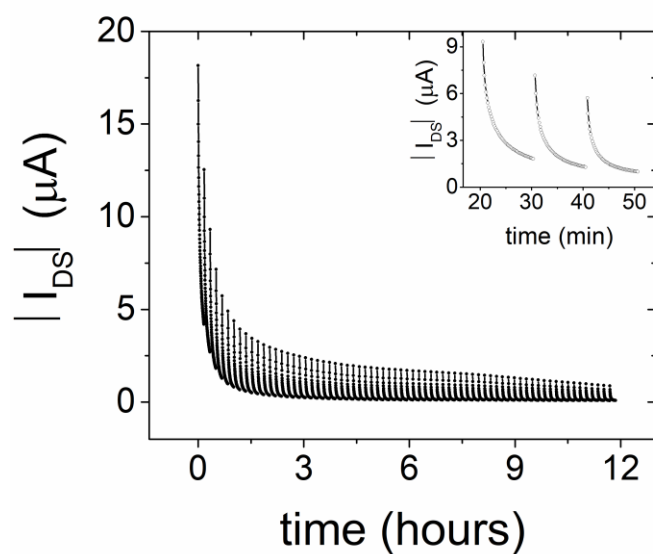


**Figure 4.15.** Current monitoring under bias-stress.  $V_{DS} = -0.4$  V,  $V_{GS} = -0.4$  V. In the inset a zoom of the  $I$ - $time$  profile curve during the 1<sup>st</sup> hour of measurement is reported. Electrolyte: PBS 1x solution, pH= 7.2.

It has been noticed that, after removing the water from the active layer, EGOFET performances decrease significantly. In order to assess the reason for this phenomenon, the characteristics and performance of the devices thin films that had been dried after a first EGOFET characterisation were investigated. First of all, XRD and AFM characterization, as well as electrical characterization in the OFET and EGOFET mode, were performed for the as-prepared devices. It is known that the conducting channel is formed in the very first monolayers of the OSC in contact with the dielectric. In our case, two different configurations are displayed, i) BGBC configuration for OFETs and ii) TGBC for EGOFETs. Consequently, the interface responsible for charge transport is different for the two configurations, being in the second case in direct contact with the liquid dielectric. Afterwards, water was removed and the devices were dried with  $N_2$  flow. Then, the films were characterised by XRD and AFM again. Subsequently, the OFET electrical measurement was repeated and then a fresh droplet of water was added again on the active layer to carry out the EGOFET electrical measurements. The performances of the devices were then compared with the initial ones.

The XRD characterisation reveals that no significant variation is observed on the thin films crystallinity after water removal, both for the bare  $C_8O$ -BTBT- $OC_8$  and  $C_8O$ -BTBT- $OC_8$ : $PS_{100k}$  thin films (**Figure 4.16**).

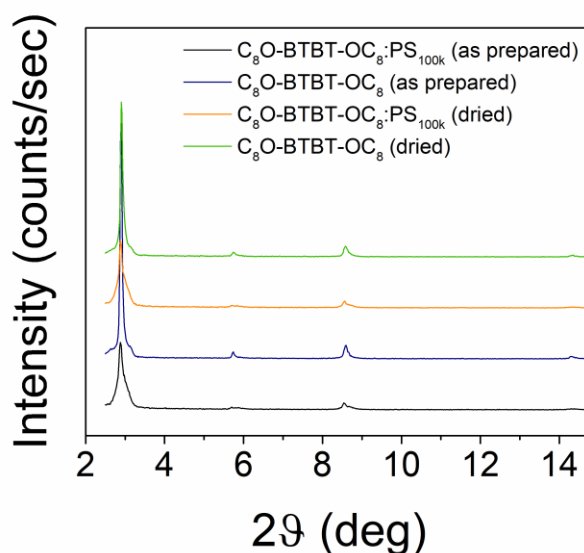


**Figure 4.16.** X-Ray diffractograms of the thin-films based on  $C_8O$ -BTBT- $OC_8$  fabricated by BAMS on Silicon substrate. Comparison of the as-prepared film diffractograms (black and blue lines) with the films diffractograms after water removal (orange and green lines).

Analysing AFM images (**Figure 4.17**), it is quite clear that initially, the pristine  $C_8O$ -BTBT- $OC_8$  thin film displays more surface defects with respect to the  $C_8O$ -BTBT- $OC_8$ : $PS_{100k}$  thin film. These defects are easy access for water to penetrate more deeply into the film, decreasing the efficiency of the devices. After drying the devices, defects increase in both thin films, but  $C_8O$ -BTBT- $OC_8$ : $PS_{100k}$  thin film appears to be the most affected by water removal in proportion.

In **Figure 4.18**  $I$ - $V$  transfer characteristics are reported. As already stated above,  $C_8O$ -BTBT- $OC_8$ : $PS_{100k}$  thin film devices exhibit better performances, both in OFET and in EGOFET configuration, with respect to the devices based on the pristine OSC. In the case of  $C_8O$ -BTBT- $OC_8$ : $PS_{100k}$  thin film device, a dramatic negative shift of the  $V_{th}$  was registered, but only in the EGOFET configuration, confirming our above hypothesis pointing a degradation of the thin film in contact with the electrolyte. Unexpectedly, in the case of pristine OSC based device, no  $V_{th}$  shift was observed, either for the EGOFET and OFET configurations. In this case, as observed also from AFM images, surface defects and inhomogeneities were present already in the as-prepared devices. Thus, a further increase of these defects does not affect significantly the device performance as in the case of the films based on the OSC blended with polystyrene.

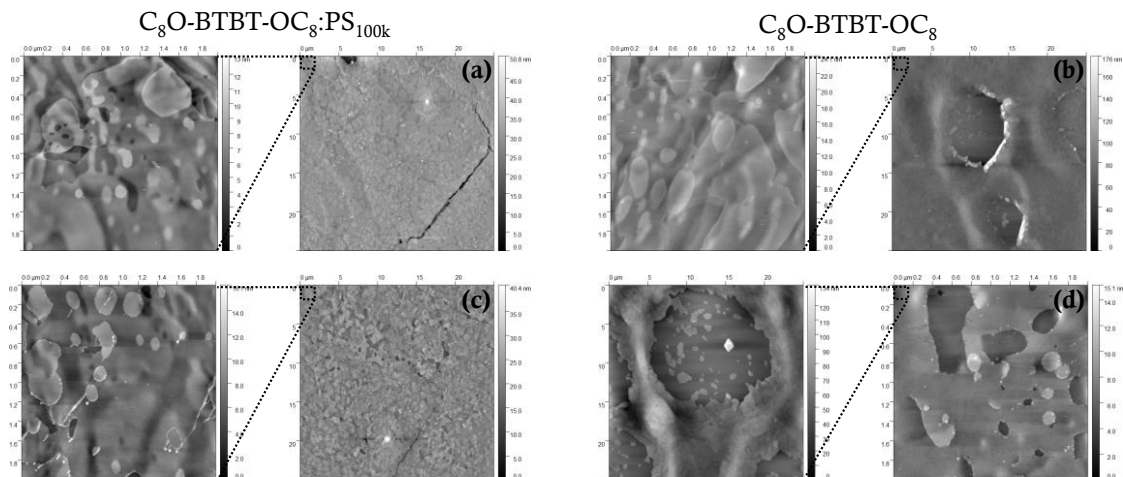


**Figure 4.17.** AFM images of thin-films based on  $C_8O$ -BTBT- $OC_8$  fabricated by BAMS on Silicon substrates, (a,b) as prepared and (c,d) after measuring the EGOFET device and drying it. The images are:  $2 \times 2 \mu m$ .

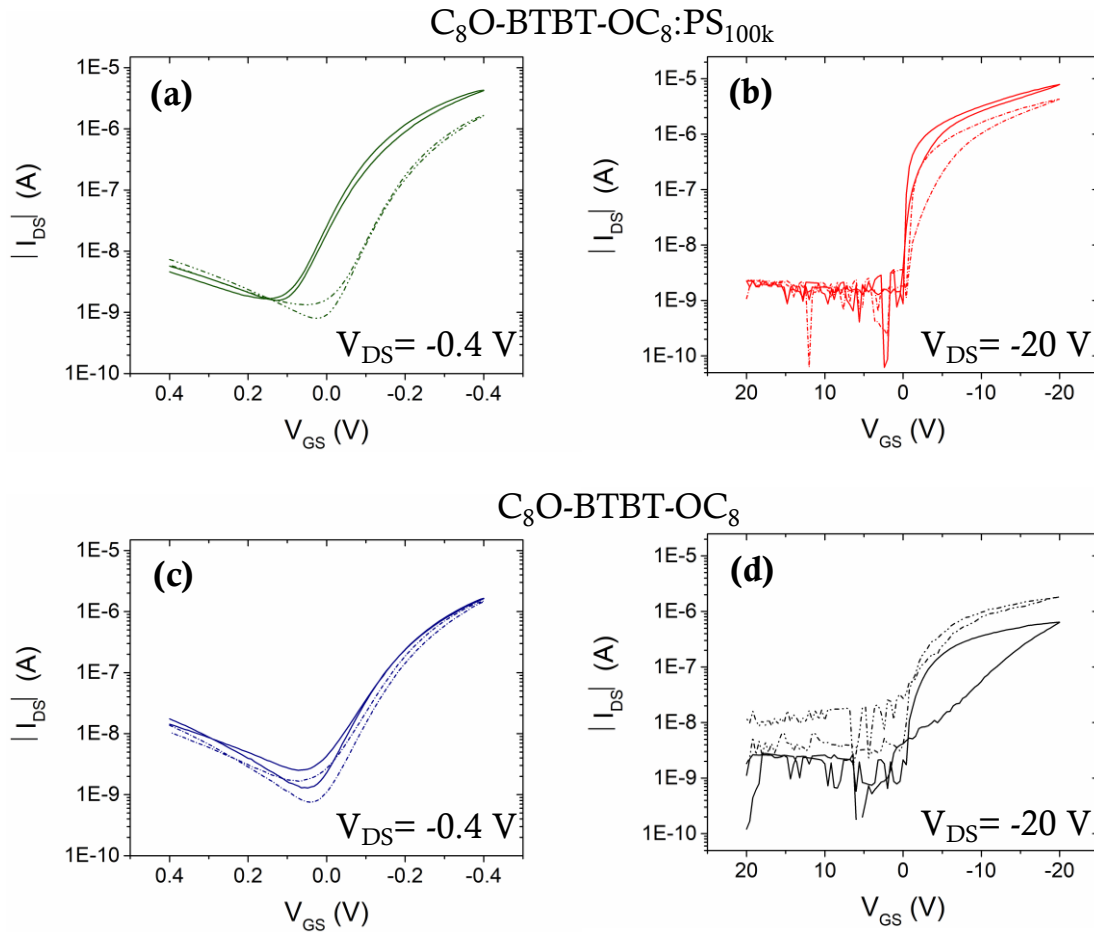


**Figure 4.18.**  $I$ - $V$  transfer characteristics recorded for the as-prepared devices (solid lines) and after the removal of water (dashed lines). (a,b)  $C_8O$ -BTBT- $OC_8$ : $PS_{100k}$  thin film devices measured in EGOFET and OFET mode, respectively; (c,d) bare  $C_8O$ -BTBT- $OC_8$  thin film devices measured in EGOFET and OFET mode, respectively.

- **$C_8O$ -BTBT- $OC_8$ : $PS_{100k}$ -based EGOFETs on plastic substrates**

Aiming at the development of an all-flexible EGOFET device, *Kapton*<sup>®</sup> foils (75  $\mu$ m thick) and polyethylene naphthalate foils (PEN) (75  $\mu$ m thick) were selected as substrates. The same device layout as before was employed using water MilliQ as the electrolyte. Only thin film of the OSC blended with PS were prepared, due to the better performances exhibited with Si/ $SiO_2$  based devices.

In **Figure 4.19** a POM image of  $C_8O$ -BTBT- $OC_8$ : $PS_{100k}$  thin film coated on *Kapton*<sup>®</sup> by BAMS is shown, demonstrating the crystallinity and homogeneity of the film. Taking a visible polarized image of the film on PEN substrate was not possible due to the transparency of both the substrate and the film.

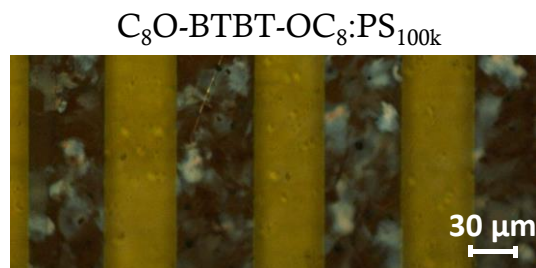


**Figure 4.19.** Polarized optical microscopy (POM) image of  $C_8O$ -BTBT- $OC_8$ : $PS_{100k}$ -based thin films on Kapton® substrate.

$I$ - $V$  transfer characteristics and output measurements were carried out and are shown in **Figure 4.20** and in **Figure 4.21**.

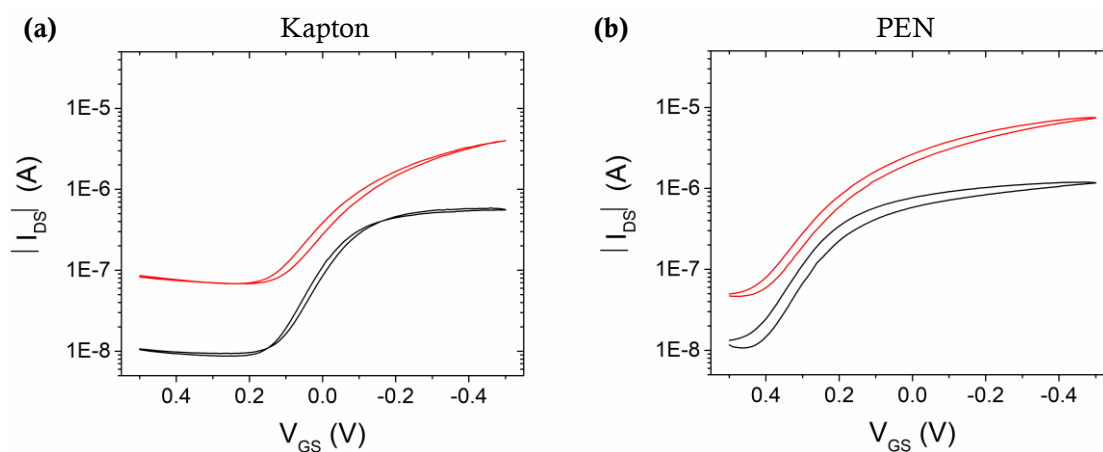


**Figure 4.20.**  $I$ - $V$  transfer characteristics of  $C_8O$ -BTBT- $OC_8$ : $PS_{100k}$ -based thin films on (a) Kapton substrate and (b) PEN substrate, plotted in semilogarithmic scale, sweeping  $V_{GS}$  from +0.5 V to -0.5 V, forward and backward directions. Black curves correspond to measurements at  $V_{DS} = -0.05$  V and red curves applying  $V_{DS} = -0.4$  V. Measurements were recorded in MilliQ water employing the coplanar Au gate.



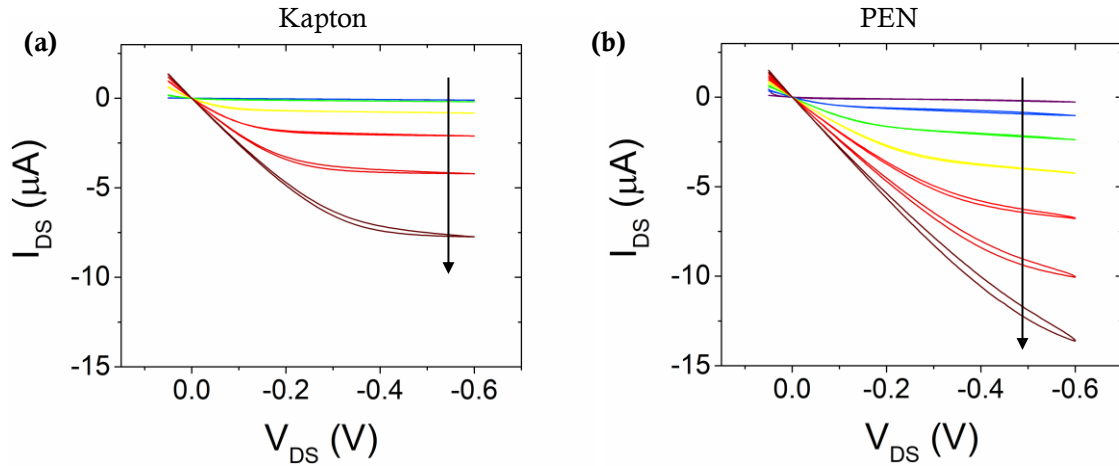


**Figure 4.21.** Output characteristics of  $C_8O$ -BTBT- $OC_8$ : $PS_{100k}$ -based thin film on (a) Kapton substrate and (b) PEN substrate, sweeping  $V_{DS}$  from +0.05 V to -0.6 V, forward and backward directions. Gate potentials applied in the following order as indicated with the arrows in the figure:  $V_{GS} = +0.35$  V,  $V_{GS} = +0.2$  V,  $V_{GS} = 0.05$  V,  $V_{GS} = -0.1$  V,  $V_{GS} = -0.25$  V,  $V_{GS} = -0.4$  V,  $V_{GS} = -0.55$  V. The measurements were recorded in MilliQ water employing the coplanar Au gate.

From the measurements of the transfer, figures-of-merit were extracted in the linear regime ( $V_{DS} = -0.05$  V) and are reported in **Table 4.2**. Devices on *Kapton*<sup>®</sup> substrates exhibited good EGOFET performances although revealed slightly worse parameters with respect to the ones extracted from the devices on Si/SiO<sub>2</sub>. In turn, devices patterned on PEN substrates resulted in lower performances. It could be ascribed to a less degree of the crystallinity of the thin film due to a higher roughness of the surface of the plastic substrate.

**Table 4.2.** EGOFET figures of merit relative to  $C_8O$ -BTBT- $OC_8$ : $PS_{100k}$  thin film on *Kapton*<sup>®</sup> and PEN substrates, recorded with the coplanar Au gate in MilliQ water. Extracted in linear regime ( $V_{DS} = -0.05$  V).

Substrate	$C_{eff} \cdot \mu_{FE,lin}$ ( $\mu S \cdot V^{-1}$ )	$g_m$ ( $\mu S$ )	$V_{th}$ (mV)	$I_{on/off}$
<b>Kapton</b>	0.13( $\pm 0.05$ )	2.2( $\pm 0.8$ )	190( $\pm 150$ )	$10^2$
<b>PEN</b>	0.07( $\pm 0.02$ )	1.1( $\pm 0.4$ )	$\approx 400$	$\approx 10^2$

Current monitoring was carried out on devices patterned on PEN substrates. The behaviour is different from the one found in the devices with Si/SiO<sub>2</sub> substrates.



Indeed, in the first hour of measurement, there is an increase in the current. Afterwards the current, instead of stabilizing, started to decrease constantly.  $I$ - $V$  transfers characteristics denote a significant loss of performance after the current monitoring experiment (**Figure 4.22, b**). This is ascribed probably to the less homogeneity of the thin films which causes a faster degradation of the surface exposed to water, and accordingly, more ions penetrate affecting the current flowing.

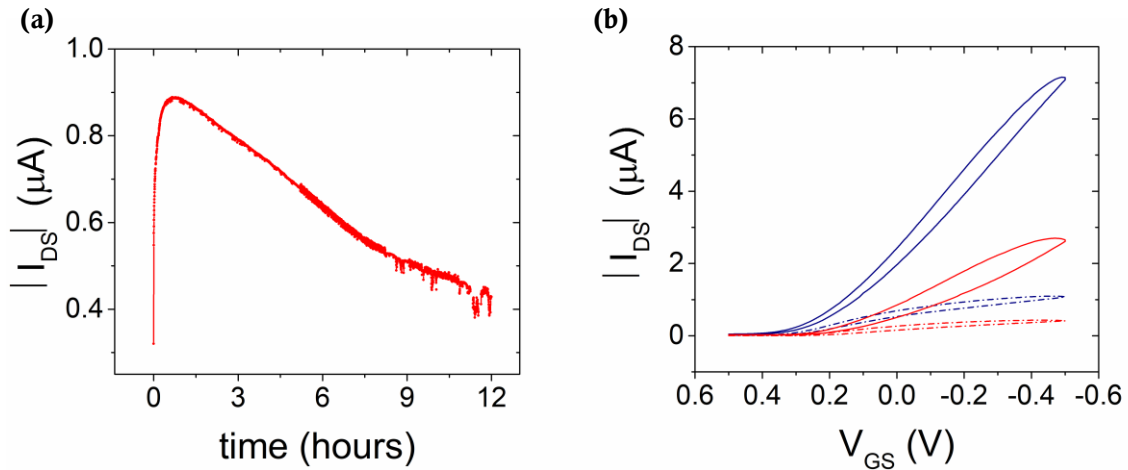


**Figure 4.22.** Stability under electrical stress performed on C8O-BTBT-OC8:PS100k-based EGOFET patterned on a PEN substrate and recorded with a coplanar Au gate. (a) Current vs time profile:  $V_{DS} = -0.05$  V,  $V_{GS} = -0.4$  V. (b)  $I$ - $V$  transfer characteristics recorded before the current monitoring (blue lines) and after it (red lines) in linear regime (dashed lines),  $V_{DS} = -0.05$  V, and saturation regime (solid line),  $V_{DS} = -0.4$  V. Electrolyte: MilliQ water.

Despite to the fact that performances of devices patterned in *Kapton*<sup>®</sup> and PEN substrates resulted to be slightly worse with respect to the ones on Si/SiO<sub>2</sub>, it can be safely stated that C<sub>8</sub>O-BTBT-OC<sub>8</sub>:PS<sub>100k</sub>-based EGOFETs on these plastic substrates, exhibit promising electrical performances, together with the advantage to dispose of flexible devices. For this reason, it was envisioned to study the influence of the electromechanical properties of the devices under compressive and tensile stress.

#### 4.4. Electrical properties under mechanical stress

To achieve a more complete study of the properties of the devices, electrical response under bending strain was evaluated. There are two different directions at which bending can be addressed, i) in the concave side of the flexible sheet, resulting in a

compressive strain, and ii) in the convex side, resulting in a tensile strain. To quantitatively estimate the applied strain, a simple relation is used:<sup>56</sup>

$$\varepsilon = \frac{\Delta L}{L_0} = t_{sub}/2r \quad (4.3)$$

where  $L_0$  is the length of the system without stress and  $\Delta L$  is the variation of the length after the application of the stress,  $t$  is the thickness of the substrate and  $r$  is the radius of curvature. This equation is an approximation valid when the film thickness is negligible with respect to the substrate thickness and the Young modulus of the two layers are similar. The radius of curvature is one of the most used parameters to estimate the deformation magnitude because it is easily derived from the experimental setup (**Figure 4.23**). Other important parameters are the curvature and the bending angle. The curvature corresponds to the inverse of the bending radius and the bending angle refers to the angle formed between two extremities of a bent sample.

A home-made apparatus was realized to apply stress to our devices (further details are explained in chapter 6).<sup>§</sup> The device is fixed by its extremities into a holder. One wall of the holder can be pushed forward or backwards manually through a pivot, to promote the bending of the substrate in the concave or convex direction (**Figure 4.23**). Source, Drain and Gate terminals were connected to a Keithley controlled by a home-made Matlab Script. The experiment was conducted by recording  $I$ - $V$  transfers at different bending radii, in compressive and in tensile strain.

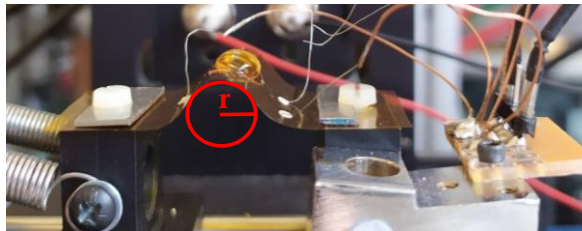


**Figure 4.23.** Real image of the bending apparatus during electrical measurements and graphic representation of the calculation of the radius of curvature, indicating as the radius of the red circle,  $r$ .

---

<sup>§</sup>The bending apparatus was designed and assembled by Dr. Tommaso Salzillo.

Devices on *Kapton*<sup>®</sup> substrates (25  $\mu\text{m}$  thick) were preferred respect to PEN substrates, according to the better electrical performances shown in the previous section. For the same reason, our attention was focused only on the OSC blended with PS. The thickness of *Kapton*<sup>®</sup> foils employed to prepare the devices was equal to 25  $\mu\text{m}$  and it was selected to have a higher resolution in modulating the stress. Once the device was fixed on the bending apparatus, a droplet of water was pipetted into the PDMS gasket, which was previously placed on top of the device. Thus, transfer and output characteristics were recorded to assess the correct operation of the device. Afterwards, a progressive bending of the substrate was induced, and after each bending, at least one transfer was recorded. The strain applied spanned from 0.02% to 0.4% approximatively. The rotation of the pivot of the bending apparatus was manual, so it was not possible to increase the curvature with a perfect linearity. Finally, the device was returned in the flat position, and a transfer was recorded to assess the recovery of the performances. This procedure was carried out for compressive and tensile strain. The results are reported in **Figure 4.24**. It is worth noting how the device response is able to recover almost completely after the strain is removed and the device is placed back in the flat position. However, after the removal of the strain, for achieving the recovering, the acquisition of a few transfer measurements was necessary. As it is clear from the graph, no  $V_{th}$  variation was observed upon application of the strain. Differences in the  $I_{DS}$  are noted, but there is no linear correlation between  $I_{DS}$  variation and the magnitude of the strain applied.

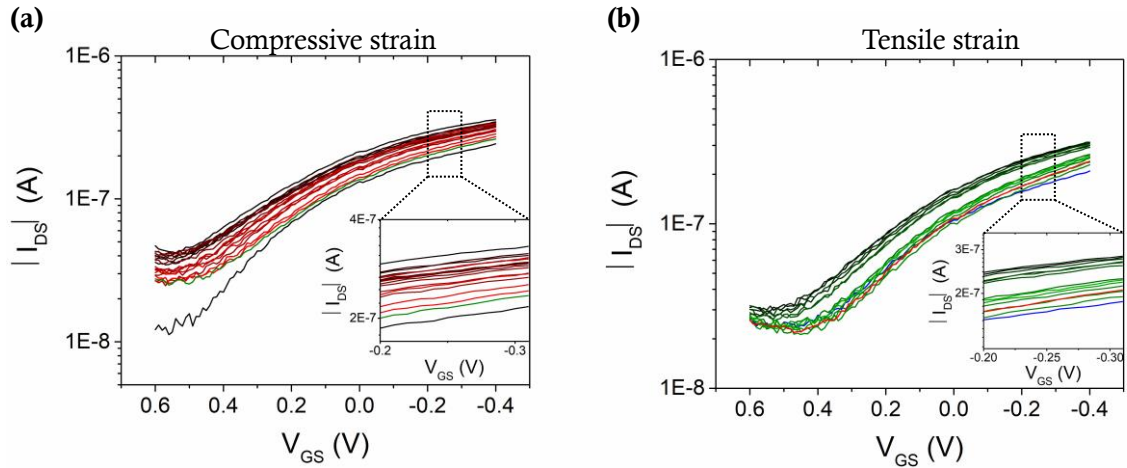


**Figure 4.24.**  $I$ - $V$  transfer characteristics recorded under compressive strain and tensile stress of  $C_8O$ -BTBT- $OC_8$ :PS<sub>100k</sub> thin-film EGOFET using Kapton as substrate and MilliQ water as electrolyte. (a)  $V_{DS} = -0.4$  V. Black and green lines refer to the flat position before and after applying the compressive strains, respectively:  $\epsilon = 0.04\%$ ,  $0.06\%$ ,  $0.07\%$ ,  $0.08\%$ ,  $0.10\%$ ,  $0.12\%$ ,  $0.13\%$ ,  $0.15\%$ ,  $0.17\%$ ,  $0.19\%$ ,  $0.21\%$ ,  $0.25\%$ ,  $0.31\%$ ,  $0.37\%$ . Red curves, from darker to lighter, represent transfer recorded at increasing compressive strains. (b)  $V_{DS} = -0.4$  V. Blue and red lines refer to flat position before and after applying the tensile strain, respectively. Green curves, from darker to lighter green colour, represent transfer recorded at increasing tensile strain,  $\epsilon = 0.04\%$ ,  $0.09\%$ ,  $0.14\%$ ,  $0.17\%$ ,  $0.22\%$ ,  $0.27\%$ ,  $0.31\%$ ,  $0.37\%$ ,  $0.39\%$ ,  $0.41\%$ ,  $0.44\%$ ,  $0.46\%$ .

In **Figure 4.25** the normalized variation of the current extracted from the recorded transfers at  $V_{GS} = -0.4$  V and  $V_{DS} = -0.4$  V as function of the applied strain is presented. Normalization of the current was calculated with respect to  $I_0$ , which is the current measured at the initial flat position. As observed, a linear correlation was not found. For both tensile and compressive strain, application of a strain as low as to  $0.04\%$ , promotes an around  $50\%$  increase of the initial current. Afterwards, further bending in the upward or downward directions, results in a decrease of the current but not following a gradual trend, up to a strain equal to  $0.25\%$ , approximately, and then the two type of strains show different trends. These results are unexpected based on the literature regarding the electrical response of bendable OFET under mechanical strain, as explained above.<sup>57-61</sup> It has been stated that strain can promote geometric changes to the dielectric in OFETs impacting on the dielectric capacitance and, hence, the device electrical response.<sup>57</sup> For EGOFET devices, there are no reported studies, to our knowledge, on the electrical response under mechanical strain. However, it can be claimed that in EGOFETs, where an electrolyte is used as dielectric, strain will not affect the double-layer capacitance,  $C_{dl}$ , as it should not be dependant on geometric

factors.<sup>62,63</sup> Thus, assuming that the contacts are well-preserved at these low strain values, the current variation should be ascribed solely to the active layer or the influence of the electrolyte penetrating it.

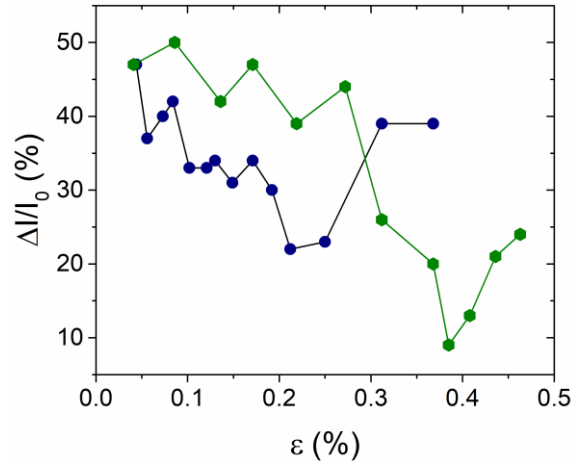


**Figure 4.25.** Normalized current variation as function of the applied strain. Blue circles refer to compressive strain and green symbols to tensile strain. Current variation was calculated at  $V_{DS} = -0.4$  V and  $V_{GS} = -0.4$  V in both cases.

However, the results were different when the stress was applied and the current variation was recorded simultaneously, in *real-time*, as illustrated in **Figure 4.26** for compressive strain and in **Figure 4.27** for tensile strain. During these experiments,  $V_{DS}$  and  $V_{GS}$  were fixed to  $-0.4$  V and the output current was measured as function of time. The current was stabilized when no stress was applied to the device, then a strain was induced until a new steady state was reached. At this point, the device was placed in the flat position again. Ten cycles were realized both for compressive and tensile strain, applying approximatively the same amount of stress, corresponding to a strain  $\epsilon \approx 0.4\%$ . As expected, the current increases when a compressive bending stress is applied to the device, whereas it decreases when a tensile bending stress is applied. After 10 cycles no significant variation of the electrical performances was observed, apart from a constant current drift possibly caused by bias stress. This behaviour is coherent with the results observed in other works.<sup>41,43,44,57,58</sup>

A key parameter to analyse the sensitivity of a material under stress is the so-called gauge factor,  $k$ , which can be defined as follows:

$$k = \frac{\frac{\Delta I}{I_0}}{\frac{\Delta L}{L_0}} = \frac{\Delta I}{I_0} \cdot \frac{1}{\varepsilon} \quad (4.4)$$

From equation (4.4) it is clear that high gauge factors mean high sensitivity in the sense that a very small strain can produce a high change in the output current.<sup>64</sup> The respective gauge factors were calculated using equation (4.4), considering the variation of the current from the flat position to the bended position. They were found to be around 16 and 18 for compressive and tensile strain, respectively. These values suggested a high sensitivity of our material to bending deformation and are in line to those found in literature for OFET devices.<sup>41,65,66</sup>

Previously, the mechanical deformation effect on OFETs based on similar organic semiconducting blends was explored.<sup>67</sup> In this work, the thin film morphology was tuned modifying the coating conditions and it was found that it had a strong influence on the OFET strain sensitivity. Therefore, it was claimed that the mechanical response was driven by the changes in intergrain distances occurring in the strained films. Here, a similar effect might be the origin of the strain response observed in the EGOFETs, although we cannot completely rule out the possibility that reversible molecular packing changes are taking place.<sup>41</sup> A deeper analysis should be conducted at this specific aim.

An interesting aspect of this study, is the difference of the results obtained depending on the measurements modality, i) static transfer recording or ii) *real-time* current monitoring. In the first case, no linear correlation was found between current variation and applied strain. Furthermore, a very small strain caused an increase of the current, both in tensile and compressive thin film deformation. On the other hand, in the case of *real-time* measurements, a fast and reversible response is achieved, also able to differentiate tensile to compressive strain. It is probably due to the fact that when the EGOFET device is under a constant  $V_{DS}$  and  $V_{GS}$ , a thermodynamic equilibrium is created and the  $C_{dl}$  is stabilised. In this case, the variation of current observed can be ascribed solely to deformation in the OSC which promotes a variation of the output current. On the contrary, during transfer recording,  $V_{GS}$  is swept from positive to negative values, in the forward and backward directions, and a transient capacitive

current arises, accordingly to  $C_{dl}$ . This transient capacitive current becomes the predominant factor, limiting a linear response to the applied strain.

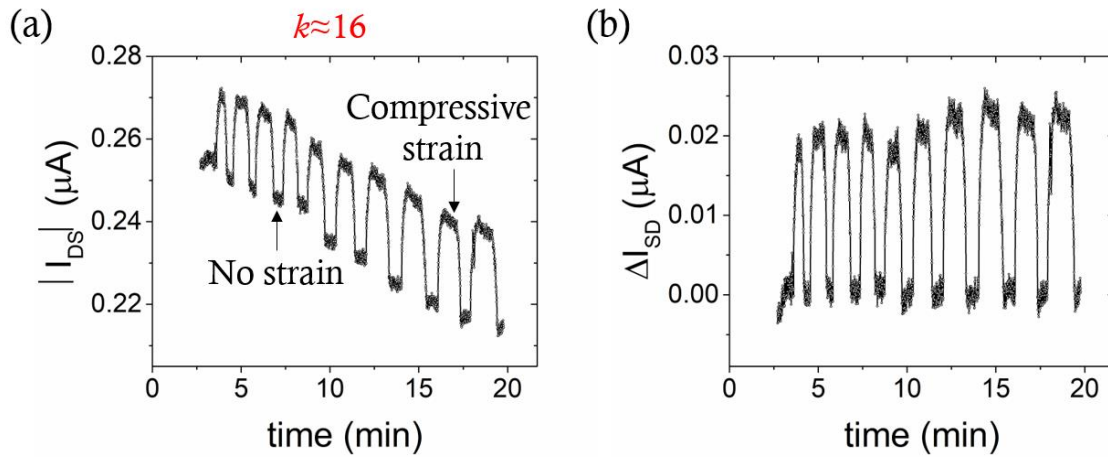


**Figure 4.26.** (a) *I-time* monitoring recorded at  $V_{GS} = -0.4$  V and  $V_{DS} = -0.4$  V, applying cyclic compressive strain. (b) The same plot as in a) but with a baseline subtraction.

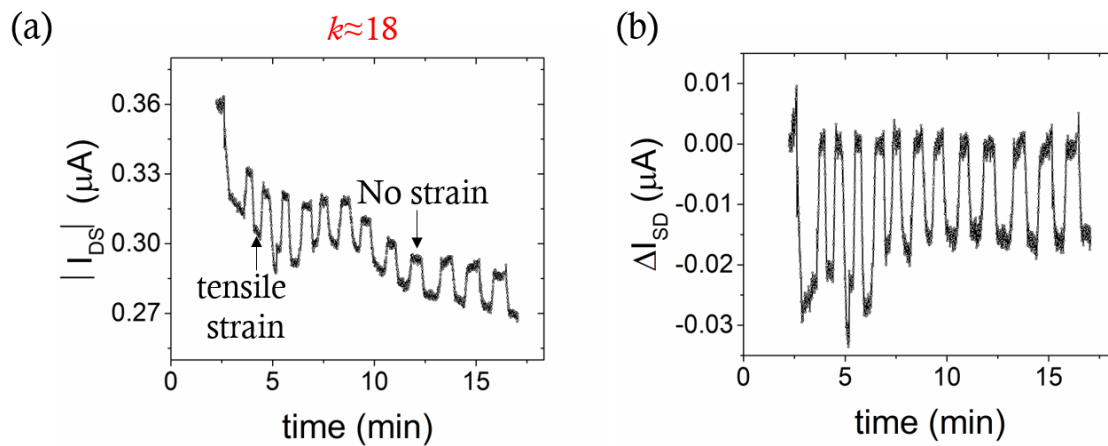


**Figure 4.27.** (a) *I-time* monitoring recorded at  $V_{GS} = -0.4$  V and  $V_{DS} = -0.4$  V, applying cyclic tensile strain. (b) The same plot as in a) but with a baseline subtraction.

Future work, will be devoted to studying the *real-time* current monitoring of the films under different strains in order to establish the dependence of the sensitivity with strain.

#### 4.5. Summary

In summary, in this work C<sub>8</sub>O-BTBT-OC<sub>8</sub>-based thin film EGOFETs were fabricated and characterized for the first time. The thin-films were prepared by BAMS technique employing the bare C<sub>8</sub>O-BTBT-OC<sub>8</sub> OSC and also this material blended with an insulating polymer (*i.e.*, PS), on Si/SiO<sub>2</sub> substrates. An in-depth electrical characterization was carried out and the principal figures of merit were extracted. It was obtained a  $C_{eff} \cdot \mu_{FE,lin} = 0.09(\pm 0.06) \mu\text{S} \cdot \text{V}^{-1}$  and  $C_{eff} \cdot \mu_{FE,lin} = 0.16(\pm 0.02) \mu\text{S} \cdot \text{V}^{-1}$  for pristine C<sub>8</sub>O-BTBT-OC<sub>8</sub> and the blended with PS, respectively. This latter value is higher than the one achieved for the BTBT-based EGOFET reported in literature, *viz.* equal to  $0.11 \mu\text{S} \cdot \text{V}^{-1}$ .<sup>50</sup> Furthermore, the blended active layer exhibited a higher working stability with respect to the pure OSC, able to operate 12 h at stable conditions and showing higher capacity to stand the liquid environment. This was attributed to the fact that the blended OSC thin film displayed a higher degree of crystallinity and homogeneity when prepared with BAMS technique. Afterwards, C<sub>8</sub>O-BTBT-OC<sub>8</sub>:PS<sub>100k</sub> thin films were deposited on flexible substrates, namely Kapton<sup>®</sup> and PEN foils, achieving good performances, with  $C_{eff} \cdot \mu_{FE,lin}$  equal to  $0.13(\pm 0.05) \mu\text{S} \cdot \text{V}^{-1}$  and  $0.07(\pm 0.02) \mu\text{S} \cdot \text{V}^{-1}$ , respectively.

The second part of the work consisted on testing the sensitivity of the thin-film to bending stress. Cycles measurements were reported and gauge factors ( $k$ ) at  $\varepsilon \approx 0.4\%$  were calculated, achieving  $k$  equal to 16 for compressive strain and 18 for tensile strain. These results demonstrate a very high device sensitivity to the application of low strains. The sensitivity can be correlated well to the strain applied only when the device is working in equilibrium condition, otherwise other factors play an important role. This is the first time, as far as we know, that bending properties have been assessed in EGOFET devices, which is crucial for the understanding of the operating mechanisms taking place in EGOFETs and for their application in implantable sensing systems.



## Bibliography

- (1) Harris, K. D.; Elias, A. L.; Chung, H. J. Flexible Electronics under Strain: A Review of Mechanical Characterization and Durability Enhancement Strategies. *Journal of Materials Science* **2016**, *51* (6), 2771–2805.
- (2) Nathan, A.; Ahnood, A.; Cole, M. T.; Lee, S.; Suzuki, Y.; Hiralal, P.; Bonaccorso, F.; Hasan, T.; Garcia-Gancedo, L.; Dyadyusha, A.; et al. Flexible Electronics: The next Ubiquitous Platform. *Proceedings of the IEEE* **2012**, *100* (SPL CONTENT), 1486–1517.
- (3) Tak, Y. J.; Keene, S. T.; Kang, B. H.; Kim, W. G.; Kim, S. J.; Salleo, A.; Kim, H. J. Multifunctional, Room-Temperature Processable, Heterogeneous Organic Passivation Layer for Oxide Semiconductor Thin-Film Transistors. *ACS Applied Materials & Interfaces* **2020**, *12* (2), 2615–2624.
- (4) K. Nomura; H. Ohta; A. Takagi; T. Kamiya; M. Hirano; Hosono, H. Room-Temperature Fabrication of Transparent Flexible Thin-Film Transistors Using Amorphous Oxide Semiconductors. *Nature* **2004**, *432* (November), 488–492.
- (5) Chang, T. C.; Tsao, Y. C.; Chen, P. H.; Tai, M. C.; Huang, S. P.; Su, W. C.; Chen, G. F. Flexible Low-Temperature Polycrystalline Silicon Thin-Film Transistors. *Materials Today Advances* **2020**, *5*, 0–9.
- (6) Park, H.; Oh, D. S.; Lee, K. J.; Jung, D. Y.; Lee, S.; Yoo, S.; Choi, S. Y. Flexible and Transparent Thin-Film Transistors Based on Two-Dimensional Materials for Active-Matrix Display. *ACS Applied Materials and Interfaces* **2020**, *12* (4), 4749–4754.
- (7) Lee, C. C.; Wang, C. W. Interfacial Fracture Investigation of Patterned Active Matrix OLED Driven by Amorphous-Si TFTs under Film-Type Packaging Technology. *Applied Surface Science* **2020**, *510* (January), 145428.
- (8) Wang, T.; Jing, L. C.; Zhu, Q.; Sagadevan Ethiraj, A.; Tian, Y.; Zhao, H.; Yuan, X. T.; Wen, J. G.; Li, L. K.; Geng, H. Z. Fabrication of Architectural Structured Polydopamine-Functionalized Reduced Graphene Oxide/Carbon

- Nanotube/PEDOT:PSS Nanocomposites as Flexible Transparent Electrodes for OLEDs. *Applied Surface Science* **2020**, *500* (September 2019), 143997.
- (9) Lozano-Hernández, L. A.; Maldonado, J. L.; Hernández-Cruz, O.; Nicasio-Collazo, J.; Rodríguez, M.; Barbosa-García, O.; Ramos-Ortíz, G.; Zolotukhin, M. G.; Scherf, U. Structurally Simple OLEDs Based on a New Fluorinated Poly(Oxindolylidenearylene). *Dyes and Pigments* **2020**, *173* (July 2019), 1–10.
- (10) Yin, D.; Chen, Z. Y.; Jiang, N. R.; Liu, Y. F.; Bi, Y. G.; Zhang, X. L.; Han, W.; Feng, J.; Sun, H. B. Highly Transparent and Flexible Fabric-Based Organic Light Emitting Devices for Unnoticeable Wearable Displays. *Organic Electronics* **2020**, *76* (July 2019), 105494.
- (11) Romanov, A. S.; Jones, S. T. E.; Gu, Q.; Conaghan, P. J.; Drummond, B. H.; Feng, J.; Chotard, F.; Buizza, L.; Foley, M.; Linnolahti, M.; et al. Carbene Metal Amide Photoemitters: Tailoring Conformationally Flexible Amides for Full Color Range Emissions Including White-Emitting OLED. *Chemical Science* **2020**, *11* (2), 435–446.
- (12) Pan, F.; Sun, C.; Bin, H.; Angunawela, I.; Lai, W.; Meng, L.; Ade, H.; Li, Y. Side-Chain Engineering of Medium Bandgap Polymer Donors for Efficient Polymer Solar Cells. *Organic Electronics* **2020**, *78* (October 2019), 105603.
- (13) Wang, S.; Wu, S.; Ling, Z.; Chen, H.; Lian, H.; Portier, X.; Gourbilleau, F.; Marszalek, T.; Zhu, F.; Wei, B.; et al. Mechanically and Thermally Stable, Transparent Electrodes with Silver Nanowires Encapsulated by Atomic Layer Deposited Aluminium Oxide for Organic Optoelectronic Devices. *Organic Electronics* **2020**, *78* (October 2019), 105593.
- (14) Tiwari, S.; Purabgola, A.; Kandasubramanian, B. Functionalised Graphene as Flexible Electrodes for Polymer Photovoltaics. *Journal of Alloys and Compounds* **2020**, *825*, 153954.
- (15) Get, R.; Islam, S. M.; Singh, S.; Mahala, P. Organic Polymer Bilayer Structures for Applications in Flexible Solar Cell Devices. *Microelectronic Engineering* **2020**, *222* (November 2019), 111200.
- (16) Li, G.; Zou, X.; Cheng, J.; Chen, D.; Yao, Y.; Chang, C.; Yu, X.; Zhou, Z.;

- Wang, J.; Liu, B. Impact of Perovskite Composition on Film Formation Quality and Photophysical Properties for Flexible Perovskite Solar Cells. *Molecules* **2020**, *25* (3), 4–13.
- (17) Park, S. J.; Yu, B. S.; Jeon, J. Y.; Kang, B. C.; Ha, T. J. Sol-Gel Based Zirconium Dioxide Dielectrics by Oxygen-Annealing at Low Temperature for Highly Stable and Robust Flexible Resistive Random Access Memory. *Journal of Alloys and Compounds* **2020**, *825*, 154086.
- (18) Xue, D.; Song, H.; Zhong, X.; Wang, J.; Zhao, N.; Guo, H.; Cong, P. Flexible Resistive Switching Device Based on the TiO<sub>2</sub> Nanorod Arrays for Non-Volatile Memory Application. *Journal of Alloys and Compounds* **2020**, *822*, 153552.
- (19) Fu, J.; Kang, W.; Guo, X.; Wen, H.; Zeng, T.; Yuan, R.; Zhang, C. 3D Hierarchically Porous NiO/Graphene Hybrid Paper Anode for Long-Life and High Rate Cycling Flexible Li-Ion Batteries. *Journal of Energy Chemistry* **2020**, *47*, 172–179.
- (20) Liu, J.; Li, D.; Wang, Y.; Zhang, S.; Kang, Z.; Xie, H.; Sun, L. MoO<sub>2</sub> Nanoparticles/Carbon Textiles Cathode for High Performance Flexible Li-O<sub>2</sub> Battery. *Journal of Energy Chemistry* **2020**, *47*, 66–71.
- (21) Gao, H.; Ning, S.; Zou, J.; Men, S.; Zhou, Y.; Wang, X.; Kang, X. The Electrocatalytic Activity of BaTiO<sub>3</sub> Nanoparticles towards Polysulfides Enables High-Performance Lithium–Sulfur Batteries. *Journal of Energy Chemistry* **2020**, *48*, 208–216.
- (22) Wang, T.; Zhang, R.; Wu, Y.; Zhu, G.; Hu, C.; Wen, J.; Luo, W. Engineering a Flexible and Mechanically Strong Composite Electrolyte for Solid-State Lithium Batteries. *Journal of Energy Chemistry* **2020**, *46*, 187–190.
- (23) Liu, J.; Li, D.; Zhang, S.; Wang, Y.; Sun, G.; Wang, Z.; Xie, H.; Sun, L. Hierarchical N-Doped Carbon Nanocages/Carbon Textiles as a Flexible O<sub>2</sub> Electrode for Li–O<sub>2</sub> Batteries. *Journal of Energy Chemistry* **2020**, *46*, 94–98.
- (24) Zhang, J.; Li, W.; Hu, D.; Ahmed Shifa, T.; Chen, S.; Xu, G.; Cui, Y. Insight into the Role of Interfacial Reconstruction of Manganese Oxides toward Enhanced Electrochemical Capacitors. *Chemical Engineering Journal* **2020**, *388*

- (January).
- (25) Guo, T.; Zhang, G.; Zhang, H.; Su, X.; Chen, X.; Wan, J.; Wu, H.; Liu, C. Highly Flexible, Stable and Transparent Capacitors with Enhanced Performances by Composite Electrodes of AZO and Metallic Nanomeshes. *Journal of Alloys and Compounds* **2020**, *819*.
- (26) Chen, S.; Meng, G.; Kong, B.; Xiao, B.; Wang, Z.; Jing, Z.; Gao, Y.; Wu, G.; Wang, H.; Cheng, Y. Asymmetric Alicyclic Amine-Polyether Amine Molecular Chain Structure for Improved Energy Storage Density of High-Temperature Crosslinked Polymer Capacitor. *Chemical Engineering Journal* **2020**, *387* (2020), 123662.
- (27) Liu, Y.; Pharr, M.; Salvatore, G. A. Lab-on-Skin: A Review of Flexible and Stretchable Electronics for Wearable Health Monitoring. *ACS Nano* **2017**, *11* (10), 9614–9635.
- (28) Dickey, M. D.; Chiechi, R. C.; Larsen, R. J.; Weiss, E. A.; Weitz, D. A.; Whitesides, G. M. Eutectic Gallium-Indium (EGaIn): A Liquid Metal Alloy for the Formation of Stable Structures in Microchannels at Room Temperature. *Advanced Functional Materials* **2008**, *18* (7), 1097–1104.
- (29) Tabatabai, A.; Fassler, A.; Usiak, C.; Majidi, C. Liquid-Phase Gallium-Indium Alloy Electronics with Microcontact Printing. *Langmuir* **2013**, *29* (20), 6194–6200.
- (30) Fan, X.; Nie, W.; Tsai, H.; Wang, N.; Huang, H.; Cheng, Y. PEDOT : PSS for Flexible and Stretchable Electronics: Modifications , Strategies , and Applications. *Advanced Science* **2019**, *6*, 1900813.
- (31) Kim, S. J.; Choi, K.; Lee, B.; Kim, Y.; Hong, B. H. Materials for Flexible, Stretchable Electronics: Graphene and 2D Materials. *Annual Review of Materials Research* **2015**, *45* (1), 63–84.
- (32) Jiang, L.; Zhang, J.; Gamota, D.; Takoudis, C. G. Organic Thin Film Transistors with Novel Thermally Cross-Linked Dielectric and Printed Electrodes on Flexible Substrates. *Organic Electronics* **2010**, *11* (5), 959–963.
- (33) Sun, W.; Zhao, J.; Chen, S.; Guo, X.; Zhang, Q. Thermally Cross-Linked

- Polyvinyl Alcohol as Gate Dielectrics for Solution Processing Organic Field-Effect Transistors. *Synthetic Metals* **2019**, *250*, 73–78.
- (34) Liu, P.; Wu, Y.; Li, Y.; Ong, B. S.; Zhu, S. Enabling Gate Dielectric Design for All Solution-Processed, High-Performance, Flexible Organic Thin-Film Transistors. *Journal of the American Chemical Society* **2006**, *128* (14), 4554–4555.
- (35) Wang, C.; Lee, W. Y.; Nakajima, R.; Mei, J.; Kim, D. H.; Bao, Z. Thiol-Ene Cross-Linked Polymer Gate Dielectrics for Low-Voltage Organic Thin-Film Transistors. *Chemistry of Materials* **2013**, *25* (23), 4806–4812.
- (36) Li, S.; Feng, L.; Zhao, J.; Guo, X.; Zhang, Q. Low Temperature Cross-Linked, High Performance Polymer Gate Dielectrics for Solution-Processed Organic Field-Effect Transistors. *Polymer Chemistry* **2015**, *6* (32), 5884–5890.
- (37) Wang, C. H.; Hsieh, C. Y.; Hwang, J. C. Flexible Organic Thin-Film Transistors with Silk Fibroin as the Gate Dielectric. *Advanced Materials* **2011**, *23* (14), 1630–1634.
- (38) Fukuda, K.; Hikichi, K.; Sekine, T.; Takeda, Y.; Minamiki, T.; Kumaki, D.; Tokito, S. Strain Sensitivity and Durability in P-Type and n-Type Organic Thin-Film Transistors with Printed Silver Electrodes. *Scientific Reports* **2013**, *3*, 1–6.
- (39) Sirringhaus, H. 25th Anniversary Article : Organic Field-Effect Transistors : The Path Beyond Amorphous Silicon. *Advanced Materials* **2014**, *26*, 1319–1335.
- (40) Cosseddu, P.; Tiddia, G.; Milita, S.; Bonfiglio, A. Continuous Tuning of the Mechanical Sensitivity of Pentacene OTFTs on Flexible Substrates : From Strain Sensors to Deformable Transistors. *Organic Electronics* **2013**, *14* (1), 206–211.
- (41) Choi, H. H.; Yi, H. T.; Tsurumi, J.; Kim, J. J.; Briseno, A. L.; Watanabe, S.; Takeya, J.; Cho, K.; Podzorov, V. A Large Anisotropic Enhancement of the Charge Carrier Mobility of Flexible Organic Transistors with Strain: A Hall Effect and Raman Study. *Advanced Science* **2019**, *7* (1), 1901824.
- (42) Cosseddu, P.; Milita, S.; Bonfiglio, A. Strain Sensitivity and Transport Properties in Organic Field-Effect Transistors. *IEEE ELECTRON DEVICE LETTERS* **2012**, *33* (1), 113–115.

- (43) Scenev, V.; Cosseddu, P.; Bonfiglio, A.; Salzmann, I.; Severin, N.; Oehzelt, M.; Koch, N. Origin of Mechanical Strain Sensitivity of Pentacene Thin-Film Transistors. *Organic Electronics* **2013**, *14* (5), 1323–1329.
- (44) Sekitani, T.; Kato, Y.; Iba, S.; Shinaoka, H.; Someya, T. Bending Experiment on Pentacene Field-Effect Transistors on Plastic Films. *Applied Physics Letters* **2005**, *86*, 073511.
- (45) Yang, C.; Yoon, J.; Kim, S. H.; Hong, K.; Chung, D. S.; Heo, K.; Eon, C.; Ree, M. Bending-Stress-Driven Phase Transitions in Pentacene Thin Films for Flexible Organic Field-Effect Transistors. *Applied Physics Letters* **2008**, *92*, 243305.
- (46) Chen, F.; Chen, T.; Zeng, B.; Chung, Y. Influence of Mechanical Strain on the Electrical Properties of Flexible Organic Thin-Film Transistors. *Semiconductor Science and Technology* **2011**, *26*, 034005.
- (47) Kaprinska, J.; Laurent, A.; Sanguinet, L.; Hunter, S.; Anthopoulos, T.; Lemaur, V.; Kennedy, A. R.; Fenwick, O.; Samori, P.; Geerts, Y. H. Design, Synthesis, Chemical Stability, Packing, and Charge Transport Characteristics of [1]Benzothieno[3,2-b][1]Benzothiophene Derivatives. *Journal of Materials Chemistry C* **2016**, *4*, 4863–4879.
- (48) Campos, A. G. Influence of Organic Semiconductors Morphology , Structure and Processability on Organic Field-Effect Transistors Performance, 2018.
- (49) Schrode, B.; Jones, A. O. F.; Resel, R.; Bedoya, N.; Schennach, R.; Geerts, Y. H.; Ruzié, C.; Sferrazza, M.; Brillante, A.; Salzillo, T.; et al. Substrate-Induced Phase of a Benzothiophene Derivative Detected by Mid-Infrared and Lattice Phonon Raman Spectroscopy. *ChemPhys* **2018**, *19* (8), 993–1000.
- (50) Lauro, M. Di; Berto, M.; Giordani, M.; Benaglia, S.; Schweicher, G.; Vuillaume, D.; Bortolotti, C. A.; Geerts, Y. H.; Biscarini, F. Liquid-Gated Organic Electronic Devices Based on High-Performance Solution-Processed Molecular Semiconductor. *Advanced Electronic Materials* **2017**, *3*, 1700159.
- (51) Casalini, S.; Bortolotti, C. A.; Leonardi, F.; Biscarini, F. Self-Assembled Monolayers in Organic Electronics. *Chemical Society Reviews* **2017**, *46* (1), 40–71.

- (52) Niazi, M. R.; Li, R.; Abdelsamie, M.; Zhao, K.; Anjum, D. H.; Payne, M. M.; Anthony, J.; Smilgies, D. M.; Amassian, A. Contact-Induced Nucleation in High-Performance Bottom-Contact Organic Thin Film Transistors Manufactured by Large-Area Compatible Solution Processing. *Advanced Functional Materials* **2016**, *26* (14), 2371–2378.
- (53) Leonardi, F.; Tamayo, A.; Casalini, S.; Mas-Torrent, M. Modification of the Gate Electrode by Self-Assembled Monolayers in Flexible Electrolyte-Gated Organic Field Effect Transistors: Work Function: Vs. Capacitance Effects. *RSC Advances* **2018**, *8* (48), 27509–27515.
- (54) Gentili, D.; Gazzano, M.; Melucci, M.; Jones, D.; Cavallini, M. Polymorphism as an Additional Functionality of Materials for Technological Applications at Surfaces and Interfaces. *Chemical Society Reviews* **2019**, *48* (9), 2502–2517.
- (55) Zhang, Q.; Leonardi, F.; Casalini, S.; Temiño, I.; Mas-Torrent, M. High Performing Solution-Coated Electrolyte-Gated Organic Field-Effect Transistors for Aqueous Media Operation. *Scientific Reports* **2016**, *6* (November), 1–10.
- (56) Lewis, J. Material Challenge for Flexible Organic Devices. *Materials Today* **2006**, *9* (4), 38–45.
- (57) Sokolov, A. N.; Cao, Y.; Johnson, O. B.; Bao, Z. Mechanistic Considerations of Bending-Strain Effects within Organic Semiconductors on Polymer Dielectrics. *Advanced Functional Materials* **2012**, *22* (1), 175–183.
- (58) Haiting, A.; Deng, L.; Tang, Q.; Tong, Y.; Liu, Y. Flexible Organic Single-Crystal Field-Effect Transistor for Ultra-Sensitivity Strain Sensing. *IEEE Electron Device Letters* **2017**, *38* (11), 1598–1601.
- (59) Lai, S.; Garufi, A.; Madeddu, F.; Angius, G.; Bonfiglio, A.; Cosseddu, P. A Wearable Platform for Monitoring Wrist Flexion and Extension in Biomedical Applications Using Organic Transistor-Based Strain Sensors. *IEEE Sensors Journal* **2019**, *19* (15), 6020–6028.
- (60) Rang, Z.; Haraldsson, A.; Kim, D. M.; Ruden, P. P.; Nathan, M. I.; Chesterfield, R. J.; Frisbie, C. D. Hydrostatic-Pressure Dependence of the Photoconductivity of Single-Crystal Pentacene and Tetracene. *Applied Physics*

- Letters* **2001**, 79 (17), 2731–2733.
- (61) Jha, P.; Koiry, S. P.; Saxena, V.; Veerender, P.; Gusain, A.; Chauhan, A. K.; Debnath, A. K.; Aswal, D. K.; Gupta, S. K. Air-Stability and Bending Properties of Flexible Organic Field-Effect Transistors Based on Poly[N-90-Heptadecanyl-2, 7-Carbazole-Alt-5,5-(40,70-Di-2- Thienyl-20,10, 30-Benzothiadiazole)]. *Organic Electronics* **2013**, 14 (10), 2635–2644.
- (62) Zhang, Q.; Leonardi, F.; Pfattner, R.; Mas-Torrent, M. A Solid-State Aqueous Electrolyte-Gated Field-Effect Transistor as a Low-Voltage Operation Pressure-Sensitive Platform. *Advanced Materials Interfaces* **2019**, 6 (16), 1–8.
- (63) Lee, K. H.; Zhang, S.; Lodge, T. P.; Frisbie, C. D. Electrical Impedance of Spin-Coatable Ion Gel Films. *Journal of Physical Chemistry B* **2011**, 115 (13), 3315–3321.
- (64) Liu, Z.; Qi, D.; Guo, P.; Liu, Y.; Zhu, B.; Yang, H.; Liu, Y.; Li, B.; Zhang, C.; Yu, J.; et al. Thickness-Gradient Films for High Gauge Factor Stretchable Strain Sensors. *Advanced Materials* **2015**, 27, 6230–6237.
- (65) Laukhina, E.; Pfattner, R.; Ferreras, L. R.; Galli, S.; Mas-Torrent, M.; Masciocchi, N.; Laukhin, V.; Rovira, C.; Veciana, J. Ultrasensitive Piezoresistive All-Organic Flexible Thin Films. *Advanced Materials* **2010**, 22 (9), 977–981.
- (66) Ferreras, L. R.; Pfattner, R.; Mas-Torrent, M.; Laukhina, E.; López, L.; Laukhin, V.; Rovira, C.; Veciana, J. Highly Piezoresistive Textiles Based on a Soft Conducting Charge Transfer Salt. *Journal of Materials Chemistry* **2011**, 21 (3), 637–640.
- (67) Lai, S.; Temiño, I.; Cramer, T.; del Pozo, F. G.; Fraboni, B.; Cosseddu, P.; Bonfiglio, A.; Mas-Torrent, M. Morphology Influence on the Mechanical Stress Response in Bendable Organic Field-Effect Transistors with Solution-Processed Semiconductors. *Advanced Electronic Materials* **2018**, 4 (10), 1–9.





# CHAPTER 5

## *General conclusions*

---

In this thesis, we have studied different aspects related to liquid-gated organic transistors, in particular electrolyte-gated organic field-effect transistors (EGOFETs) and organic electrochemical transistors (OECTs), including their fabrication, their electrical characterization and their application in biosensing. The EGOFET devices were fabricated mainly on plastic substrates by depositing from solution, *p*-type small molecule organic semiconductors (OSC) blended with insulating polymers exploiting the bar-assisted meniscus shearing technique (BAMS). OECT devices were realized by the microfabrication process employing the conducting polymer PEDOT:PSS as active layer.

The main part of the project was dedicated to the design and development of a biosensor for the detection of an important biomarker for neurodegenerative diseases, including Parkinson's disease, namely  $\alpha$ -synuclein. Then, the research was focused on the study of a BTBT-based EGOFET, with special attention on its electrical performances, stability in liquid environment and response to mechanical deformation. The main conclusions of the investigations reported in this thesis are the following:

1. An ultra-sensitive, label-free, low-cost and easy-to-use biosensor for the detection of  $\alpha$ -synuclein at the sub-picomolar level is still urgent for the early diagnosis and follow up of neurodegenerative diseases. Here, we have designed label-free immunosensors based on liquid-gated transistors, EGOFET and OECT devices, by exploiting the functionalization of the gold gate surface with anti-( $\alpha$ -

synuclein) antibodies to act as the biorecognition element. Different immobilization strategies have been explored. Regarding EGOFET biosensors, they exhibited a limit of detection (LOD) in the sub-picomolar level and a sensitivity which spanned six orders of magnitude, from  $10^{-13}$  M to  $10^{-7}$  M, proving to be promising candidates for the ultimate development of an  $\alpha$ -synuclein biosensor. Despite the much less explored use of OECTs in immunosensing, we demonstrated that they are also responsive towards  $\alpha$ -synuclein. Although a lower sensitivity was achieved with respect to EGOFETs due to the different operating principles driving these devices, OECTs could bring other advantages such as the current measured is higher and the stability in water of the active layer is, in principle, also greater.

2. Apart from the studies at the lab scale, it is important to develop a low-cost, fast, easy-to-use and portable biosensing chip. For this aim, a more compact device displaying a unique engineered layout was conceived for a more applicative  $\alpha$ -synuclein biosensor based on EGOFETs. The system was embedded with a microfluidics cell and a coplanar gold gate, to allow the *in-situ* functionalization of the gate electrode and the physical separation between the sensing area and the active layer, avoiding cross-contamination and achieving a more stable system. This microfluidics chip permits a semi-automated measurement in a short time (in the range of a few minutes) including the gate functionalization and the transistor measurement.

3. The fabrication of highly performing EGOFETs requires finding stable organic semiconductor thin films to their exposition and operation in water. A route to improve the device stability in aqueous media is the blending of organic semiconductor with an insulating polymer. In particular, we have shown that thin films of the organic semiconductor  $C_8O$ -BTBT- $OC_8$  blended with  $PS_{100k}$  and deposited by BAMS exhibit an excellent performance as EGOFET. On Si/SiO<sub>2</sub> substrates they showed a  $C_{eff} \cdot \mu_{FE,lin} = 0.16(\pm 0.02) \mu S \cdot V^{-1}$ , while the films based on only the  $C_8O$ -BTBT- $OC_8$  displayed a  $C_{eff} \cdot \mu_{FE,lin} = 0.09(\pm 0.06) \mu S \cdot V^{-1}$ . The OSC blended with PS thin film exhibited also better stability, able to operate 12 h at stable conditions and showing higher capacity to stand the liquid environment.

4. To integrate EGOFET devices into wearable applications it is for utmost important to fabricate them on flexible substrates and also to investigate their response to mechanical deformations. Here, the  $C_8O$ -BTBT- $OC_8$ : $PS_{100k}$  thin films were deposited on plastic substrates, namely *Kapton*® and PEN, displaying a high state-of-the-art performance with  $C_{eff} \cdot \mu_{FE,lin}$  equal to  $0.13(\pm 0.05) \mu S \cdot V^{-1}$  and  $0.07(\pm 0.02) \mu S \cdot V^{-1}$ , respectively. In a second step, electrical response to tensile and compressive strain was studied. We observed that the transfer integrals were not importantly affected and did not follow any trend by the application of small deformations. However, by current monitoring a high device sensitivity at low strains was observed. This was attributed to the fact that in these conditions the electrical equilibrium was reached. This is the first time, as far as we know, that bending properties have been assessed in EGOFET devices, which is crucial for the understanding of the operating mechanisms taking place in EGOFETs and for their application in implantable sensing systems.



# CHAPTER 6

## *Experimental methodologies*

---

### 6.1. Materials

- **Materials for device fabrication**

**Highly *n*-doped Silicon wafers** were purchased from SiMat with the following characteristics: Diameter: 100 mm; Type/Dopant: N/Sb; Orientation: <1-0-0>; Resistivity: <0.05-0.02>  $\Omega\cdot\text{cm}$ ; Thickness:  $525\pm 25\ \mu\text{m}$ ; Front Surface: Polished; Back Surface: Etched; Flats: SEMI Standard.

**Kapton<sup>®</sup>HN foils** were purchased from DuPont, 25  $\mu\text{m}$ , 75  $\mu\text{m}$  and 125  $\mu\text{m}$  thick.

**Polyethylene naphthalate (PEN)** foils were purchased from GoodFellow, 75  $\mu\text{m}$  and 125  $\mu\text{m}$  thick.

Shipley Microposit **S1813** photoresist and Shipley Microposit **MF-319** developer were purchased from Shipley.

2,8-difluoro-5,11-bis(triethylsilylethynyl)anthradithiophene (**diF-TES-ADT**) was obtained from Lumtec and used as received (purity>99%), racemic mixture.

2,7-dioctyloxy[1]benzothieno[3,2-b]benzo-thiophene (**C<sub>8</sub>O-BTBT-OC<sub>8</sub>**) was synthesized by the group of Prof. Y. Geerts from Université Libre de Bruxelles.<sup>1</sup>

**Polystyrene (PS)** (MW: 3000 g/mol, 10000 g/mol, 100000 g/mol) was purchased from Sigma-Aldrich and used without any further purification.

## Chapter 6

2,3,4,5,6-pentafluorothiophenol (**PFBT**) was purchased from Sigma-Aldrich.

**Dextran** was purchased from *Leuconostoc spp.* ( $M_r$  <450000-650000> g/mol) was procured from Sigma-Aldrich.

Poly(3,4-ethylenedioxythiophene)-poly(styrenesulfonate) (**PEDOT:PSS**), PH1000, was purchased from Heraeus GmbH.

(3-glycidyloxypropyl)trimethoxysilane (**GOPS**) was purchased from Sigma-Aldrich.

Ethylene glycol (**EG**) was obtained from Sigma-Aldrich.

Poly(methyl methacrylate) (**PMMA**) was received from Sigma-Aldrich.

**SU-8 2010**, negative photoresist was purchased from MicroChem.

- **Biological molecules**

**$\alpha$ -synuclein human**, recombinant, expressed in *E. coli*, was purchased from Sigma-Aldrich.

**$\alpha$ -synuclein antibody (211)** was obtained from Santa Cruz Biotechnology, Inc.

**Recombinant His-tag protein G (PG)**, was purchased from BioVision, Inc.

- **General products and procedures**

**Polydimethylsiloxane (PDMS)**, *Qsil216 A/B* was purchased from Farnell Componentes.

HS-(CH<sub>2</sub>)<sub>11</sub>-(OCH<sub>2</sub>CH<sub>2</sub>)<sub>6</sub>-NH<sub>2</sub>·HCl (abbreviated as **HS-C<sub>11</sub>-EG<sub>6</sub>-NH<sub>2</sub>**) was purchased from ProChimia Surfaces and used as received.

**1-mercaptohexanol (HS-C<sub>6</sub>-OH)** and **8-amino-1-octanethiol (HS-C<sub>8</sub>-NH<sub>2</sub>)** were purchased from Sigma-Aldrich and used as received.

**Glutaraldehyde (Gl)**, 25% wt water-based solution, was obtained from Sigma-Aldrich.

**Inorganic salts:** NaCl, KCl, Na<sub>2</sub>HPO<sub>4</sub>, NaH<sub>2</sub>PO<sub>4</sub>, K<sub>3</sub>Fe(CN)<sub>6</sub> were purchased from Sigma-Aldrich.

**Organic solvents:** anhydrous chlorobenzene (CB) was purchased from Sigma-Aldrich. Acetone, isopropanol, ethanol (HPLC grade) were purchased from Teknocroma Analítica S.A.

**Electrodes:** Pt wire (Ø= 0.5 mm) and Au wire (Ø= 0.5 mm) were purchased from Sigma-Aldrich, Au disk electrode (Ø= 1.6 mm) from BASi<sup>®</sup>, Ag/AgCl reference electrode from Allum.

**Phosphate Buffer Saline (PBS)** was prepared according to the following recipe: NaCl 0.137 M, KCl 0.00027 M, Na<sub>2</sub>HPO<sub>4</sub> 0.01 M, KH<sub>2</sub>PO<sub>4</sub> 0.0018 M. The pH of the solutions was adjusted by employing HCl 1 M or NaOH 1 M.

**PDMS gasket production:** the two components of the *Qsil216* kit were weighted in a ratio 10:1. They were mixed strongly for approximately two minutes in a Petri dish. Thus, the Petri dish was put under vacuum for 1 h in order to remove bubbles air. Afterwards, it was cured at 70°C overnight.

## 6.2. Au surface biofunctionalization

### • Chapter 2

The Au cleaning procedure was common for both Approach I and Approach II functionalization routes. It consisted in: i) immersion of a Au wire (Ø= 0.5 mm) in a solution of NaOH 1 M for 15 minutes heating to 100 °C, ii) Au wire dipping in concentrated H<sub>2</sub>SO<sub>4</sub> for 15 minutes at 100 °C, iii) cyclic voltammetry (CV) in H<sub>2</sub>SO<sub>4</sub> 1 M, sweeping the potential from -0.1 V to 1.6 V, approximately 15 cycles.



### **Ab immobilization protocol for Approach I**

1. HS-C<sub>11</sub>-EG<sub>6</sub>-NH<sub>2</sub>-based SAM formation: incubation of the cleaned Au wire into an Eppendorf containing 1 mM thiol solution in EtOH, overnight at 4 °C.
2. Activation of the amino group of the SAM: the SAM-coated Au wire was rinsed with EtOH and water and dried with a N<sub>2</sub> flow. Afterwards, it was immersed in a glutaraldehyde solution (2.5% wt in water) for 1 h at 4 °C.
3. Ab immobilization: the Au wire was rinsed with distilled water prior to its incubation into the Ab solution (40 µg/mL in PBS 1x at pH 7.2) for 15 minutes at room temperature (R.T.). Finally, the substrates were rinsed with distilled water.

### **Ab immobilization protocol for Approach II**

1. Functionalisation of Au with PG: the cleaned Au wire was incubated in a PG solution (140 µg/mL in PBS 1x at pH 5.5) for 15 minutes at R.T.
2. Ab immobilisation: PG-coated Au wire was rinsed with PBS 1x solution to remove physisorbed material and then incubated in the Ab solution (40 µg/mL in PBS 1x at pH 5.5) for 15 minutes at R.T.

These protocols were followed for both electrochemistry and EGOFETs measurements.

### **Sensing studies with EGOFET devices**

1. **Top-gated EGOFETs:** all the functionalization steps of the gold gate were carried out *ex-situ*, by immersion of the gold wire (Ø= 0.5 mm) into Eppendorf containing the solutions of interest. The two sensing platforms were exposed to  $\alpha$ -synuclein solutions at increasing concentrations, namely 0.25 pM, 2.5 pM, 10 pM, 50 pM, 250 pM, 1 nM, 2.5 nM, 25 nM, 250 nM, incubating for 15 minutes at R.T. Dilutions were prepared from the stock solution (1 mg/mL) in PBS 1x at physiological pH. Before performing electrical measurements, the electrodes were first rinsed with water to wash away physisorbed molecules and then inserted in

the EGOFET platform as the gate terminal. For each functionalization step at least three transfer characteristics were recorded by sweeping  $V_{GS}$  from +0.4 V to -0.1 V at a constant  $V_{DS} = -0.1$  V.

2. **Microfluidics coplanar-gated EGOFETs:** HS-C<sub>11</sub>-EG<sub>6</sub>-NH<sub>2</sub>-based SAM was immobilized on the coplanar Au gate surface and prepared *ex-situ* by microcontact printing technique ( $\mu$ CP).<sup>2</sup> A droplet of 1 mM solution of HS-C<sub>11</sub>-EG<sub>6</sub>-NH<sub>2</sub> in EtOH was cast onto the surface of cured polydimethylsiloxane (PDMS) stamp, which was subsequently pushed onto the Au film surface and stored at 4 °C for 10 minutes. Afterwards, the PDMS stamp was removed and the surface was rinsed with EtOH and MilliQ water. Once the SAM was formed, the microfluidics system was mounted on top of the device which was connected to the potentiostat in order to carry out the sensing experiment. The microfluidics system is explained in detail in section 6.7. The electrolyte used for operating the device (PBS 0.01x, pH=7) was flown from *Inlet1* to fill up the so-called chamber 1 containing the interdigitated electrodes (IDEs) and a reference gate, RG. The protein-containing solutions were injected from *Inlet2* through the chamber 2, which contains the sensing gate, SG. The SAM was activated *in-situ* by flowing glutaraldehyde (50  $\mu$ L, 2.5% wt in water) at a flow rate equal to 10  $\mu$ L/min and, subsequently, the Ab solution was streamed (50  $\mu$ L, 40  $\mu$ g/mL in PBS 1x at pH 7). Afterwards, PBS 1x solution was flown continuously for at least 3 minutes, to wash away physisorbed materials. A peristaltic pump was operating simultaneously both at the *Inlet2* and at the *Outlet*, to help the pumping out of the liquids injected from *Inlet2*, maintaining the same flow rate, namely 10  $\mu$ L/min. At this point the flow was stopped and at least three transfer characteristics were recorded with SG, by sweeping  $V_{GS}$  from +0.1 V to -0.4 V at a constant  $V_{DS} = -0.1$  V. The same procedure was followed for the  $\alpha$ -synuclein detection: i) flow of 50  $\mu$ L of the  $\alpha$ -synuclein at a known concentration in PBS 1x at physiological pH, employing a low flow rate of 10  $\mu$ L/min, ii) 3 minutes wash with PBS 1x at pH 7 at 10  $\mu$ L/min, iii) stop of the flow and recording of transfer characteristics with the SG. The following  $\alpha$ -synuclein concentrations were used: 0.25 pM, 2.5 pM, 25 pM, 250 pM, 2.5 nM, 25 nM.

A stabilization of the device was carried out before the sensing experiment employing RG. Transfers measurements were recorded before and after the experiment session with RG, in order to check the integrity of the active layer.

- **Chapter 3**

Two different thiol molecules were used for the formation of a mixed SAM on Au surface, *viz.* 6-mercaptohexanol (HS-C<sub>6</sub>-OH) and 8-amino-1-octanethiol (HS-C<sub>8</sub>-NH<sub>2</sub>). Au disk electrodes (Ø= 1.6 mm) were employed. These electrodes were mechanically polished with a 0.5 µm Alumina powder and electropolished in H<sub>2</sub>SO<sub>4</sub> by CV, sweeping the potential from -0.1 V to 1.6 V for 15 cycles.

### **Ab immobilisation protocol**

1. Preparation of the mixed SAM: 1 mM solutions of HS-C<sub>6</sub>-OH and HS-C<sub>8</sub>-NH<sub>2</sub> in EtOH were prepared. Afterwards, these solutions were mixed in the following ratio: 1:1, 1:10, 1:100 (HS-C<sub>8</sub>-NH<sub>2</sub>:HS-C<sub>6</sub>-OH). The Au disk electrodes were incubated in these solutions overnight at 4 °C.
2. Activation of the amino groups: the Au disk was rinsed with EtOH and distilled water and incubated in glutaraldehyde solution (2.5% wt in water) for 1 h at 4 °C.
3. Ab immobilisation: the Au disk was rinsed with distilled water and incubated in the Ab solution (10 µg/mL in PBS 1x pH 7.2) for 1 h at R.T.
4. Deactivation of the non-reacted terminal aldehyde groups: the Ab-coated surface was immersed in a Tris buffer solution (2-Amino-2-hydroxymethylpropane-1,3-diol) at physiological pH for 15 minutes at R.T.

### **Sensing studies with OECT devices**

1. α-synuclein detection: the Ab-coated surfaces were dipped in increasing concentration of α-synuclein solutions for 1 h at R.T. The following concentrations

were used: 0.05 nM, 0.25 nM, 5 nM, 50 nM, 250 nM. Before performing the electrical measurements, the Au surface was rinsed with water to remove physisorbed molecules and implemented as the gate terminal in the OECT devices. At least three transfer characteristics were recorded by sweeping  $V_{GS}$  from -0.1 V to +0.6 V at a constant  $V_{DS} = -0.1$  V and  $V_{DS} = -0.5$  V. Alternatively, pulsed measurements were performed by applying 10 s  $V_{GS}$  pulses (0.05 V, 0.10 V, 0.15 V, 0.20 V, 0.25 V, 0.30 V, 0.35 V, 0.40 V) under a constant  $V_{DS} = -0.1$  V.

These procedures were used also for electrochemical analysis.

### **6.3. Morphological and Structural Thin films and SAMs Characterization**

- **Optical microscopy**

Olympus BX51 microscope was employed to obtain cross-polarized images. The microscope was equipped with a light polarizer and 90° analyser in order to assess the crystallinity of the semiconductor films.

- **X-ray Photoelectron Spectroscopy (XPS)**

XPS measurements were performed at R.T. with a SPECS PHOIBOS 150 hemispherical analyser (SPECS GmbH, Berlin, Germany) in a base pressure of  $5 \times 10^{-10}$  mbar using monochromatic Al K-alpha radiation (1486.74 eV) as excitation source.

- **Atomic Force Microscopy (AFM)**

AFM images were acquired by a 5500LS SPM system from Agilent Technologies, in tapping mode. Kelvin Probe Force Microscopy (KPFM) images were obtained by working in amplitude mode and applying AC and DC voltage to the sample. The measurements were carried out in ambient conditions. The results were analysed with Gwyddion 2.47 software.

- **X-Ray Diffraction (XRD)**

The crystal phase identification and thin film orientation were performed by X-ray powder diffractograms in the  $2\theta$  range 5-40° (step size: 0.02°; time/step: 1 s; 35 mA x 45kV) collected on a Siemens D-5000 diffractometer using as source a ceramic Tub DRX and Cu anode ( $\lambda$ : CuK $\alpha$ 1= 1.540560 Å, CuK $\alpha$ 2= 1.544390 Å), equipped with scintillation detector in Bragg-Brentano geometry. The program Mercury2 was used for simulation of X-ray powder patterns on the basis of single crystal data. Chemical and structural identity between bulk material and single crystal was verified by comparing experimental and simulated powder diffraction patterns. Thin film orientation and crystal plane were identified by comparison with theoretical morphologies calculated by classic BFDH model (Bravais, Friedel, Donnay and Harker).<sup>3-5</sup>

- **Polarization Modulation-Infrared Reflection-Absorption Spectroscopy (PM-IRRAS)**

Polarization Modulation-Infrared Reflection-Absorption Spectroscopy (PM-IRRAS) spectra were recorded by using a Bruker Vertex 70 spectrometer with PM50 module equipped with a liquid-nitrogen-cooled mercury-cadmium-telluride (MCT) photodetector and a permanently aligned Rock Solid interferometer. To reduce absorption due to water and carbon dioxide, the spectrometer was purged by fluxing nitrogen gas. The Bruker spectroscopy software OPUS, version4.2, was used to operate the spectrometer. Reflection measurements were performed with an aperture of 6 mm in diameter on the primary side and on aperture of the secondary side at a resolution of 2 cm<sup>-1</sup>. The incidence angle was set to the Brewster angle of the SiO<sub>2</sub> at 57° to get the best signal-to-noise ratio.

## **6.4. Devices fabrication and characterization**

- **EGOFETs**

The devices were fabricated either on Si/SiO<sub>2</sub>, Kapton® and PEN substrates employing the following protocol.

### Au electrodes design and Au evaporation

Au electrodes were made up by photolithography process in the 10000 class Clean Room facility at the ICMAB-CSIC. The electrodes pattern was designed by CleWin4 software. The substrate was cleaned up by rinsing with acetone and isopropanol and dried with a N<sub>2</sub> flow. The positive photoresist (Shipley 1813) was deposited by spin-coating at 5000 rpm for 25 s, employing a spin-coater from Laurell Technologies, WS- 650SZ-6NPP/LITE. The photoresist-coated substrate was subsequently baked on a hotplate for 1 minute at 90 °C and next placed on the laser micro-writer system, MLTM from Durham Magneto Optics LTD. After exposure to the laser source (405 nm laser wavelength), the substrate was dipped into the developer solution (Shipley Microposit MF-319) for approximately 1 minute, agitating the baker. During this process, the portion of photoresist exposed to the laser beam, corresponding to Source, Drain and Gate electrodes, was solubilized and washed away. Afterwards, the substrates were rinsed with distilled water and dried with a N<sub>2</sub> flow. At this point, the substrate was located into the evaporation chamber (Evaporation System Auto 306 from Boc Edwards) and a thin layer of Cr (5 nm) was first evaporated acting as adhesive layer for the successive deposition of Au (40 nm). Finally, lift-off process removed the photoresist and metals layers in excess, by sonication of the substrate in acetone and isopropanol during 15 minutes, repeating the process three times for each solvent.

Concerning the layout of the electrodes employed, in **Figure 6.1** the general pattern of the interdigitated electrodes is presented. The devices fabricated for the work developed in chapter 2 exhibited the following characteristics: channel length,  $L= 30 \mu\text{m}$ , channel width,  $W= 18000 \mu\text{m}$ ,  $W/L= 600$ . For the devices reported in chapter 4:  $L= 50 \mu\text{m}$ ,  $W= 18000 \mu\text{m}$ ,  $W/L= 360$ .

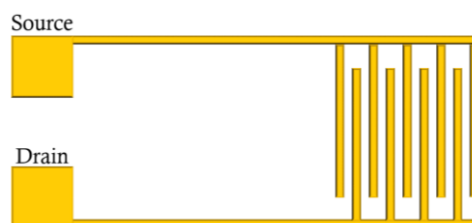


**Figure 6.1.** Scheme of the interdigitated Source and Drain electrodes employed.

### Organic Semiconductor formulation and deposition

The OSC formulations were prepared by following a well-established protocol in our group.<sup>6-8</sup> The pure OSC was dissolved in CB in 2% wt. Regarding the OSC:PS blend preparation, both OSC and PS were dissolved in CB in 2% wt. and afterwards mixed in a 4:1 ratio. Before OSC deposition, the substrate was cleaned with acetone and isopropanol rinsing and then exposed to UV Ozone cleaner for 25 minutes. Afterwards, it was immediately dipped into the 2,3,4,5,6-pentafluorothiophenol (PFBT) solution (2  $\mu\text{L}/\text{mL}$  in isopropanol) for 15 minutes. Then, it was rinsed abundantly with isopropanol to remove physisorbed thiol molecules and dried with a  $\text{N}_2$  flow. Concerning the coplanar gate device configuration, previously to PFBT functionalization of the IDEs, the gate surface was covered with a sacrificial layer, specifically a drop of dextran solution (10 mg/mL in water) was cast into the Au surface and let it dry. Indeed, dextran is not soluble in isopropanol but it is in water and, hence, it was removed by rinsing with distilled water, after the source-drain PFBT functionalisation and OSC deposition.

The OSC was deposited on the substrate by Bar-Assisted Meniscus Shearing technique (BAMS).<sup>9,10</sup> A custom-made bar-coater or a commercial one from RK were employed (see **Figure 6.2**). The hot-plate of the BAMS was heated to 105  $^\circ\text{C}$ , beyond the boiling point of CB. A droplet of the OSC formulation (approximately 25-50  $\mu\text{L}$  depending on the substrate dimension) was placed in between the bar and the substrate until a meniscus was formed. The bar was then moved at a speed rate of 1  $\text{cm}\cdot\text{s}^{-1}$ .



**Figure 6.2.** (a) Commercial bar-coater from RK, (b) Custom-made bar-coater.

- **OECTs**

The OECTs were fabricated in the 1000 class Clean Room facility at the Department of Science and Technology in Linköping University.

The substrate used was polyethylene naphthalate, PEN (Teonex Q65HA, 125  $\mu\text{m}$ , Peutz Folien GMBH).

### **Au evaporation and electrodes patterning**

The substrates were washed with distilled water and acetone and dried with a  $\text{N}_2$  flow. The cleaned substrates were mounted into a metal evaporator (Moorfield, model T090M) placed within a glovebox and a thin adhesive layer of Cr (2 nm) was evaporated before the Au deposition (50 nm).

Afterwards, the samples were washed again with distilled water and acetone. A soft baking was performed (90 s at 110  $^\circ\text{C}$ ) to remove any residual solvent. Subsequently, a positive photoresist (Shipley 1805) was spin-coated at 4000 rpm for 30 s. The soft baking was repeated. The photoresist-coated samples were mounted into the mask-aligner (Karl Suss MA/MB 6 mask aligner) and exposed to the laser beam through a negative mask. Then, the samples were dipped into the developer solution (Shipley MF-319) in order to dissolve the portion of the photoresist which was exposed to the laser. The Au and Cr in excess were removed by wet etching: the substrates were i) immersed in a  $\text{I}_2/\text{KI}$  solution for at least 20 s agitating, ii) washed abundantly with distilled water, iii) immersed into the Cr etcher solution for at least 20 s and under agitation, iv) washed abundantly with distilled water and v) dried with a  $\text{N}_2$  flow. Finally, the substrates were stripped with acetone to remove the residual photoresist.

### **PEDOT: PSS deposition: active channel and gate patterning**

A PEDOT:PSS (Clevios PH1000) solution was prepared by adding 5% v/v of ethylene glycol (EG) and 0.5% v/v of 3-glycidyloxypropyl (GOPS) to the commercial preparation, and sonicating 30 minutes to make the solution homogeneous. Then this solution was spin-coated on the substrate at 2500 rpm for 30 s. PEDOT:PSS thin film was annealed at 110  $^\circ\text{C}$  for 2 h. Poly(methyl methacrylate) (PMMA) and the positive



photoresist (Shipley 1813) were subsequently spin-coated on the PEDOT-coated substrate. PMMA was used in order to i) increase the adhesion of the photoresist and ii) protect the PEDOT:PSS layer upon the exposure to the developer solution. At this stage, the substrate was processed again with the mask-aligner and then dipped into the developing solution (DM-319). The portion of PEDOT:PSS deprotected from the photoresist was removed by dry-etching. The dry-etching was carried out with a  $\text{CF}_4/\text{O}_2$  reactive ion etch (RIE from Advanced Vacuum, Vacutec). Finally, the sample was dipped in acetone to remove residual photoresist. At this point, the sample was immersed into a solution of NaCl 1 M in order to re-establish the correct pH neutrality of PEDOT:PSS.

### Encapsulation layer

The last step of the OEETs fabrication consisted in making an encapsulation layer in order to protect the Au source-drain electrode contacts from electrolyte exposure during the electrical measurements. For this aim an epoxy-based negative photoresist was used (SU-8 2010, MicroChem). This resist was spin-coated at 3000 rpm for 30 s. Afterwards, a baking under vacuum was performed applying a gradient of temperature, reaching 110 °C in 10 minutes.

Afterwards, the sample was exposed to the laser beam in the mask-aligner using a specific pre-formed mask. After the photolithographic process, the sample was baked under vacuum 4 minutes at 110°C. The sample was dipped into the developer solution (MR DEV 600) to remove the undesired photoresist.

Finally, the sample was immersed in isopropanol for about 30 s and dried with a  $\text{N}_2$  flow. The channel length,  $L$  was equal to 20  $\mu\text{m}$ ,  $W$  was equal to 100  $\mu\text{m}$  and the gate area was equal to 0.25  $\text{mm}^2$ .



**Figure 6.3.** Layout of the microfabricated OEET (S: source, D: drain and G: gate).

Finally, for both EGOFET and OECT devices, a polydimethylsiloxane (PDMS) pool was conceived in order to confine the liquid electrolyte on the active layer and the coplanar gate area.

- **Electrical measurements and device parameters extraction**

The electrical characterization of the EGOFET devices described in **chapter 2** were carried out by two-channel Keithley Source Meters 2400 and 2601 operated with a homemade MATLAB script. The OECT devices reported in **chapter 3** were measured by Keithley Source Meters and homemade software. Devices reported in **chapter 4** were characterized by means of an Agilent B1500A analyser equipped with Easy Expert software. Electrical measurements under strain were performed with a Keithley 2612A Source Meter controlled by a homemade MATLAB script.

Regarding the extraction of devices parameters, MOSFET theory was used.

1. **Threshold voltage,  $V_{th}$**

It was calculated by the linear fit of the  $I_{DS}$  vs  $V_{GS}$  curve for the linear regime, or the  $|I_{SD}|^{1/2}$  vs  $V_{GS}$  curve for the saturation regime and using the following equation:

$$V_{th} = -\frac{b}{a} \quad (6.1)$$

where  $b$  is the slope and  $a$  is the y-intercept of the linear fittings.

2. **Field-effect mobility,  $\mu_{FE}$ , and capacitance,  $C$**

They were calculated using (6.2) from the transfer characteristics in the linear regime:

$$\mu_{FE} \cdot C = \frac{L}{W} \frac{a}{V_{DS}} \quad (6.2)$$

where  $L$  is the channel length,  $W$  is the channel width,  $a$  is the slope of the linear fit of the  $I_{DS}$  vs  $V_{GS}$  curve.

In the saturation regime equation (6.3) was used:

$$\mu_{FE} \cdot C = \frac{2L}{W} a^2 \quad (6.3)$$

where  $a$  represents the slope of the  $|I_{SD}|^{1/2}$  vs  $V_{GS}$  curve of the transfer characteristics.

### 3. Transconductance, $g_m$

$$g_m = \frac{\partial I_{DS}}{\partial V_{GS}} \quad (6.4)$$

where  $I_{DS}$  is the drain-source current,  $V_{GS}$  is the gate-source potential and  $V_{DS}$  is the drain-source potential.

### 4. Subthreshold swing, $SS$

$$SS = \left( \frac{\partial \log |I_{DS}|}{\partial V_{DS}} \right)^{-1} \quad (6.5)$$

## 6.5. Electrochemistry

Electrochemical experiments were performed with an Autolab potentiostat/galvanostat (PGSTAT128N), employing a three-electrode standard cell, Pt wire as the counter electrode, Ag/AgCl as the reference electrode and a Au wire ( $\varnothing = 0.5$  mm) or Au disk ( $\varnothing = 1.6$  mm) as the working electrode (see **Figure 6.4**).

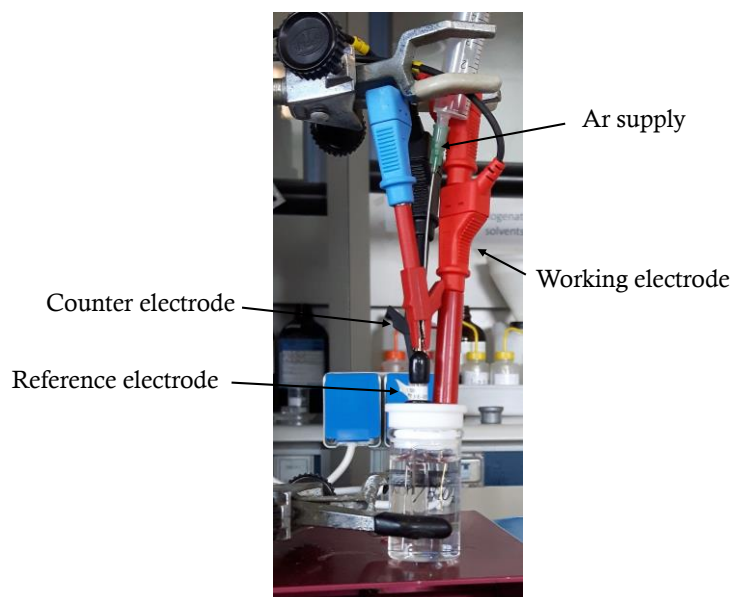


**Figure 6.4.** Real picture of the electrochemical setup used.

- **Cyclic Voltammetry**

Cyclic Voltammetry (CV) is a widely used electrochemical technique for the assessment of electroactive molecules and for the study of processes occurring at metal/liquid interfaces.<sup>11</sup> It consists in sweeping the potential back and forward to a working electrode with respect to a reference electrode and measuring the resulting current flowing at the counter electrode. The data obtained are plotted in the so-called cyclic voltammograms. The appearance of peaks in the forward direction are an indication of oxidation events, on the contrary, peaks in the backward scans are an estimation of reductive processes, according to IUPAC convention. The area underneath the peak is proportional to the charge involved in the redox reaction, according to the Faraday's law:

$$Q = z F n \quad (6.6)$$

where  $Q$  is the total charge,  $z$  is the number of the electrons involved in the reaction,  $F$  is the Faraday's constant equal to  $9.6485 \cdot 10^4 \text{ C} \cdot \text{mol}^{-1}$ , and  $n$  is the number of moles of the electroactive substance. To extract  $Q$ , the area obtained by the integration of the reductive peak must be divided for the scan rate used during the measurement.

In this thesis work, CV was performed at different scan rates and at different window potentials depending on the specific experiment.

- **Differential Pulse Voltammetry**

Differential Pulse Voltammetry (DPV) is a sub-class of pulsed voltammetry techniques in which a pulsed ramp potential is applied to the working electrode, in a one direction. The current is measured just before and after the pulse in a manner that subtracting these current values, the contribution to the capacitive current is eliminated, enhancing the sensitivity of this technique with respect to CV. Indeed, DPV curves can be seen as the first derivative of CV curves (see **Figure 6.5**).<sup>11,12</sup>

Differential Pulse Voltammetry (DPV) was carried out with the redox probe in solution, specifically  $K_3[Fe(CN)_6]$ , sweeping the potential from -0.1 V to +0.5 V applying a modulation amplitude equal to 25 mV and a scan rate equal to  $10 \text{ mV}\cdot\text{s}^{-1}$ .

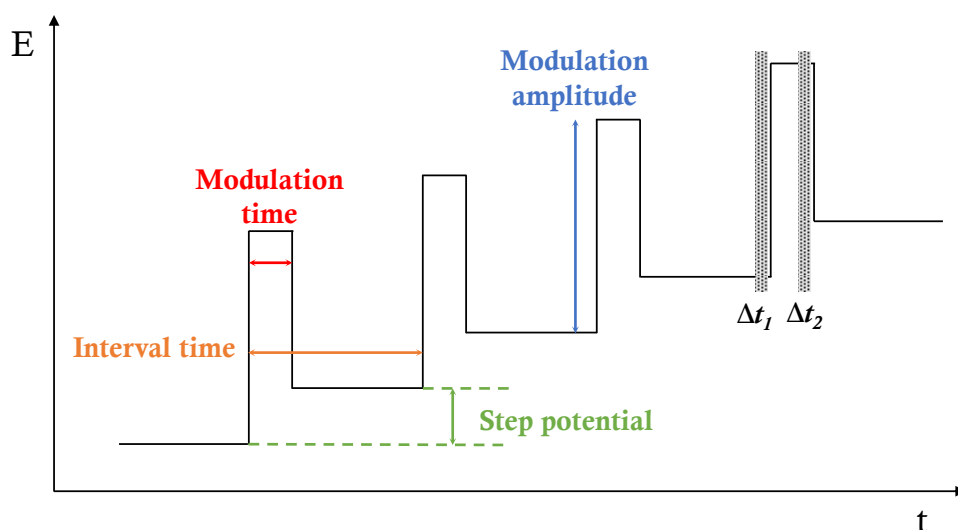


**Figure 6.5.** Time-potential profile in DPV measurements.

- **Electrochemical Impedance Spectroscopy**

Electrochemical Impedance Spectroscopy (EIS) is a widely employed technique for the study of the phenomena occurring at the interface between a metal electrode and an

electrolyte. It measures the response of the system when it is perturbed with an alternating signal of small magnitude. The characteristic representations of the results are the so-called i) Nyquist plot in which the imaginary part of the impedance is plotted as a function of the real part, ii) Bode plot in which the angle phase variation or the impedance module are plotted as a function of the frequency. From the Nyquist plot, different parameters can be extrapolated by fitting the data with the so-called *Randles* equivalent circuit: solution resistance ( $R_s$ ), charge-transfer resistance ( $R_{ct}$ ), double-layer capacitance ( $C_{dl}$ ).<sup>11</sup> Indeed, the current flowing through the working interface depends on faradaic processes and on double layer charging ( $C_{dl}$ ), which are inserted in parallel, as it is shown in **Figure 6.6**. In this case, the faradaic contribution is represented by the general impedance,  $Z$ , which can be further divided into the charge-transfer resistance ( $R_{ct}$ ), a pure resistance, and the Warburg element ( $W$ ), which is an indication of resistance to mass transfer and takes into account non ideal behaviours. Finally, in series with these elements, there is  $R_s$ , which represents the intrinsic resistance of the solution to current flowing.

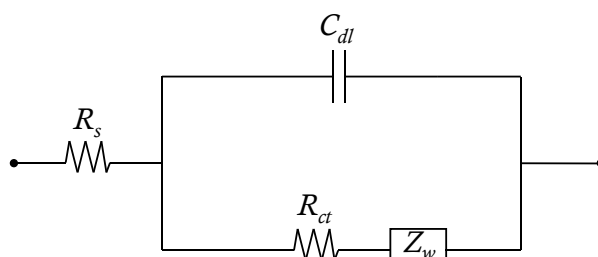


**Figure 6.6.** *Randles* equivalent circuit.

Electrochemical Impedance Spectroscopy (EIS) was recorded sweeping the frequency from 0.1 MHz to 0.1 Hz and using an AC amplitude equal to 10 mV. The DC voltage potential was set according to the redox potential of the redox probe or according to the open circuit potential (OCP) when no redox probe was employed.

## 6.6. Surface Plasmon Resonance

The characterization of the biofunctionalized Au surface by means of Surface Plasmon Resonance (SPR) technique has been performed through the ICTS NANBIOSIS platform, more specifically in the Biodeposition and Biodetection Unit of the CIBER

in Bioengineering, Biomaterials & Nanomedicine (CIBER-BBN) at the Catalan Institute of Nanoscience and Nanotechnology (ICN2).

The SPR platform adopted was a home-made instrument (*Sensia  $\beta$ -SPR*), that employed the Kretschmann configuration and incorporated two flow cells (300 nL each) for independent analysis. The device used 1 cm<sup>2</sup> gold chips (2 nm Cr, 50 nm Au) and incorporated all the optics, electronics and fluidics components necessary to operate autonomously. The laser wavelength was equal to 670 nm.

Before use, Au chips were cleaned according to the following protocol: i) sonication in acetone, ethanol and water for 1 minute each, ii) exposure to UV Ozone cleaner for 30 minutes. The flow rate was equal to 25  $\mu$ L/min.

The Au surface functionalization was carried out *in-situ*, except for the immobilization of the HS-C<sub>11</sub>-EG<sub>6</sub>-NH<sub>2</sub> due to the incompatibility of the microfluidic tubes with ethanol solvent.

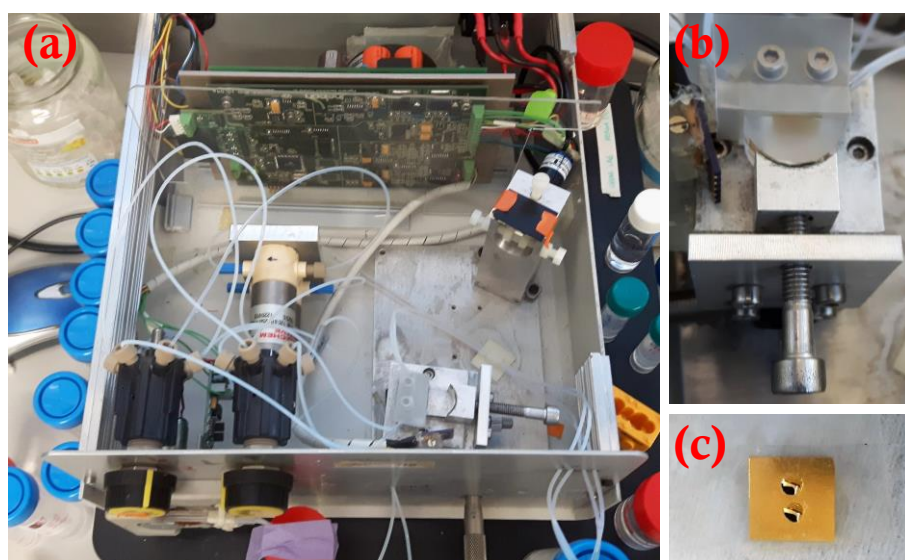


**Figure 6.7.** Real pictures of the *Sensia  $\beta$ -SPR* instrument. (a) inner top-view of the apparatus, formed by two 6-loop valves injectors (bottom left part), laser source (top right part), prism, cell containing Au chip and light collector (bottom right part). (b) zoom of the prism attached to the Au chip. (c) Au chip covered with pre-patterned parafilm for the confinement of the electrolyte into the two separate cells.

## 6.7. Microfluidics fabrication

The microfluidics setup was designed and developed in collaboration with SCRIBA Nanotecnologie S.r.l.

It was designed in order to have the sensing platform separate from the transducing zone, aiming at no cross-contamination between the two chambers and, thus, at having a more reliable sensing system. The system was formed by two main components: i) an inner part which comprises a polydimethylsiloxane (PDMS) circuit which serves to confine/flow the electrolyte and the electronic substrate, which was made of Si/SiO<sub>2</sub> or plastic materials and ii) an outer holder which was thought to fix the entire system (see **Figure 6.8**). The holder was designed for having a better liquid insulation and for fixing all the components: i) the substrates containing the electrode, ii) the PDMS microfluidic chambers, iii) the microfluidics tubes. The top part of the holder contained openings for the positioning of the tips and windows at the corresponding part of the sensing gate and the chamber 1 in order to facilitate the control of the solution flow. Furthermore, a removable tailor-made cap was 3D printed to prevent the IDEs zone from ambient light exposure. The top and bottom parts of the holder were secured with M2 screws (**Figure 6.8,c**).

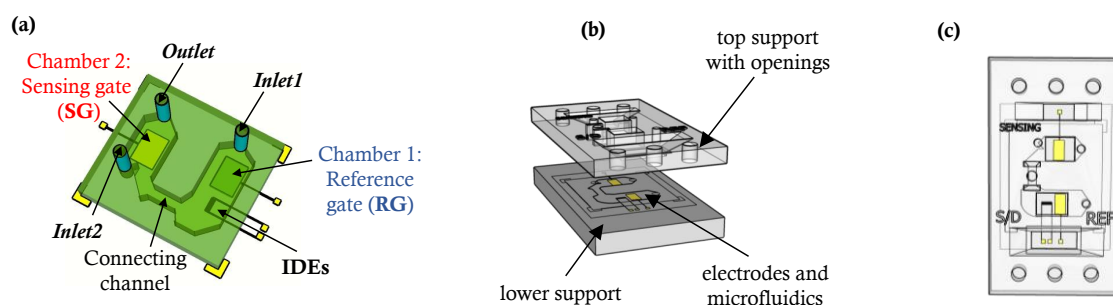


**Figure 6.8.** 3D scheme of the microfluidics device. (a) schematic representation of the inner components: microfluidic channel assembled on the substrates containing the interdigitated electrodes (IDEs) and the reference gate electrode (chamber 1), sensing gate (chamber 2). (b) Cartoon of the outer holder lateral and (c) top view.

The PDMS circuit was shaped through plastic moulds (see **Figure 6.9**) in which the PDMS was cured, employing the same procedure explained above. When the PDMS was ready, it was detached from the moulds with the aid of a cutter, paying attention to not damage the cured polymer.



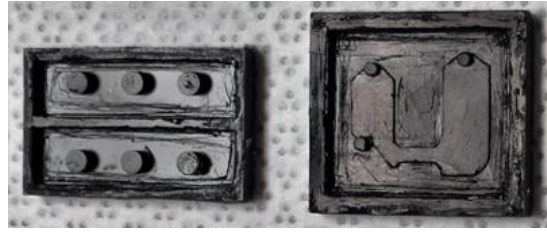


**Figure 6.9.** Real pictures of the PDMS curing moulds for the fabrication of the microfluidics channels.

For the design of the holder and the microfluidics channel moulds, SketchUp 2017 software was used. These components were printed with Digital Light Processing (DLP) 3D printer model “B9Creator V1.2HD”, featuring high-precision characteristics ( $z, x, y$  resolution =  $30\ \mu\text{m}$ ). The resin of choice was “B9R-2-Black”.

In **Figure 6.10** is shown the final setup mounted and integrated into the probe station during electrical measurements.

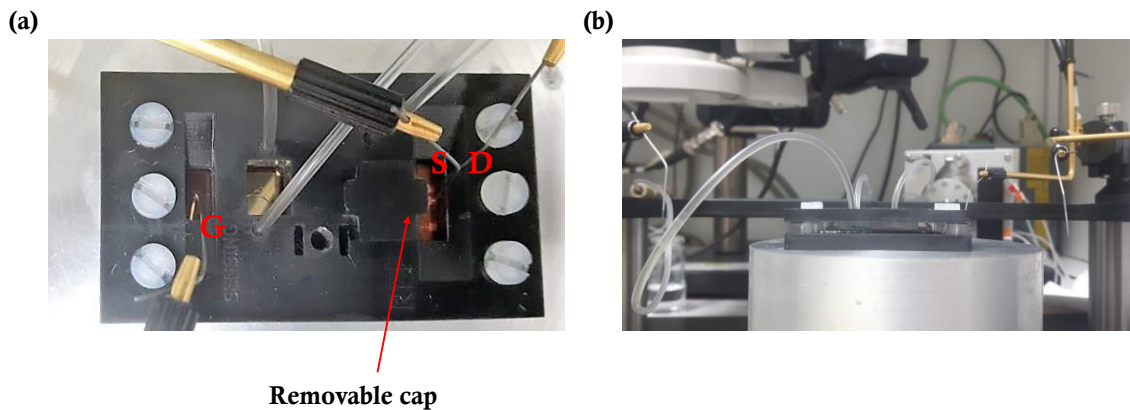


**Figure 6.10.** (a) Top image of the microfluidics setup integrated in the probe station for electrical measurements. (b) Lateral image of the final setup.

## 6.8. Bending measurement setup

For the bending measurements, a home-made apparatus was conceived, by assembling different components.

The electrodes were patterned on  $25\ \mu\text{m}$  thick *Kapton*<sup>®</sup> foils. The devices were placed into the holder shown in **Figure 6.11** and secured at the extremities by M2 screws. A pivot allowed the stretching and compression of the spring situated beyond

the holder, by manually rotating it. The stretching of the spring promoted the bending of the *Kapton*<sup>®</sup> substrate towards the up, tensile stress, or down, compressive stress, direction.

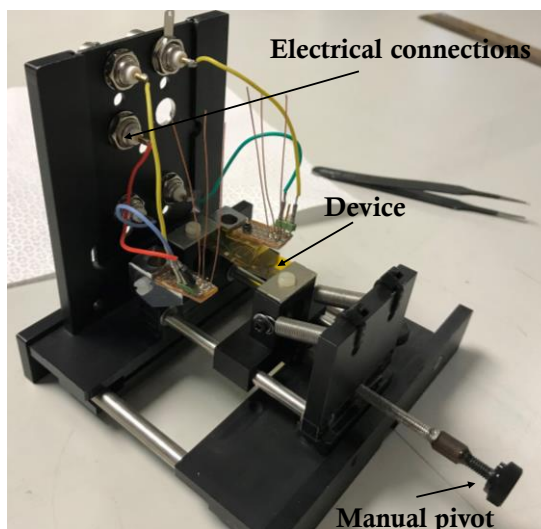


**Figure 6.11.** Central core of the bending apparatus, real picture.

At one extremity of the sample holder, Copper wires were welded with a micro welding torch into a breadboard, along with electric cable which were connected to the potentiostat through banana connectors (BCN). To the extremity of the Copper wires thin Al wires ( $\text{Ø} = 110(\pm 10) \mu\text{m}$ ) were welded, which were attached to the pads of the device with Silver paste. A thin layer of PDMS was cured in a Petri dish. A small circular pool was obtained by a puncher ( $\text{Ø} = 6.5 \text{ mm}$ ), and then it was placed on top of the source-drain interdigitated and gate electrodes, in order to confine water and allow electrical connection. After having mounted the substrate into the bending apparatus, a droplet of water, approximately  $100 \mu\text{L}$ , was placed within the PDMS pool. At this point, all the cables were connected through BCN at the Keithley.

The applied strain was estimated from the following equation:

$$\varepsilon = t/2r \quad (6.7)$$

where  $\varepsilon$  is the applied strain,  $t$  is the thickness of the substrate and  $r$  is the radius of curvature. In order to quantitatively calculate the bending radius, a camera was placed near the bending apparatus and for each rotation of the pivot a picture was taken, as

illustrated in **Figure 6.12**. Thus, by drawing an imaginary circumference matching the substrate bending, the radius was extracted and used to estimate the strain.



**Figure 6.12.** Real picture of the setup used for bending measurements. 1: electrical connections. 2: apparatus for the samples bending. 3: optical camera. 4: laptop connected to the camera.

## Bibliography

- (1) Ruzie, C.; Karpinska, J.; Laurent, A.; Sanguinet, L.; Hunter, S.; Anthopoulos, T. D.; Lemaire, V.; Cornil, J.; Kennedy, A. R.; Fenwick, O.; et al. Design, Synthesis, Chemical Stability, Packing, Cyclic Voltammetry, Ionisation Potential, and Charge Transport of [1]Benzothieno[3,2-b]-[1]Benzothiophene Derivatives. *Journal of Materials Chemistry C* **2016**, *4*, 4863–4879.
- (2) Wilbur, J. L.; Whitesides, G. M.; Kumar, A.; Biebuyck, H. A.; Kim, E. Microcontact Printing of Self-Assembled Monolayers: Applications in Microfabrication. *Nanotechnology* **2002**, *7*(4), 452–457.
- (3) Donnay J.D.H., D. H. A New Law of Crystal Morphology Extending the Law of Bravais. **1937**, *22* (5), 446–467.
- (4) M. G, F. Études Sur La Loi de Bravais. *Bulletin de Minéralogie* **1907**.
- (5) Bravais, A. *Études Cristallographiques*; Gauthier-Villars, 1866.
- (6) Leonardi, F.; Casalini, S.; Zhang, Q.; Galindo, S.; Gutiérrez, D.; Mas-Torrent, M. Electrolyte-Gated Organic Field-Effect Transistor Based on a Solution Sheared Organic Semiconductor Blend. *Advanced Materials* **2016**, *28* (46), 10311–10316.
- (7) Pérez-Rodríguez, A.; Temiño, I.; Ocal, C.; Mas-Torrent, M.; Barrena, E. Decoding the Vertical Phase Separation and Its Impact on C8-BTBT/PS Transistors Properties. *ACS Applied Materials & Interfaces* **2018**, *10*, 7296–7303.
- (8) Zhang, Q.; Leonardi, F.; Casalini, S.; Temiño, I.; Mas-Torrent, M. High Performing Solution-Coated Electrolyte-Gated Organic Field-Effect Transistors for Aqueous Media Operation. *Scientific Reports* **2016**, *6* (November), 1–10.
- (9) Del Pozo, F. G.; Fabiano, S.; Pfattner, R.; Georgakopoulos, S.; Galindo, S.; Liu, X.; Braun, S.; Fahlman, M.; Veciana, J.; Rovira, C.; et al. Single Crystal-like Performance in Solution-Coated Thin-Film Organic Field-Effect Transistors. *Advanced Functional Materials* **2016**, *26* (14), 2379–2386.
- (10) Temiño, I.; Del Pozo, F. G.; Ajayakumar, M. R.; Galindo, S.; Puigdollers, J.;

Mas-Torrent, M. A Rapid, Low-Cost, and Scalable Technique for Printing State-of-the-Art Organic Field-Effect Transistors. *Advanced Materials Technologies* **2016**, *1* (5), 1–7.

- (11) Bard, A. J.; Faulkner, L. R. *Electrochemical Methods. Fundamentals and Applications*; 2001.
- (12) Scholz, F. Voltammetric Techniques of Analysis: The Essentials. *ChemTexts* **2015**, *1* (4), 1–24.

